Emplacement, alteration history, ore genesis, and timing of mineralization, of iron oxide apatite ores and their host rocks in the Norrbotten region of northern Sweden

by

© Anne Westhues

A Thesis submitted to the

School of Graduate Studies

in partial fulfillment of the requirements for the degree of

Doctor of Philosophy

Department of Earth Sciences

Memorial University of Newfoundland

May 2017

St. John's, Newfoundland

ABSTRACT

The origin of the iron oxide apatite (IOA) deposits around Kiruna in the Norrbotten region of northern Sweden, and similar deposits worldwide, has been debated for decades. Contrasting theories include: 1) iron oxide extracted from an immiscible silicate liquid-iron oxide melt; or 2) iron oxide transported and subsequently emplaced by hydrothermal fluids. This study is the first to combine detailed geochemical studies and in situ U-Pb dating on accessory minerals with tracer isotope geochemistry on the whole rock and mineral scale to explore the different hypotheses.

In situ U-Pb geochronology of zircon and titanite confirms a previously documented event around 1880-1900 Ma in the Norrbotten region, but dates the altered metavolcanic rocks in the footwall and hanging wall of the ore and a syenite more accurately at 1884 to 1880 Ma. A granite pluton has an age of 1874 Ma, in close overlap with zircon from two ore bodies (1877 – 1874 Ma). Zircon from the host rocks and the granite exhibit typical igneous growth zoning, whereas all zircon from the iron ore and some from intrusions show hydrothermal influences in texture and chemistry, including weight percent of water. Younger U-Pb dates from monazite and titanite suggest later events influencing the Kiruna IOA deposits between 1772 and 1628 Ma.

The isotopic systems used in this study, ranging from whole rock Sm-Nd and Lu-Hf to in situ oxygen and Lu-Hf in zircon, all show significant differences between samples from host rocks and ore. These differences can be best explained when invoking hydrothermal fluids at the magmatic-to-hydrothermal transition (T > 600 ºC) possibly exsolved from the intrusions, to mobilise and concentrate iron oxides as the massive IOA

deposits. The main ore forming event is thought to have occurred around 1874 Ma, and Hf and Nd isotopic signatures suggest a depleted mantle source for these fluids, potentially related to the Kiruna greenstone group, which could also be an important iron source. Later hydrothermal events influenced the iron ores between 1772 and 1628 Ma and Sm-Nd isotope signatures of monazite indicate crustal inputs during this time frame, when part of the ore may have been remobilized.

ACKNOWLEDGEMENTS

My first big “thank you” goes to my PhD supervisor Dr. John M. Hanchar, who designed this thesis and allowed me to put my personal stamp on the project. John established the initial contact with the mining company LKAB in northern Sweden, ensured the financing of the project and enabled me to travel for field work, analyses and several conferences. The discussion with John and his advice during the last years have been invaluable for this PhD project. Many thanks go to Kirsten Holme, who during her time at LKAB did everything to make our work go as smoothly as possible, and numerous others at the mining company, including, but not limited to U.B. Anderson, H. Rutanen, and C. Debras. Martin Whitehouse introduced me to the SIMS technology and his guidance was vital during data processing and interpretation of results. Olof Martinsson is thanked for introducing me to the geology of Kiruna, assistance during field work and many discussions over the years. There are almost too many people to thank for assistance in the labs, discussions, and general advice at Memorial University, including, but by no means limited to M. Wilson, S. Piercey, G. Layne, G. Dunning, C. Fisher, S. Strong, P. King, R. Lam, W. Aylward, S. Jantzi, L. Hewa, C. Voisey, M. LeMessurier, S. Phillips and S. Broughm. For help with analyses outside of MUN, I want to thank K. Lindén, A. Bouvier, C. Fisher, R. Wirth, and G. Rossman. J. Anderson, A. Hallberg, S. Bergman, and J. Perdåhl at the Geological Survey of Sweden are thanked for helpful discussion of the regional geology of Sweden. The project was financially supported by NSERC, MUN, SEG, and MAC.

And, finally, I would not have been able to come to this point without the patient support of my husband Edgars Rudzitis and my family in Germany. My friends and fellow

grad students (wherever they are right now, in Newfoundland or around the world) were always there for me, and my colleagues at the Geological Survey of Newfoundland and Labrador have been very supportive over the final year of this project.

Table of Contents

ABSTRACT ii

ACKNOWLEDGEMENTS iv

Table of Contents vi

List of Appendices ix

List of Tables x

List of Figures xi

List of Abbreviations and Symbols xii

1 Introduction and Overview - The iron oxide apatite ore deposits of Kiruna in northern Sweden 1-1

1.1 Background 1-1

1.2 Aims & Methods 1-4

1.3 Geological overview and previous work 1-6

1.4 Structure of thesis 1-12

1.5 Co-authorship Statement 1-14

1.6 Bibliography - Introduction 1-17

2 New constraints on the timing of the host rock emplacement, hydrothermal alteration, and iron oxide-apatite in the Kiruna district, Norrbotten region, Sweden 2-1

2.1 Abstract 2-1

2.2 Introduction 2-2

2.3 Geological Setting 2-4

2.3.1 Proterozoic host rocks around the town of Kiruna 2-5

2.3.2 Iron ore types and contacts to host rocks 2-9

2.3.3 Previous dating results 2-12

2.4 Sampling: Lithology and Alteration 2-14

2.4.1 Metavolcanic host rocks 2-18

2.4.2 Syenite and granite intrusions 2-20

2.4.3 Iron oxide apatite ore 2-20

2.5 Analytical techniques 2-21

2.6 Results 2-24

2.6.1 Petrography, whole-rock major and trace geochemistry 2-24

2.6.2 Zircon imaging and U-Pb geochronology 2-30
2.6.3 Titanite imaging and U-Pb geochronology 2-40
2.7 Discussion 2-42
2.7.1 Alteration effects inferred from petrography and whole-rock geochemistry 2-42
2.7.2 U-Pb dating – Ages of host rocks and ores 2-44
2.7.3 Implications for ore formation models of Kiruna iron ores 2-48
2.8 Conclusions 2-52
2.9 Acknowledgments 2-53
2.10 Bibliography – Chapter two 2-54
3 Tracing the fluid evolution of the Kiruna iron oxide apatite deposits using zircon, monazite and whole rock trace elements and isotopic studies 3-1
3.1 Abstract 3-1
3.2 Introduction 3-2
3.3 Geological background and samples 3-5
3.4 Analytical procedures 3-8
3.5 Results 3-11
3.5.1 Major and trace elements of zircon 3-11
3.5.2 Monazite U-Pb geochronology 3-23
3.5.3 Monazite X-ray mapping 3-25
3.5.4 Whole rock rare earth element chemistry 3-27
3.5.5 Sm-Nd and Lu-Hf isotopes 3-30
3.6 Discussion 3-33
3.6.1 Hydrothermal zircon features 3-33
3.6.2 Secondary event in the Mesoproterozoic 3-39
3.6.3 Source regions based on Nd and Hf isotopes 3-40
3.7 Conclusions 3-42
3.8 Acknowledgements 3-43
3.9 Bibliography – Chapter three 3-44
4 Evidence for hydrothermal alteration and source regions for the Kiruna iron oxide apatite ore from zircon Hf and O isotopes 4-1
4.1 Abstract 4-1
4.2 Introduction 4-1

4.3 In situ Hf and O isotope results 4-4
4.4 Discussion 4-7
4.4.1 Magmatic versus hydrothermal ore genesis based on oxygen isotopes 4-7
4.4.2 Hf isotopes and source regions 4-10
4.4.3 Model for the formation of the Kiruna iron ores 4-11
4.5 Conclusions 4-12
4.6 Acknowledgements 4-14
4.7 Bibliography – Chapter four 4-14
5 Summary and Outlook 5-1
5.1 Implications of results of this project for the origin of the Kiruna IOA deposits 5-1
5.2 Comparisons with IOA and IOCG deposits worldwide, open questions, and suggested further research 5-4
5.3 Bibliography - Summary 5-9

List of Appendices

6 Appendix A – Sample description and U-Pb geochronology data for zircon and titanite, chapter two 6-1
6.1 Detailed sample description and petrography 6-1
6.1.1 Metavolcanic host rocks 6-1
6.1.2 Syenite and granite intrusions 6-3
6.1.3 Iron oxide apatite ore 6-5
6.2 References – Appendix A 6-7
7 Appendix B – Detailed analytical methods for chapter three, LA-ICPMS trace element data and U-Pb geochronology for monazite 7-1
7.1 Detailed analytical procedures 7-1
7.1.1 Sample preparation 7-1
7.1.2 Sm-Nd whole rock analyses 7-1
7.1.3 Lu-Hf whole rock analyses 7-3
7.1.4 Electron Probe Micro-Analyzer (EPMA) 7-5
7.1.5 Transmission Electron Microscopy (TEM) and Fourier Transform Infrared (FTIR) analyses 7-6
7.1.6 Trace element composition using Laser Ablation Inductively Coupled Plasma Mass Spectrometry (LA-ICPMS) 7-7
7.1.7 In situ dating of monazite by Secondary Ion Mass Spectrometry (SIMS) 7-8
7.1.8 In situ Sm-Nd analyses of monazite by Laser Ablation Inductively Coupled Plasma Mass Spectrometry (LA-ICPMS) 7-9
7.2 Reference – Appendix B 7-10
8 Appendix C– Sample preparation and analytical methods for chapter four, detailed in situ oxygen and Lu-Hf data for zircon 8-1
8.1 Samples, sample preparation, and detailed results 8-1
8.2 References – Appendix C 8-11

List of Tables

Table 2-1. Sample list with GPS locations, rock types, and mineralogy (sorted by location). ... 2-15
Table 2-2. Whole rock geochemistry from the Kiirunavaara mine. ... 2-59
Table 2-3. Whole rock geochemistry from the Per Geijer and Tuollavaara (Siam) ores. ... 2-60
Table 3-1. Summary of sample locations, mineralogy, alteration, zircon U-Pb ages, zircon Lu-Hf and oxygen isotopic signatures. ... 3-50
Table 3-2. Results of EPMA quantitative zircon analyses. ... 3-52
Table 3-3. LA-ICPMS results zircon analyses. ... 3-53
Table 3-4. Whole rock tracer radiogenic isotope compositions and initial ε values. ... 3-56
Table 3-5. Radiation damage calculation for zircon grains. ... 3-57
Table 6-1. Geochronology results for zircon from Kiirunavaara ore and host rock. ... 6-8
Table 6-2. Geochronology results for zircon from Kiirunavaara intrusions. ... 6-11
Table 6-3. Geochronology results for zircon from Nukutus, Rektorn and Tuolluvaara. ... 6-14
Table 6-4. Geochronology results for titanite. ... 6-17
Table 7-1. Electron probe micro-analyser elements measured, standards and parameters used. 7-13
Table 7-2. LA-ICPMS results (in ppm) for secondary glass standard BCR2G. ... 7-14
Table 7-3. LA-ICPMS results (in ppm) for secondary glass standard NIST-612. ... 7-15
Table 7-4. LA-ICPMS results (in ppm) for secondary standard zircon 91500. ... 7-16
Table 7-5. Average LA-ICPMS results for secondary standards in comparison with long-term MUN averages and recommended values. ... 7-17
Table 7-6. Geochronology results for monazite. ... 7-18
Table 7-7. Cup configuration and instrument operation parameters for Sm-Nd monazite LA-MC-ICPMS laser analyses at Washington State University. ... 7-22
Table 8-1. Sample list with GPS locations, rock types, and mineralogy; sorted by location. ... 8-9
Table 8-2. SIMS oxygen ratio analyses for zircon standards. ... 8-10
Table 8-3. Neptune MC-ICPMS cup configuration. ... 8-10
Table 8-4. Accepted $^{176}Hf/^{177}Hf$ isotopic composition of zircon standards. ... 8-10
Table 8-5. LA-MC-ICPMS Lu-Hf isotopic analyses of zircon standards. ... 8-13
Table 8-6. SIMS oxygen ratio analyses for zircon of Kiruna, northern Sweden. ... 8-15
Table 8-7. LA-MC-ICPMS Lu-Hf isotopic analyses of zircon from Kiruna, Sweden. ... 8-18
Table 8-8. Summary SIMS U-Pb dates, oxygen analyses and LA-MC-ICPMS Lu-Hf ratios. ... 8-22
Table 8-9. Calculation of theoretical oxygen isotopic compositions for rhyolite and dacite magmas in equilibrium with magnetite from Kiruna. ... 8-25
Table 8-10. Calculation of theoretical oxygen isotopic compositions of fluids in equilibrium with metavolcanic and intrusive rocks from Kiruna. ... 8-26

List of Figures

Figure 1-1. Simplified regional geology of the Norrbotten region. 1-8
Figure 1-2. Simplified geological map of the Kiruna area. 1-11
Figure 1-3. View of the Kiirunavaara mine. 1-11
Figure 2-1. Simplified geological map of the Kiruna area. 2-6
Figure 2-2. Ore types and different contact relationships between host rock and ore. 2-11
Figure 2-3. Selected photomicrographs of minerals and effects of metasomatic alteration. 2-17
Figure 2-4. Schematic E-W cross section through the Kiirunavaara deposit. 2-19
Figure 2-5. Plots of whole-rock geochemical data for host rocks and intrusions from Kiruna area in total alkali vs. silica diagram after Le Bas et al. (1986), and trace element discrimination diagram after Pearce (1996) and Winchester and Floyd (1977). 2-26
Figure 2-6. Plots of whole-rock geochemical data from this study shown in metasomatism discrimination diagram, modified after Hughes (1973), and in IOCG alteration discrimination diagram, modified after Montreuil et al. (2013). 2-27
Figure 2-7. Whole-rock geochemistry of ore samples. 2-29
Figure 2-8. Representative images of zircon grains from selected dated samples. 2-33
Figure 2-9. U-Pb data plotted in Tera-Wasserburg concordia diagrams for Kiirunavaara ore and host rocks. 2-39
Figure 2-10. U-Pb data shown in Tera-Wasserburg concordia diagrams for zircon from Nukutus, Rektorn, and titanite. 2-41
Figure 2-11. Summary of geochronological data for Kiruna area. 2-46
Figure 3-1. Geological map of the Kiruna area. 3-7
Figure 3-2. Quantitative EPMA results in weight percent. 3-13
Figure 3-3. Fourier transform infrared (FTIR) spectroscopy results as wavenumber (cm^{-1}) vs. absorbance for the broad water spectrum. 3-13
Figure 3-4. Selected zircon BSE images and EPMA X-ray maps. 3-15
Figure 3-5. Rare earth element concentration of zircon grains, normalized to chondrite. 3-19
Figure 3-6. Zircon from the Kiirunavaara ore sample K-1 with high REE contents in their LA signal in detail and TEM image. 3-22
Figure 3-7. Monazite U-Th-Pb geochronology. 3-24
Figure 3-8. X-ray maps of selected monazite grains. 3-26
Figure 3-9. Whole rock REE, normalized to chondritic compositions Nukutus. 3-29
Figure 3-10. εNd_i composition vs. time for whole rock (WR) ores, host rock and altered samples and monazite from the Kiruna area, Norrbotten region, Sweden and WR εNd vs. εHf. 3-32
Figure 3-11. REE patterns of grains from each KRN-11-05 and K-1, one with patterns typical for zircon (low in LREE, high in HREE) and one with elevated REE contents. 3-36
Figure 4-1. Geological map of the Kiruna area. 4-3
Figure 4-2. Zircon oxygen and Hf isotopic results. 4-6
Figure 4-3. Schematic diagram illustrating the possible formation of the Kiruna iron ore deposits by magmatic-hydrothermal processes. 4-13
Figure 6-1. Further photomicrographs of thin sections from Kiruna. 6-7
Figure 8-1. Representative CL and BSE images of zircon grains with oxygen (as $\delta^{18}O$ V-SMOW) and Lu-Hf (as initial εHf) isotopic compositions. 8-6
Figure 8-2. Oxygen analyses session overview for September 2013 and January 2014. 8-7
Figure 8-3. Plot of $^{176}Hf/^{177}Hf$ vs. $^{176}Yb/^{177}Hf$ for zircon standard measurements. 8-8

List of Abbreviations and Symbols

%	percent
‰	permille
ºC	degree Celsius
ab	albite
act	actinolite
ap	apatite
Au	Gold
B.Sc.	Bachelor of Science
BIF	banded iron formation
BSE	Back-scattered electron
bt	biotite
Ca	Calcium
CA	centrala anläggningar
cal	calcite
Caltech	California Institute of Technology
CCD	charge coupled device
Ce	Cerium
CL	cathodoluminescence
Cl	Chlorine
cm	centimeter
CREAIT	Core Research Equipment and Instrument Training Network (at MUN)
Cu	Copper
E	east
e.g.	exempli gratia (for example)
EDS	energy dispensive spectroscopy
EPMA	electron probe microanalyser
et al.	et alia (and others)
Eu	Europium
F	Fluorine
Fe	Iron
Fig.	Figure
FTIR	Fourier Transform infrared
FW	footwall
Ga	Giga Annum (billion years ago)
GFZ	Helmholtz Centre Potsdam GFZ (Geoforschungszentrum) German Research Centre for Geosciences
GIS	geographic information system
GPS	geographic positioning system
H	Hydrogen
Hf	Hafnium
hm	hematite
HW	hanging wall

Hz	Hertz
i.e.	id est (that is)
ICP-MS	inductively coupled plasma mass spectrometry
ID	isotope dilution
IOA	iron oxide apatite
IOCG	iron oxide copper gold
J	Joule
K	Potassium
Kfs	alkali feldspar
km	kilometer
KRN	Kiirunavaara
LA	laser ablation
La	Lanthanum
LKAB	Luossavaara-Kiirunavaara Aktiebolag
LREE	light rare earth elements
LTU	Luleå University of Technology
Lu	Lutetium
m	meter
M.Sc.	Master of Science
Ma	Mega Annum (million years ago)
mag	magnetite
MC	multi collector
mm	millimeter
Mn	Manganese
ms	millisecond
MSWD	mean square weighted deviation
Mt	million metric tons
MUN	Memorial University of Newfoundland
Myrs	million years
N	north
n	number of analyses, sample size
Na	Sodium
Nb	Niobium
Nd	Neodymium
NSERC	Natural Sciences and Engineering Research Council of Canada
NUK	Nukutus
O	Oxygen
P	phosphorous
p.	page
Pb	Lead
PhD	Doctor of Philosophy
PPL	plain polarized light
ppm	parts per million
qz	quartz

Rb	Rubidium
REE	rare earth elements
REK	Rektorn
RL	reflected light
rt	rutile
S	south
SE	southeast
sec	seconds
SEM	scanning electron microscope
ser	seritization
SGU	Geological Survey of Sweden (Sverige Geologiska Undersökning)
Si	Silicon
SIMS	secondary ion mass spectrometry
Sm	Samarium
Sr	Strontium
T	temperature
t	time
TAS	total alkali versus silica diagram
TEM	transmission electron microscopy
Th	Thorium
Ti	Titanium
TIMS	thermal ionization mass spectrometry
tt	titanite
TUV	Tuolluvaara
U	Uranium
V	Vanadium
VSMOW	Vienna Standard Mean Ocean Water
vol.	Volume
WR	whole rock
wt. %	weight percent
XPL	cross polarized light
Y	Yttrium
Zr	Zirconium
μm	micrometer
α	alpha, emission lines of atoms in X-ray spectroscopy (e.g., Kα of Ca)
δ	delta, notation for one part per 1,000 deviation from a standard
ε	epsilon, notation for one part per 10,000 deviation from a standard
σ	sigma, standard deviation

1 Introduction and Overview - The iron oxide apatite ore deposits of Kiruna in northern Sweden

1.1 Background

The large world-class Kiirunavaara iron ore body in the Norrbotten region of Sweden and smaller ones in the direct vicinity (e.g., Parák, 1975; Frietsch, 1978; Bergman et al., 2001) are considered the type locality for iron oxide apatite (IOA), sometimes referred to as "Kiruna-type" deposits (e.g., Hildebrand, 1986; Mücke and Younessi, 1994; Valley et al., 2010). However, both their origin and classification among the iron oxide copper gold (IOCG) group of deposits is highly debated. IOA deposits are massive, low-Ti magnetite and/or hematite deposits that commonly include apatite and share many similarities with IOCG deposits, including intense wall rock alteration, but lack economic grades of Cu and Au.

IOCG deposits sensu stricto, such as the Olympic Dam deposit in Australia, are considered by most authors to have formed involving hydrothermal fluids (Hitzman et al., 1992; Williams, 2009; Porter, 2010), however, the discussion about the origin of IOA deposits is ongoing. For Kiruna, the debate has lasted for decades whether these deposits are of magmatic origin involving an immiscible iron oxide melt (Geijer, 1935; Frietsch, 1978), of sedimentary-exhalative origin (Parák, 1975) or of hydrothermal origin (Hitzman et al., 1992; Storey and Smith, 2017). While being very well known, and economically important for iron oxides, IOA deposits are, surprisingly, not particularly well studied and clearly require further investigation. The deposits around the town of Kiruna, while being mined for over a century, are poorly understood and have been chosen as the object of this study.

The two currently favored, but contrasting formation models for IOA deposits worldwide are: 1) the emplacement of the iron ore by immiscible silicate liquid-iron oxide melts; or 2) the transportation and deposition of iron by hydrothermal fluids, similar to models for the formation of IOCG deposits. Arguments for a magmatic origin of IOA deposits are often presented in comparison to the El Laco deposit in Chile (e.g., Nyström and Henríquez, 1994; Naslund et al., 2002). The magnetite-rich deposits at El Laco strongly resembles basaltic lava flows and shows vesicles and degassing structures in parts of the deposit. However, involvement of hydrothermal fluids and metasomatic replacement in the ore forming processes have been suggested based on magnetite veining surrounding altered host rocks (Rhodes et al., 1999; Sillitoe and Burrows, 2002). The most recent model for El Laco combines a magmatic origin with an hydrothermal overprint to explain many of the observed features (Tornos et al., 2016). Early experiments showed that immiscible iron oxide melts can exist with high Ti contents enhancing the immiscibility gap (Philpotts, 1967) and Fe-Ti-P-rich melt globules have also been reported in natural systems (Kamenetsky et al., 2013). Immiscible iron melts are likely responsible for the formation of nelsonites, Fe-Ti oxide apatite rocks, which commonly contains about 30-50 percent apatite (Rakovan, 2007) and potentially for layered intrusions with iron-rich and silica-rich endmembers (Charlier et al., 2011). More recent experiments suggest that high contents of phosphorous lower the liquidus temperature, enhance iron enrichment and are one of the main factors in generating an immiscible iron liquid (Charlier and Grove, 2012). In contrast to nelsonites, iron oxide apatite ores contain less apatite, are defined by their low Ti contents, and the associated rock type (altered calc-alkaline volcanic rocks vs. anorthosites)

distinguishes them from nelsonites (Rakovan, 2007). Given the chemical composition of IOA deposits worldwide and their occurrence in calc-alkaline districts, where iron immiscibility has not been reported and is improbable to form based on experimental results (Charlier and Grove, 2012), an immiscible iron oxide melt seems less likely as a sole source for Kiruna-type deposits.

Thus, the similarities between IOA and IOCG deposits, including intense wall rock alkali alteration (Na, K ± Ca), abundant low-Ti Fe oxides, enrichment in rare earth elements (REE), especially light REE (LREE), and lack of abundant quartz, have led to the suggestion of similar hydrothermal origins (Hitzman et al., 1992). IOA deposits are either considered as endmember of the IOCG group (e.g., Barton and Johnson, 1996; Dill, 2010), or represent their own deposit type, unique from IOCG deposits sensu stricto with economic grades of Cu and/or Au (e.g., Williams, 2009; Groves et al., 2010). The most recent classifications (e.g., Porter, 2010) tend to treat IOCG deposits sensu stricto and Kiruna-type deposits as separate deposit classes in the larger spectrum of iron oxide-alkali altered mineralized systems. Many IOA deposits worldwide have seen a recent peak in interest, such as El Laco (Tornos et al., 2016) and other deposits in Chile (Knipping et al., 2015), Pea Ridge, USA and Great Bear magmatic zone, Canada (Slack et al., 2016) using a variety of approaches, but no unifying model has been developed yet. For a clearer answer whether IOCG deposits sensu stricto and IOA deposits are genetically related and whether IOA deposits are of hydrothermal or magmatic origin, more data, especially from the deposits around Kiruna, are required to get a better understanding of the processes that create these deposits.

1.2 Aims & Methods

A variety of geochemical tools was used in this study to gain insights on the emplacement history of the host rocks, their subsequent alteration and the ore genesis of the IOA deposits around Kiruna. This study is the first ever using the robust U-Pb system in zircon to directly date the iron oxide apatite ores in the Norrbotten area to constrain the timing between host rock emplacement, and subsequent hydrothermal alkali metasomatic alteration, and mineralization. Further, the use of in situ geochemical tracer isotopes on dated grains gave insights on the source and nature of the hydrothermal alteration, the ore forming processes and the source of the iron ore (+REE). This combination of in situ U-Pb dating with trace element tracer isotopes on grain scale (including Lu-Hf, Sm-Nd, and O isotope systems) has never been done in the Norrbotten region to this extent. The study of distinct hydrothermal characteristics of major minerals by detailed microscopy and of accessory minerals by in situ chemical analyses and elemental mapping, especially zircon, further helped to shed light on the question of an magmatic or hydrothermal origin of the Kiruna IOA deposits.

The initial fieldwork for this PhD project was done in June 2010 under the direct supervision of Prof. John M. Hanchar and in close collaboration with colleagues from the Geological Survey of Sweden (SGU), the Swedish Museum of Natural History, the Luleå University of Technology (LTU), and from the operating mining company Luossavaara-Kiirunavaara AB (LKAB). Further samples from the operating mines Kiirunavaara and Gruvberget were taken by geologists from LKAB to increase sample sizes in 2011 to get more representative samples for geochronology. A second period of field work was done

in the summer of 2012 by myself with colleagues from LTU and LKAB. Our extensive sample set consists of unaltered host rock, altered host rock near the IOA ores (hanging wall and footwall, veins), and the IOA ores from Kiirunavaara, and the Tuolluvaara, Rektorn and Nukutus ore bodies from precisely known locations.

All samples were studied by polarized, reflected and cathodoluminescence (CL) petrography of thin sections for an assessment of the mineral paragenesis and the extent of alteration. Bulk samples were crushed using jaw crusher and disk mill so that the majority of material processed was less than 500 μm and larger than 63 μm. A split of each sample was then pulverized for whole rock analysis of major and trace element geochemistry, determined at the CREAIT facility (Core Research Equipment & Instrument Training Network) at Memorial University of Newfoundland (MUN) and at Activation Laboratories Ltd., Ontario, using X-ray fluorescence spectrometry and fusion inductively coupled plasma mass spectrometry (ICP-MS) techniques. Selected whole rock samples were prepared for tracer radiogenic isotopes (Nd and Hf) and measured by thermal ionization mass spectrometry (TIMS) for Sm-Nd and solution multi collector (MC) ICPMS for Lu-Hf.

Heavy minerals were separated from the sieved fraction using standard techniques (Wilfley Table, manual separation of the magnetic fraction, heavy liquid separation, and a Frantz magnetic separator), handpicked and mounted for in situ analyses. All grains were imaged before the in situ analyses using CL and back-scattered electron (BSE) capabilities of the FEI Quanta 400 scanning electron microscope (SEM) at MUN or the Hitachi S4300 SEM at the Swedish Museum of Natural History. Uranium-Pb geochronology on zircon,

monazite and titanite was done using a large radius secondary ion mass spectrometer (SIMS) at the NordSIM facility at the Swedish Museum of Natural History. The oxygen isotopic composition of zircon was also determined on dated grains using SIMS. Major and trace element concentrations of zircon have been analysed using electron probe microanalyzer (EPMA) and laser ablation (LA) ICPMS. Selected zircon grains were studied by Fourier transform infrared spectroscopy (FTIR) analyses at California Institute of Technology (Caltech) and by transmission electron microscopy (TEM) at the Helmholtz Centre Potsdam GeoForschungsZentrum (GFZ) German Research Centre for Geosciences Potsdam. Tracer radiogenic isotopes in situ at the mineral scale (Lu-Hf in zircon and Sm-Nd in monazite) using LA-MC-ICPMS (Finnigan Neptune) have been done at MUN and at Washington State University.

1.3 Geological overview and previous work

The deposits around Kiruna in the Norrbotten region of northern Sweden are a classic area in which to investigate IOA mineral deposits. In that region of Sweden, about 40 known iron oxide-apatite deposits and several other mineralization types have been discovered (Fig. 1.1; Bergman et al., 2001; Martinsson, 2004). They are some of the largest deposits of this kind in the world, and are the largest in Europe. Several ore bodies occur around the town of Kiruna, which led to the expression “Kiruna-type” deposits for this class of low Ti apatite-rich iron ore deposits. The deposits in this part of Sweden have been mined intermittently since 1645 (Bergman et al., 2001) and continue to be an important source of iron and copper. A total of 2500 million tons (Mt) of iron ore has been produced in the Norrbotten region to date with 682 Mt @ 46 % Fe proven and probable reserves at

the Kiirunavaara main mine (LKAB, 2014). The Norrbotten region is characterized by a regional Na-Cl metasomatism, evident in regional scale albitization and associated widespread occurrence of scapolite $Na_4Al_3Si_9O_{24}Cl$ – $Ca_4Al_6Si_6O_{24}CO_3$ with a dominance of the Cl-rich end member (Frietsch et al., 1997). Besides the economically important apatite iron ores, also Cu sulphide mineralisation (both stratiform and epigenetic, e.g., Pahtohavara, Fig. 1.1), skarn-rich iron formations, and banded iron formations (BIF) occur in that area (Bergman et al., 2001). Aitik, Sweden's largest Cu mine southeast of Kiruna, is suggested to have formed as a porphyry copper system with a subsequent overprint by hydrothermal IOCG fluids (Wanhainen and Martinsson, 2010).

The iron oxide-apatite deposits are generally hosted by Svecofennian age metavolcanic rocks, the Porphyry Group and the Porphyrite Group (ca. 1.91 - 1.88 Ga, Bergman et al., 2001). Their average content of Fe and P is 30 - 70 % and 0.05 - 5 %, respectively, and they are enriched in REE, with a dominance of LREE (Parák, 1973). The Kiruna ore bodies include the huge underground mine Kiirunavaara (in operation), and the closed mines Luossavaara, Tuolluvaara and the Per Geijer ores (see Fig. 1.2). The second underground mine Malmberget is situated ca. 85 km SE of Kiruna in the Gällivare area and consists of several massive ore bodies. There are several closed open pits in the area between Kiruna and Malmberget. In the Svappavaara area, the new open pit mine Gruvberget commenced operation in May 2010, and two open pit mines are planned at Leveäniemi and Mertainen (LKAB, 2014). The Tjårrojåkka deposit SE of Kiruna is the only known deposit where apatite iron ore and abundant Cu-sulphides are spatially and potentially also genetically related (Edfelt et al., 2005).

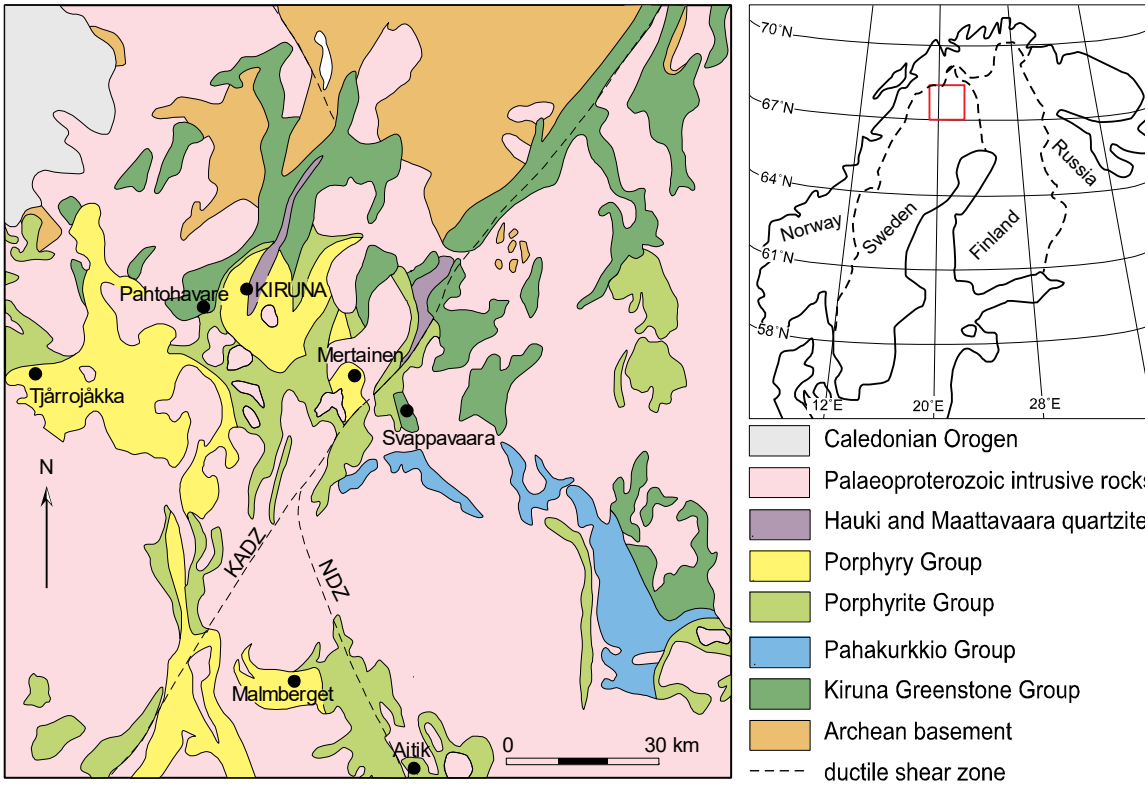

Figure 1-1. Simplified regional geology of the Norrbotten region, showing locations of selected ore deposits (modified after Martinsson and Wanhainen, 2000). KADZ: Karesuando-Arjeplog deformation zone; NDZ: Nautanen deformation zone. The area around the town of Kiruna is the focus of this study.

The apatite iron ore bodies in the Norrbotten region show a variation in their composition (namely Fe and P contents), but also in host rock relations, lithology, alteration, grade of metamorphism, and associated minor components. The mineralisation has been divided into tabular ore bodies and breccia-like mineralisation style with ore veins in altered host rock (Martinsson, 1994). Characteristic for breccia-like occurrences (e.g., Tuolluvaara) are low P contents, and amphibole, pyrite, chalcopyrite, and titanite as accessory minerals. The tabular ore bodies (e.g., the Per Geijer ores Nukutus and Rektorn) tend to have slightly higher P contents (up to 4.5 wt.%) and higher amounts of hematite. The largest ore body Kiirunavaara (Fig. 1.3) is currently mined at 1300 m below the surface, is ca. 5 km long in the N-S direction, and up to 100 m thick (Bergman et al., 2001). Both Kiirunavaara and the smaller Luossavaara occur at the contact between trachyandesitic lavas (footwall) and pyroclastic rhyodacite (hanging wall, Fig. 1.2). The smaller ore bodies at Tuolluvaara (6 km E of Kiruna) and at Rektorn, Henry and Nukutus (sometimes referred to as Per Geijer ore bodies, about 3 km NE of Kiruna) instead occur within the pyroclastic rhyodacite unit, which is intensely altered in the vicinity of the ore bodies.

Until now, age constraints for the Kiruna area have been based on altered host rocks or late phase samples and their associated minerals; the ore itself has not been dated directly. For instance, one approach tried to bracket the age of the main ore at Kiirunavaara with a U-Pb zircon age by Welin (1987) of 1882 ± 24 Ma from the hanging wall and a whole rock Sm-Nd isochron yielding an age of 1890 ± 90 Ma for the footwall, hanging wall and dikes crosscutting the ore (Cliff et al., 1990). In the same study, a granophyric dike and a granitoid, both sampled underground at Kiirunavaara, yielded U-Pb multigrain zircon

dates of 1880 ± 35 Ma (upper intercept age) and 1880 ± 3 Ma (concordia age), respectively. The granophyric dike is described as cutting the ore, therefore providing a minimum age for ore formation. Combining these ages and taking in account the large uncertainties, Cliff et al. (1990) suggest a period of 20 Ma for the ore forming processes between 1900 and 1880 Ma. In a following study, eight ore samples from the Kiirunavaara mine were used to produce a whole rock Sm-Nd isochron with a distinct younger age of 1.49 ± 0.13 Ga (Cliff and Rickard, 1992). The authors interpret these results with a major geochemical disturbance close to 1.5 Ga. Titanite grains from the magnetite-titanite veins in the Kiruna area were dated to fall within error in the 1900 and 1880 Ma period (U-Pb TIMS multigrain, Romer et al., 1994). In the same study, titanite from an amygdule gives a slightly younger upper intercept age of 1876 ±9 Ma, also within error of the previous suggested period. In more recent studies, Storey et al. (2007) and Smith et al. (2009) used the weighted mean of $^{206}Pb/^{207}Pb$ dates of in situ U-Pb dating in titanite, apatite, allanite, and rutile grains from the Norrbotten region by laser ablation inductively coupled plasma mass spectrometry (LA-ICPMS). This technique provides a higher spatial resolution on single grains and can avoid inclusions or impurities. But in contrast to zircon, the minerals used can contain significant amounts of common Pb, and are susceptible to resetting by hydrothermal alteration. The data in these studies show a large spread of more than 400 million years within the individual samples (ranging from ca. 1600-2100 Ma), have large error ellipses and do not improve our understanding of the Norrbotten region. One key step is therefore to better understand the timing between host rock emplacement, hydrothermal alteration, and ore formation in the area.

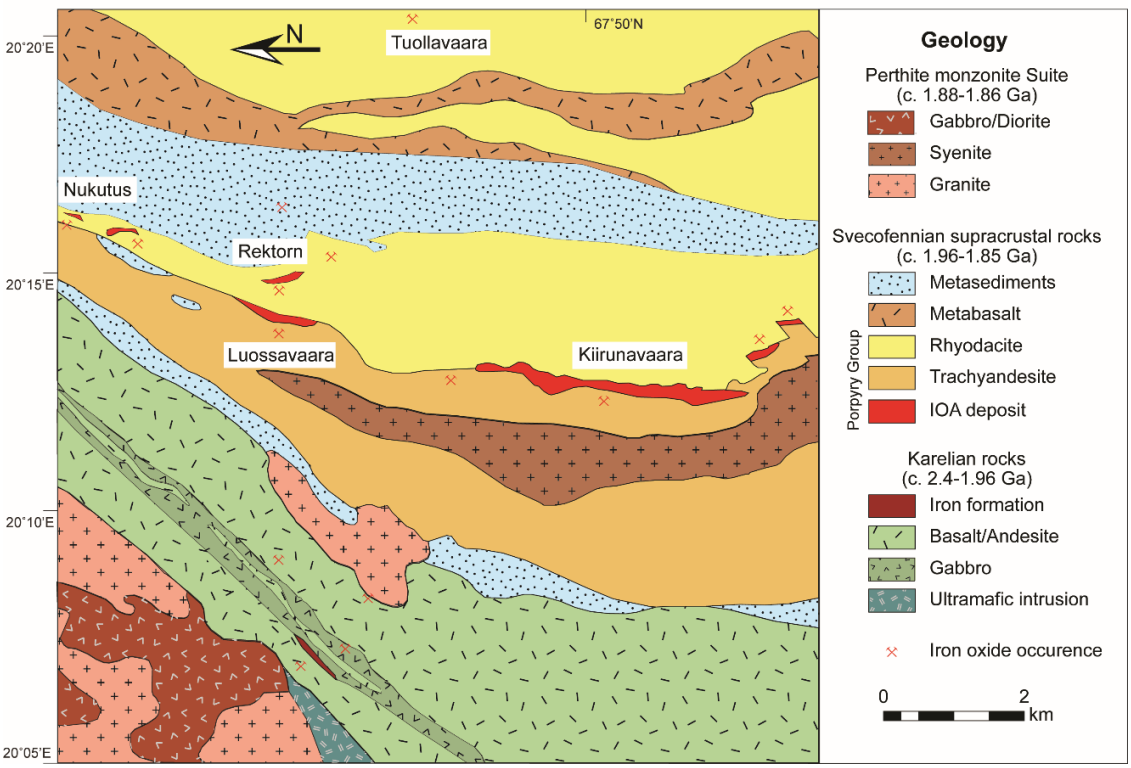

Figure 1-2. Simplified geological map of the Kiruna area, based on data provided by the Geological Survey of Sweden and as found in Bergman et al. (2001). Iron oxide occurrences are marked, and localities included in this study are labelled.

Figure 1-3. View of the Kiirunavaara mine and associated facilities and tailings, looking south from Luossavaara.

1.4 Structure of thesis

This thesis is presented in manuscript format with three separate manuscripts that each represent a stand-alone article for publication in peer-reviewed journals (chapters two, three and four). This first chapter is an introduction to the project and the objectives and methods of this study, gives an overview about the regional geology and some previous work in the area. The connection between the three manuscripts is explained in the following paragraphs. Since chapters two, three and four represent individual research articles, some repetition in the context is unavoidable.

Chapter two is titled "New constraints on the timing of the host rock emplacement, hydrothermal alteration, and iron oxide-apatite in the Kiruna district, Norrbotten region, Sweden", authored by Anne Westhues, John M. Hanchar, Martin J. Whitehouse and Olof Martinsson. This manuscript has been published in *Economic Geology*, Vol. 111, p.1595-1618, 2016. In this chapter, the zircon U-Pb geochronology of this project is presented, which provides new constraints on the timing of the mineralisation in the Kiruna area. Until this present study, the Kiruna ore has not been directly dated, and only broad constraints between 1900 and 1880 Ma existed for the formation of volcanic host rocks and the ore. We confirm previously published dates for the host rocks with better precision and accuracy, but most interestingly, are able to obtain U-Pb ages from zircon directly from two iron ore bodies and constrain the duration of hydrothermal alteration. This is one of the first times that zircon grains have been separated directly from an iron ore body and been dated successfully. This chapter further documents the pervasive Na and K metasomatism of the area using whole-rock geochemical data and detailed microscopy. With detailed

sample description and introduction to the regional geology, it forms the basis for the further geochemical studies in the following manuscripts.

Chapter three is titled “Tracing the fluid evolution of the Kiruna iron oxide apatite deposits using zircon, monazite and whole rock trace elements and isotopic studies” by Anne Westhues, John M. Hanchar, Christopher R. Voisey, Martin J. Whitehouse, George R. Rossman, and Richard Wirth. This manuscript has been re-submitted to *Chemical Geology* after a first round of peer-reviews. In this chapter, we studied the different nature of zircon grains from ore and host rocks that were revealed in chapter two by several techniques to show that ore zircon was likely influenced by hydrothermal fluids. The study demonstrates that zircon can be a crucial mineral used in understanding ore deposits. We further present U-Pb geochronology of monazite, which indicates secondary events influencing the area. Isotopic studies (Sm-Nd and Lu-Hf) on whole grain and mineral scale point to different source regions for ore and host rocks.

Chapter four is titled “Evidence for hydrothermal alteration and source regions for the Kiruna iron oxide apatite ore from zircon Hf and O isotopes” by Anne Westhues, John M. Hanchar, Mark J. LeMessurier and Martin J. Whitehouse. This chapter has been published in *Geology*, Vol. 45, p. 571-574. Combining hafnium and oxygen isotopic systems of zircon together with detailed U-Pb geochronology has been shown to help resolve questions about crustal evolution or to understand the formation of various rock types (e.g., Hawkesworth and Kemp, 2006; Kemp et al., 2007). Here, we apply this approach for one of the first times to zircon originating from an ore deposit and its related host rocks. In this chapter, we show that ore zircon grains are distinctively different from

those from metavolcanic host rocks, not only in appearance, but also in both Hf and O isotopic systems. These data, in combination with the geochronology results from chapter two and the hydrothermal features of zircon presented in chapter three, are used to suggest a model for the formation of the Kiruna iron ores.

A conclusion chapter at the end summarizes the findings of the three manuscripts and brings the results of this thesis into the global context of IOA deposits. To generate a predictive exploration model for IOA deposits worldwide, some further approaches to study these deposits are suggested.

1.5 Co-authorship Statement

Anne Westhues: While my supervisor John Hanchar initialized the PhD project, many ideas of different ways of analyzing the samples of this project and interpretation of results originated from discussions between John and myself over the period of the project. I collected most samples during several weeks of field work in Sweden over three years, except for a few samples that were kindly provided by the mining company LKAB. I further carried out all sample preparation for both whole rock and in situ analytical work. This involved the crushing of samples, isotopic separation by column chemistry, separation, picking and imaging of zircon, monazite and titanite grains. I analyzed the whole rock Sm-Nd isotopic signature using the TIMS and Lu-Hf using the Neptune ICP-MS at MUN. I further carried out the in situ analysis of zircon, monazite and titanite U-Pb and oxygen isotope analysis by SIMS under the guidance of Martin Whitehouse at the Swedish Museum of Natural History in Stockholm. I analysed the Lu-Hf isotopic composition and trace element contents of zircon by LA-ICPMS together with two B.Sc. Honours students,

and provided guidance for their sub-projects. I reduced all data collected during this study and interpreted the results. I was awarded the Student Travel/Research Grant of the Mineralogical Association of Canada (MAC) and the Student Research Grant of the Society of Economic Geology (SEG), which secured additional funding for this project. I presented my research at several conferences, including, but not limited to, the fall meeting of the American Geophysical Union in California, 2011, the Gordon Research Conference in New Hampshire, 2012, the Society of Geology Applied to Mineral Deposits' biennial meeting in Sweden, 2013, and as an invited speaker at the Goldschmidt Conference in California, 2014. The three manuscripts (chapters two, three, and four) were written by myself and then passed on to the co-authors. The interpretations and conclusions presented benefitted from continuous discussion with my co-authors at all stages of the project. All co-authors reviewed the manuscripts and helped to improve it; their individual contributions are summarized below in alphabetical order.

John M. Hanchar: John provided the principal design and helped with the implementation of the PhD project. He initiated contact with the mining company LKAB and provided most of the funding for this project. He further assisted with fieldwork, sample collection and preparation and provided help and guidance throughout the project. John provided constructive criticism and discussions during preparation of the manuscripts included in this thesis.

Mark LeMessurier: Mark helped in carrying out part of the Hf isotopes analyses and interpretation of these results as part of a B.Sc. honours thesis done at MUN. The data resulting from this project are now part of chapter four.

Olof Martinsson: Olof provided in-depth knowledge of the Kiruna iron oxide during the field work, as well as helpful discussions during manuscript preparation.

George Rossman: George carried out the FTIR analyses on zircon grains at Caltech University, as this technique is not available at MUN, and assisted with the interpretation of the results, presented in chapter three.

Chris Voisey: Chris helped in carrying out part of the zircon trace element analyses and interpretation of these results as part of a B.Sc. honours thesis done at MUN. The data resulting from this project are now part of chapter three.

Martin Whitehouse: Martin provided technical assistance with sample analysis and data reduction during my visits to the Swedish Museum of Natural History in Stockholm. Martin further assisted with field work and discussions with him regarding the interpretation of the results improved the thesis. His constructive comments on all three manuscript chapters were invaluable in completing this thesis.

Richard Wirth: Richard carried out the TEM analyses at the GFZ Potsdam, Germany, on selected zircon grains, another technique not available at MUN. His interpretation of the results, part of chapter 3, was invaluable for understanding these complicated zircons.

1.6 Bibliography - Introduction

Barton, M. D., and Johnson, D. A., 1996, Evaporitic-source model for igneous-related Fe oxide-(REE-Cu-Au-U) mineralization: Geology, v. 24, p. 259-262.

Bergman, S., Kübler, L., and Martinsson, O., 2001, Description of regional geological and geophysical maps of northern Norrbotten County (east of the Caledonian Orogen), Sveriges Geologiska Undersökning, Ba 56, 110 pp.

Charlie, B., and Grove, T., 2012, Experiments on liquid immiscibility along tholeiitic liquid lines of descent: Contributions to Mineralogy & Petrology, v. 164, p. 27-44.

Charlier, B., Namur, O., Toplis, M. J., Schiano, P., Cluzel, N., Higgins, M. D., and Auwera, J. V., 2011, Large-scale silicate liquid immiscibility during differentiation of tholeiitic basalt to granite and the origin of the Daly gap: Geology, v. 39, p. 907-910.

Cliff, R. A., and Rickard, D., 1992, Isotope systematics of the Kiruna magnetite ores, Sweden: Part 2. Evidence for a secondary event 400 m.y. after ore formation: Economic Geology, v. 87, p. 1121-1129.

Cliff, R. A., Rickard, D., and Blake, K., 1990, Isotope systematics of the Kiruna magnetite ores, Sweden: Part 1. Age of the ore: Economic Geology, v. 85, p. 1770 - 1776.

Dill, H. G., 2010, The "chessboard" classification scheme of mineral deposits: Mineralogy and geology from aluminum to zirconium: Earth-Science Reviews, v. 100, p. 1-420.

Edfelt, A., Weihed, P., Armstrong, R. N., Smith, M., Martinsson, O., and Williams, P. J., 2005, Alteration paragenesis and mineral chemistry of the Tjarrojakka apatite-iron and Cu (-Au) occurrences, Kiruna area, northern Sweden: Mineralium Deposita, v. 40, p. 409-434.

Frietsch, R., 1978, On the magmatic origin of iron ores of the Kiruna type: Economic Geology, v. 73, p. 478-485.

Frietsch, R., Tuisku, P., Martinsson, O., and Perdahl, J. A., 1997, Early Proterozoic Cu-(Au) and Fe ore deposits associated with regional Na-Cl metasomatism in northern Fennoscandia: Ore Geology Reviews, v. 12, p. 1-34.

Geijer, P., 1935, Die nordschwedischen Eisenerze und verwandte Lagerstätten als Beispiele eruptiver Spaltungsprozesse: Geologische Rundschau, v. 26, p. 351-366.

Groves, D. I., Bierlein, F. P., Meinert, L. D., and Hitzman, M. W., 2010, Iron oxide copper-gold (IOCG) deposits through Earth history: Implications for origin, lithospheric setting, and distinction from other epigenetic iron oxide deposits: Economic Geology, v. 105, p. 641-654.

Hawkesworth, C. J., and Kemp, A. I. S., 2006, Using hafnium and oxygen isotopes in zircons to unravel the record of crustal evolution: Chemical Geology, v. 226, p. 144-162.

Hildebrand, R. S., 1986, Kiruna-type deposits - their origin and relationship to intermediate subvolcanic plutons in the Great Bear magmatic zone, Northwest Canada: Economic Geology, v. 81, p. 640-659.

Hitzman, M. W., Oreskes, N., and Einaudi, M. T., 1992, Geological characteristics and tectonic setting of Proterozoic iron oxide (Cu-U-Au-REE) deposits: Precambrian Research, v. 58, p. 241-287.

Kamenetsky, V. S., Charlier, B., Zhitova, L., Sharygin, V., Davidson, P., and Feig, S., 2013, Magma chamber–scale liquid immiscibility in the Siberian Traps represented by melt pools in native iron: Geology, v. 41, p. 1091-1094.

Kemp, A. I. S., Hawkesworth, C. J., Foster, G. L., Paterson, B. A., Woodhead, J. D., Hergt, J. M., Gray, C. M., and Whitehouse, M. J., 2007, Magmatic and crustal differentiation history of granitic rocks from Hf-O isotopes in zircon: Science, v. 315, p. 980-983.

Knipping, J. L., Bilenker, L. D., Simon, A. C., Reich, M., Barra, F., Deditius, A. P., Lundstrom, C., Bindeman, I., and Munizaga, R., 2015, Giant Kiruna-type deposits form by efficient flotation of magmatic magnetite suspensions: Geology, v. 43, p. 591-594.

LKAB, 2014, Integrated report - Annual report and sustainability report 2013, http://www.lkab.com/en/, Luleå, LKAB, 161 pp.

Martinsson, O., 1994, Greenstone and porphyry hosted ore deposits in northern Norrbotten, NUTEK report nr 92-00752P, Luleå, 31 pp.

Martinsson, O., and Wanhainen, C., 2000, Excursion Guide, GEODE Work shop, August 28 to September 1, 2000, 14 pp.

Mücke, A., and Younessi, R., 1994, Magnetite-apatite deposits (Kiruna-type) along the Sanandaj-Sirjan zone and in the Bafq area, Iran, associated with ultramafic and calcalkaline rocks and carbonatites: Mineralogy and Petrology, v. 50, p. 219-244.

Naslund, H. R., Henriquez, F., Nyström, J. O., Vivallo, W., and Dobbs, F. M., 2002, Magmatic iron ores and associated mineralisation: Examples from the Chilean high Andes and costal Cordillera, *in* Porter, T. M., ed., Hydrothermal Iron Oxide Copper-Gold Related Deposits: A Global Perspective, 2: Adelaide, PGC Publishing, p. 207-226.

Nyström, J. O., and Henríquez, F., 1994, Magmatic features of iron ores of the Kiruna type in Chile and Sweden; ore textures and magnetite geochemistry: Economic Geology, v. 89, p. 820-839.

Parák, T., 1973, Rare earths in apatite iron ores of Lappland together with some data about Sr, Th and U content of these ores: Economic Geology, v. 68, p. 210-221.

Parák, T., 1975, Kiruna iron ores are not 'intrusive-magmatic ores of the Kiruna type': Economic Geology, v. 70, p. 1242-1258.

Porter, T. M., 2010, Current understanding of iron oxide associated-alkali altered mineralised systems: Part I - An overview, *in* Porter, T. M., ed., Hydrothermal iron oxide copper-gold and related deposits: a global perspective, 3: Adelaide, PGC Publishing, p. 5-32.

Rakovan, J., 2007, Nelsonite and Kiruna-type deposits: Rocks & Minerals, v. 82, p. 249-251.

Rhodes, A. L., Oreskes, N., and Sheets, S. A., 1999, Geology and rare earth element (REE) geochemistry of magnetite deposits at El Laco, Chile, *in* Skinner, B. J., ed., Geology and Ore Deposits of the Central Andes, 7, Society of Economic Geologists Special Publication, p. p. 299 – 332.

Romer, R. L., Martinsson, O., and Perdahl, J. A., 1994, Geochronology of the Kiruna Iron-Ores and Hydrothermal Alterations: Economic Geology and the Bulletin of the Society of Economic Geologists, v. 89, p. 1249-1261.

Sillitoe, R. H., and Burrows, D. R., 2002, New field evidence bearing on the origin of the El Laco magnetite deposit, northern Chile: Economic Geology and the Bulletin of the Society of Economic Geologists, v. 97, p. 1101-1109.

Slack, J. F., Corriveau, L., and Hitzman, M. W., 2016, A special issue devoted to Proterozoic iron oxide-apatite (±REE) and iron oxide copper-gold and affiliated deposits of southeast Missouri, USA, and the Great Bear magmatic zone, Northwest Territories, Canada: Preface: Economic Geology, v. 111, p. 1803-1814.

Smith, M. P., Storey, C. D., Jeffries, T. E., and Ryan, C., 2009, In situ U-Pb and trace element analysis of accessory minerals in the Kiruna district, Norrbotten, Sweden: New constraints on the timing and origin of mineralization: Journal of Petrology, v. 50, p. 2063-2094.

Storey, C. D., and Smith, M. P., 2017, Metal source and tectonic setting of iron oxide-copper-gold (IOCG) deposits: Evidence from an in situ Nd isotope study of titanite from Norrbotten, Sweden: Ore Geology Reviews, v. 81, p. 1287-1302.

Storey, C. D., Smith, M. P., and Jeffries, T. E., 2007, In situ LA-ICP-MS U-Pb dating of metavolcanics of Norrbotten, Sweden: Records of extended geological histories in complex titanite grains: Chemical Geology, v. 240, p. 163-181.

Tornos, F., Velasco, F., and Hanchar, J. M., 2016, Iron-rich melts, magmatic magnetite, and superheated hydrothermal systems: The El Laco deposit, Chile: Geology, v. 44, p. 427-430.

Valley, P. M., Fisher, C. M., Hanchar, J. M., Lam, R., and Tubrett, M., 2010, Hafnium isotopes in zircon: A tracer of fluid-rock interaction during magnetite-apatite ("Kiruna-type") mineralization: Chemical Geology, v. 275, p. 208-220.

Wanhainen, C., and Martinsson, O., 2010, The hybrid character of the Aitik Deposit, Norrbotten, Sweden: a porphyry Cu-Au-Ag(-Mo) system overprinted by iron-oxide Cu-Au hydrothermal fluids, *in* Porter, T. M., ed., Hydrothermal iron oxide copper-gold and related deposits: a global perspective, 4: Adelaide, PGC Publishing, p. 427-440.

Welin, E., 1987, The depositional evolution of the Svecofennian supracrustal sequence in Finland and Sweden: Precambrian Research, v. 35, p. 95-113.

Williams, P. J., 2009, Classifying IOCG deposits, *in* Corriveau, L., and Mumin, A. H., eds., Exploring for iron oxide copper-gold deposits: Canada and global analogues. Geological Association of Canada, Short Course Notes, 20, p. 89-110.

2 New constraints on the timing of the host rock emplacement, hydrothermal alteration, and iron oxide-apatite in the Kiruna district, Norrbotten region, Sweden

2.1 Abstract

High spatial resolution zircon U-Pb geochronological data obtained directly on the Kiirunavaara iron oxide-apatite (IOA) deposit, related ore bodies and host rocks provide new constraints on the timing of mineralization in these deposits. These data raise new arguments in the debate of a magmatic vs. hydrothermal/metasomatic genesis of these major (2500 Mt @ 30-70 wt.% Fe) Paleoproterozoic deposits. The main ore body at Kiirunavaara contains Ti-poor magnetite and minor (0.05 to 5 wt.% P) apatite, located between a trachyandesite footwall and a rhyodacite hanging wall, which also hosts smaller ore bodies (Nukutus, Rektorn, Tuolluvaara). The pervasive Na and K metasomatism in the host rock is documented by whole-rock geochemical data and CL microscopy. Zircon U-Pb data for the metavolcanic rocks in the footwall and hanging wall cluster between 1884 ± 4 and 1880 ± 3 Ma. In the footwall, a syenite-aplite system yields ages of 1880 ± 7 and 1881 ± 4 Ma; a granite pluton exposed underground has an age of 1874 ± 4 Ma. Zircons in two ore samples, never directly dated before this study, yield ages of 1877 ± 4 and 1874 ± 7 Ma. Brecciation at the contacts between the ore and host rocks, the tight age at ca. 1880 Ma for most volcanic and plutonic rocks in the footwall and hanging wall, and the marginally younger age for ore at ca. 1877-74 Ma, matching the age of the spatially related

granite pluton, are all consistent with a magmatic-hydrothermal emplacement model for the Kiruna area IOA ores.

2.2 Introduction

Iron oxide apatite (IOA) ore deposits are economically important in the Norrbotten region of northern Sweden (e.g., Bergman et al., 2001). Several ore bodies, mined for over a century for their iron content, occur around the town of Kiruna (e.g., Geijer, 1910). The term "Kiruna-type" for this class of low-Ti iron oxide-apatite deposits is used for similar deposits worldwide (e.g., Hildebrand, 1986; Mücke and Younessi, 1994; Valley et al., 2010; Nold et al., 2014). About 40 IOA deposits are known in the Norrbotten region having average Fe and P contents of 30 to 70 wt. % and 0.05 to 5 wt. % P, respectively (Bergman et al., 2001). Approximately 2500 Mt of iron ore has been mined in the region to date. This study focuses on the main Kiirunavaara ore body, mined by Luossavaara-Kiirunavaara Aktiebolag (LKAB), as well as on some smaller deposits in the vicinity (Fig. 2-1). Characteristics including low Ti content of the ore-forming iron oxides, regional Na-Cl metasomatism (Frietsch et al., 1997), and high contents of rare earth elements (REE) with a dominance of light REE (Parák, 1973), have led several authors to suggest a connection to the iron oxide-copper-gold (IOCG) class of deposits (Hitzman et al., 1992; Barton and Johnson, 1996). However, due to the lack of economic Cu and Au in IOA deposits, they are assigned to a separate class, distinct from IOCG deposits sensu stricto in the larger spectrum of iron oxide-alkali altered mineralized systems (e.g., Porter, 2010).

The genesis of IOA deposits in the Norrbotten region has been debated since their discovery. Early theories suggested a sedimentary origin (Bäckström, 1894), whereas a

magmatic origin was supported by Geijer, first as extrusive iron oxide lava (Geijer, 1910), then in later studies as an intrusive magma (Geijer, 1919). Parák (1975) suggested a sedimentary-exhalative origin at moderate temperatures, similar to ore deposition at modern continental rifts, such as the Red Sea. This hypothesis was strongly opposed by several authors who favored a magmatic-intrusive origin (e.g., Frietsch, 1978, 1984; Nyström and Henríquez, 1994). Involvement of hydrothermal fluids in ore formation has been suggested based on similarities of the Norrbotten IOA deposits to IOCG deposits and to numerous hydrothermal features such as brecciation and intense wall rock alteration (Hitzman et al., 1992; Barton and Johnson, 1996; Porter, 2010). Textural evidence remains inconclusive; features such as columnar magnetite have been described in the Norrbotten region and at the El Laco deposit in Chile as clear evidence for a magmatic origin of the iron (Nyström and Henríquez, 1994), which has been debated by others (e.g., Bookstrom, 1995). Similarly, the "ore breccia" consisting of magnetite veins in the hanging wall of the Kiirunavaara deposit, has been interpreted as both magmatic (forceful magma injection; Nyström and Henríquez, 1994) and as a product of "hydrofracturing" analogous to hydrothermal brecciation in porphyry deposits (Cliff et al., 1990). Similar brecciation with mineralized veins in altered host rocks is present in IOCG deposits of hydrothermal origin including those in Australia (e.g., Olympic Dam region, Johnson and Cross, 1995) and in South America (e.g., Mantoverde deposit, Benavides et al., 2007). Macroscopic evidence alone, therefore, seems insufficient to establish the origin of IOA deposits.

Clarifying the age relationships among host-rock emplacement, hydrothermal alteration, and metal deposition is one key step towards obtaining a more thorough

understanding of ore formation in this region. Until now, the ore has not been dated directly, and only broad constraints on ore formation between 1900 and 1880 Ma have been suggested based on host rock ages and poorly constrained age of a crosscutting dike (Welin, 1987; Cliff et al., 1990). Additionally, whole rock Sm-Nd and Rb-Sr isotopic systems record dates from ca. 1750 to ca. 1495 Ma for intrusive and metavolcanic rocks from the Norrbotten region (e.g., Skiöld and Öhlander, 1989; Cliff and Rickard, 1992).

The present study is the first to use zircon, and titanite, for high spatial resolution, large-radius secondary ion mass spectrometry (SIMS) U-Th-Pb analysis to determine the ages of different units in the area. Further, petrography and whole rock geochemistry are used to investigate metasomatic alteration that is prevalent in the region.

2.3 Geological Setting

The focus of this study is the IOA deposits surrounding the town of Kiruna including the world-class underground Kiirunavaara mine that has produced ca. 2500 Mt of ore @ 50 – 60 % Fe and contains 682 Mt @ 46 % Fe proven and probable reserves (LKAB, 2014). Several closed open pit mines, for instance, Luossavaara, Tuolluvaara, Nukutus, and Rektorn, are located around Kiruna (Fig. 2-1). A second underground mine, Malmberget, is situated ca. 100 km SSE of Kiruna in the Gällivare area. Several open pit mines started operation recently or are about to begin production in the Svappavaara area, about 45 km SE of Kiruna.

The Kiirunavaara ore body and other known IOA deposits in the Norrbotten region are hosted by Proterozoic metavolcanic rocks of the Porphyry Group (also called Kiirunavaara Group; Martinsson, 2004) of Svecokarelian age (ca. 1960 - 1750 Ma,

Bergman et al., 2001; Billström et al., 2010). These rocks form part of a Paleoproterozoic volcano-sedimentary succession that unconformably overlies the Archean basement of the Fennoscandian shield, and are described in detail by Bergman et al. (2001) and Martinsson (2004). As a consequence of pervasive metasomatic overprinting of this succession, petrologic classification of the metavolcanic rocks has traditionally been problematic. The diversity of names used for each of the units in the literature attests to this challenge. The following overview of the geology of the Kiruna area follows the regional terminology used by Bergman et al. (2001). Important local and traditionally used stratigraphic names are indicated between brackets (e.g., Geijer, 1910; Parák, 1975; Witschard, 1984).

2.3.1 Proterozoic host rocks around the town of Kiruna

West of Kiruna, the lowermost Proterozoic unit, the Kovo Group, lies discordantly above the Archean basement and consists of metasedimentary rocks, metabasalt, and meta-volcanoclastic rocks. The Kiruna Greenstone Group (estimated to have formed between 2300 and 1930 Ma, Skiöld and Cliff, 1984; Skiöld, 1986) overlies the Kovo Group, and includes basalt, komatiite, volcaniclastic and chemical sedimentary rocks that display evidence of earlier evaporites (e.g., Martinsson, 2004). The Kovo Group and Kiruna Greenstone Group (Karelian units) are part of extension-related rocks that can be found throughout the Fennoscandian shield. Intracratonic basins evolved between ca. 2500 to 2000 Ma during several episodes of continental rifting, possibly involving mantle hotspot activity (Amelin et al., 1995). In the immediate Kiruna vicinity, mid-ocean ridge basalt (MORB)-type pillow lavas occur in the upper parts of the Kiruna Greenstone Group and suggest deep marine conditions during formation (Martinsson, 2004).

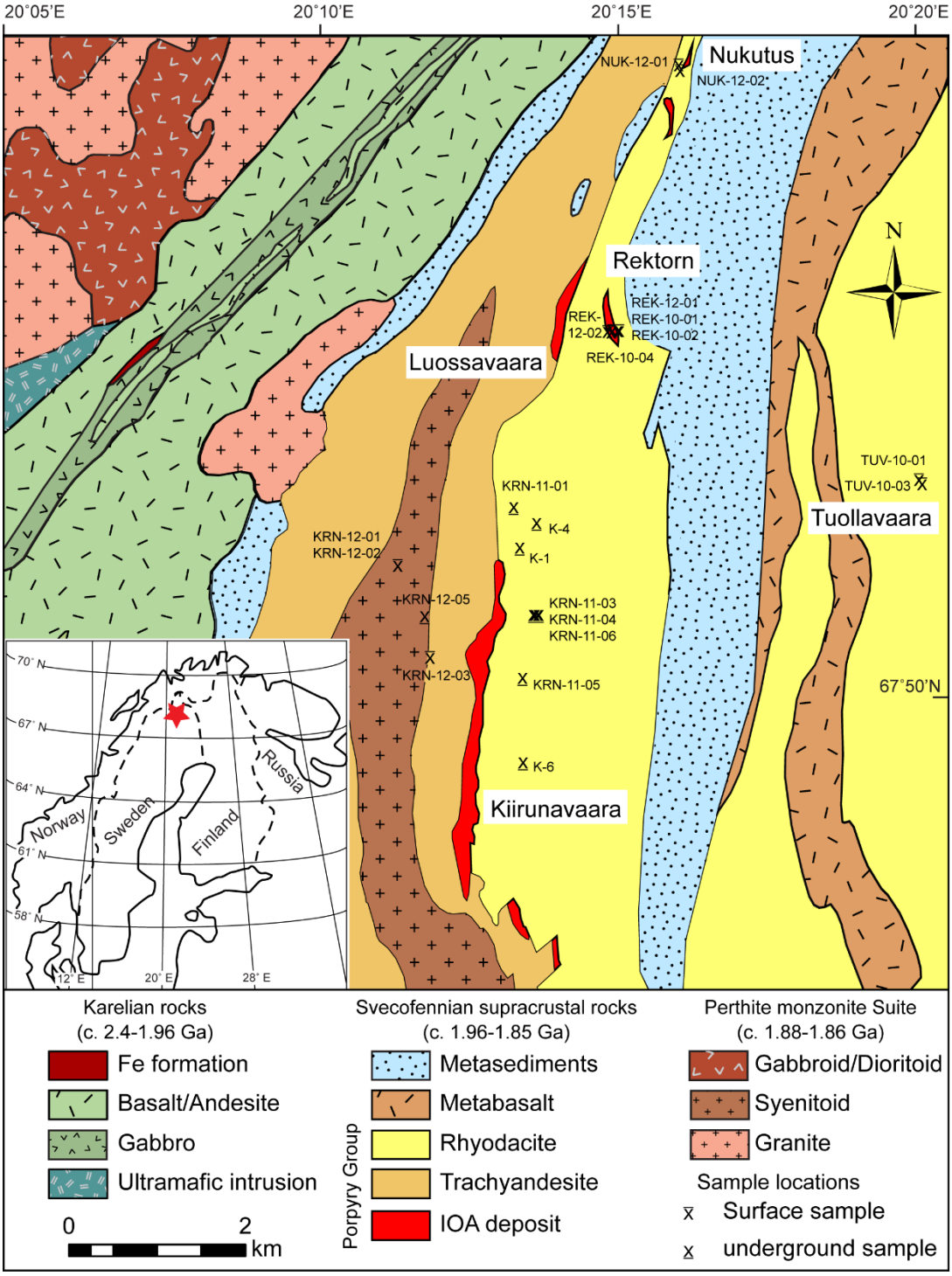

Figure 2-1. Simplified geological map of the Kiruna area, northern Sweden, based on data provided by the Geological Survey of Sweden (Bergman et al., 2001), showing sample locations of this study. Underground sample locations at Kiirunavaara are projected to surface and appear east of orebody, due to its eastward dip. Consequently, underground granite sample appears to be west of the ore body.

The first Svecofennian supracrustal rocks on top of the Kiruna Greenstone Group are the Kurravaara conglomerate and volcanic rocks, mainly of andesitic composition, of the Porphyrite Group. Both these volcanic rocks and the conglomerate probably record the onset of subduction during the Svecokarelian orogeny at ca. 1900-1800 Ma (Martinsson, 2004; Billström et al., 2010). In the central Kiruna area, the Kurravaara conglomerate is predominant for this age, and is found stratigraphically below the Porphyry Group, which contains the mafic to felsic, and commonly strongly altered, volcanic rocks that host the IOA mineralization (Fig. 2-1). These rocks were likely emplaced 1890 to 1800 Ma during the height of the Svecokarelian orogeny (1900-1800 Ma). The lower part of the Porphyry Group is dominated by amygdaloidal volcanic lava flows of intermediate composition, accompanied by minor felsic and mafic beds (Martinsson, 2004). The footwall of the Kiirunavaara ore (syenite porphyry) is of intermediate composition and contains amygdules of magnetite, actinolite, titanite, and locally minor tourmaline (Geijer, 1910). The hanging wall of the ore, stratigraphically higher in the Porphyry Group, is made of felsic pyroclastic material (quartz-bearing porphyry). A few smaller iron oxide deposits, for instance Nukutus and Rektorn, occur in the upper parts of the pyroclastic unit. The hanging wall of these deposits (called Rektorn porphyry above the Rektorn ore body, Lundbohm, 1910) is strongly potassium-altered and silicified. Ignimbritic textures found locally suggest a volcanic origin (Frietsch, 1979). Basaltic volcanic rocks and clastic sedimentary rocks form the uppermost units of the Porphyry Group in the Kiruna area. The Hauki Quartzite and Conglomerate occur on top of the Porphyry Group east of Kiruna, and are referred to as the Younger Svecofennian supracrustal rocks (Bergman et al., 2001).

A number of Svecokarelian intrusive suites have been documented in the Norrbotten region (Bergman et al., 2001). In the Kiruna area, the most important are the Haparanda suite (ca. 1890-1860 Ma), the Perthite monzonite suite (ca. 1880-1860 Ma), and the Granite-pegmatite association (or Lina suite, ca. 1810-1780 Ma). The Perthite monzonite suite is most common in the western parts of the Norrbotten region and in proximity to the Kiirunavaara deposit, and is considered to be co-magmatic with the Porphyry Group (Witschard, 1984; Martinsson, 2004). The Haparanda suite, dominant in the eastern parts of Norrbotten, shows similarities to the Porphyrite Group and higher degrees of deformation than the Perthite monzonite suite (Martinsson, 2004). Most intrusions of the Granite-pegmatite association occur in the southern Norrbotten region. This younger suite of intrusions mostly shows a geochemical signature of syn-collisional granitoids, whereas data for both the Perthite monzonite suite and Haparanda suite plot in the volcanic arc granite field on a Rb vs. Y + Nb discrimination diagram (Bergman et al., 2001).

In the Kiruna area, effects of upper greenschist- to lower amphibolite-facies metamorphism are prevalent (Bergman et al., 2001). The Norrbotten region is further characterized by extensive alkali alteration (Na ± K) that formed albite-rich rocks in many localities (Bergman et al., 2001). Scapolite (with up to 4.7 wt. % Cl) can be found throughout the Norrbotten region (Frietsch et al., 1997). This regional alteration has been attributed to fluids mobilized during metamorphism, and evaporites could have been a source of the chlorine (Frietsch et al., 1997, Billström et al., 2010). Furthermore, Witschard (1984) noted that samples taken close to the ore bodies are typically extremely rich in

alkalis, which he attributed to “special tectonic conditions” that may be an expression of a more intense metasomatic alteration and fluid mobilization surrounding the ore bodies.

2.3.2 Iron ore types and contacts to host rocks

IOA deposits in the Norrbotten region are characterized by iron oxide minerals that are very low in Ti, ranging from 0.04 to 0.24 wt. % Ti (Loberg and Horndahl, 1983). Magnetite is the predominant iron oxide mineral in the Kiruna area, but the content of hematite can vary among the different deposits. The average Fe content is about 50 to 65 %; however, massive and high-grade lenses can reach 60 to 70 % Fe in central parts of some deposits (Bergman et al., 2001). Apatite is spatially associated with the ores to varying extents, with whole-rock analyses showing average concentrations of 0.05 to 5 wt. % P (Bergman et al., 2001). The Kiirunavaara ore occurs in two varieties (as defined by LKAB): B-ore having less than 0.05 % P; and D-ore with more than 1 % P (Fig. 2-2a). The D-ore occurs mainly towards the hanging wall, but the relationship and timing between the two ore types is unclear. The deposits show an overall enrichment in REE, especially in the light REE (LREE), which is likely related to the apatite content (Parák, 1973). Amphibole, mainly actinolite, is a very common minor mineral in the ore. The sulfide content is generally low, but pyrite, chalcopyrite, or bornite can be found, for instance, as veins cutting the magnetite ore. Economic Cu (± Au) deposits in the region (e. g., the Aitik deposit in the Gällivare area, Wanhainen et al., 2003) are not believed to be genetically related to the Norrbotten IOA deposits (Martinsson, 2004). One exception may be the Tjårrojåkka deposit southwest of Kiruna, where an IOA deposit and a Cu-sulfide deposit occur within 750 m of each other and are potentially genetically related (Edfelt et al., 2005).

The main Kiirunavaara ore body (5 km N-S, up to 100 m thick, and extending at least 1500 m below ground) forms a tabular body between trachyandesitic lava flows and the overlying rhyodacitic pyroclastic rocks of the Porphyry Group (Bergman et al., 2001). Contacts between the ore and host rocks are characterised by ore veins and brecciation (Geijer, 1910), which can extend tens of meters into the host rocks (Fig. 2-2b-d). Near the footwall contact at Kiirunavaara, a breccia with a magnetite-actinolite matrix contains footwall fragments; this texture changes into a magnetite-veined trachyandesite farther from the contact. Within the ore breccia at the top of Kiirunavaara (Fig. 2-2b), magnetite is a matrix around fragments of subrounded altered host rock. At the Tuolluvaara deposit, veins of magnetite-actinolite form a network through angular fragments of the host rock (Fig. 2-2c, d). These contact relations have been described as intrusive contacts by Frietsch (1978), and as sedimentary-exhalative by Parák (1975), but also resemble textures reported elsewhere from hydrothermal IOCG deposits (e.g., Bookstrom, 1995; Johnson and Cross, 1995; Benavides et al., 2007). Host rocks of IOA deposits in the Norrbotten region with breccia-dominated contacts have albite and scapolite as the most common alteration minerals, suggesting predominantly sodic alteration.

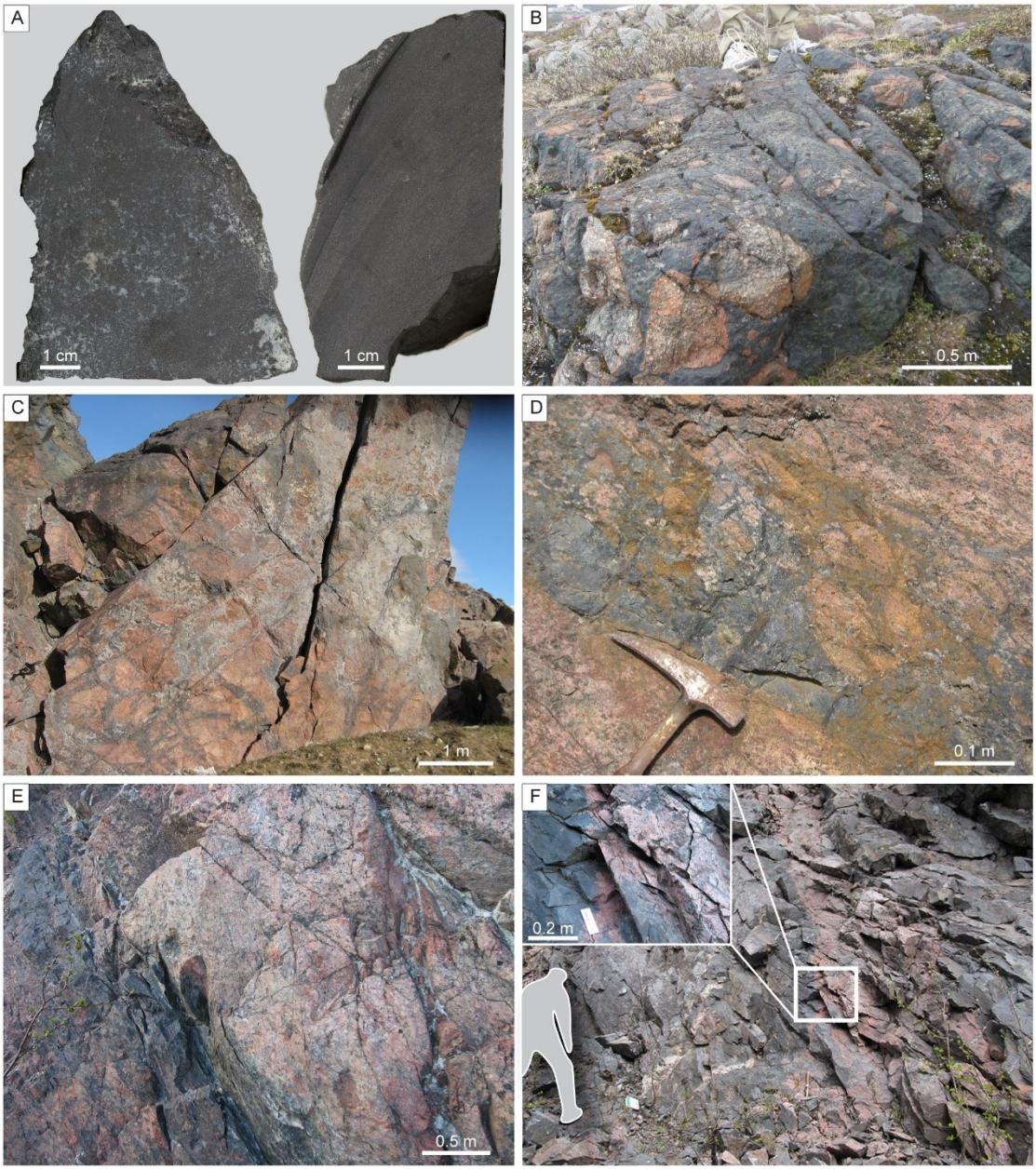

Figure 2-2. Ore types and different contact relationships between host rock and ore for IOA deposits around Kiruna. (A) Kiirunavaara apatite-rich D-ore (KRN-11-01, left) and apatite-low B-ore (K-2, right). (B) Magnetite-actinolite ore matrix with fragments of hanging wall called "ore breccia" on top of Kiirunavaara. (C) Ore veins in metavolcanic host rock at Tuolluvaara. (D) Close-up of ore breccia, ore enclosing pieces of host rock, Tuolluvaara. (E) stratiform-stratabound contact between Rektorn porphyry and Rektorn ore body. (F) Apatite-rich vein in Rektorn ore body, inset shows close-up. See details in text. Scales on field pictures are approximate.

A second IOA deposit type having different characteristics than described above occurs in the area, is termed the stratiform-stratabound (or tabular) type (e.g., Martinsson, 1994). Examples of this type are the Rektorn, Nukutus, and Henry deposits that are often collectively referred to as the "Per Geijer ores" (Fig. 2-1) north of Kiirunavaara (detailed description in Martinsson, 2015). Relative to Kiirunavaara, the contacts between mostly tabular ore bodies and host rocks are sharper, but can show some undulated features in detail (Fig. 2-2e). Amphibole and titanite are absent; the main gangue phases are apatite (on average 1 to 4.5 % P in the ore), quartz, and carbonate. In the main ore bodies, apatite forms disseminations, layers, breccias, or occurs as large, coarse-grained veins that cut the ore (Fig. 2-2f). Typical alteration minerals in the host rocks are sericite, biotite, tourmaline, and carbonate, reflecting pervasive K and Ca alteration. The footwall is strongly altered in a 5- to 10-m wide zone along the ore contact. The hanging wall consists of the K-altered and silicified Rektorn porphyry, as described above, which contains intercalations of siliceous hematite ore that are poor in apatite. Sericite-chlorite altered rocks are also present in the basaltic tuff overlying the Rektorn porphyry (Bergman et al., 2001).

2.3.3 Previous dating results

The Kiirunavaara ore body has not been previously dated directly. Instead, ages of associated host rocks and their minerals were used to constrain the timing of the ore-forming processes at Kiirunavaara and elsewhere in the Norrbotten region. The rhyodacitic hanging wall (metarhyolite) was dated using multigrain zircon U-Pb geochronology, which gave an age of 1882 ± 24 Ma (Welin, 1987). Whole-rock Sm-Nd data for five samples from the footwall, hanging wall, and a granophyre dike complex plot on an 1890 ± 90 Ma

isochron (Cliff et al., 1990). In the same study, zircons from the granophyric dike and a granitoid, both sampled underground at Kiirunavaara, were analyzed for their U-Pb isotopic composition. The granophyric dike is described as cutting the ore, therefore providing a minimum age for ore formation. Whereas the granitoid yielded a concordant result and an age of 1880 ± 3 Ma, the granophyre shows highly discordant data with an upper intercept at 1880 ± 35 Ma. Based on these results, 1900 to 1880 Ma has been proposed as the best estimate for the time period of ore formation at Kiirunavaara (Cliff et al., 1990).

Titanite associated with hydrothermal actinolite-calcite from an amygdule in the Kiirunavaara footwall and from a coarse-grained, magnetite-titanite vein in the footwall of the Luossavaara deposit were dated by U-Pb geochronology at 1876 ± 9 and 1888 ± 6 Ma, respectively (Romer et al., 1994). Martinsson et al. (2016) also report a titanite age of 1882 ± 5 Ma for a sample from close to the contact of the Kiirunavaara ore. In situ techniques were used more recently to date titanite, apatite, allanite, and rutile by laser ablation-inductively coupled plasma mass spectrometry (LA-ICPMS) from different locations within the Norrbotten region (Storey et al., 2007; Smith et al., 2009). The only samples dated from the Kiruna area are titanite from amygdules in the altered footwall of Luossavaara (Storey et al., 2007), and titanite in a “porphyry breccia” from the Kiirunavaara hanging wall (Smith et al., 2009). Those analyses show a large spread along a concordia line (see Fig. 2 in Storey et al., 2007 and Fig. 6b in Smith et al., 2009). In the case of Luossavaara, Storey et al. (2007) argued for two growth episodes of the titanite, one between 1950 and 1850 Ma, and an older episode of ca. 2050 Ma. The authors suggested that the older dates represent the actual igneous and/or initial metamorphic age

of the titanite, whereas the younger dates in the outer parts of the crystals indicate later metasomatic alteration by hydrothermal fluids. However, only three of the older dates are concordant and have large uncertainties, and thus it is questionable if they represent a separate geologic event distinct from the younger dates. Analyses of the Kiirunavaara "porphyry breccia" reported in Smith et al. (2009) lack older dates, but instead show a spread from 1950 to 1720 Ma. The authors proposed that titanite began crystallization around the upper end of the age spectrum (1894 ± 35 Ma) and was reset at ca. 1780 Ma during later metasomatic event(s) caused by infiltrating hydrothermal fluids. Alternatively, the spread in data reported in both studies may reflect the susceptibility of titanite to metasomatic alteration (or crystallization in hydrothermal fluids) and subsequent changes of its U-Pb contents (i.e., ~4% Pb loss could produce a spread in the data of ca. 70 million years), and/or the difficulties of correcting for ^{204}Pb in LA-ICPMS U-Pb analyses (e.g., Tubrett et al., 2001). Therefore, titanite may not be the optimal mineral to date by LA-ICPMS methods in an area known to have been influenced by multiple episodes of metasomatic alteration and metamorphism.

2.4 Sampling: Lithology and Alteration

Locations of samples analyzed in this study, which include IOA ores, their adjacent host rocks with different degrees of metasomatic alteration, and intrusions that are in proximity to the Kiirunavaara ores within the Norrbotten area, can be found in Figure 2-1 and Table 2-1. Underground samples are located using the grid of the operating mining company LKAB and then projected to surface positions. The Geological Survey of Sweden (SGU) provided regional geological GIS data (Bergman et al., 2001), on which the geologic

map in this study (Fig. 2-1) is based. Table 2-1 gives the rock type and mineralogy of each sample; Figure 2-3 shows selected photomicrographs. More detailed rock descriptions and additional photomicrographs can be found in Appendix A.

Table 2-1. Sample list with GPS locations, rock types, and mineralogy (sorted by location).

Sample	Latitude	Longitude	Underground level	Rock type + mineralogy
K-1	N 67° 51' 00.6"	E 20° 12' 23.8"	767 m	D-ore*: mag, ap, act ±fsp-qz*
KRN-11-01	N 67° 51' 15.7"	E 20° 12' 20.7"	816 m	D-ore: *mag, ap, act*
K-6	N 67° 49' 42.2"	E 20° 12' 12.2"	1065 m	(trachy-) andesite (FW): *ab, kfsp ±act-tt-qz*
KRN-11-03	N 67° 50' 13.1"	E 20° 12' 17.4"	1365 m	(trachy-) andesite(FW): *ab, kfsp ±act-tt-qz*
K-4	N 67° 51' 11.4"	E 20° 12' 43.2"	1060 m	rhyodacite (HW): *kfsp, qz ±hbl-tt*
KRN-11-05	N 67° 50' 35.6"	E 20° 12' 37.4"	1065 m	rhyodacite (HW): *kfsp, qz ±hbl-tt*
KRN-11-06	N 67° 50' 35.8"	E 20° 12' 32.4"	1076 m	rhyodacite (HW): *kfsp (ser, Fe incl.), qz ±hbl-tt*
KRN-12-01	N 67° 50' 57.8"	E 20° 10' 24.7"	Surface	syenite: *kfsp (ser), amph, tt ±ab-qz*
KRN-12-02	N 67° 50' 57.8"	E 20° 10' 24.7"	Surface	aplite: *qz, Kfsp, ab ±hbl-tt-mag*
KRN-12-03	N 67° 50' 23.4"	E 20° 10' 49.7"	Surface	syenite: *kfsp (Fe incl.), amph, tt ±ab-qz*
KRN-12-05	N 67° 50' 30.1"	E 20° 10' 50.1"	1365 m	granite: *kfsp, qz ±ab-bt-tt*
REK-10-04	N 67° 52' 17.4"	E 20° 14' 07.4"	Surface	ore: *ap, mag ±cc-qz*
NUK-12-02	N 67° 53' 50.8"	E 20° 15' 33.9"	Surface	ore + host: *mt, ap – qz, ser ±ap, mag*
REK-12-02	N 67° 52' 17.6"	E 20° 14' 08.9"	Surface	rhyodacite (FW): *qz, ap, kfsp (ser) ±bt-rt-mag-hm*
NUK-12-01	N 67° 53' 53.1"	E 20° 15' 31.1"	Surface	rhyodacite (FW): *qz, kfsp ±bt-rt-act-mag*
REK-10-01	N 67° 52' 17.8"	E 20° 14' 15.1"	Surface	Rektorn porphyry (HW): *fsp (Fe incl., ser), qz ±Fe ox*
REK-10-02	N 67° 52' 17.8"	E 20° 14' 15.1"	Surface	Rektorn porphyry (HW) *kfsp (Fe incl., ser), qz, Fe oxide*
REK-12-01	N 67° 52' 17.8"	E 20° 14' 13.6"	Surface	Rektorn porphyry (HW) *kfsp (Fe incl., ser), qz, Fe ox*
TUV-10-01	N 67° 51' 15.1"	E 20° 18' 54.1"	Surface	ore: *mag, act, ap*
TUV-10-03	N 67° 51' 13.9"	E 20° 18' 57.0"	Surface	rhyodacite: *kfsp, qz ±hbl-tt*

Notes: KRN/K: Kiirunavaara, REK: Rektorn, NUK: Nukutus, TUV: Tuolluvaara; FW: footwall; HW: hanging wall, ser.: seritization
Abbreviations: Ab: albite, act: actinolite, ap: apatite, bt: biotite, cal: calcite, hm: hematite, Kfs: K-feldspar, mag: magnetite, qz: quartz, rt: rutile, tt: titanite

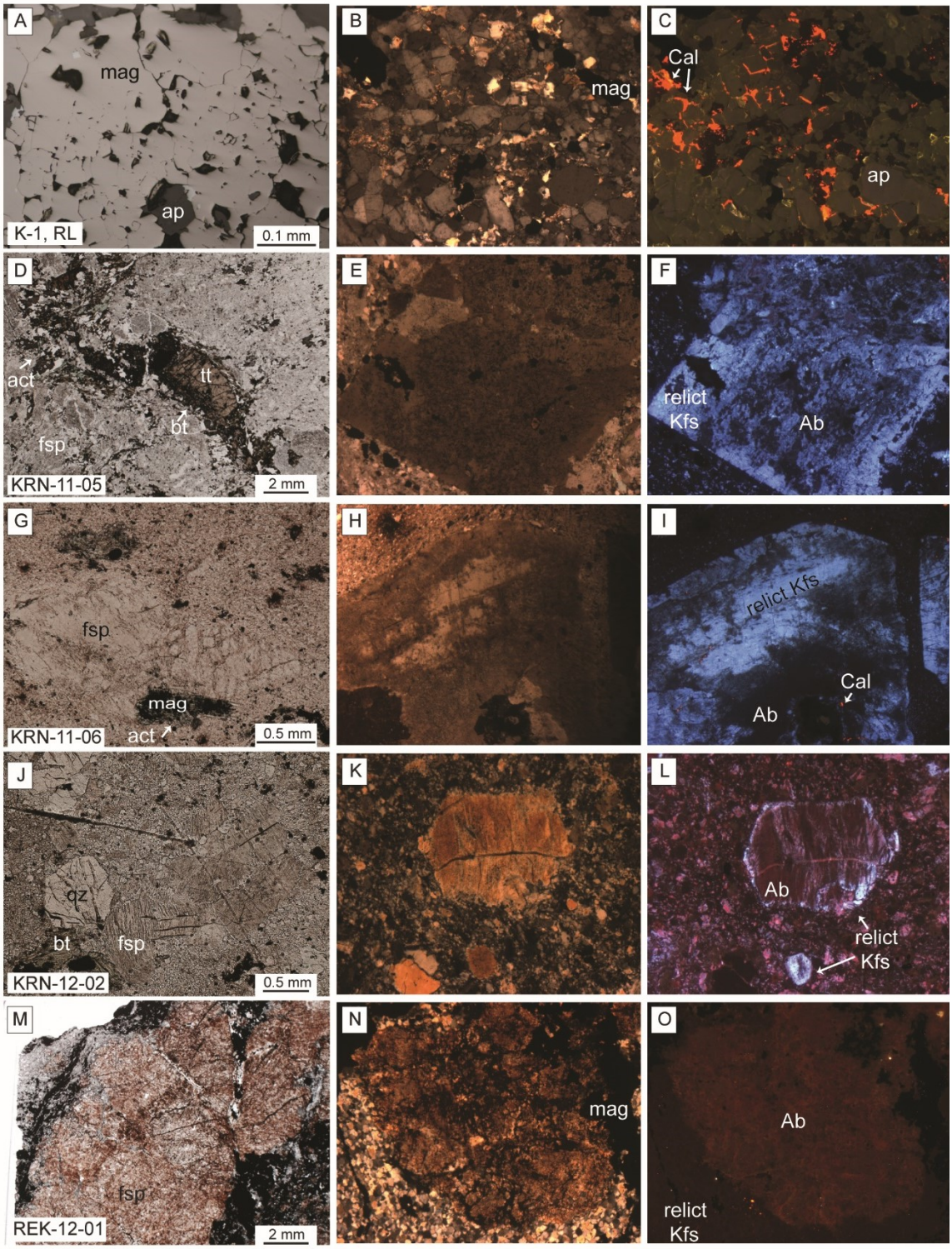
A
mag
ap
K-1, RL
0.1 mm
B
mag
C
Cal
ap
D
act
tt
bt
fsp
KRN-11-05
2 mm
E
F
relict
Kfs
Ab
G
fsp
mag
KRN-11-06
act
0.5 mm
H
I
relict Kfs
Cal
Ab
J
qz
bt
fsp
KRN-12-02
0.5 mm
K
L
Ab
relict
Kfs
M
fsp
REK-12-01
2 mm
N
mag
O
Ab
relict
Kfs

Figure 2-3 on previous page. Selected photomicrographs of minerals and effects of metasomatic alteration. Left column: reflected light (RL) or plain-polarized light (PPL), center: cross-polarized light (XPL), right: cathodoluminescence (CL); field of view for XPL and CL 2.5 mm. Mineral abbreviations as in Table 1. (A-C). Kiirunavaara ore (K-1): (A). Oxides are nearly pure magnetite (light gray, RL). (B). Predominant gray crystals are apatite (main gangue mineral, plus actinolite), (C). CL colors are green to gray from activation by 3+REEs, atypical of magmatic apatite. (D-F) Kiirunavaara hanging wall (KRN-11-05): (D). Feldspar phenocrysts plus actinolite, titanite, and magnetite in fine-grained matrix, (E). Feldspar grains have a dusty appearance. (F). Intense Na alteration, expressed as albite (dull, dark blue colors in CL) replacing original K-feldspar (bright blue). (G-I). Kiirunavaara hanging wall, altered (KRN-11-06): (G). Similar mineralogy to (D) but with reddish tint (also in hand sample). (H). Dusty feldspar grain, in finer grained matrix than (E). (I) K-feldspar (blue) only remains in cores of crystals. (J-L). Aplite dike (KRN-12-02): (J). Large K-feldspar and quartz (plus actinolite, titanite, magnetite) phenocrysts in medium to fine-grained matrix. (K). Feldspar crystal with diffuse boundary. (L). Albite alteration of original K-feldspar (blue CL) is characterized by reddish colors in CL in this sample, and also affects the matrix. (M-O). Rektorn Hanging wall (REK-12-01): (M). Large feldspar crystals have reddish tint and are surrounded by magnetite. (N). Small polycrystalline grains (at left and bottom) surrounding phenocrysts are mostly K-feldspar and quartz. (O). K-feldspar phenocrysts are nearly completely replaced by albite and quartz. All samples also contain varying amount of carbonate (bright orange in CL).

2.4.1 Metavolcanic host rocks

Host rocks adjacent to the iron oxide-apatite ore in the Kiruna area are metavolcanic rocks that belong to the Porphyry Group as noted above (e.g., Bergman et al., 2001). The Kiirunavaara footwall samples K-6 and KRN-11-03 were collected underground at the Kiirunavaara mine, on the 1065 and 1365 m mining levels (meters below former summit of Kiirunavaara hill), respectively. Two varieties of the Kiirunavaara hanging wall rock have been sampled on the 1060 to 1076 m mining levels: (1) a more-altered, reddish rhyodacite (sample KRN-11-06); and (2) a less-altered gray rhyodacite (samples KRN-11-05 and K-4). Both varieties display similar mineral assemblages and textures including phenocrysts of K-feldspar, commonly altered to albite, and quartz, within a fine-grained matrix. The footwall of the Nukutus and Rektorn deposits belongs to the same rhyodacite unit as the hanging wall of Kiirunavaara, and has also been sampled at Rektorn (REK-12-02) and Nukutus (NUK-12-01). Sample REK-12-02 is from an altered zone close to the ore body and contains abundant apatite. The hanging wall at Rektorn is a highly altered, probably originally volcanic, rock termed the Rektorn porphyry (samples REK-10-01, REK-10-02, and REK-12-01).

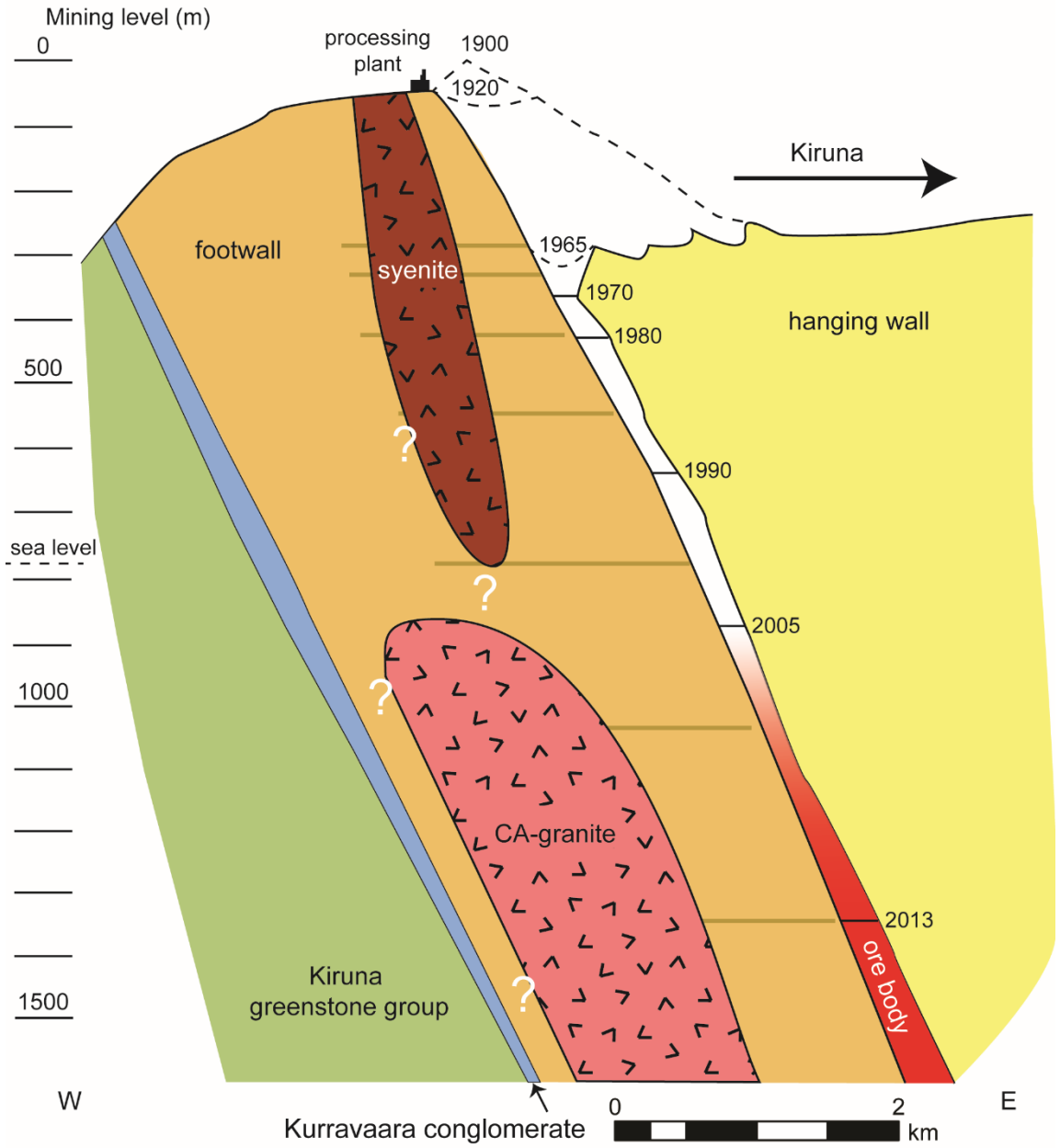

Figure 2-4. Schematic E-W cross section through the Kiirunavaara deposit (assembled based on Geological Survey of Sweden map data, Luossavaara-Kiirunavaara Aktiebolag publications and data base, and suggestions by U.B. Andersson, pers. comm., 2013), showing estimated locations of syenite body and CA [centrala anläggningar]-granite within footwall of iron orebody. Westward extension of intrusions and contact relationships among Kiruna porphyries, greenstone group, and two intrusions are unclear (denoted by question marks).

2.4.2 Syenite and granite intrusions

A syenite body occurs in the footwall of the Kiirunavaara orebody, cropping out at the surface and extending underground (Fig. 2-4). It intrudes stratigraphically below the ore body and has been sampled in two locations at the surface (samples KRN-12-01 and KRN-12-03). In some previous publications, this intrusive body was mapped as gabbro/monzonite (e.g., Bergman et al., 2001). Samples in this study, however, have the modal mineralogy of a syenite (predominant K-feldspar and <5 vol. % quartz). The appearance of the two syenite hand samples is quite different and can be related to different degrees of metasomatic alteration (strong sericitization in KRN-12-01 vs. albitization and Fe overprint in KRN-12-03). The first syenite location (KRN-12-01) contains aplitic dikes that have also been sampled (KRN-12-02).

The footwall is intruded by a granitic body that is found in deep levels of the mine (sampled at 1365 m level, KRN-12-05) and does not crop out at the surface. Since drilling by LKAB has not gone deeper, extension of the granite into lower stratigraphic layers is unknown, but is considered likely, because a similar granite body intrudes both the Kiruna Greenstone Group and the Kurravaara conglomerate northwest of Kiruna (Fig. 2-1).

2.4.3 Iron oxide apatite ore

Ore samples selected for this study are mostly those elevated in P due to their higher contents of accessory minerals. Apatite in sample K-1 (Kiirunavaara) occurs as layers between magnetite. Other gangue minerals are actinolite, interstitial plagioclase, K-feldspar, and quartz. Small monazite crystals were found associated with magnetite and between quartz grains. In the second Kiirunavaara ore sample (KRN-11-01), apatite is

distributed more randomly within the ore and the quartz content is lower than in K-1. The ore sample from Nukutus (NUK-12-02) is also quite rich in apatite (e.g., whole-rock content is 11.4 wt. % P_2O_5). Grains of magnetite and apatite are similar in size and no apatite layers or veins were observed. This sample shows the contact between the ore and metasomatically altered host rock, which consists of a very fine-grained mixture of sericite and quartz, and contains only a small amount of iron oxides and apatite. In the Rektorn ore sample (REK-10-04), apatite also is randomly distributed throughout the iron oxide minerals, but the crystals are smaller than at Nukutus. Minute monazite crystals occur within quartz in a vein of quartz and calcite that cuts the ore.

2.5 Analytical techniques

Thin sections of samples collected during this study were analyzed by optical and cathodoluminescence (CL) microscopy using a PATCO ELM-3 Cathodoluminoscope at Memorial University of Newfoundland. CL operating conditions were 12 kV, 0.7 mA, a vacuum of ~7 Pa, using an unfocused electron beam. Images were acquired using a KAPPA DX-30C Peltier cooled charge-coupled device (CCD) camera and KAPPA Image software. All CL images were acquired using the same red-green-blue settings so that CL colors could be directly compared among samples. In order to identify mineral phases observed with CL, energy dispersive spectroscopy (EDS) data were acquired using a Jeol 7100F field-emission SEM with a Thermo Ultra Dry Silicon Drift X-ray-Detector system running Thermo NSS3 software. EDS data were acquired using 15 kV, 30-50 nA, and acquisition times of 60 to 240 sec depending on the mineral phase being analyzed.

Bulk samples were crushed using a jaw crusher and disk mill so that the majority of material processed was less than 500 μm and larger than 63 μm. A split of each sample was then pulverized in a tungsten carbide shatter box for whole rock analysis of major and trace element geochemistry. Concentrations were determined at the CREAIT facility at Memorial University (Longerich et al., 1990) and at Activation Laboratories Ltd., Ontario, using X-ray fluorescence spectrometry and fusion ICP-MS techniques.

Heavy minerals were separated from the sieved fraction using standard techniques, including use of a Wilfley table, manual separation of the magnetic fraction, heavy liquid separation, and a Frantz magnetic separator. Crystals were then handpicked under a binocular microscope to select grains free of inclusions and fractures where possible. Selected zircon and titanite grains, and reference materials, were mounted in transparent, 25 mm diameter epoxy disks and polished to reveal centers for optimum analysis.

Back-scattered electron (BSE) and CL images of all mounted mineral grains were acquired prior to in situ U-Pb geochronology to select locations for the analyses. The polished epoxy mounts were imaged using an FEI Quanta 400 SEM at Memorial University, or a Hitachi S-4300 FM-SEM at the Swedish Museum of Natural History in Stockholm. After all analyses were completed (including by LA-ICPMS), new CL images were taken with a JEOL JSM-7100F field emission SEM at Memorial University to document precisely where the in situ analyses were done.

High spatial resolution U-Th-Pb mineral analyses were done using the Cameca ims1280 large-format, high mass resolution ion microprobe at the Swedish Museum of Natural History (NordSIM Facility). Zircon was analyzed following the methods described

by Whitehouse et al. (1999) and Whitehouse and Kamber (2005). Zircon standard 91500 with an age of 1065 Ma (Wiedenbeck et al., 1995) was used for U-Pb calibration. Analysis of titanite followed the methods outlined in Kiel et al. (2003); U-Pb ratios were calibrated using reference material OLT-1 (Kennedy et al., 2010) that has an age of 1014.8 ± 2.0 Ma. The Khan titanite standard having a reported age of 518 ± 2 Ma (Kinny et al., 1994; Heaman, 2009) was analyzed as a secondary standard, yielding an age of 517 ± 19 Ma (mean $^{207}Pb/^{206}Pb$ date, MSWD = 0.29, probability = 0.95, n = 7). Data reduction and common Pb corrections were done using the NordSIM in house software written by Martin Whitehouse. Correction for common Pb was made when measured ^{204}Pb counts were greater than average background by 3σ, using the model lead isotope composition of Stacey and Kramers (1975). All data are presented on Tera-Wasserburg plots (inverse concordia diagrams, $^{207}Pb/^{206}Pb$ vs. $^{238}U/^{206}Pb$) using Isoplot 3.0 (Ludwig, 2003). Concordia ages are calculated in Isoplot for samples that have overlapping concordant points. In a few cases, although it is technically feasible to calculate a concordia age, a small discordance towards younger Pb/U ages (attributed to a small amount of Pb-loss) means that the concordia age will be underestimated. Hence, in these cases, which are identified in the results, we prefer the weighted mean $^{207}Pb/^{206}Pb$ ages, calculated from the least-discordant analyses (<5% discordance). For weighted mean $^{207}Pb/^{206}Pb$ ages and concordia ages that agree closely within error, we choose to report the concordia age. Concordia age errors are 2σ unless stated otherwise; weighted mean $^{207}Pb/^{206}Pb$ ages and intercepts for Discordia lines are reported at the 95% confidence level.

2.6 Results

2.6.1 Petrography, whole-rock major and trace geochemistry

Samples from this study have been studied using reflected light, polarized light, and CL microscopy for an assessment of the mineral paragenesis and extent of alteration (Fig. 2-3 and Fig. 6-1 in Appendix A). CL microscopy is a useful tool for identifying and characterizing metasomatic alteration in rock-forming and accessory minerals. Iron oxides occurring within the Kiirunavaara ore (sample K-1) are nearly wholly magnetite. Apatite has green to gray CL colors from activation by trivalent REEs, untypical of magmatic apatite that is commonly yellow in CL and activated by Mn^{2+} (Ireland and Williams, 2003). Unaltered K-feldspar (e.g., microcline, orthoclase, sanidine) emits a bright-blue CL (Hanchar and Watson, 2003), and unaltered plagioclase (anorthite to albite) emits a green CL (Valley, 2003). In metasomatically altered feldspar, CL is either supressed (dull colors) due to limited incorporation of trace element impurities during alteration, or red, typically in albite, related to the presence of Fe^{3+} or trivalent REEs (e.g., Sm^{3+}, Eu^{3+}; Finch and Klein, 1999). All of the host rocks and intrusions show overall a strong albitization, expressed in CL as dull, dark-blue albite replacing original K-feldspar (bright blue in CL) in the Kiirunavaara hanging wall (sample KRN-11-05, -06), or as reddish albite in the aplite dike (sample KRN-12-02). In the Rektorn hanging wall (sample REK-12-01), original K-feldspar phenocrysts are nearly completely replaced by albite and quartz. All samples also contain varying amounts of carbonates (bright orange in CL).

Whole-rock geochemical compositions of the samples obtained in this study (Tables 2-2, 2-3) are plotted on different classification diagrams and metasomatism discrimination

diagrams to investigate the effects of metasomatic alteration by hydrothermal fluids. In a total alkali vs silica diagram (TAS) after Le Bas et al. (1986), data for the footwall samples from Kiirunavaara plot within the trachyandesite field, whereas those for the hanging wall samples and host rock from Tuolluvaara and footwall from Nukutus plot in the rhyolite field (Fig. 2-5a). Data for the Rektorn footwall plot as trachybasalt to basalt, and the Rektorn porphyry samples as dacite and trachyte. Both Na_2O and K_2O, which are sensitive to alteration, are elevated to varying degrees in rocks from this study (Tables 2-2 and 2-3). The TAS diagram is therefore not applicable to metasomatically altered rocks such as those in the Norrbotten region.

To evaluate effects of metasomatic alteration, the same samples were also plotted on a discrimination diagram (Winchester and Floyd, 1977; Pearce, 1996) that uses immobile trace elements for rock type classification (Fig. 2-5b). Here, data for samples from the Kiirunavaara hanging wall plot as trachyte or rhyolite/dacite, whereas those for the Tuolluvaara host rock, Nukutus footwall, and Rektorn footwall (mafic composition in the TAS diagram) plot in the rhyolite/dacite field. The Kiirunavaara footwall samples plot in the basalt and andesite/basalt fields instead of the trachyandesite field as in the TAS diagram. The Rektorn porphyry samples plot as trachyte and trachyandesite, with the exception of sample REK-10-02 that falls outside the boundaries of the diagram owing to a very high Zr content.

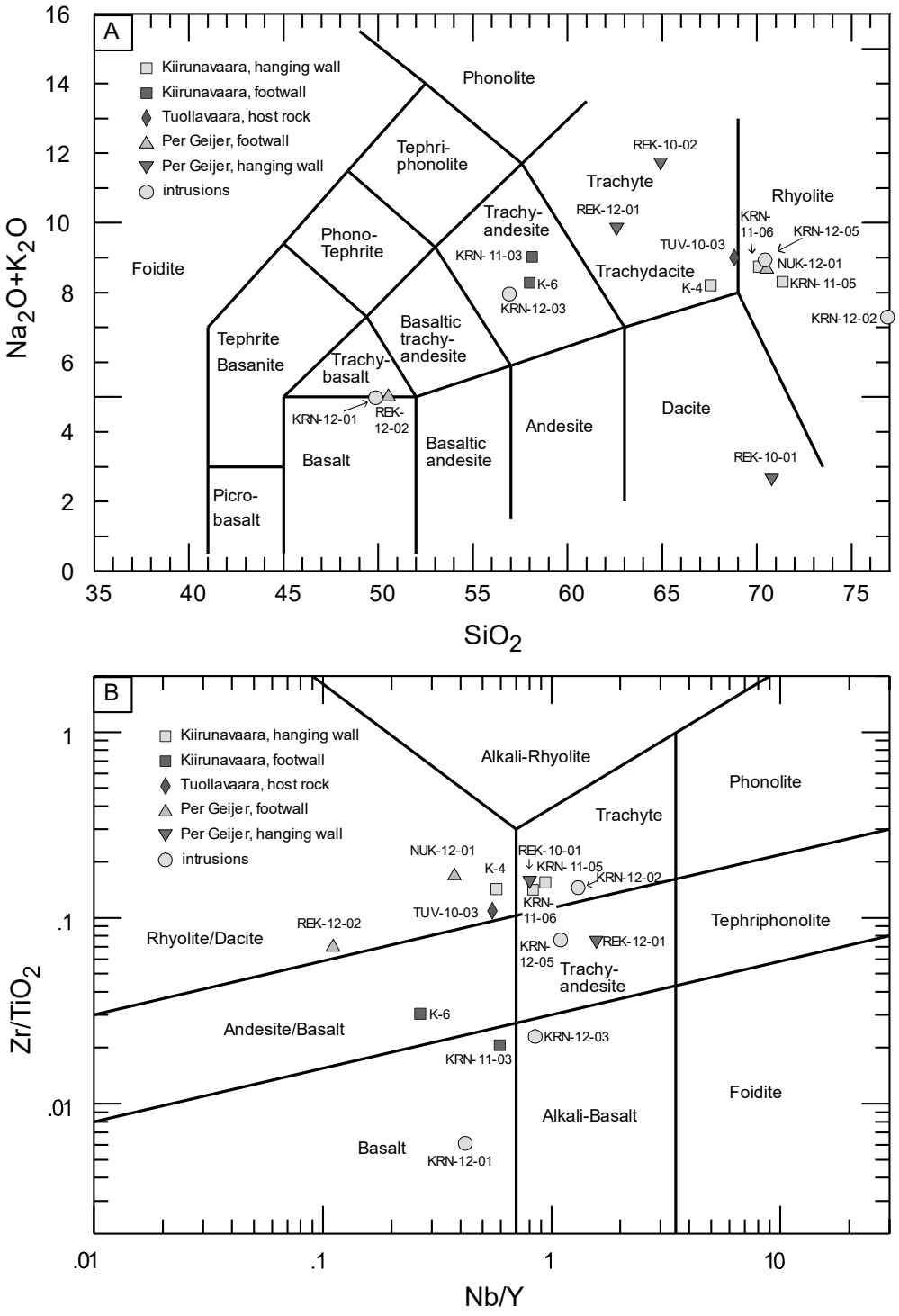

Figure 2-5. Plots of whole-rock geochemical data for host rocks and intrusions from Kiruna area in (A) total alkali vs. silica diagram after Le Bas et al. (1986), and (B) trace element discrimination diagram after Pearce (1996) and Winchester and Floyd (1977). Data for plutonic rocks are included for comparison but are classified based on modal mineralogy.

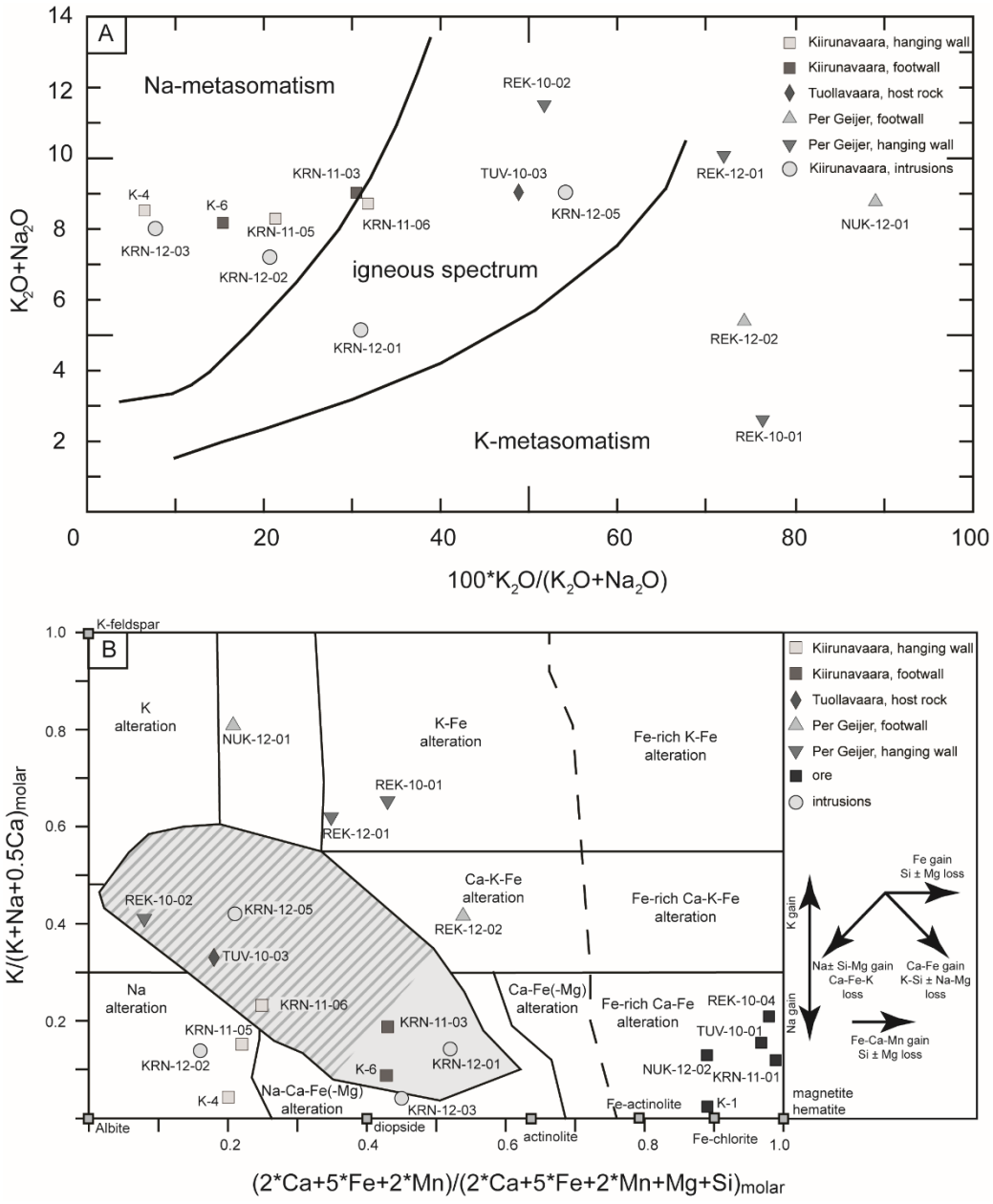

Figure 2-6. Plots of whole-rock geochemical data from this study shown in (A) metasomatism discrimination diagram, modified after Hughes (1973), and (B) in IOCG alteration discrimination diagram, modified after Montreuil et al. (2013). (A). Samples with strong K or Na alteration are distinguished from the unaltered igneous spectrum - ore samples not shown due to low contents of K and Na. (B). Alkali (Na-K) alteration is further distinguished from Fe-rich alteration on x-axis; extent of K alteration is expressed on y-axis (empirical indices based on principal component analysis). Gray field represents weakly altered samples from IOCG systems in Great Bear magmatic zone (Canada) and the Andes; striped portion of field shows Ca-Fe alteration. Both diagrams indicate that Nukutus and Rektorn host rocks show stronger K alteration than Kiirunavaara host rocks, and that influence of Ca-Fe alteration varies. See text for details.

Samples of metavolcanic host rock and ore from this study have been plotted on the metasomatic discrimination diagram modified after Hughes (2004, Fig. 2-6a), which shows that most samples plot outside the igneous compositional range. Samples from Kiirunavaara record predominant Na metasomatism, whereas K metasomatism is prevalent in the Rektorn and Nukutus samples. The IOCG alteration discrimination diagram of Montreuil et al. (2013, Fig. 2-6b) further shows the influence of Ca and Fe alteration. Ore samples plot very close to pure magnetite/hematite compositions, with only minor influence from other phases. Hanging wall samples from Kiirunavaara are Na altered, whereas footwall samples display an influence of Fe-Ca alteration, as well. Nukutus and Rektorn host rocks show a shift towards K alteration.

The ore samples from Kiruna chosen for this study are generally more enriched in P than average Kiirunavaara ore samples (e.g., Bergman et al., 2001), since these samples contain more useful accessory minerals for U-Pb geochronology. This is especially true for samples K-1 and NUK-12-02. More typical low-P ore compositions are represented by sample KRN-11-01 from Kiirunavaara and those from the Tuolluvaara ore (see Tables 2-2, 2-3, and Fig. 2-7). Most ore samples in this study share a very high content of REE (e.g., 313 to 1526 ppm Ce) and V (565 to 1216 ppm). All samples are very low in TiO_2, which is characteristic of IOA deposits globally, compared to magmatic titaniferous iron deposits like in the Roseland-Piney River district of Virginia or the Labrieville massif in Québec, containing 22 to 37 wt. % TiO_2 (Dymek and Owens, 2001).

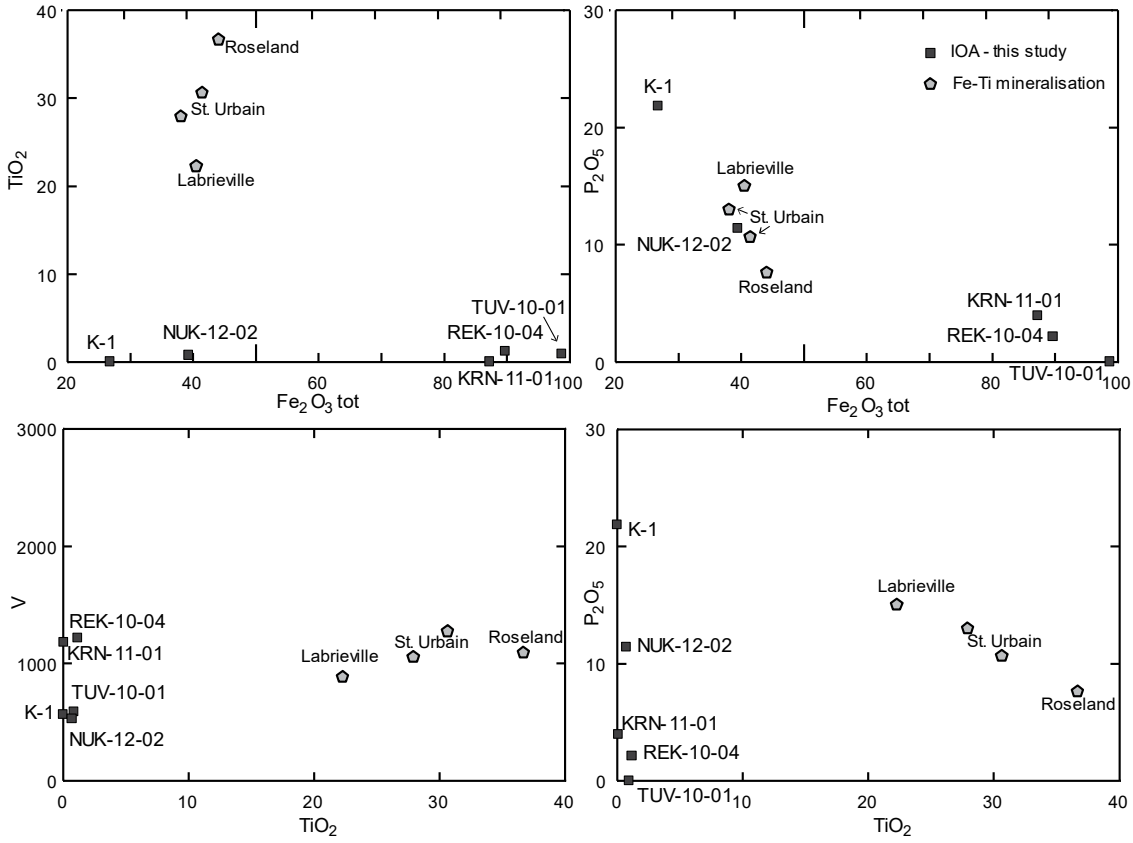

Figure 2-7. Whole-rock geochemistry of ore samples of this study plotted on different variation diagrams (Fe_2O_3 tot vs. TiO_2, Fe_2O_3 tot vs. P_2O_5, TiO_2 vs. V, and TiO_2 vs. P_2O_5). Included for comparison are compositions of four nelsonite Fe-Ti-P deposits from Roseland, Virginia, and two localities in Québec, Labrieville and St. Urbain (Dymek and Owens, 2001).

2.6.2 Zircon imaging and U-Pb geochronology

Zircon grains, although rare in most samples studied, were found and dated in the host rocks, intrusions and, most interestingly, within two magnetite ore samples (K-1 and NUK-12-02) despite their relatively low Zr contents of 45.5 and 25.0 ppm, respectively. These zircon grains show very different characteristics from host-rock zircon crystals (Fig. 2-8), described below and in chapter three. All SIMS U-Pb data for zircon grain analyses are presented in Appendix A, tables 6-1 to 6-3, sorted for each sample by decreasing $^{207}Pb/^{206}Pb$ ages.

Metavolcanic host rocks: The footwall of the Kiirunavaara deposit contains very sparse zircon grains. Samples K-6 and KRN-11-04 did not yield any zircon even after exhaustive processing. Only a few zircon grains were found in the (trachy-) andesite sample KRN-11-03, generally 100 to 150 μm long, the largest grain reaching 200 μm. CL and BSE images of the most complex grain from this sample (Fig. 2-8a) show zoning and an elongate apatite inclusion in the core area. This core is overgrown by a zircon bright in CL with well-developed growth zoning, which is followed outward by a zone that is particularly rich in small inclusions of apatite and K-feldspar. The outermost zone is patchy and dark in CL. Other grains may contain patchy and/or igneous-type (oscillatory) growth-zoned sections, as well as inclusions along particular zones. For the four overlapping zircon analyses from samples in the Kiirunavaara footwall (KRN-11-03), the weighted mean $^{207}Pb/^{206}Pb$ age of 1884.1 ± 3.7 Ma (MSWD = 0.69, n = 4) is considered most meaningful. The concordia age (1877.3 ± 12 Ma) overlaps with this mean, but plots slightly off the concordia curve (Fig. 2-9b).

Metavolcanic samples from the hanging wall are generally rich in zircon. Rhyodacite samples K-4 and KRN-11-05 contain numerous grains with typical doubly-terminated prismatic zircon shapes and well-developed growth zoning patterns throughout the crystals in both CL and BSE images (Fig. 2-8b), described as typical features of magmatic zircon (e.g., Corfu et al., 2003). Several grains exceed 200 μm in length and some can be more than 100 μm wide. Rare inclusions of mostly apatite are quite large and randomly distributed. Data for samples K-4 (not shown) and KRN-11-05 yield concordia ages with overlapping errors of 1879.5 ± 7.1 Ma (MSWD = 0.96, n = 9, weighted mean $^{207}Pb/^{206}Pb$ = 1878.4 ± 6.3 Ma) and 1880.5 ± 4.5 Ma (MSWD = 0.95, n = 8, Fig. 2-9c, weighted mean $^{207}Pb/^{206}Pb$ = 1881.4 ± 5.1 Ma). More strongly altered hanging wall sample KRN-11-06 contains fewer and smaller zircon grains that are commonly fragmented and rich in inclusions (Fig. 2-8c, grains 1 and 2). A weighted mean $^{207}Pb/^{206}Pb$ date of 1880.1 ± 2.7 Ma (MSWD = 0.97, n = 18, concordia age 1872.3 ± 6.6 Ma) is considered the most robust age, and more narrowly overlaps with the dates for the other hanging wall samples. Grains having $^{207}Pb/^{206}Pb$ ages in this range display zoning patterns similar to those of other hanging wall zircon grains (Fig. 2-8c, grain 1), but typically occur as fragments derived from larger grains. However, a number of grains that are especially rich in fractures and inclusions (Fig. 2-8c, grain 2) yield a weighted mean $^{207}Pb/^{206}Pb$ date of 1875.4 ± 3.8 Ma (MSWD = 0.36, n = 7). Ages of such grains may have been influenced by later processes.

Zircons from the Nukutus footwall (rhyodacite sample NUK-12-01, Fig. 2-8d) are of medium size (100 to 200 μm long) and show a mixture of patchy and regular growth zoning. Inclusions are rare, small, and randomly distributed. A few zircon grains have areas with

no zoning and different imaging properties (light in BSE, dark in CL) that display irregular contacts with the rest of the grain (bottom left corner in Fig. 2-8d). These textures, which cut the earlier zones, might represent areas of dissolution/re-precipitation. Therefore, these areas are probably younger than the other parts of the zircon grains, but have not been dated. The most concordant analyses from this sample (Fig. 2-10b) produce a concordia age of 1871.9 ± 5.2 Ma (MSWD = 1.5, n = 9), plotting slightly off concordia; a preferred weighted average of individual $^{207}Pb/^{206}Pb$ ages yields a date of 1881.7 ± 2.2 Ma (MSWD = 1.09, n = 24).

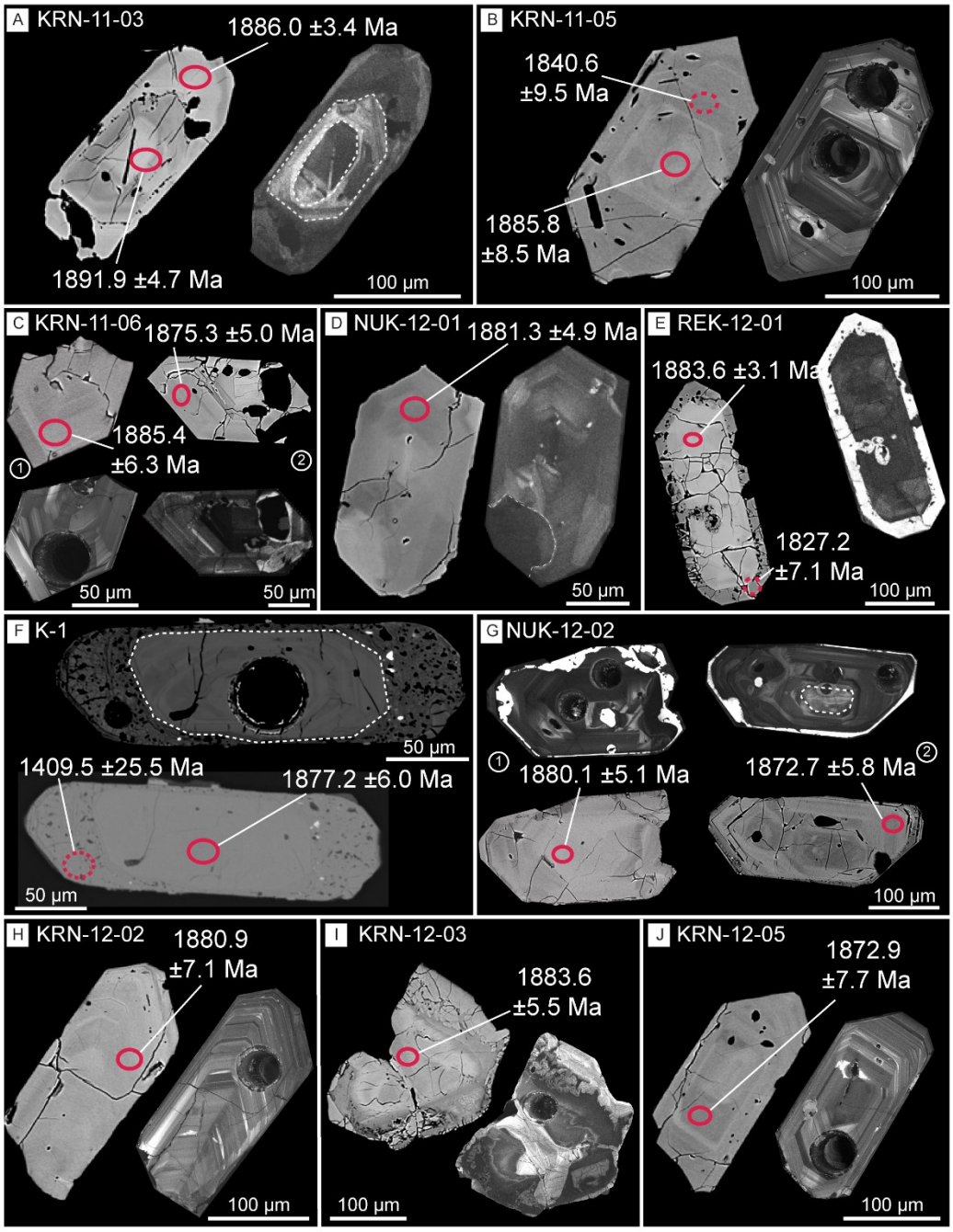

Figure 2-8. Representative images of zircon grains from selected dated samples: BSE image of each grain is on left (or at bottom for K-1 and NUK-12-02); corresponding CL image is on right (or top). Dashed lines highlight features of some grains. Red ellipses in BSE images show locations of NordSIM U-Th-Pb analyses, dashed circles are locations of discordant ages, dates are $^{207}Pb/^{206}Pb$ ages with ±1σ uncertainties. Some CL images show subsequent LA-ICPMS Lu-Hf or trace element analyses (not reported here, see chapter three and four), done after U-Pb analyses.

Only two small grains (<100 μm) were recovered from the footwall of the Rektorn orebody. However, abundant zircon was found within the Rektorn porphyry (samples REK-10-01/-02 and REK-12-01, Fig. 2-8e) and has a very distinct appearance, showing patchy cores and rims very bright in CL. These zircon grains are up to 400 μm in length. Cores are highly fractured and can have apatite inclusions of different sizes; rims contain numerous inclusions that seem to concentrate at the boundary with the core. In some cases, the "rim" grows into the core along fractures. Attempts to date the rim yielded highly discordant analyses. A Discordia line combining data for samples REK-10-01 and REK-10-02 results in an upper intercept age of 1884 ± 20 Ma and lower intercept of 383 ± 97 Ma (MSWD = 2.6, n = 10, Fig. 2-10c). The three most concordant analyses from the two samples yield a concordia age of 1873.7 ± 9.1 Ma (MSWD = 0.97, n = 3). Sample REK-12-01 has a concordia age of 1876.2 ± 6.8 Ma (MSWD = 2.1, n = 10, Fig. 2-10d), and a weighted mean $^{207}Pb/^{206}Pb$ date of 1877.1 ± 3.9 Ma (MSWD = 3.5, n = 15). A Discordia line including some of the discordant analyses results in an upper intercept age of 1883.5 ± 9.1 Ma and a lower intercept of 338 ± 60 Ma (MSWD = 5.8, n = 17). Combining the concordant analyses from the three samples yields a concordia age of 1876.3 ± 6.2 Ma (MSWD = 1.8, n = 13, not shown).

Iron ore: Zircon grains recovered from the Kiirunavaara high-P ore sample K-1 (Fig. 2-8f) are distinctly different from the zircons in the host rocks in having rims that are rich in inclusions of apatite, monazite, and Fe-rich phases. The inclusions are so numerous that the rims display a sieve-like appearance. Preliminary results of electron microprobe analysis (EMPA) and Fourier transform infrared (FTIR) analysis of selected grains from

this sample show elevated Fe, P, and H_2O contents within the zircon (Hanchar et al., 2015), which will be discussed in further detail in chapter three. The grains vary from less than 100 μm to about 150 μm in length. Although some are broken, several grains have a doubly-terminated prismatic zircon shape. Cores are either finely zoned, bright in BSE and relatively dark in CL (Fig. 2-8f, more common); or patchy, dark in BSE and very bright in CL. Both types are fractured, and overgrown by a similar looking rim. The rims clearly define a later event in the zircon growth history. Some grains have a second, thin rim that is inclusion-free and very bright in CL. Only a few concordant analyses were obtained, exclusively in the cores, plus a number of highly discordant analyses in both cores and rims of the individual grains. A concordia age obtained from four analyses is 1874.1 ± 7.1 Ma (MSWD = 1.7, n = 4, Fig. 2-9a, weighted mean $^{207}Pb/^{206}Pb$ = 1877.1 ± 4.7). The upper intercept of the Discordia line gives an age of 1884 ± 15 Ma (MSWD = 3.6, n = 33; lower intercept of 443 ± 22 Ma).

Three zircon grains recovered from the Tuolluvaara ore (sample TUV-10-01) resulted in highly discordant U-Pb analyses (> -40 % age discordance at closest approach of error ellipse to concordia at 2σ level). No zircon was found in the Rektorn ore, but several grains were obtained from the Nukutus orebody, being very large (300 μm long, up to 200 μm wide) and showing a complex growth history (sample NUK-12-02, Fig. 2-8g, grain 1, 2). Larger inclusions and cracks are common. The cores may display remnants of growth zoning, and locally shown two growth zones (Fig. 2-8g, grain 2). Concordant analyses from zircon cores (Fig. 2-10a) result in a concordia age of 1877.1 ± 3.5 Ma (MSWD = 1.3, n = 21, weighted mean $^{207}Pb/^{206}Pb$ = 1879.5 ± 2.3 Ma). All zircon grains from this sample have

rims bright in CL and rich in inclusions, resembling textures seen in zircon grains from the Rektorn porphyry (Fig. 2-8e). In several grains, a second narrow overgrowth can be observed (e.g., left tip of grain 1). Both features are too thin to be analyzed in situ by SIMS. However, one concordant analysis placed in what appears to be a second growth zone in the core has an individual $^{207}Pb/^{206}Pb$ date of 1872 ± 5.8 Ma (Fig. 2-8g, grain 2), which records a possible maximum constraint on the surrounding rim bright in CL.

Intrusions: Both samples of the syenite (KRN-12-01 and KRN-12-03) that parallels the Kiirunavaara ore body are relatively poor in zircon. Sizes can vary from less than 100 μm to over 200 μm (Fig. 2-8i) and shapes can differ significantly from that of a typical igneous zircon (Corfu et al., 2003). The grains display complex internal textures with several different zones, and contain fractures and inclusions. Within several grains a chaotic zoning pattern is observed, consisting of patchy zones penetrated by vein-like structures having large differences in CL intensity. Other grains display a faint zoning, which is generally unlike the well-defined zoning visible in grains from the metavolcanic host rocks. These parts of the grains are typically more fractured than other sections. Chaotic zones have elevated Fe and Y contents (Hanchar et al., 2015). Several grains are rich in inclusions of apatite, monazite, and Fe-oxides (see Fig. 3-4 in chapter three). The relation between the two textures (chaotic and zoned) is ambiguous. Data for zircons from both syenite intrusions yield Discordia lines with upper intercepts of 1879.7 ± 6.9 Ma (MSWD = 1.14, n = 6 for KRN-12-01, Fig. 2-9e) and 1896 ± 19 Ma (MSWD = 4.5, n = 12 for KRN-12-03, Fig. 2-9f). Lower intercepts for the two samples are 436 ± 11 Ma (KRN-12-01) and 433 ± 23 Ma (KRN-12-03). The aplite dike (sample KRN-12-02), collected from within syenite

sample KRN-12-01, is very rich in zircon grains up to 250 μm in length. Some of these grains show an internal complexity similar to zircon from the syenite, being rich in fractures, inclusions, and having areas of elevated Fe and Y concentrations. Most, however, show distinct zoning that can be seen clearly in BSE and CL images (Fig. 2-8h), are fractured, and contain some small inclusions. The CL images reveal much brighter cores in some grains. Zircons from this sample yield a concordia age of 1880.6 ± 3.7 Ma (MSWD = 0.99, *n* = 18, Fig. 2-9g), a weighted mean $^{207}Pb/^{206}Pb$ of 1880.7 ± 3.2 Ma (MSWD = 1.3, *n* = 18), and an upper intercept of 1880.2 ± 9.3 Ma and a lower intercept of 398 ± 12 Ma (MSWD = 6.5, *n* = 34).

The sample from underground granite intrusion (KRN-12-05) has numerous zircon grains up to 250 μm in length and over 100 μm wide (Fig. 2-8j). Most grains show a regular igneous growth zoning, which can either be quite distinct, or a smooth zoning that lacks major differences in BSE or CL colors or hues. Almost all grains contain a few to several fractures. Inclusions are of various types: large apatite inclusions can be found along fractures, whereas other smaller inclusions seem to occur in certain zones. No unusual Fe contents were observed in zircon grains from this sample, which yields a concordia age of 1874.2 ± 3.8 Ma (MSWD = 1.3, *n* = 24, Fig. 2-9h, weighted mean $^{207}Pb/^{206}Pb$ = 1877.4 ± 2.8 Ma).

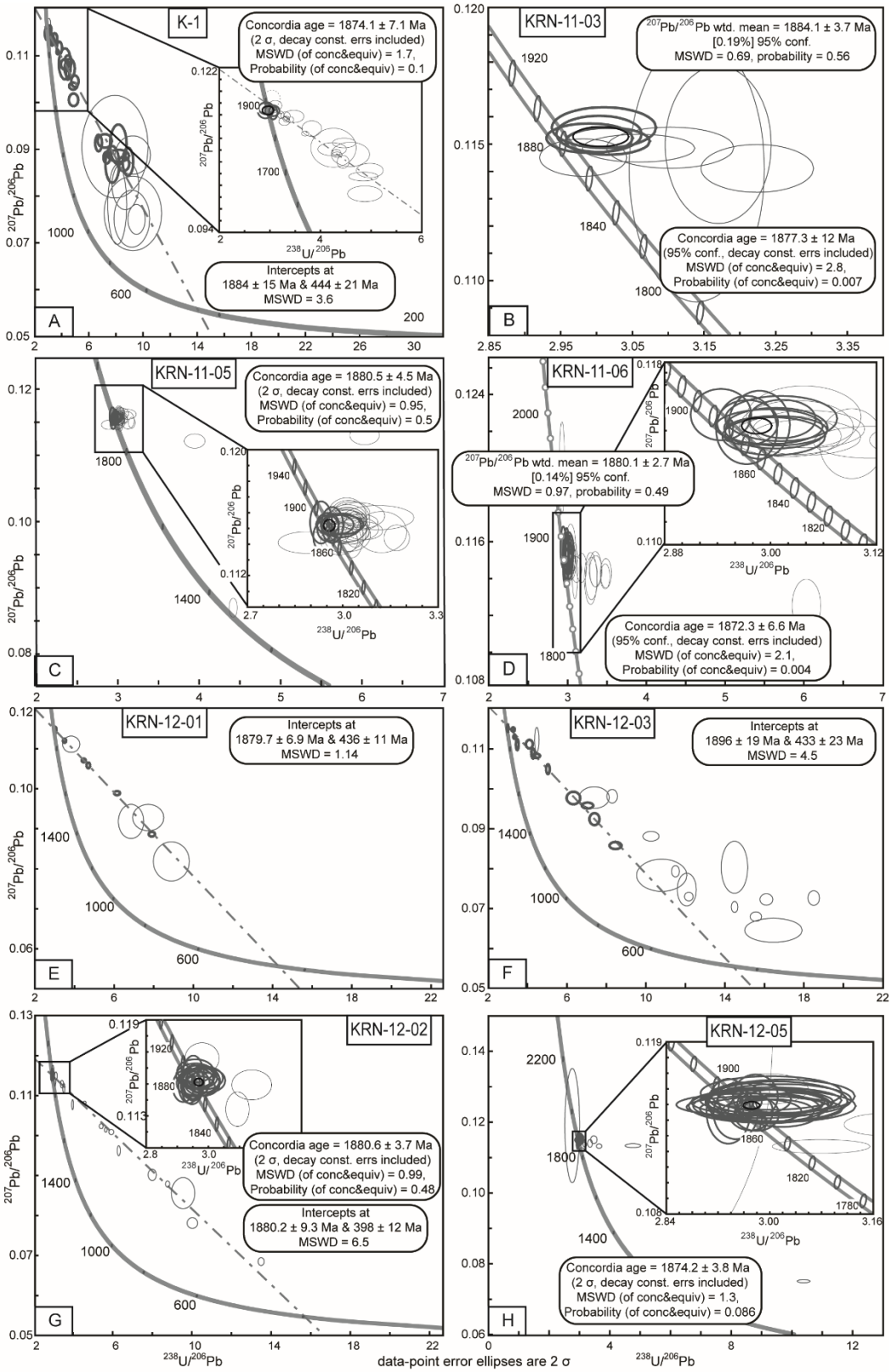
K-1
Concordia age = 1874.1 ± 7.1 Ma
(2 σ, decay const. errs included)
MSWD (of conc&equiv) = 1.7,
Probability (of conc&equiv) = 0.1
Intercepts at
1884 ± 15 Ma & 444 ± 21 Ma
MSWD = 3.6
A
KRN-11-03
207Pb/206Pb wtd. mean = 1884.1 ± 3.7 Ma
[0.19%] 95% conf.
MSWD = 0.69, probability = 0.56
Concordia age = 1877.3 ± 12 Ma
(95% conf., decay const. errs included)
MSWD (of conc&equiv) = 2.8,
Probability (of conc&equiv) = 0.007
B
KRN-11-05
Concordia age = 1880.5 ± 4.5 Ma
(2 σ, decay const. errs included)
MSWD (of conc&equiv) = 0.95,
Probability (of conc&equiv) = 0.5
C
KRN-11-06
207Pb/206Pb wtd. mean = 1880.1 ± 2.7 Ma
[0.14%] 95% conf.
MSWD = 0.97, probability = 0.49
Concordia age = 1872.3 ± 6.6 Ma
(95% conf., decay const. errs included)
MSWD (of conc&equiv) = 2.1,
Probability (of conc&equiv) = 0.004
D
KRN-12-01
Intercepts at
1879.7 ± 6.9 Ma & 436 ± 11 Ma
MSWD = 1.14
E
KRN-12-03
Intercepts at
1896 ± 19 Ma & 433 ± 23 Ma
MSWD = 4.5
F
KRN-12-02
Concordia age = 1880.6 ± 3.7 Ma
(2 σ, decay const. errs included)
MSWD (of conc&equiv) = 0.99,
Probability (of conc&equiv) = 0.48
Intercepts at
1880.2 ± 9.3 Ma & 398 ± 12 Ma
MSWD = 6.5
G
KRN-12-05
Concordia age = 1874.2 ± 3.8 Ma
(2 σ, decay const. errs included)
MSWD (of conc&equiv) = 1.3,
Probability (of conc&equiv) = 0.086
H
207Pb/206Pb
238U/206Pb
data-point error ellipses are 2 σ

Figure 2-9 on previous page. U-Pb data plotted in Tera-Wasserburg concordia diagrams for Kiirunavaara ore and host rocks. (A). Ore sample K-1, intercept age based on bold data point error ellipses, inset shows four concordant points (in bold) and data points included for Discordia; dashed ellipse is not included in concordia or intercept calculations. (B). Footwall sample KRN-11-03, weighted mean of $^{207}Pb/^{206}Pb$ dates and concordia age based on ellipses shown in bold. (C). and (D). Hanging-wall samples KRN-11-05 and KRN-11-06, bold ellipses are used for concordia age calculation in each sample, weighted mean of (D) based on 18 analyses. (E). Syenite sample KRN-12-01. (F). Syenite sample KRN-12-03; Discordia is based on bold ellipses for (E) and (F). (G). Aplite sample KRN-12-02, Discordia of all analyses, bold analyses in inset used for concordia age calculation. (H). Granite sample KRN-12-05, inset shows analyses in bold used for concordia calculation.

2.6.3 Titanite imaging and U-Pb geochronology

Titanite has been separated and dated from two samples: a footwall sample from Kiirunavaara (K-6); and a host-rock sample from Tuolluvaara (TUV-10-03). U-Th-Pb analyses of titanite are reported in Appendix A, table 6-4. Grains from both samples lack internal zonation in BSE (Fig. 2-10e, f). The analyses from sample K-6 yield a concordia age of 1876 ± 17 Ma (MSWD = 0.97, *n* = 8, Fig. 2-10e). Titanite from the Tuolluvaara rhyodacite (sample TUV-10-03) contains inclusions of Fe-oxides, apatite, or allanite. Data from this sample provide a much younger concordia age of 1685 ± 11 Ma (MSWD = 0.49, *n* = 9, Fig. 2-10f). The results from this sample show a larger spread, and one older concordant $^{207}Pb/^{206}Pb$ age of 1772.2 ± 15.5 Ma.

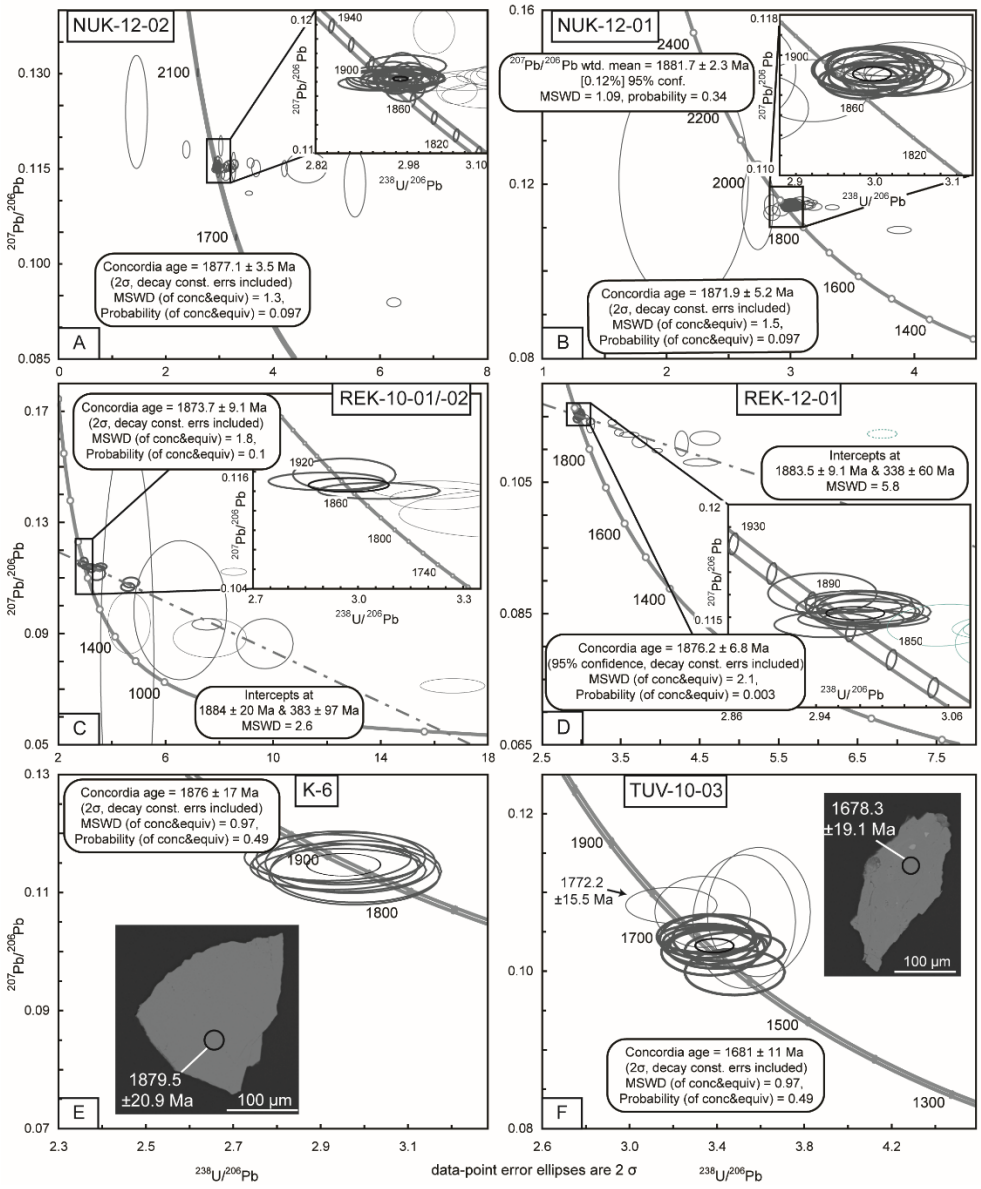

Figure 2-10. U-Pb data shown in Tera-Wasserburg concordia diagrams for zircon from Nukutus (A, B), Rektorn (C, D), and titanite (E, F), including representative BSE images. Circles in BSE images show locations of NordSIM U-Th-Pb analyses; dates are $^{207}Pb/^{206}Pb$ ages with ±1σ uncertainties. (A). Ore sample NUK-12-02, concordia age based on bold data point error ellipses as shown in inset. (B). Footwall sample NUK-12-01, concordia age based on bold ellipses shown in inset, weighted mean of $^{207}Pb/^{206}Pb$ dates based on 24 analyses. (C). Hanging-wall samples REK-10-01 and REK-10-02, Discordia based on analyses from both samples shown in bold, concordia age based on bold analyses in inset. (E). Hanging-wall sample REK-12-01, bold ellipses are used for intercept age calculation and for concordia age in inset, analyses shown in dashed are not used. (E). Titanite from Kiirunavaara footwall K-6, concordia age based on solid data point error ellipses. (F). Titanite from Tuolluvaara host rock TUV-10-03, concordia age based on bold data point error ellipses.

2.7 Discussion

2.7.1 Alteration effects inferred from petrography and whole-rock geochemistry

Metavolcanic rocks of the Porphyry Group that host the IOA mineralization in the Norrbotten region have had a number of different lithologic classifications. The footwall and hanging wall of the Kiirunavaara deposit were described as syenite porphyry and quartz-bearing porphyry by Geijer (1910), and keratophyre and quartz keratophyre by Parák (1975), but more recently are classified as trachyandesite lava and rhyodacitic pyroclastic rock by Bergman et al. (2001). The challenge in classifying these rock units is likely due to effects of pervasive post-emplacement metasomatism and regional metamorphism. Detailed petrography and whole-rock geochemical compositions have been used in this study to investigate the impact of alteration in this sample set.

Cathodoluminescence microscopy reveals the extent of metasomatic alteration of rocks sampled from Kiirunavaara (Fig. 2-3). All feldspar crystals in the metavolcanic host rocks and intrusions are pervasively altered and partially to fully replaced. Characteristic overall is strong albitization, which is reflected by high Na contents in the whole-rock geochemistry. The Rektorn porphyry further shows the influence of K metasomatism in the groundmass. The alkaline trend that these samples show in the TAS diagram (Fig. 2-5a) is therefore mostly likely influenced by this intense Na (±K) alteration. Nevertheless, data shown on that diagram and the trace element discrimination diagram (Fig. 2-5b) for the hanging wall rocks of Kiirunavaara and related units are in general agreement with the latest rock classification presented in Bergman et al. (2001). An exception is the Rektorn footwall (sample REK-12-02) taken within 2 m of the orebody that plots as trachybasalt or

basalt on the TAS diagram, instead of as rhyolite/dacite due to high apatite contents. The discrimination diagram based on relatively immobile trace elements shows the originally more felsic nature of this rock. Data for Rektorn porphyry samples plot inconsistently as trachyte (highest alkali contents of the sample suite) or as dacite (lowest alkali contents, REK-10-01), revealing varying degrees of alteration in this unit.

For the Kiirunavaara footwall samples, the classifications from the TAS and trace element discrimination diagrams do not agree. In the latter, data for the two samples plot in the andesite/basalt and basalt fields, not in the trachyandesite field. Differences in petrologic classification between the two diagrams suggest that the more alkali-rich compositions displayed in the TAS diagram are an effect of alteration. This effect appears to be more pronounced below the Kiirunavaara orebody, where trachyandesitic compositions are observed. Southwest of Kiruna, for instance, the lowest part of the Porphyry Group instead consists of basalt (Bergman et al., 2001). More whole-rock analyses from the Kiirunavaara footwall are needed in order to determine whether rocks in this location should be reconsidered andesite (silica content of ~58 wt. % is too high for a basaltic composition) instead of trachyandesite.

Use of both the metasomatism discrimination diagram of Hughes (1973) and the IOCG alteration discrimination diagram of Montreuil et al. (2013, Fig. 2-6) confirm that most samples have experienced Na and/or K metasomatism, as also observed in thin section. Both diagrams distinguish the stronger influence of K alteration within the Nukutus and Rektorn deposits from the mostly Na-altered Kiirunavaara deposit, as noted previously by Parák (1975), for instance. The IOCG alteration discrimination diagram, which has been

applied to several IOCG deposits worldwide (Montreuil et al., 2013), further distinguishes alkali (Na-K) alteration from Fe-rich alteration. Ore samples plot close to pure magnetite-hematite composition; a sample from close to a deposit (REK-12-02) shows the strongest Fe gain. In that diagram, data for weakly altered samples (gray field) overlap partly with those for Ca-Fe-altered samples. Therefore, samples that plot within this "ambiguous area" of the diagram must be interpreted carefully with knowledge of the particular rock and regional geologic history. For instance, data for both the Kiirunavaara footwall and the intruding granite fall within the weakly altered field of Montreuil et al. (2013). However, CL microscopy reveals strong metasomatic alteration of both samples. Similarly, data for the petrographically more altered hanging wall sample (KRN-11-06) plot within the ambiguous area of the diagram, distinct from those for the less-altered hanging wall samples (KRN-11-05, K-4). An Fe gain in sample KRN-11-06 is a likely reason and is in agreement with its reddish tint. This diagram also shows differences between the Nukutus and Rektorn deposits: whereas both the footwall of the Nukutus deposit and the host rocks of the Rektorn deposit are K-altered (similar to results in the Hughes discrimination diagram), most samples from Rektorn also show an influence of Ca-Fe alteration.

2.7.2 U-Pb dating – Ages of host rocks and ores

Although some calculated ages determined in this study overlap within error and all of the U-Th-Pb zircon dates fall within a period of not much more than 15 Myrs, the data may suggest an order of events for the formation of the different rock units (Fig. 2-11). The (trachy-) andesitic lava flows that constitute the footwall of the Kiirunavaara deposit were emplaced at ca. 1884 ± 4 Ma (Fig. 2-9b), discordantly on top of the Kiruna greenstones

(2.2 to 1.9 Ga, Skiöld and Cliff, 1984; Skiöld, 1986). The Kiirunavaara footwall is probably one of the oldest units related to the Svecokarelian orogeny in our data set. The lack of zircon in these samples may be explained by the intermediate composition of the lava flows (see above); even though their Zr content is quite high (337.9-347.0 ppm), it may not be high enough to have saturated this melt to form zircon (Watson and Harrison, 1983). Samples from the Kiirunavaara hanging wall have only slightly higher amounts of Zr than the footwall samples, but contain more and better-developed zircon grains. Ages of ca. 1880 Ma determined for this felsic pyroclastic unit (Fig. 2-9c) overlap with the isotope dilution thermal ionization mass spectrometry (ID-TIMS) U-Pb age of 1882 ± 24 Ma reported for the same unit by Welin (1987). Both U-Pb dates of the footwall and hanging wall determined in the present study also confirm the Sm-Nd isochron age of 1890 ± 90 Ma by Cliff et al (1990), albeit with higher precision. Younger syenite and aplite intruded the intermediate levels of the footwall at ca. 1880 Ma (Fig. 2-9e-g), contemporaneously with emplacement of the felsic pyroclastic rocks. This age for the syenite-aplite system overlaps with the age range of the Perthite monzonite suite (1880-1860 Ma), as suggested in the SGU map data (Fig. 2-1).

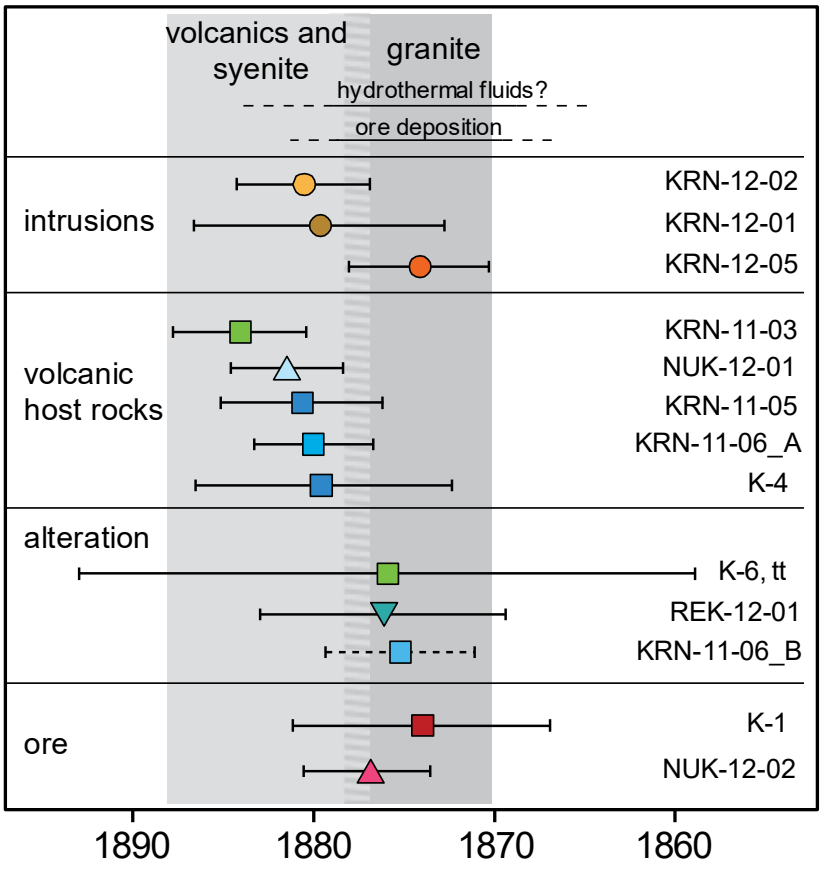

Figure 2-11. Summary of geochronological data for Kiruna area based on samples dated in this study (excluding titanite sample TUV-10-03), errors represent 2σ or 95% confidence. Light gray field represents approximate time period of emplacement of volcanic host rocks and syenite intrusions; dark gray field is age of granite intrusion (striped area = overlap). Timing of ore formation is estimated from U-Pb zircon data for ores and overlaps with age for granite intrusion; dates from altered host rock suggest that hydrothermal fluids were active during the same period. All data based on zircons, except for titanite (tt) used in sample K-6.

The underground granite intrusion at Kiirunavaara, previously dated by Cliff et al. (1990) at 1880 ± 3 Ma by multigrain zircon TIMS analysis, is now dated herein by SIMS at 1874.2 Ma ± 3.8 Ma (2σ, Fig. 2-9h). This is a somewhat younger age than for the syenite-aplite system, but is likely part of the same larger magmatic system and the Perthite monzonite suite. No age constraints exist for the low-P magnetite ore at Kiirunavaara, but the few concordant analyses of zircon grains from the high-P ore (Fig. 2-9a), overlap closely with the age of the granite, although with a larger uncertainty. Zircon from the Nukutus orebody also has a concordant age within a similar time period of ca. 1877 Ma (Fig. 2-10a). Titanite in the footwall of Kiirunavaara, as dated in the present study at 1876 ± 17 Ma (Fig. 2-10e), and by Romer et al. (1994) at 1876 ± 9 Ma, most likely records a period of metasomatic alteration when the titanite crystallized from hydrothermal fluids. Zircon from the Rektorn porphyry, the highly altered unit above the Rektorn orebody, is dated here to be of the same age (Fig. 2-10c-d). These zircon grains, and potentially the few slightly younger grains (1875 Ma) from altered hanging wall sample KRN-11-06 (Fig. 2-8d), also could have been affected by alteration during this period.

Titanite from the Tuolluvaara host rock (sample TUV-10-03) has a younger concordia age of 1685 ±11 Ma (2σ, Fig. 2-10f). This age overlaps with ages of regional isotopic disturbances recorded in Sm-Nd and Rb-Sr systems (e.g., Skiöld and Öhlander, 1989; Cliff and Rickard, 1992), and may be an expression of a later period of alteration or metamorphism. A further Caledonian influence is observed in lower intercept ages of some samples, and is not surprising, because this orogeny happened only a few tens of kilometers to the west (e.g., Bergman et al., 2001). This Caledonian influence was proposed earlier by

Romer et al. (1994), however, it is still unclear if the ore deposits were affected during this event besides what is recorded in the U-Pb system of zircons.

2.7.3 Implications for ore formation models of Kiruna iron ores

The new zircon U-Pb data for the Kiruna area obtained from this study are consistent with an interpretation of an ore formation at 1877 to 1874 Ma, shortly after emplacement of the volcanic host rocks and syenite intrusions (1880 Ma) and more or less contemporaneously with crystallization of the granitic rocks (1874 Ma) that intrude the footwall of the main deposit. Nonetheless, the narrow time interval of U-Pb zircon dates and, in some cases large age uncertainties, do not preclude coeval formation of the Kiirunavaara deposit and the hanging wall rocks. This coeval scenario could in theory include a sedimentary-exhalative genesis as proposed by Parák (1975), or an extrusive magnetite lava flow, comparable to the magmatic models applied to the El Laco deposit in Chile (e.g., Nyström and Henríquez, 1994) and as first suggested by Geijer (1910). However, combination of the suggested time line, as described above (Fig. 2-11), and the presence of brecciated contacts between ore and hanging wall, make an epigenetic ore formation, at least for the high-P magnetite ore, more likely.

The age data alone cannot discriminate between purely magmatic intrusive or hydrothermal origins of the iron ore bodies. Compared to magmatic nelsonites, for example, the typical Kiruna iron ores are low in Ti and relatively low in P (see KRN-11-01 or TUV-10-01, Fig. 2-7). Both of these elements, especially Ti, have been shown in early experiments to enhance the formation of an iron oxide melt (Philpotts, 1967; Naslund, 1983), and the differences in Fe oxide composition and generally lower apatite contents in

IOA deposits, compared to nelsonite, may be indicative of different modes of formation. In addition, zircon grains from Kiruna and Nukutus ore and the Rektorn hanging wall show distinct rims, several inclusions and fractures (Fig. 2-8e-g), and have elevated contents of Fe, P, and REE (Hanchar et al., 2015). These textures and geochemical signatures are not typical of magmatic or metamorphic zircon (e.g., Corfu et al., 2003), and thus suggest a hydrothermal influence on these samples (e.g., Hoskin, 2005). A recently proposed interpretation by (Knipping et al., 2015) for the iron oxide deposit of Los Colorados, Chile, suggests a transition from solely igneous to magmatic-hydrothermal processes was responsible for forming the compositionally zoned magnetite observed in that deposit. Magnetite cores there have characteristics of igneous Ti-rich magnetite, comparable to those of nelsonites, whereas surrounding magnetite shows magmatic-hydrothermal compositional signatures. A combination of magmatic and hydrothermal processes has also been proposed in a recent interpretation for the El Laco deposit (Tornos et al., 2016), and by analogy could explain many features of the Kiruna IOA ores.

For Kiruna, we suggest a formation process wherein at least the high-P iron ore crystallized from a highly volatile, late-stage magmatic fluid. A similar possibility was explored by Geijer (1935), based on the intrusive contacts of the ore body to the host rocks (ore breccia), mineral assemblages pointing towards high temperatures (>600°C), and structures comparable with pegmatites. In this early study, Geijer (1935) proposed involvement of a “pneumotectic” fluid, which is a magmatic liquid having a high content of volatiles that in modern nomenclature would be described as a magmatic-hydrothermal

fluid generated in the continuum between purely magmatic and high-T hydrothermal systems.

IOCG systems have recently been compared to porphyry Cu deposits (Richards and Mumin, 2013) and a similar comparison may apply to IOA deposits. Indeed, the time frame documented here for mineralization at Kiruna is comparable to those for typical porphyry Cu deposits that formed by hydrothermal fluids, such as the giant El Teniente orebody in Chile (e.g., Cannell et al., 2005). The geologic evolution for that deposit is well documented and is summarized here, for comparison: (1) volcanic and volcaniclastic rocks were intruded by mafic and tonalitic rocks at 11 to 9 Ma and 9 to 7 Ma; (2) emplacement of a large pluton and contemporaneous felsic intrusions at higher levels between 5.3 to 5.7 Ma; and (3) hydrothermal fluids and late magmatic-stage mineralization developed at ca. 4.9 Ma. The main hydrothermal stage at El Teniente was a very short-lived event of less than 100,000 years, whereas the hydrothermal system remained active until ca. 4.4 Ma.

In the case of Kiruna, analytical uncertainties on ages reported here are less well constrained than at El Teniente owing to the greater age and textural complexity of the dated minerals. However, similarities to the evolution of El Teniente are clear. Volcanic country rocks at the Kiirunavaara deposit were intruded by syenites (1884 to 1880 Ma), and shortly after, a granitic intrusion was emplaced (1874 Ma), in the same time frame as hydrothermal alteration and ore formation took place. Most importantly, the example of El Teniente shows that hydrothermal fluids were active shortly after the emplacement of intrusions, and that only a limited time is needed to produce significant mineralization.

Concordia ages of zircon from the Kiirunavaara ore (ca. 1874 Ma) and those of the smaller Nukutus deposit (ca. 1877 Ma) overlap within uncertainty. Based on narrow overlap of the ages of the granite and ores, we speculate that the heat and hydrothermal fluids provided by the intrusion were responsible for deposition of the iron ore bodies. Smaller volumes of the ore-forming hydrothermal fluids may have ascended farther upwards within the upper volcanic unit to form the Nukutus and Rektorn ores. These deposits formed potentially closer to the paleo-surface (Bergman et al., 2001), which could explain various differences compared to Kiirunavaara, such as a greater degree of K alteration. Moreover, both the granite and syenite intrusions could have acted as heat and fluid sources for forming a long-lived, high-T (>600 or 700°C) hydrothermal fluid system that transported iron and metasomatically altered the surrounding host rocks.

Although Geijer (1935) suggested a similar mechanism (see above), the magmatic aspect of the process was stressed later (e.g., Frietsch, 1978) to distinguish from the low- to moderate-temperature, sedimentary-exhalative aspects of the model as promoted by Parák (1975). However, a high-temperature (>600°C), magmatic-hydrothermal system is not only capable of explaining the intrusive contact relationships, textures, and host-rock alteration, it is also consistent with high-temperature constraints based on stable isotopes (e.g., Nyström et al., 2008). The age of this proposed magmatic-hydrothermal system is most likely constrained by the age grouping of ca. 1874 to 1877 Ma, found in zircon grains from the granite, iron ores, and altered host rocks. A metasomatic event driven by infiltrating, high-temperature hydrothermal fluids at ca. 1876 Ma was suggested by Romer

et al. (1994); together with the new data presented here, it is clear that at least some ore formation is of that same age.

With a magmatic-hydrothermal model in mind, the next step is to understand the source of the iron and REE. This goal will be investigated in a future study using whole-rock and in situ mineral radiogenic tracer isotopes (e.g., Sm-Nd, Lu-Hf, see chapters three and four). The hydrothermal nature of some zircon grains from this study will also be examined further; preliminary results can be found in Hanchar et al. (2015). Another point of interest is the mechanism of ore deposition, for which further comparisons with porphyry Cu and epithermal systems are suggested.

2.8 Conclusions

The origin of the massive Kiirunavaara IOA orebody in northern Sweden has long been an enigma. However, using new U-Pb zircon age data reported here from a well-characterized sample set, this study clarifies some details in their formation during the Svecokarelian orogeny. Based on new zircon U-Pb geochronology, an epigenetic period of iron mineralization, possibly coeval with emplacement of a granitic intrusion into the volcanic host rocks, seems likely. The footwall and hanging wall have been dated to ca. 1884 and 1880 Ma, respectively, whereas two iron ore bodies have been dated at ca. 1877 to 1874 Ma. It is suggested here that ore formation was a magmatic-hydrothermal process, powered by heat and fluids provided by emplacement of syenite intrusions at ca. 1880 Ma and later by the granitic intrusion at 1874 Ma. Existing host rocks were altered, iron was likely mobilized by these high-temperature (>600°C) fluids, and most was deposited at a boundary between two volcanic host rocks, resulting in the sheet-like geometry of the

Kiirunavaara ore deposit. The smaller Nukutus and Rektorn deposits may have formed by hydrothermal fluids that rose farther up within the upper volcanic unit. The intense metasomatic alteration of the host rocks, as expressed in alkaline bulk composition, is best explained by the involvement of magmatic-hydrothermal fluids.

2.9 Acknowledgments

This paper represents the first of three parts of the PhD research of the senior author. Great thanks are due to LKAB (Kiirunavaara operations) for financial and logistical support, especially K. Holme for making the project possible, and many others for fruitful discussions and help during sampling, including, but not limited to, U.B. Anderson, H. Rutanen, and C. Debras. Comments by U.B. Andersson and K. Holme improved an earlier version of the manuscript. The project was financially supported by NSERC, MUN, SEG, and MAC. Numerous people are thanked for discussions and assistance in the labs including M. Wilson, S.J. Piercey, G. Layne, G.R. Dunning, C.M. Fisher, S.G. Broughm, P. King, and L. Hewa at MUN, K. Lindén and A.S. Bouvier at the Swedish Museum of Natural History, and J. Anderson, A. Hallberg, S. Bergman, J.A. Perdåhl and others at the Geological Survey of Sweden. Constructive reviews by B. Bingen and S. Bergman helped improve the manuscript; J.F. Slack is thanked for editorial handling.

2.10 Bibliography – Chapter two

Amelin, Y. V., Heaman, L. M., and Semenov, V. S., 1995, U-Pb geochronology of layered mafic intrusions in the eastern Baltic Shield: implications for the timing and duration of Paleoproterozoic continental rifting: Precambrian Research, v. 75, p. 31-46.

Barton, M. D., and Johnson, D. A., 1996, Evaporitic-source model for igneous-related Fe oxide-(REE-Cu-Au-U) mineralization: Geology, v. 24, p. 259-262.

Benavides, J., Kyser, T. K., Clark, A. H., Oates, C. J., Zamora, R., Tarnovschi, R., and Castillo, B., 2007, The Mantoverde Iron Oxide-Copper-Gold district, III Región, Chile: The role of regionally derived, nonmagmatic fluids in chalcopyrite mineralization: Economic Geology, v. 102, p. 415-440.

Bergman, S., Kübler, L., and Martinsson, O., 2001, Description of regional geological and geophysical maps of northern Norrbotten County (east of the Caledonian Orogen), Sveriges Geologiska Undersökning, Ba 56, 110 pp.

Billström, K., Eilu, P., Martinsson, O., Niiranen, T., Broman, C., Weihed, P., Wanhainen, C., and Ojala, J., 2010, IOCG and related deposits of the Northern Fennoscandian Shield, *in* Porter, T. M., ed., Hydrothermal iron oxide copper-gold and related deposits: a global perspective, 4: Adelaide, PGC Publishing, p. 415-426.

Black, L. P., Kamo, S. L., Allen, C. M., Davis, D. W., Aleinikoff, J. N., Valley, J. W., Mundil, R., Campbell, I. H., Korsch, R. J., Williams, I. S., and Foudoulis, C., 2004, Improved $^{206}Pb/^{238}U$ microprobe geochronology by the monitoring of a trace-element-related matrix effect; SHRIMP, ID–TIMS, ELA–ICP–MS and oxygen isotope documentation for a series of zircon standards: Chemical Geology, v. 205, p. 115-140.

Bookstrom, A. A., 1995, Magmatic features of iron ores of the Kiruna type in Chile and Sweden; ore textures and magnetite geochemistry; discussion: Economic Geology and the Bulletin of the Society of Economic Geologists, v. 90, p. 469-473.

Cannell, J., Cooke, D. R., Walshe, J. L., and Stein, H., 2005, Geology, mineralization, alteration, and structural evolution of the El Teniente porphyry Cu-Mo deposit: Economic Geology, v. 100, p. 979-1003.

Cliff, R. A., and Rickard, D., 1992, Isotope systematics of the Kiruna magnetite ores, Sweden: Part 2. Evidence for a secondary event 400 m.y. after ore formation: Economic Geology, v. 87, p. 1121-1129.

Cliff, R. A., Rickard, D., and Blake, K., 1990, Isotope systematics of the Kiruna magnetite ores, Sweden: Part 1. Age of the ore: Economic Geology, v. 85, p. 1770 - 1776.

Corfu, F., Hanchar, J. M., Hoskin, P. W. O., and Kinny, P., 2003, Atlas of zircon textures: Reviews in Mineralogy and Geochemistry, v. 53, p. 469-500.

Dymek, R. F., and Owens, B. E., 2001, Petrogenesis of apatite-rich rocks (nelsonites and oxide-apatite gabbronorites) associated with massif anorthosites: Economic Geology, v. 96, p. 797-815.

Frietsch, R., 1978, On the magmatic origin of iron ores of the Kiruna type: Economic Geology, v. 73, p. 478-485.

Frietsch, R., 1979, Petrology of the Kurravaara area, northeast of Kiruna, northern Sweden, Sveriges Geologiska Undersökning, C 522, 38 pp.

Frietsch, R., 1984, On the magmatic origin of iron ores of the Kiruna type - a reply: Economic Geology, v. 79, p. 1949-1951.

Frietsch, R., Tuisku, P., Martinsson, O., and Perdahl, J. A., 1997, Early Proterozoic Cu-(Au) and Fe ore deposits associated with regional Na-Cl metasomatism in northern Fennoscandia: Ore Geology Reviews, v. 12, p. 1-34.

Geijer, P., 1910, Igneous rocks and iron ores of Kiirunavaara, Luossavaara and Tuolluvaara, Scientific and practical researches in Lapland arranged by Luossavaara-Kiirunavaara Aktiebolag - Geology of the Kiruna district, 2: Stockholm, 278 pp.

Geijer, P., 1935, Die nordschwedischen Eisenerze und verwandte Lagerstätten als Beispiele eruptiver Spaltungsprozesse: Geologische Rundschau, v. 26, p. 351-366.

Hanchar, J. M., and Watson, E. B., 2003, Zircon saturation thermometry, *in* Hanchar, J. M., and Hoskin, P. W. O., eds., Zircon, Reviews in Mineralogy and Geochemistry, 53: Washington, DC, Mineralogical Society of America/Geochemical Society, p. 89-112.

Hanchar, J. M., Westhues, A., Voisey, C. M., Whitehouse, M. J., and Rossman, G. R., 2015, U-Pb, Hf, O, trace element, and H_2O, constraints for the Kiruna apatite iron oxide deposits, Sweden: 25th Goldschmidt conference, Prague, Aug 16-21, Abstract 1166.

Heaman, L. M., 2009, The application of U–Pb geochronology to mafic, ultramafic and alkaline rocks: An evaluation of three mineral standards: Chemical Geology, v. 261, p. 43-52.

Hildebrand, R. S., 1986, Kiruna-type deposits - their origin and relationship to intermediate subvolcanic plutons in the Great Bear magmatic zone, Northwest Canada: Economic Geology, v. 81, p. 640-659.

Hitzman, M. W., Oreskes, N., and Einaudi, M. T., 1992, Geological characteristics and tectonic setting of Proterozoic iron oxide (Cu-U-Au-Ree) deposits: Precambrian Research, v. 58, p. 241-287.

Hoskin, P. W. O., 2005, Trace-element composition of hydrothermal zircon and the alteration of Hadean zircon from the Jack Hills, Australia: Geochimica Et Cosmochimica Acta, v. 69, p. 637-648.

Ireland, T. R., and Williams, I. S., 2003, Considerations in zircon geochronology by SIMS, *in* Hanchar, J. M., and Hoskin, P. W. O., eds., Zircon, Reviews in Mineralogy and Geochemistry, 53: Washington, DC, Mineralogical Society of America/Geochemical Society, p. 215-241.

Johnson, J. P., and Cross, K. C., 1995, U-Pb geochronological constraints on the genesis of the Olympic Dam Cu-U-Au-Ag deposit, South Australia: Economic Geology, v. 90, p. 1046-1063.

Kennedy, A. K., Kamo, S. L., Nasdala, L., and Tams, N. E., 2010, Grenville skarn titanite: Potential reference material for SIMS U–Th–Pb analysis: The Canadian Mineralogist, v. 48, p. 1423-1443.

Kiel, H. M., Cornell, D. H., and Whitehouse, M. J., 2003, Age and emplacement conditions of the Chalmers mafic intrusion deduced from contact melts: GFF, v. 125, p. 213-220.

Kinny, P. D., McNaughton, N. J., Fanning, C. M., and Maas, R., 1994, 518 Ma sphene (titanite) from the Khan pegmatite, Namibia, southwest Africa: a potential ion-microprobe standard: 8th International Conference on Geochronology, Cosmochronology and Isotope Geology, Berkeley, USA, June 5 -11, 1994, 1994, p. 171

Knipping, J. L., Bilenker, L. D., Simon, A. C., Reich, M., Barra, F., Deditius, A. P., Lundstrom, C., Bindeman, I., and Munizaga, R., 2015, Giant Kiruna-type deposits form by efficient flotation of magmatic magnetite suspensions: Geology, v. 43, p. 591-594.

LeBas, M. J., LeMaitre, R. W., Streckeisen, A., Zanettin, B., and IUGS Subcommission on the Systematics of Igneous Rocks, 1986, A Chemical Classification of Volcanic Rocks Based on the Total Alkali-Silica Diagram: Journal of Petrology, v. 27, p. 745-750.

LKAB, 2014, Integrated report - Annual report and sustainability report 2013, http://www.lkab.com/en/, Luleå, LKAB, 161 pp.

Loberg, B. E. H., and Horndahl, A. K., 1983, Ferride geochemistry of Swedish Precambrian iron ores: Mineralium Deposita, v. 18, p. 487-504.

Longerich, H. P., Jenner, G. A., Fryer, B. J., and Jackson, S. E., 1990, Inductively coupled plasma-mass spectrometric analysis of geological samples: A critical evaluation based on case studies: Chemical Geology, v. 83, p. 105-118.

Ludwig, K. R., 2003, User's manual for Isoplot 3.00, A geochronological toolkit for Microsoft Excel: Berkley Geochronology Center Special Publication, v. 4, p. 71.

Lundbohm, H., 1910, Sketch of the Geology of the Kiruna district: Geologiska Forefingers I Stockholm Forhandlingar, v. 32, p. 751-788.

Martinsson, O., 2004, Geology and metallogeny of the northern Norrbotten Fe-Cu-Au province: Society of Economic Geologists, Guidebook Series, v. 33, p. 131-148.

Martinsson, O., Billström, K., Broman, C., Weihed, P., and Wanhainen, C., 2016, Metallogeny of the northern Norrbotten ore province, northern Fennoscandian shield with emphasis on IOCG and apatite-iron ore deposits: Ore Geology Reviews, v.78, p. 447-492.

Mücke, A., and Younessi, R., 1994, Magnetite-apatite deposits (Kiruna-type) along the Sanandaj-Sirjan zone and in the Bafq area, Iran, associated with ultramafic and calc-alkaline rocks and carbonatites: Mineralogy and Petrology, v. 50, p. 219-244.

Naslund, H. R., 1983, The effect of oxygen fugacity on liquid immiscibility in iron-bearing silicate melts: American Journal of Science, v. 283, p. 1034-1059.

Nold, J. L., Dudley, M. A., and Davidson, P., 2014, The Southeast Missouri (USA) Proterozoic iron metallogenic province—Types of deposits and genetic relationships to magnetite–apatite and iron oxide–copper–gold deposits: Ore Geology Reviews, v. 57, p. 154-171.

Nyström, J. O., Billström, K., Henríquez, F., Fallick, A. E., and Naslund, H. R., 2008, Oxygen isotope composition of magnetite in iron ores of the Kiruna type in Chile and Sweden: Gff, v. 130, p. 177 - 188.

Nyström, J. O., and Henríquez, F., 1994, Magmatic features of iron ores of the Kiruna type in Chile and Sweden; ore textures and magnetite geochemistry: Economic Geology, v. 89, p. 820-839.

Parák, T., 1973, Rare earths in apatite iron ores of Lappland together with some data about Sr, Th and U content of these ores: Economic Geology, v. 68, p. 210-221.

Parák, T., 1975, Kiruna iron ores are not 'intrusive-magmatic ores of the Kiruna type': Economic Geology, v. 70, p. 1242-1258.

Pearce, J. A., 1996, A user's guide to basalt discrimination diagrams, *in* Wyman, D. A., ed., Trace Element Geochemistry of Volcanic Rocks: Applications for Massive Sulphide Exploration, Geological Association of Canada, Short Course Notes, 12, p. 79–113.

Philpotts, A. R., 1967, Origin of certain iron-titanium oxide and apatite rocks: Economic Geology, v. 62, p. 303-315.

Porter, T. M., 2010, Current understanding of iron oxide associated-alkali altered mineralised systems: Part I - An overview, *in* Porter, T. M., ed., Hydrothermal iron oxide copper-gold and related deposits: a global perspective, 3: Adelaide, PGC Publishing, p. 5-32.

Richards, J. P., and Mumin, A. H., 2013, Magmatic-hydrothermal processes within an evolving Earth: Iron oxide-copper-gold and porphyry Cu ± Mo ± Au deposits: Geology, v. 41, p. 767-770.

Romer, R. L., Martinsson, O., and Perdahl, J. A., 1994, Geochronology of the Kiruna Iron-Ores and Hydrothermal Alterations: Economic Geology and the Bulletin of the Society of Economic Geologists, v. 89, p. 1249-1261.

Skiöld, T., 1986, On the age of the Kiruna Greenstones, northern Sweden: Precambrian Research, v. 32, p. 35-44.

Skiöld, T., and Cliff, R. A., 1984, Sm-Nd and U-Pb dating of Early Proterozoic mafic-felsic volcanism in northernmost Sweden: Precambrian Research, v. 26, p. 1-13.

Skiöld, T., and Öhlander, B., 1989, Chronology and geochemistry of late Svecofennian processes in northern Sweden: Geologiska Föreningen i Stockholm Förhandlingar, v. 111, p. 347-354.

Smith, M. P., Storey, C. D., Jeffries, T. E., and Ryan, C., 2009, In situ U-Pb and trace element analysis of accessory minerals in the Kiruna district, Norrbotten, Sweden: New constraints on the timing and origin of mineralization: Journal of Petrology, v. 50, p. 2063-2094.

Stacey, J. S., and Kramers, J. D., 1975, Approximation of terrestrial lead isotope evolution by a two-stage model: Earth and Planetary Science Letters, v. 26, p. 207-221.

Storey, C. D., Smith, M. P., and Jeffries, T. E., 2007, In situ LA-ICP-MS U-Pb dating of metavolcanics of Norrbotten, Sweden: Records of extended geological histories in complex titanite grains: Chemical Geology, v. 240, p. 163-181.

Tornos, F., Velasco, F., and Hanchar, J. M., 2016, Iron-rich melts, magmatic magnetite, and superheated hydrothermal systems: The El Laco deposit, Chile: Geology, v. 44, p. 427-430.

Tubrett, M., Košler, J., and Sylvester, P., 2001, Applying a common Pb correction in dating of accessory minerals by laser ablation-ICP-MS, GAC MAC Annual Meeting, 26: St. John's, p. 151-152.

Valley, J. W., 2003, Oxygen isotopes in zircon, *in* Hanchar, J. M., and Hoskin, P. W. O., eds., Zircon, Reviews in Mineralogy and Geochemistry, 53: Washington, DC, Mineralogical Society of America/Geochemical Society, p. 343-385.

Valley, P. M., Fisher, C. M., Hanchar, J. M., Lam, R., and Tubrett, M., 2010, Hafnium isotopes in zircon: A tracer of fluid-rock interaction during magnetite-apatite ("Kiruna-type") mineralization: Chemical Geology, v. 275, p. 208-220.

Wanhainen, C., Broman, C., and Martinsson, O., 2003, The Aitik Cu-Au-Ag deposit in northern Sweden: a product of high salinity fluids: Mineralium Deposita, v. 38, p. 715-726.

Watson, E. B., and Harrison, T. M., 1983, Zircon saturation revisited: temperature and composition effects in a variety of crustal magma types: Earth and Planetary Science Letters, v. 64, p. 295-304.

Welin, E., 1987, The depositional evolution of the Svecofennian supracrustal sequence in Finland and Sweden: Precambrian Research, v. 35, p. 95-113.

Whitehouse, M. J., and Kamber, B. S., 2005, Assigning dates to thin gneissic veins in high-grade metamorphic terranes: A cautionary tale from Akilia, southwest Greenland: Journal of Petrology, v. 46, p. 291-318.

Whitehouse, M. J., Kamber, B. S., and Moorbath, S., 1999, Age significance of U–Th–Pb zircon data from early Archaean rocks of west Greenland—a reassessment based on combined ion-microprobe and imaging studies: Chemical Geology, v. 160, p. 201-224.

Wiedenbeck, M., Alle, P., Corfu, F., Griffin, W. L., Meier, M., Oberli, F., Vonquadt, A., Roddick, J. C., and Speigel, W., 1995, 3 natural zircon standards for U-Th-Pb, Lu-Hf, trace-element and REE analyses: Geostandards Newsletter, v. 19, p. 1-23.

Winchester, J. A., and Floyd, P. A., 1977, Geochemical magma type discrimination: Application to altered and metamorphosed basic igneous rocks: Chemical Geology, v. 20, p. 325-343.

Witschard, F., 1984, The geological and tectonic evolution of the Precambrian of northern Sweden — A case for basement reactivation?: Precambrian Research, v. 23, p. 273-315.

Table 2-2. Whole rock geochemistry of ore, volcanic host rocks and intrusions from the Kiirunavaara mine.

sample	**K-1**	**KRN-11-01**	**K-6**	**KRN-11-03**	**K-4**	**KRN-11-05**	**KRN-11-06**	**KRN-12-01**	**KRN-12-02**	**KRN-12-03**	**KRN-12-05**
type	D-ore	D-ore	footwall	footwall	hanging wall	hanging wall	hanging wall	syenite	aplite	syenite	granite
SiO_2	15.4[1]	1.81	58.0[1]	58.1	67.6[1]	71.4	70.2	50.0	77.0	56.8	70.4
TiO_2	0.01[1]	0.09	1.11[1]	1.66	0.33[1]	0.31	0.34	0.86	0.13	1.55	0.29
Al_2O_2	2.66[1]	1.20	13.31[1]	13.63	13.74[1]	13.63	14	17.71	11.93	14.24	13.44
Fe_2O3_{tot}	26.79[1]	87.27	10.34[1]	9.7	3.47[1]	4.93	5.7	10.15	3.77	10.92	4.53
MnO	0.07[1]	0.06	0.08[1]	0.06	0.02[1]	0.03	0.04	0.10	0.02	0.12	0.02
MgO	3.55[1]	0.22	5.06[1]	2.78	0.73[1]	0.54	0.64	5.12	0.16	3.39	0.4
CaO	28.99[1]	5.15	4.80[1]	5.07	1.76[1]	0.92	0.86	10.63	0.2	4.65	0.75
Na_2O	1.44[1]	0.10	7.02[1]	6.26	7.62[1]	6.49	5.94	3.52	5.74	7.31	4.1
K_2O	0.36[1]	0.33	1.27[1]	2.74	0.54[1]	1.77	2.78	1.58	1.49	0.61	4.82
P_2O_5	21.82[1]	3.94	1.19[1]	0.45	0.05[1]	n.d.	0.04	0.11	0.02	0.01	0.07
LOI	-	-2.06	-	0.02	-	0.89	-0.02	0.94	-0.29	0.72	0.61
Total	**101.09**	**98.11**	**102.16**	**100.49**	**95.86**	**100.89**	**100.50**	**100.65**	**100.07**	**100.34**	**99.47**
S	420[1]	-	265[1]	-	6703[1]	-	-	-	-	-	-
Cl	481[1]	-	159[1]	-	414[1]	-	-	-	-	-	-
Sc	28[1]	4	28[1]	21	10[1]	4	5	39	1	19	3
V	565[1]	1179	184[1]	142	12[1]	20	22	255	29	96	25
Co		-	-	79	-	97	93	62	114	49	119
Ni	120[1]	-	22[1]	n.d.	n.d.	n.d.	n.d.	50	n.d.	n.d.	n.d.
Cu	20[1]	-	n.d.	20	28[1]	50	40	30	50	170	30
As	81[1]	-	n.d.	n.d.	n.d.	n.d.	n.d.	n.d.	n.d.	n.d.	n.d.
Rb	10[1]	-	20[1]	41	14[1]	30	37	64	17	29	134
Sr	122[1]	37	63[1]	57	63[1]	52	55	489	13	106	61
Y	383.1[1]	72.5[2]	70.6[1]	59.6[2]	46.4[1]	18.8[2]	42.2[2]	20.1[2]	27.4[2]	31.2[2]	18.5[2]
Zr	45.4[1]	17.5[2]	337.9[1]	347.0[2]	474.1[1]	486.5[2]	487.1[2]	53.5[2]	192.5[2]	362.8[2]	223.9[2]
Nb	2.5[2]	35.6[2]	18.6[2]	34.9[2]	26.5[2]	17.6[2]	34.9[2]	8.2[2]	35.3[2]	26.1[2]	20.0[2]
Ag	-	-	-	1.8	-	2.4	2.7	n.d.	1.6	1.4	1.2
Ba	18[2]	437[2]	172[2]	401	484[2]	334	606	306	140	93	509
La	671.4[2]	138.9[2]	89.4[2]	243.5[2]	56.3[2]	39.3[2]	48.3[2]	21.5[2]	11.4[2]	82.7[2]	59.0[2]
Ce	1526.2[2]	313.5[2]	141.3[2]	351.9[2]	112.6[2]	63.2[2]	104.9[2]	40.9[2]	27.4[2]	137.6[2]	107.0[2]
Pr	175.1[2]	36.5[2]	15.2[2]	32.8[2]	13.5[2]	6.3[2]	13.2[2]	5.1[2]	4.0[2]	13.0[2]	11.1[2]
Nd	637.7[2]	140.9[2]	59.5[2]	100.9[2]	53.1[2]	21.7[2]	49.9[2]	21.2[2]	16.8[2]	43.0[2]	36.4[2]
Sm	90.8[2]	21.9[2]	12.3[2]	15.1[2]	10.0[2]	4.0[2]	9.2[2]	4.3[2]	4.0[2]	6.8[2]	5.4[2]
Eu	13.2[2]	5.4[2]	2.1[2]	2.5[2]	1.7[2]	0.9[2]	1.5[2]	1.2[2]	0.3[2]	1.6[2]	0.9[2]
Gd	71.9[2]	18.6[2]	11.9[2]	12.3[2]	8.5[2]	3.4[2]	8.4[2]	4.3[2]	3.9[2]	6.0[2]	4.0[2]
Tb	9.0[2]	2.4[2]	1.8[2]	1.9[2]	1.4[2]	0.6[2]	1.4[2]	0.6[2]	0.7[2]	0.9[2]	0.6[2]
Dy	48.3[2]	12.6[2]	11.1[2]	10.7[2]	8.6[2]	3.6[2]	8.0[2]	4.0[2]	5.2[2]	5.5[2]	3.6[2]
Ho	9.1[2]	2.6[2]	2.3[2]	2.3[2]	1.7[2]	0.9[2]	1.7[2]	0.8[2]	1.1[2]	1.1[2]	0.7[2]
Er	24.4[2]	7.3[2]	6.6[2]	7.3[2]	5.2[2]	2.8[2]	5.6[2]	2.3[2]	3.6[2]	3.5[2]	2.1[2]
Tm	3.1[2]	1.0[2]	1.0[2]	1.2[2]	0.8[2]	0.5[2]	0.9[2]	0.3[2]	0.6[2]	0.5[2]	0.3[2]
Yb	18.8[2]	5.7[2]	6.7[2]	8.0[2]	5.5[2]	3.4[2]	6.1[2]	2.2[2]	4.0[2]	3.8[2]	2.1[2]
Lu	2.7[2]	0.8[2]	1.0[2]	1.4[2]	0.9[2]	0.5[2]	0.8[2]	0.3[2]	0.5[2]	0.6[2]	0.3[2]
Hf	1.1[2]	0.8[2]	7.3[2]	8.7[2]	9.8[2]	10.7[2]	10.1[2]	1.4[2]	5.9[2]	7.5[2]	4.8[2]
Ta	0.2[2]	0.4[2]	1.2[2]	2.1	1.7[2]	2.6	2.6	0.7	4.9	1.1	3.0
W	-	-	-	218	-	292	295	146	375	94	417
Pb	n.d.	-	19[1]	7	n.d.	n.d.	n.d.	6	n.d.	n.d.	n.d.
Th	21.6[2]	4.4[2]	13.5[2]	6.3[2]	12.8[2]	15.4[2]	12.4[2]	1.2[2]	16.7[2]	6.9[2]	10.9[2]
	n.d.	-	n.d.	3.1	n.d.	4.6	3.3	0.6	2.5	4.4	3.1

Notes: [1]MUN – XRF, [2]MUN-ICPMS, all others Actlabs (FUS-ICPMS); "-" not measured, "n.d." not detected.

Table 2-3. Whole rock geochemistry of ore and volcanic host rocks from the Per Geijer and Tuolluvaara (Siam) ores.

sample	**REK-10-04**	**NUK-12-02**	**REK-12-02**	**NUK-12-01**	**REK-10-01**	**REK-10-02**	**REK-12-01**	**TUV-10-01**	**TUV-10-03**
type	ore	ore	footwall	footwall	hanging wall	hanging wall	hanging wall	ore	host
SiO_2	3.1	21.18	50.51	70.5	70.8	65.0[1]	62.57	2.1	69.0
TiO_2	1.19	0.74	0.45	0.25	0.24	0.02[1]	0.59	0.89	0.41
Al_2O_2	1.05	4.83	11.25	12.21	3.75	21.96[1]	15.35	0.34	13.19
Fe_2O3_{tot}	89.73	39.31	12.60	4.56	23.05	1.44[1]	8.80	98.79	6.05
MnO	0.06	0.08	0.09	0.03	0.01	0.01[1]	0.01	0.06	0.03
MgO	0.28	1.06	2.83	1.67	0.08	0.47[1]	0.33	0.8	1.15
CaO	3.33	16.24	7.45	0.99	0.11	0.26[1]	0.42	0.24	1.05
Na_2O	0.02	1.03	1.30	0.96	0.62	5.65[1]	2.77	0.03	4.6
K_2O	0.37	1.26	3.74	7.77	1.99	6.03[1]	7.08	0.04	4.38
P_2O_5	2.12	11.38	3.14	0.07	0.06	0.10[1]	0.29	n.d.	0.04
LOI	-0.7	2.16	5.43	1.17	0.16	-	1.46	-2.59	0.17
Total	**100.59**	**99.27**	**98.79**	**100.15**	**100.90**	**100.86**	**99.68**	**100.72**	**99.88**
S	711[1]	-	-	-	173[1]	134[1]	-	240[1]	122[1]
Cl	148[1]	-	-	-	167[1]	155[1]	-	295[1]	301[1]
Sc	8	-	-	2	1	n.d.	-	11	9
V	1216	-	-	25	204	46[1]	-	585	36
Co	63	-	-	89	193	-	-	135	101
Ni	175[1]	-	-	n.d.	9[1]	17[1]	-	204[1]	9[1]
Cu	75[1]	-	-	120	50[1]	n.d.	-	50[1]	6[1]
As	36[1]	-	-	n.d.	35[1]	n.d.	-	n.d.	n.d.
Rb	8	-	-	97	31[1]	117[1]	-	2[1]	96[1]
Sr	33[1]	-	-	23	5[1]	24[1]	-	n.d.	18[1]
Y	74.6[1]	331.1[2]	113.9[2]	48.2[2]	4.8[1]	14.5[1]	17.5[2]	6.0[1]	26.2[1]
Zr	n.d.	25.0[2]	328.6[2]	440.0[2]	390.2[1]	1806.4[1]	459.7[2]	9.0[1]	457.4[1]
Nb	2.4[2]	8.4[2]	12.4[2]	17.8[2]	3.9[2]	4.1[2]	27.1[2]	5.0[2]	14.2[2]
Ag	n.d.	-	-	2.4	1.2	-	-	< 0.5	1.1
Ba	135[2]	394[2]	1149[2]	1711	254[2]	1234[2]	1291[2]	9[2]	979[2]
La	398.2[2]	496.3[2]	164.3[2]	75.4[2]	33.7[2]	39.8[2]	148.2[2]	1.2[2]	25.9[2]
Ce	799.9[2]	1165.9[2]	338.6[2]	127.6[2]	33.0[2]	49.4[2]	142.0[2]	2.4[2]	46.0[2]
Pr	89.7[2]	141.8[2]	38.8[2]	14.6[2]	2.8[2]	4.6[2]	11.9[2]	0.3[2]	5.3[2]
Nd	338.8[2]	555.9[2]	147.7[2]	56.1[2]	8.1[2]	15.5[2]	33.6[2]	1.5[2]	20.7[2]
Sm	47.8[2]	91.8[2]	24.5[2]	10.1[2]	0.9[2]	2.1[2]	3.9[2]	0.5[2]	3.8[2]
Eu	4.6[2]	10.8[2]	2.7[2]	1.2[2]	0.2[2]	0.5[2]	1.0[2]	0.2[2]	1.0[2]
Gd	29.6[2]	81.3[2]	22.8[2]	7.3[2]	0.8[2]	1.6[2]	3.3[2]	0.5[2]	3.5[2]
Tb	2.8[2]	10.8[2]	3.3[2]	1.2[2]	0.1[2]	0.2[2]	0.5[2]	0.1[2]	0.6[2]
Dy	11.4[2]	61.6[2]	20.3[2]	8.0[2]	0.7[2]	1.6[2]	2.7[2]	0.6[2]	3.9[2]
Ho	1.9[2]	11.8[2]	4.2[2]	1.8[2]	0.2[2]	0.4[2]	0.6[2]	0.1[2]	0.9[2]
Er	4.5[2]	31.9[2]	12.0[2]	5.8[2]	0.5[2]	1.2[2]	1.6[2]	0.4[2]	2.8[2]
Tm	0.6[2]	4.2[2]	1.7[2]	0.9[2]	0.1[2]	0.2[2]	0.2[2]	0.1[2]	0.5[2]
Yb	3.0[2]	24.5[2]	10.4[2]	6.4[2]	0.5[2]	1.6[2]	1.3[2]	0.5[2]	3.5[2]
Lu	0.4[2]	3.3[2]	1.6[2]	1.0[2]	0.1[2]	0.4[2]	0.2[2]	0.1[2]	0.6[2]
Hf	0.1[2]	0.7[2]	7.1[2]	9.7[2]	9.5[2]	51.8[2]	10.9[2]	0.1[2]	9.4[2]
Ta	0.4	0.4[2]	1.1[2]	2.0	5.4	1.5[2]	1.6[2]	0.8	2.9
W	104	-	-	284	841	-	-	108	330
Pb	n.d.	-	-	7	n.d.	n.d.	-	n.d.	n.d.
Th	9.1[2]	77.0[2]	10.0[2]	4.9[2]	0.5[2]	0.3[2]	2.3[2]	16.4[2]	6.2[2]
U	4.3	-	-	2.4	3.1	n.d.	-	0.8	2.2

Notes: [1]MUN – XRF, [2]MUN-ICPMS, all others Actlabs (FUS-ICPMS); "-" not measured, "n.d." not detected.

3 Tracing the fluid evolution of the Kiruna iron oxide apatite deposits using zircon, monazite and whole rock trace elements and isotopic studies

3.1 Abstract

The ore genesis of the Paleoproterozoic iron oxide apatite deposits around the town of Kiruna in northern Sweden is poorly understood, despite a century-long mining history and 2500 Mt of iron ore with grades of 30 to 70 wt.% Fe produced in the region to date. Zircon grains from the ore, recently dated at ca. 1874 Ma, show very different appearances compared to zircon from surrounding host rocks (1880 Ma) and related intrusions (1880 and 1874 Ma), particularly an inclusion-rich rim that is interpreted to be of hydrothermal origin. In contrast, zircon from the host rocks and a proximal granite intrusion exhibit typical igneous growth zoning. Electron microprobe results show near stoichiometric composition for Zr, Si, and Hf in the host rock zircon grains while the ore zircon crystals have low analytical totals and are shown to contain significant Ca, Fe, Y, and P several weight percent of water with infrared spectroscopy. These zircon grains further show Fe-rich inclusions, zones and/or veins in elemental X-ray maps, and light rare earth elements (LREE) enrichment; features that are not present in zircon from the metavolcanic host rocks. Uranium-Pb in monazite from the ore, measured by SIMS, suggests a secondary event influencing the area at ca. 1628 Ma, a period of known geologic activity in

Fennoscandia. Electron microprobe X-ray mapping of these monazite grains shows no zoning and relatively low U and Th concentrations.

Stark contrasts are visible between the ore (depleted mantle influence) and host rocks (crustal influence) in the whole rock Lu-Hf and Sm-Nd data. The depleted mantle signature of the ore could be related to the Kiruna greenstone group as a potential source region for the iron. The Sm-Nd isotopic composition of monazite from the ore shows a crustal influence, and indicates that the younger event has not disturbed the whole rock Sm-Nd signature of the ore. Combining the hydrothermal features of the ore zircon grains and the isotopic signatures points to a hydrothermal influence on the ore formation, with a high temperature magmatic fluid related to the intrusions as most likely heat and fluid source.

3.2 Introduction

The iron oxide apatite (IOA) deposits around Kiruna in the Norrbotten region of northern Sweden have been known for over a century; however, their formation is still debated. The two favoured, but contrasting, theories are the formation as an immiscible iron oxide melt on one hand (e.g., Frietsch, 1978; Nyström and Henríquez, 1994), and the involvement of hydrothermal fluids producing the ore through metasomatic processes on the other (e.g., Parák, 1975; Hitzman et al., 1992). Similarities with iron oxide copper gold (IOCG) deposits such as low Ti iron oxides (mainly magnetite and hematite), enrichment of rare earth elements (REE), and widespread Na-Cl metasomatism have been used to group IOA as an end member of IOCG deposits (Hitzman et al., 1992). The main difference between IOA and IOCG deposits is the lack of economic concentrations of Cu or Au in the former (e.g., Groves et al., 2010). In contrast to a low temperature hydrothermal formation

suggested for the Kiruna area deposits by Parák (1975), Westhues et al. (2016; 2017) proposed the formation of the Kiruna deposits from high temperature magmatic-hydrothermal fluids, based on new, detailed zircon U-Pb dating, oxygen and hafnium isotopic constraints, and microstructural information (Chapters two and four).

Zircon is a refractory accessory mineral that can be used to decipher the history of a rock and has been shown to not only be of magmatic or metamorphic, but also of hydrothermal, origin (e.g., Hoskin and Schaltegger, 2003; Schaltegger, 2007). The concentrations of trace elements such as U, Th, Hf, P, Ti, and REE provide insight into the conditions (i.e., temperatures, pressures, and composition of their growth environment) in which the zircon crystallized (Hanchar and van Westrenen, 2007). Zircon that is potentially of hydrothermal origin has also been reported in relation to different types of economic mineral deposits (e.g., Claoué-Long et al., 1990; Pettke et al., 2005) and requires that Zr, which is commonly considered to be an immobile element, to be moved by fluids. This concept was met with criticism in some early studies of hydrothermal zircon (Claoué-Long et al., 1990; Corfu and Davis, 1991), but has been shown to be possible in alkali- and F-rich natural systems (Rubin et al., 1993) and under experimental conditions (Yang et al., 2014), where fluorine increases the mobility of Zr.

A consistent set of hydrothermal zircon textures and compositions that relates to all occurrences has not been fully established to date. Common criteria include the presence of hydrothermal mineral and/or fluid inclusions within the zircon itself (Schaltegger, 2007), a “spongy texture” that is attributed to micro-porosity within the crystal (Yang et al., 2014), complex internal textures (cross-cutting, overgrowth), and the increase in concentrations of

trace elements such as Ca, Al and Fe that are otherwise incompatible in zircon (e.g., Rayner et al., 2005; Schaltegger, 2007; Toscano et al., 2014). Several zircon grains in this study show significant textural variations and complexities, and their potential hydrothermal origin is explored by detailed investigations using electron probe microanalyzer (EPMA), laser ablation multiple-collection inductively coupled plasma mass spectrometry (LA-ICPMS), transmission electron microscopy (TEM), and Fourier transform infrared (FTIR) spectroscopy.

Similar to zircon, monazite can also be used a geochronometer (e.g., Janots et al., 2012; Allaz et al., 2013). However, monazite is more susceptible to recrystallization than zircon and have its U-Pb ages reset during alteration (Williams et al., 2011) or metamorphism (Liu et al., 2017) and may record different events than zircon. Monazite is therefore a good indicator for fluid movements in different environments (e.g., Allaz et al., 2013). Since it has a high affinity for light REE (LREE), it is also an ideal candidate for determining its Sm-Nd isotopic composition (e.g., McFarlane and McCulloch, 2007). In combination with precise U-Pb geochronology, done here by secondary ion mass spectrometry (SIMS), the radiogenic isotope systematics of monazite can be used as an isotopic tracer.

In this study, we combine detailed trace element analyses of previously dated zircon and new U-Th-Pb dating of monazite to understand the evolution of the iron oxide deposits around Kiruna and the metasomatic alteration of the area caused by the infiltration of hydrothermal fluids. In addition, in situ and whole rock Sm-Nd and Lu-Hf isotopic systematics are used to identify the source regions of fluids and iron ore.

3.3 Geological background and samples

The Norrbotten region in northern Sweden is host to several mineral deposits, most significantly about 40 IOA deposits (Bergman et al., 2001). The largest ore body Kiirunavaara (Fig. 3-1) is ~5 kilometres long, up 100 metres think and currently mined at ca. 1300 m below the surface. The IOA ores in the region are dominantly low Ti magnetite ±hematite, with varying amounts of apatite (>0.01 to a few wt.% of P) and actinolite as a gangue mineral. Sulfides such as pyrite and chalcopyrite occur in traces, often as a late feature. The iron ores are mostly hosted by metavolcanic rocks of Svecokarelian age from 1.9 to 1.8 Ga (Billström et al., 2010). In the Kiruna area, the ore-hosting succession discordantly overlies the rifting-related Kiruna greenstone group (ca. 2.3 to 1.93 Ga, Bergman et al., 2001). During the Svecokarelian orogeny, several suites of intrusions were emplaced, and now make up the majority of the bedrock in the Norrbotten region. The whole region was substantially altered, resulting in a regional occurrence of alkali enriched rocks and scapolite (Frietsch et al., 1997). Most rocks have experienced Na and/or K alteration, which complicates identifying original rock types of the metavolcanic rocks (Westhues et al., 2016). The Kiirunavaara deposit occurs directly at the contact of an andesite unit that was later altered to trachyandesite, and pyroclastic rhyodacite. The latter unit is also the host to several smaller deposits in the Kiruna area.

Metavolcanic host rocks with different degrees of alteration, IOA ores, a syenite and a granite intrusion found within the footwall of the Kiirunavaara deposit are the subject of this study (see Fig. 3-1 for sample locations). Table 3-1 gives an overview of the samples studied, their mineralogy, and major alteration patterns, and in situ U-Pb ages (Westhues

et al., 2016) and Hf and oxygen zircon results (Westhues et al., 2017). The study of oxygen isotopes from zircon of the immediate Kiruna region gave unexpected low $\delta^{18}O$ signatures, similar to ones from hydrothermally active regions such as Yellowstone (e.g., Bindeman and Valley, 2001). This suggests a large scale magmatic-hydrothermal fluid system that has metasomatically altered the rocks of this region. The drive for such a system could be a large magma chamber, likely within the Archean crust, as Hf isotopic results indicate (Westhues et al., 2017, see Table 3-1).

The immediate host rocks of the ore have been dated at 1884.1 ±3.7 Ma (footwall) and 1880.5 ± 4.5 Ma to 1879.5 ±7.1 Ma (hanging wall); intrusions into the footwall are dated at 1880.6 ±3.7 Ma (syenite), and 1874.2 ±3.8 Ma (granite). Zircon from the ore is dated to 1877.1 ±3.5 Ma (Nukutus) and 1874.1 ±7.1 Ma (Kiirunavaara) and similar in age to the granite intrusion (Westhues et al., 2016). In addition to the Paleoproterozoic ages documented in that study and by several other authors (e.g., Cliff et al., 1990; Romer et al., 1994), a few other studies reported a younger episode in the geologic record of the Norrbotten region in the Mesoproterozoic. Whole rock and mineral Rb-Sr studies report isochron ages from 1500 to 1750 Ma (Skiöld, 1979; Welin, 1980; Skiöld and Öhlander, 1989). Skiöld (1986) found a zircon fraction in an albite-rich diabase with a weighted mean $^{207}Pb/^{206}Pb$ age of 1592.9 ±7.3 Ma (95% confidence), younger than the emplacement age of the rock (c. 2.2 Ga).

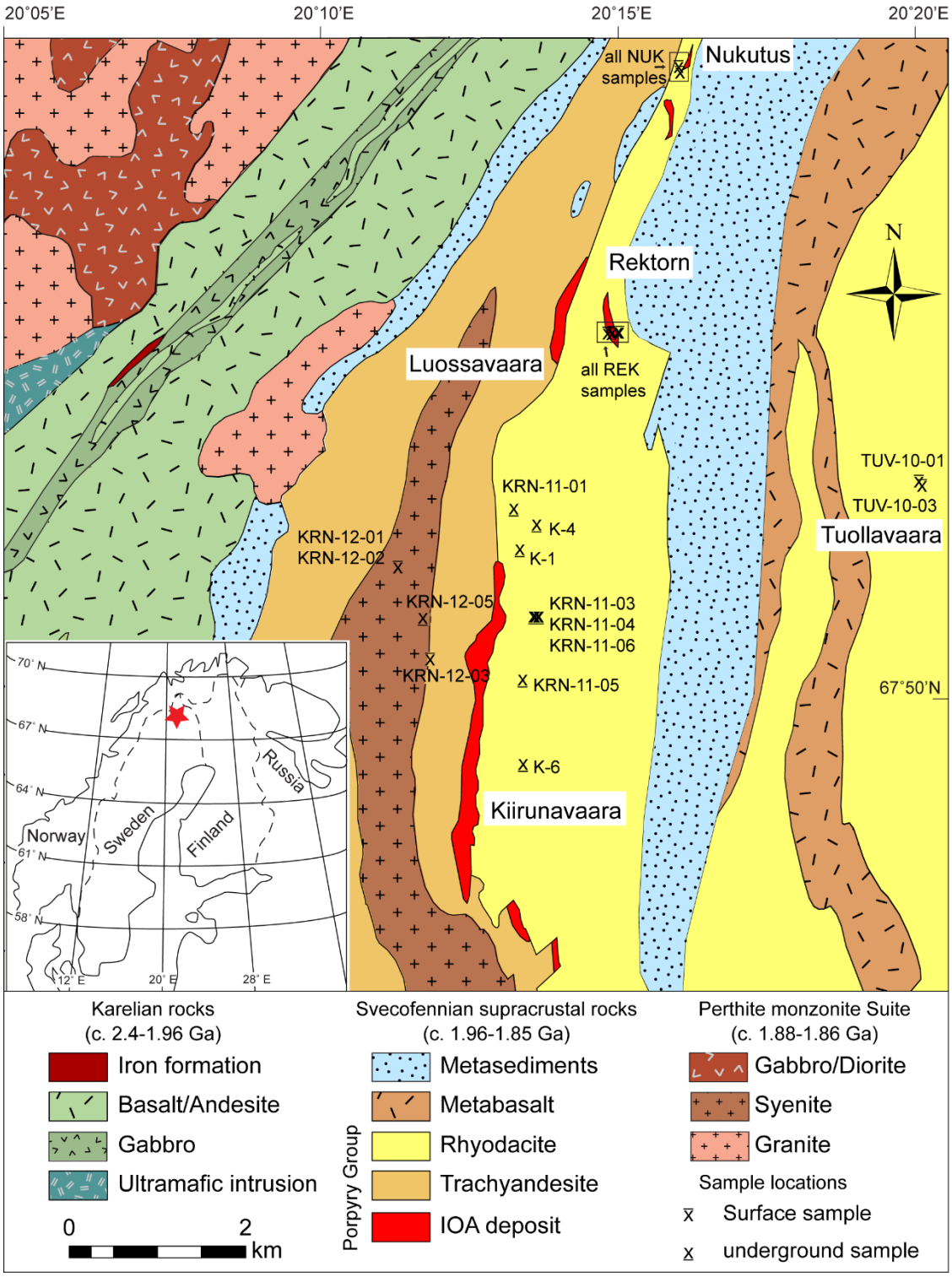

Figure 3-1. Geological map of the Kiruna area, based on data provided by the Geological Survey of Sweden (SGU) and Bergman et al. (2001), modified from Westhues et al. (2016), with sample locations (see Table 3-1), projected to surface for underground samples.

Bergman et al. (2001) reported U-Pb monazite dates from a felsic dike at Maatavaara (about 40 km ENE from Kiruna) with a date of 1633 ± 7 Ma. Cliff and Rickard (1992) present an Sm-Nd isochron from ore samples at 1490 ± 130 Ma. In combination with lead isotopic compositions of host rocks, ore, and sulfides that form a secondary isochron of 1540 ± 70 Ma, a "major isotopic reequilibration" around 1.5 Ga is suggested by those authors. Despite some large uncertainties, the reoccurrence of dates between 1500 and 1700 Ma, using different techniques, cannot be ignored.

3.4 Analytical procedures

Whole rock samples were crushed using standard jaw crusher and disk mill techniques and a split of each sample was further pulverized with a shatter box for analysis of major and trace element geochemistry and tracer radiogenic isotopes (Sm-Nd and Lu-Hf). Trace element concentrations were determined at the CREAIT facility at Memorial University of Newfoundland (MUN) using a PerkinElmer Elan DRCII ICP-MS using the methods of Longerich et al. (1990). Sm and Nd were separated from selected whole rock samples following an in-house protocol at MUN (see details in appendix 7.1.2), and Sm-Nd isotopic compositions measured with a multicollector Finnigan Mat 262 mass spectrometer in static and dynamic mode. Representative samples were selected for whole-rock Lu-Hf analyses and analyzed following methods described by Patchett and Tatsumoto (1980), Vervoort and Blichert-Toft (1999), Vervoort et al. (2004) and adjusted at MUN as described in detail in the appendix and in Phillips (2015). One sample each was randomly selected for duplicate analyses of whole rock Sm-Nd and Lu-Hf isotopic composition for quality control. Epsilon Nd (εNd) and Hf (εHf) values are reported as deviation from the

chondritic uniform reservoir (CHUR) using a $^{147}Sm/^{144}Nd$ ratio of 0.1967 and a $^{143}Nd/^{144}Nd$ ratio of 0.512638 for εNd, and for εHf the values from Bouvier et al. (2008) of $^{176}Hf/^{177}Hf$ = 0.282785 and $^{176}Lu/^{177}Hf$ = 0.0336 were used. Initial $^{143}Nd/^{144}Nd$ ($^{143}Nd/^{144}Nd_i$) and $^{176}Hf/^{177}Hf$ ($^{176}Hf/^{177}Hf_i$) have been calculated for the best age estimate for each sample, using the decay constant of Steiger and Jäger (1977) for Nd and of Söderlund et al. (2004) for Hf. Initial εHf (εHf_i) and uncertainties have been calculated following the algorithm of Ickert (2010).

The remainder of each sample was used for heavy mineral separation using Wilfley Table, heavy liquids and magnetic separation. Zircon and monazite were subsequently handpicked from the heavy mineral fraction under a binocular microscope and mounted in epoxy and polished to expose the crystal centers. Back-scattered electron (BSE) imaging of all mineral grains mounted were acquired prior to further analyses to select the locations for the in situ spot analysis using the FEI Quanta 400 scanning electron microscope (SEM) at Memorial University of Newfoundland. To distinguish individual grains, the position of each zircon grain within each sample is represented as sample name, row and grain number "sample_rXgY" (e.g., KRN-11-05_r1g3 stands for sample KRN-11-05, row 1, grain 3). For sample K-1, the mount number (m2 or m4) is further given, since zircon grains from this sample were analyzed in two epoxy mounts.

Zircon grains previously dated (Westhues et al., 2016) have been analyzed quantitatively with wavelength dispersive spectroscopy (WDS) using a JEOL JXA-8230 electron probe micro-analyzer at MUN with an accelerating voltage of 15 kV and a beam current of 20 nA. High resolution EPMA WDS X-ray maps of selected zircon crystals were

also done using a voltage of 15 kV and a current of 250 nA. Elements mapped in zircon were Hf Mα, Ca Kα, Y Lα, P Kα, and Fe Kα with a 1.0 μm step size and a 200 ms dwell time per step. Zircon grains were further analyzed for their trace element compositions using a Thermo-Finnigan ELEMENT XR ICPMS coupled with a GeoLas 193 nm Excimer laser system at MUN using a repetition rate of 8 Hz, and a fluence of 3 J/cm^2 using Hf from the EPMA analyses as the internal standard.

Four zircon grains from the Kiirunavaara ore were also studied by FEI Tecnai G2 F20 X-Twin transmission electron microscope (TEM) at the GFZ German Research Centre for Geosciences, Potsdam. Representative zircon grains from the Kiirunavaara ore that were not previously mounted have been analyzed by Fourier transform infrared spectroscopy (FTIR) at the California Institute of Technology to detect OH molecule vibrations. Results are reported as if they were water molecules for analytical convenience and were calibrated using a rhyolite glass as an approximation (Rossman, 2006) in the lack of an OH- or H_2O -bearing zircon standard.

High resolution EPMA WDS X-ray maps of Ca Kα, Nd Lα, Th Mα, U Mα and La Lα were acquired from selected monazite grains using a voltage of 15 kV, a current of 250 nA, a dwell time of 200 ms per step, and a step size of 0.5 μm (e.g., Williams et al., 2006; Allaz et al., 2013).

The high spatial resolution U-Th-Pb monazite analyses were done using the Cameca IMS1280 large-format high mass resolution ion microprobe at the Swedish Museum of Natural History, NordSIM facility, broadly following the methods by Kirkland et al. (2009) and Gasser et al. (2015). Data reduction and common Pb corrections were done using the

NordSIM in house software written by Martin Whitehouse. Correction for common Pb was made when measured ^{204}Pb counts were greater than average background by 3σ, using the model lead isotope composition of Stacey and Kramers (1975). All data are presented on Tera-Wasserburg plots (inverse concordia diagrams, $^{207}Pb/^{206}Pb$ vs. $^{238}U/^{206}Pb$) using Isoplot 3.0 (Ludwig, 2003). Concordia ages are calculated in Isoplot for samples that have overlapping concordant points and age errors are reported as 2σ. Sm-Nd in monazite have been measured using the LA-MC-ICPMS (Finnigan Neptune) interfaced with a New Wave 213 nm laser at Washington State University following the methods discussed in Fisher et al. (2011). More details for all methods used can be found in the appendix.

3.5 Results

3.5.1 Major and trace elements of zircon

Almost all EPMA analyses of samples KRN-11-05 (hanging wall) and KRN-12-02 (aplite) yielded stoichiometric zircon compositions with acceptable analytical totals (i.e., not less than 99.5 and not greater than 100.5 wt. %), variable HfO_2, P_2O_5, Y_2O_3, and undetectable amounts of CaO and FeO (see Table 3-2 and Fig. 3-2) for the conditions used. KRN-12-05 (granite) has slightly lower totals (not less than 98.5 wt. %), but does not contain detectable amounts of CaO and FeO.

In contrast, several zircon analyses from the ore samples K-1 (Kiruna ore), NUK-12-02 (Nukutus ore), a few analyses from aplite KRN-12-02, and syenite KRN-12-03, have variable non-stoichiometric amounts of ZrO_2 and SiO_2 and low analytical totals (< 98 wt. %). Especially K-1 and KRN-12-03 have elevated FeO contents, and in some crystals

analyzed elevated CaO. FTIR analyses further reveal that the zircon crystals from those two samples may contain several weight percent of water (Fig. 3-3).

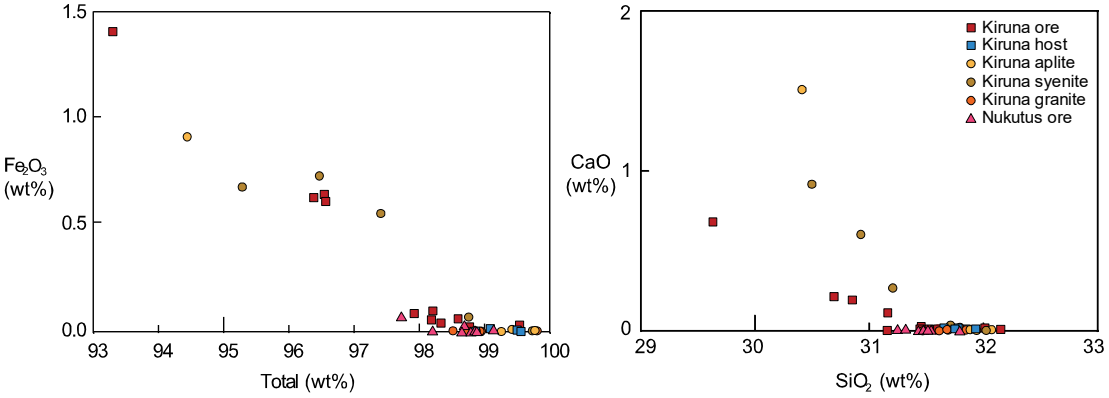

Figure 3-2. Quantitative EPMA results in weight percent: a) Total (wt. % oxide) vs. Fe_2O_3; b) SiO_2 vs. CaO. Zircon grains from host rocks have good totals and low contents of Fe and Ca, while several analyses of zircon from ores, syenite and aplite have lower totals, non-stoichiometric contents of Si and elevated Fe and Ca contents.

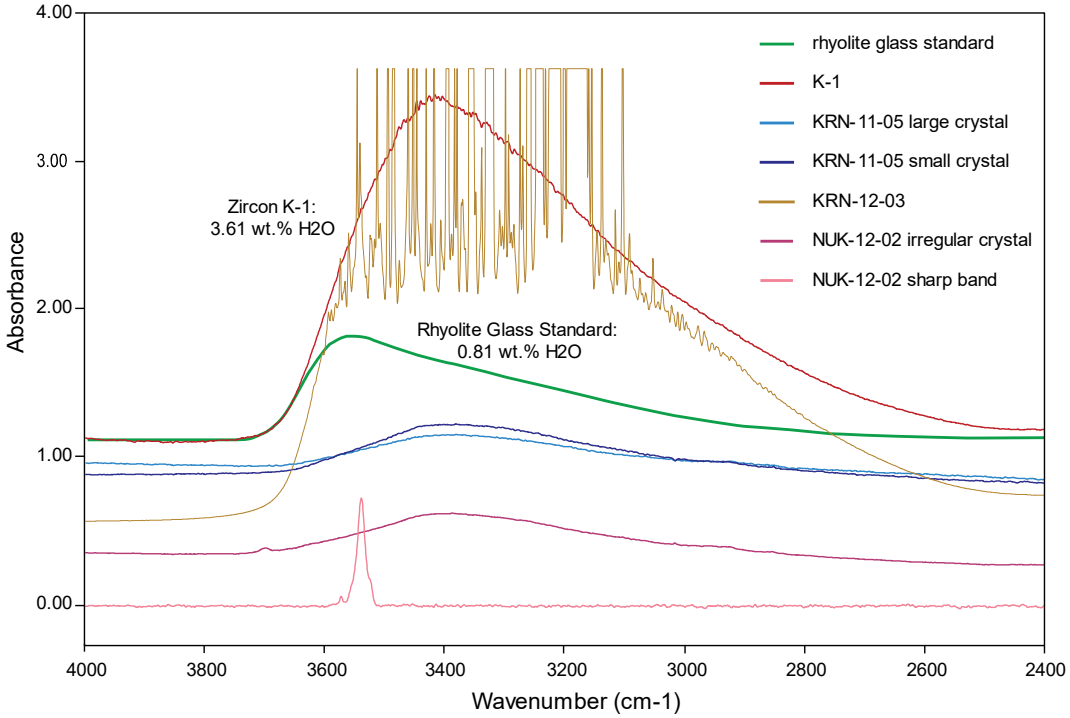

Figure 3-3. Fourier transform infrared (FTIR) spectroscopy results as wavenumber (cm^{-1}) vs. absorbance for the broad water spectrum. Samples and rhyolite standard have been plotted normalized to 0.100 mm thickness for comparison. The rhyolite glass standard contains 0.81 wt.% of H_2O and its broad water spectrum has an area of 312.9 units on this plot. Ore sample K-1 has an area of 1222 units, and its water content can therefore be calculated as 3.61 wt.% H_2O. Lacking a mineral-specific calibration for zircon, this is only an estimate for the actual value, but still shows that zircon crystals from K-1 and KRN-12-03 contain significant water contents. In contrast, zircon analysed from KRN-11-05 and NUK-12-02 have lower water contents than the rhyolite standard. The sharp band in one analyses from NUK-12-02 represents the vibration of OH-ions instead of the broad water spectrum.

Back-scattered electron images of selected zircon grains, and corresponding X-ray maps, are shown in Figure 3-4. Zircon grains from the rhyodacitic host rock (KRN-11-05, Fig. 3-4a) are subhedral to euhedral and commonly exceeding 200 μm in length and 100 μm in width. Several grains show doubly terminated prismatic zircon shapes and well-developed growth zoning patterns revealed in BSE imaging. Although rare, some crystals contain observable fractures and notably large inclusions. In the X-ray maps, Y and, to some extent, Hf, show growth zoning in these zircon grains. Corresponding bright spots on the Ca and P images are attributed to apatite inclusions. Fe is slightly elevated along cracks through the crystal and along a narrow rim. The grain shown in Figure 3-4 contains a Fe-rich inclusion.

Zircon grains from the granite intrusion (KRN-12-05, not shown in Figure 3-4) show very similar features to the ones described above. Sub- to euhedral grains are commonly 200 to 250 μm in length and 100 to 150 μm in width and show typical igneous growth zoning. Most crystals have fractures and variably sized inclusions, mostly apatite (high Ca and P in X-ray maps). Fe is very low in these zircon grains.

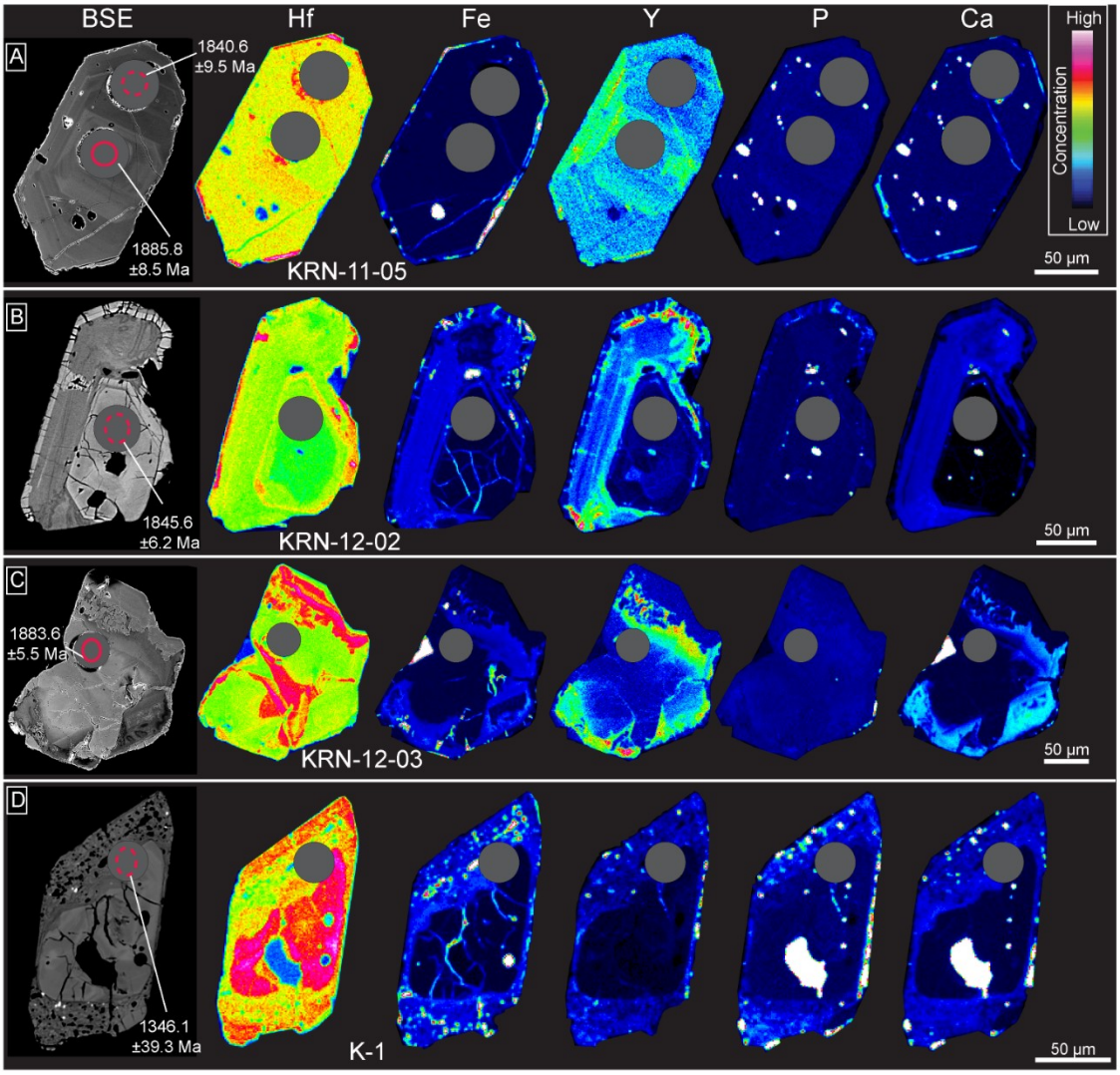

Figure 3-4. Selected zircon BSE images and EPMA X-ray maps for elements Hf, Fe, Y, P and Ca: a) hanging wall KRN-11-05; b) aplite KRN-12-02; c) syenite KRN-12-03; d) Kiirunavaara ore K-1. Maps are processed independently to maximise contrast and thus relative intensities. Therefore, different element maps do not reflect actual concentration differences (e.g., Ca and P generally have high counts, even though the maps show dominantly cool blue colors, since the zircon crystals contain apatite inclusions (white spots) with very high Ca and P contents).

Several grains from an aplite dike (KRN-12-02, Fig. 3-4b) have well developed growth zoning typical of magmatic zircon (core of grain shown here) and are subhedral in shape (commonly exceeding 200 μm in length and 150 μm in width). Some crystals show complex internal structures; in the grain shown, two rims with different characteristics (one dark, one bright in BSE images) are developed. Most crystals contain abundant fractures and variably sized inclusions. Apatite inclusions are related to corresponding enrichment of Ca and P. Ca distribution within the crystal also shows a relative enrichment in the darker area of the zircon compared to the core and outer most rim. Y and Fe are elevated in parts of this dark BSE area, while P, Fe and Hf are elevated in the outer rim. The Fe content is higher along fractures throughout the crystal and in some inclusions. Hf is highest in the outer rim, and shows only small changes in the rest of the crystal.

Zircon from the syenite (KRN-12-03, Fig. 3-4c) vary in size from less than 100 μm to over 200 μm in length and less than 50 μm to over 200 μm in width. The external morphology is variable and grains show unique shapes unlike a more typical doubly prismatic zircon shape. The internal textures of the grains are very complex and contain chaotic patterns with different colored zones in BSE, fractures and inclusions. Some areas are cross-cut by vein-like structures and patchy zones, which resemble resorption textures, sometimes overgrown by highly fractured rims. In the grain shown here, zones light in BSE correspond to elevated Hf contents, while dark areas have higher contents of Ca, Fe and Y. P content is low and shows no variations throughout the crystal, except for a few small inclusions.

Zircon grains from the Nukutus ore (NUK-12-02, not shown in Figure 3-4) are subhedral and are quite large (>250 μm in length and almost 200 μm in width). Cores of these grains sometimes show growth zoning or patchy textures; fractures and inclusions are common. Cores are overgrown by one or two rim generations with different BSE intensities. Similar to grains from KRN-12-03 and KRN-12-02, the Y, Hf, Fe, Ca, and P contents are elevated in different areas of these grains, and Fe is further elevated along fractures. Inclusions, often apatite, are common.

Zircon from the Kiirunavaara ore differ significantly from other grains in this study, showing very distinct core and rim regions. Grains are typically fractured and smaller, varying from less than 100 μm to over 200 μm in length, but do exhibit remnants of a doubly-terminated prismatic zircon shape. Most cores show igneous growth zoning patterns, while the rims of these grains are very inclusion rich and resemble a sieve-like or "spongy" texture. The Hf content is highest within the cores, while Y, Fe, Ca, and P are elevated in the rim regions. Apatite inclusions are related to corresponding high Ca and P contents (note the big inclusion within the core of this grain). Related high contents of Y and P could be related to the presence of xenotime in the rims. Fe-rich zones are common in the rim, but Fe is also elevated along fractures through the core of the grain.

Chondrite normalized rare earth elements (REE) plots of selected zircon grains are shown in Figure 3-5 (Table 3-3). Analyses from KRN-11-05, KRN-12-05, and KRN-12-02 mostly show a REE pattern very typical of magmatic zircon, with HREE enriched relative to LREE in a smooth trend, a positive Ce and a negative Eu anomaly (Fig. 3-5a-c). Some analyses show an atypical enrichment of LREE, for example KRN-11-05_r3g2a. One

analysis of KRN-12-02 done within a rim zone is overall enriched in REE and the Eu and Ce anomalies are relatively less pronounced (KRN-12-02_r3g1_rim, Fig. 3-5c). Most zircon grains from the Kiirunavaara syenite KRN-12-03 (Fig. 3-5d) and the ore sample K-1 (Fig. 3-5e) have atypically flat REE patterns with strong enrichment of LREE. Only four analyses done in K-1 show a more typical magmatic zircon chondrite normalized REE pattern with positive Ce and negative Eu anomalies. Some zircon analyses from the Nukutus ore (Fig. 3-5f) also show a REE pattern more typical for zircon, while others show enrichment of LREE and an Eu anomaly.

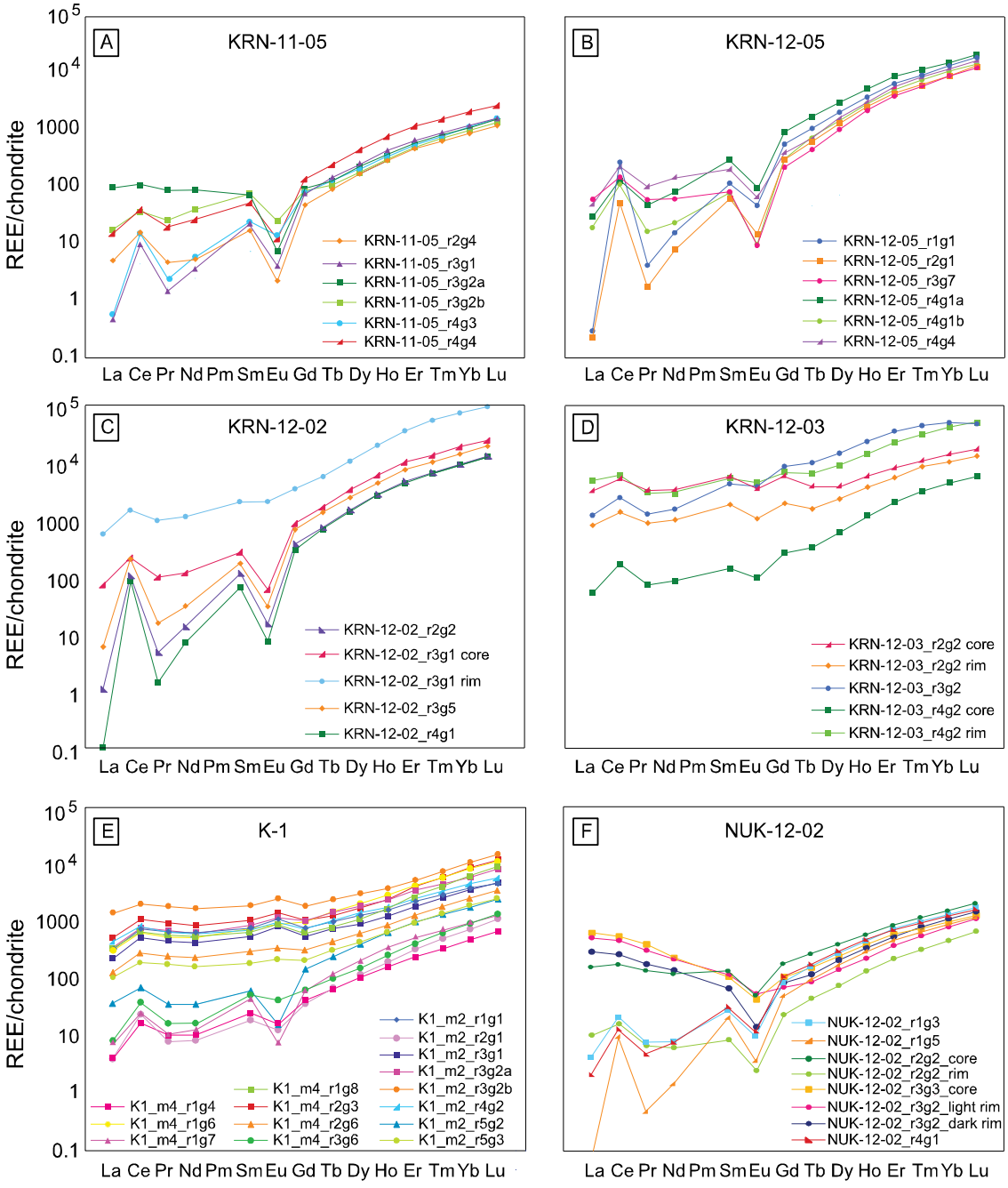

Figure 3-5. Rare earth element concentration of zircon grains, normalized to chondrite (chrondrite values after Anders and Grevesse, 1989). rXgY = row X, grain Y, which represents the position of each zircon grain in the grain mount to distinguish individual grains, m2 or m4 represent different epoxy mounts for K-1.

To confirm that the REE patterns with elevated LREE contents are not a result of inclusions of phases rich in LREE, such as monazite, allanite, or chevkinite, the chondrite normalized REE patterns have been studied in detail. In a few instances, an inclusion of most likely monazite was included in the ablation when drilling down into the crystal during the laser ablation (see Fig. 3-6a). Here, the careful avoidance of this region of the ablation signal when processing the data resulted in a more typical zircon-like REE pattern in a chondrite normalized REE plot (see Fig. 3-6c). In most cases, instead of inclusions, the laser signal was elevated in LREE and Y throughout (Fig. 3-6b), and the REE pattern is elevated independent of what integration period was chosen (Fig. 3-6c).

Four crystals of sample K-1 have been further studied by TEM (see Fig. 3-6d) to investigate if nano-inclusions of high LREE phases (such as monazite) are responsible for the REE patterns observed that are atypical for zircon, and occurring in sub-micron crystals. TEM foils were cut in close vicinity to the previously done LA-ICPMS trace element analyses spots and include rim and core regions of the crystals.

The first grain selected for TEM analyses (K1_m2_r1g1) shows high LREE contents (around 1000 times enriched over chondrite), even though the LA-ICPMS analysis was done completely within the core. The time resolved LA signal does not show an indication that an inclusion may have been analysed, i.e., no elements show a sudden rise in signal intensities during the analyses. TEM analyses show no sign of nano-inclusions of a LREE rich phase such as monazite. That zircon grain is composed of twins and the twins consist of nano-crystals of zircon with a grain size of 5-10 nm. They have all the same orientation within a twin lamella thus forming a single crystal electron diffraction pattern. They

represent a mosaic crystal with many pores in between the nano-crystals that were most likely previously filled with a fluid.

An LA-ICPMS trace element analysis straddles the core and rim of zircon grain K1_m2_r3g1 and has elevated LREE contents, so the TEM foil is cut in the core region this grain to inspect the zircon structure there. The area shows no porosity or nano-inclusions, but shows high contents of Y in energy dispersive X-ray spectrum (EDS). The crystal shows a faint compositional zoning on a micrometer scale, but the nature of this zonation is beyond the limit of the EDS system: no elemental differences are visible between EDS spectra of a light and a dark zone.

The location of the TEM foil cut from K1_m2_r3g2 was chosen to include an area of the zircon core and rim. The TEM image of this grain shows the two different areas of the zircon crystal (Fig. 3-6d). The zircon grain is a single crystal, and both core and rims have no evidence of micro-inclusions of other phases. While the core region consists of fairly massive zircon with no inclusions, the rim area shows large void areas that were likely previously fluid filled. The rim has lighter and darker areas, with the latter being enriched in Y, Ca, Fe, and Mn. Partially amorphous regions are followed by crystalline zircon at the nanometer scale.

As a comparison, the core region of grain K1_m2_r2g1 with a relatively typical chondrite normalized REE pattern for zircon and low LREE contents, was also analysed by TEM. This grain is single zircon crystal with some radiation damage, but shows no voids, microporosity or nano-inclusions.

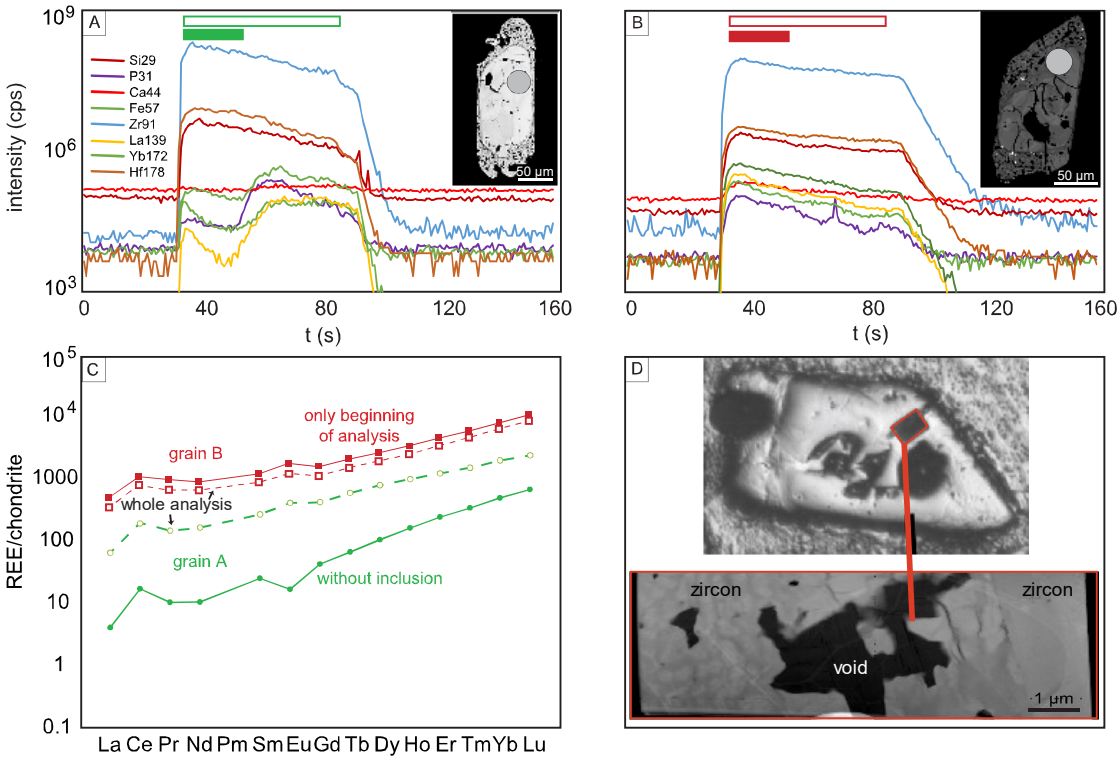

Figure 3-6. Zircon from the Kiirunavaara ore sample K-1 with high REE contents in their LA signal in detail. A) Time-resolved LA-analyses of zircon grain with inclusion of probably monazite, inset shows BSE image and location of laser ablation, green boxes show two different integration periods; B) Time-resolved LA-analyses of zircon grain with an inclusion-free analyses and location of laser ablation in BSE image, red boxes show two different integration periods; C) comparison of different integrations in a chondrite normalised REE plot: For grain A, integration of the whole analysis, including the inclusion, results in elevated REE contents, while avoiding the inclusion results in a more typical REE pattern of zircon. In contrast, for grain B, the REE contents are elevated regardless of the integration period; D) Location of TEM foil in grain B, cut and analysed at GFZ Potsdam (upper part), and TEM image (lower part), suggesting no evidence of micro- or nano- inclusions of a LREE-rich phase such as monazite in this grain – everything is zircon except the black areas, which are void.

3.5.2 Monazite U-Pb geochronology

Monazite has been found in three ore samples, namely K-1 and KRN-11-01 (Kiirunavaara) and REK-10-04 (Rektorn), and in the footwall of the Rektorn ore (REK-12-02). Monazite is not uncommon within the Kiirunavaara ore samples and crystals occur in various forms about 50 to 100 μm in size, and some show faint zoning in BSE images (Fig. 3-7a). Small inclusions of monazite within apatite are common, as well, as previously shown by Harlov et al. (2002) for samples from Kiirunavaara and Rektorn. Monazite in REK-10-04 shows more pronounced zoning in BSE images (Fig. 3-7b), and can also occur as larger inclusion within apatite. REK-12-02 has only small monazite grains that are zoned and contain numerous inclusions of apatite. All SIMS U-Pb data for monazite grain analyses are presented in Appendix B, Table 7-5, sorted for each sample by decreasing $^{207}Pb/^{206}Pb$ age. Analyses from K-1 resulted in a concordia age of 1628 ±12 Ma (MSWD=1.3, n=45, Fig. 3-7a), while KRN-11-01 shows a larger spread in ages from 1515 to 1905 Ma ($^{207}Pb/^{206}Pb$ dates of single analyses). Monazite from REK-10-04 yields a concordia age of 1738 ±19 Ma (MSWD=1.06, n=12, Fig. 3-7b). Analyses of REK-12-02 monazite show a larger spread in $^{206}Pb/^{207}Pb$ dates from 1651 to 1853 Ma and large errors, no concordia age could be calculated.

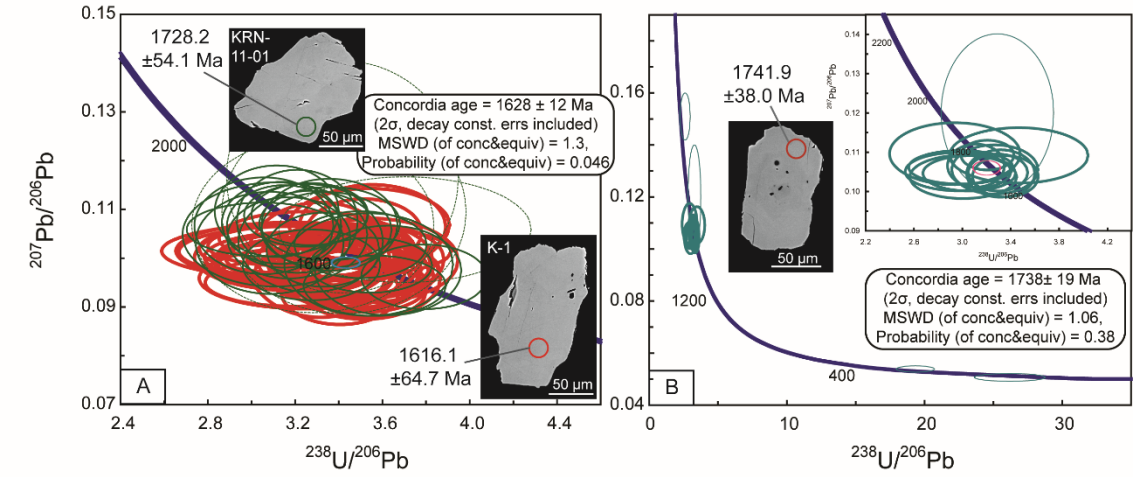

Figure 3-7. Monazite U-Th-Pb geochronology results and BSE images presented on Tera-Wasserburg diagrams: a) Kiirunavaara ore K-1 (red) and KRN-11-01 (green), concordia age is based on analyses from K-1, analyses from KRN-11-01 shown in dashed have large errors; b) Rektorn ore REK-10-04, concordia age based on bold data point error ellipses, as shown in inset.

3.5.3 Monazite X-ray mapping

Selected grains were mapped by electron microprobe in addition to the BSE imaging done before the U-Th-Pb analyses. The BSE images only show faint zoning, which was used to guide the U-Th-Pb analyses. The X-ray maps done afterwards reveal small elemental differences in the monazite crystals (Fig. 3-8). Generally, Ca and Nd contents are relatively high and these elements show the strongest zoning pattern for individual crystals, while U and Th contents are low in all monazites from the Kiruna area, as also observed by Harlov et al. (2002). Monazite from K-1 is relatively uniform and shows only minor zonation (Fig. 3-8a). These grains also have the most consistent U-Pb dating results (see monazite geochronology). KRN-11-01, on the other hand, has monazite with some zonation of Ca and Nd (Fig. 3-8b). However, U-Pb spots and LA spots are always within one zone of the crystals, therefore, those results are not the effect of mixed analyses. Nevertheless, the different zones present in these crystals may explain the somewhat larger spread of U-Pb results. Monazite from REK-10-04 has more distinct zoning with distinctly different zones (Fig. 3-8c, d). One grain (Fig. 3-8c) has a distinctive core with an older U-Pb age, while another grain (Fig. 3-8d) has two zones that have U-Pb dates about 90 Ma apart.

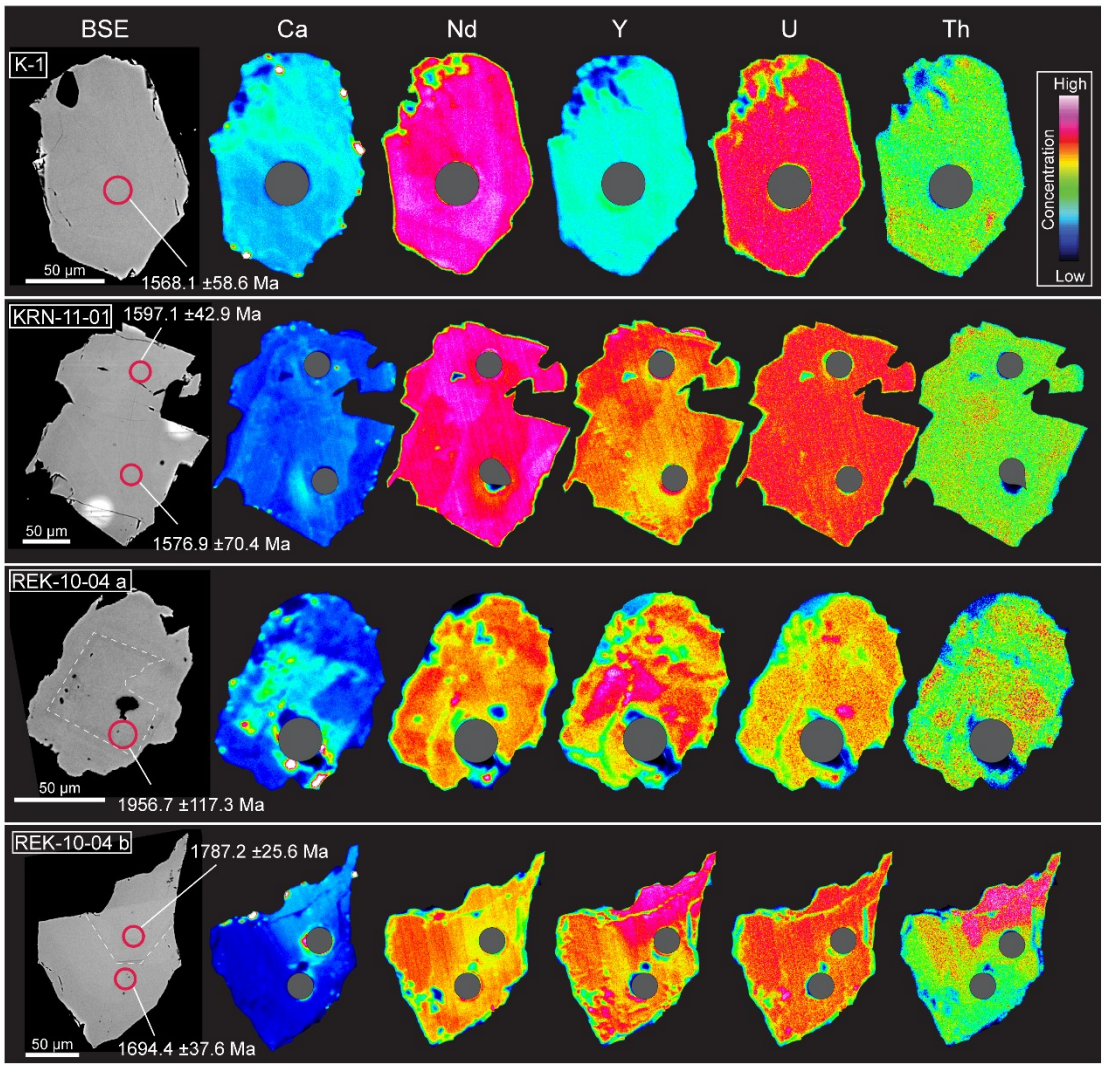

Figure 3-8. X-ray maps of selected monazite grains showing distribution of Ca, Nd, Y, U, and Th concentrations: a, b) Kiirunavaara ore K-1 and KRN-11-01; and c, d) Rektorn ore REK-10-04. Relatively high concentrations are reflected by warm colors, low concentration by cold colors. Maps are processed independently to maximise contrast. Therefore, different element maps do not reflect actual concentration differences (e.g., Ca generally has the highest counts of all elements, even though the maps show relatively low concentrations (blue to green colors) since the monazite crystals contain apatite inclusions (white spots) with very high Ca contents). Red ellipses show U-Pb dating spots (SIMS), and dark grey circles are location of Sm-Nd analyses (LA-ICPMS). Dates are $^{207}Pb/^{206}Pb$ dates.

3.5.4 Whole rock rare earth element chemistry

Most whole rock samples show a pronounced enrichment in REE, especially LREE elements, relative to chondritic values (Fig. 3-9), even the low-phosphorous iron ores from Kiirunavaara are up to ten times enriched in LREE. Generally, the volcanic host rocks and intrusions at the Kiirunavaara mine show similar patterns (high LREE and flat HREE, Fig. 3-9a), with the footwall showing the highest, and the aplitic intrusion the lowest REE concentration of the sample suite. All samples here have a negative Eu anomaly that is most pronounced in the aplite. The two ore types at Kiirunavaara have different patterns in relation to their apatite content (Fig. 3-9b): the apatite-rich ore have highly enriched REE patterns that overlap with apatite from the Kiruna area (Frietsch and Perdahl, 1995; Harlov et al., 2002), especially for the LREE. KRN-11-01 does not have the pronounced Eu anomaly that can be found in apatite analyses and K-1. In contrast to the apatite-high ore, the ones low in apatite have the lowest REE contents of the whole sample set. Samples from the Rektorn deposit have quite varied patterns (Fig. 3-9c). The lowest contents are found in the Rektorn porphyry, the highly altered hanging wall to this smaller ore body. The HREE are only a few times enriched over chondritic level, while contents of LREE are very high. These samples do not have a Eu anomaly like most other samples in this set. The footwall of the ore is higher in REE compared the similar unit at Kiirunavaara, but has a similar shape, including a Eu anomaly.

The ore itself has a similar LREE pattern, but HREE are depleted in comparison. An apatite-rich vein within the Rektorn porphyry shows the highest enrichment of REE, with an overall similar pattern as the apatite in the Kiruna area. The REE pattern of the host rock

of Nukutus overlaps perfectly with the comparable units at Kiirunavaara (Fig. 3-9d). Both ore samples show an enrichment in REE, and plot very similar to the ores at Kiirunavaara and the apatite-rich vein at Rektorn. NUK-12-02 consists to some degree of host rock, and is therefore lower in REE than NUK-10-01.

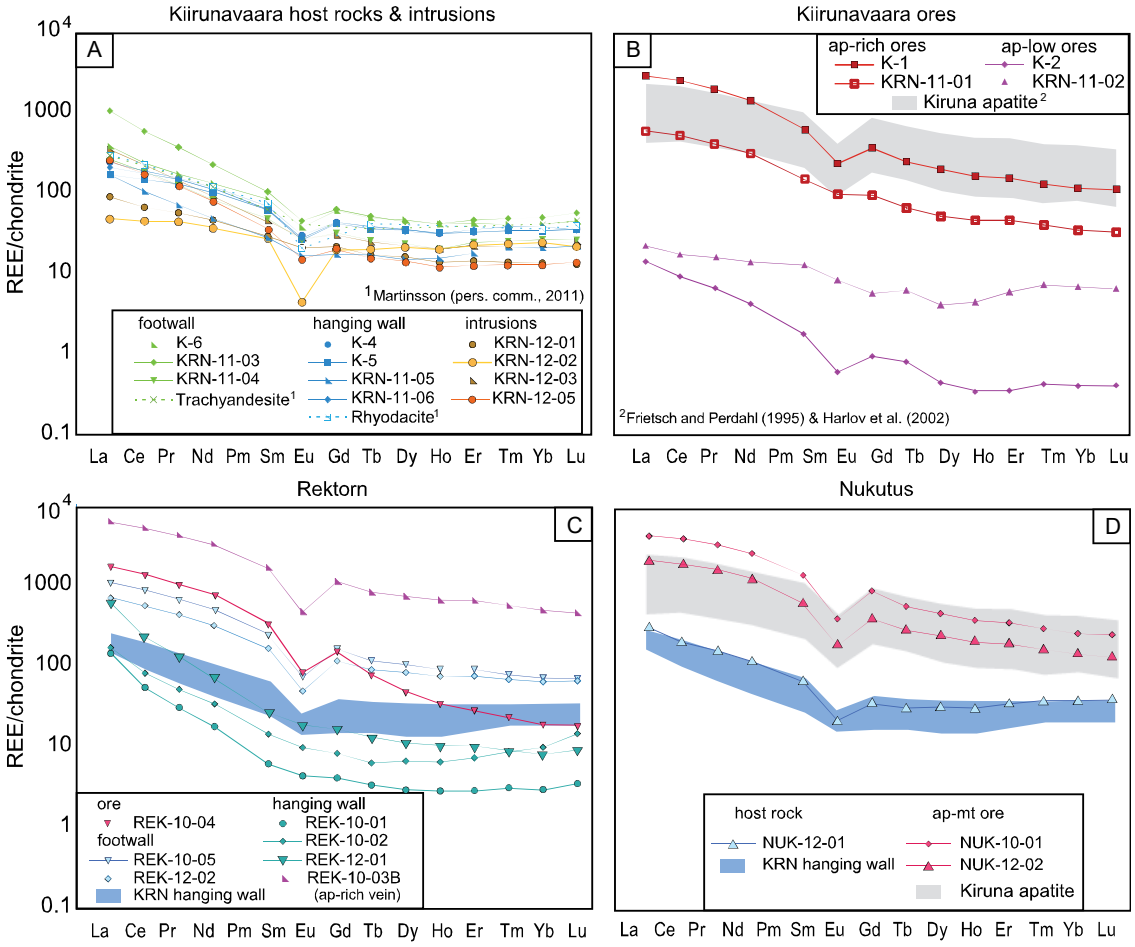

Figure 3-9. Whole rock REE, normalized to chondritic compositions (chrondrite values after Anders and Grevesse, 1989) for the samples of this study: a) Kiirunavaara host rocks and intrusions; b) Kiirunavaara ores with typical apatite from the Kiruna area for comparison (Frietsch and Perdahl, 1995; Harlov et al., 2002); host rock and ore from c) Rektorn; and from d) Nukutus, both with the envelope of the Kiirunavaara hanging wall for comparison.

3.5.5 Sm-Nd and Lu-Hf isotopes

Whole rock Sm-Nd isotopic data for ores, host rocks, intrusions, and extensively altered host rocks from Kiirunavaara, Rektorn, and Tuolluvaara, are shown in Figure 3-10 and Table 3-4. εNd_i (and εHf_i) have been calculated at 1.88 Ga for comparison. Most host rocks and intrusions fall within a small constrained range between εNd_i of -5.8 to -6.7. This overlaps well with existing data for the volcanic (Cliff et al., 1990) and intrusive (e.g., Öhlander et al., 1993) rocks within the Kiruna area. Most ores, on the other hand, have a less negative εNd_i signature than less altered host rocks. The Kiirunavaara ore (K-1, εNd_i = -3.1) and Rektorn ore (REK-10-04, εNd_i = -3.3) are also comparable in their Nd signature to some highly altered rocks (REK-10-03B, REK-10-05, NUK-10-01 with εNd_i from -3.5 to -3.9). Rocks with less negative εNd_i signatures like this are more common the area around Malmberget, south Norrbotten region, which shows higher metamorphism (e.g., Öhlander et al., 1993).

The 1.93 Ma Kiruna greenstone group underlying the ore hosting stratigraphy has positive εNd_i signature of 3.5 (Skiöld and Cliff, 1984). In figure 3-10a, the εNd_i ratios are plotted vs. time in comparison with previously published results and different source regions to show the contrast between normal host rocks and ore-related samples. Sm-Nd has also been determined in dated monazite grains from three ore samples. The εNd_i of the individual monazite grains is plotted against the corresponding U-Pb date of that grain. The evolution of the whole rock values of this study have been plotted for comparison. In contrast to the whole rock ore signature, the monazite has lower εNd_i, and is even more negative than most of the host rocks and closest to Archean crust and the granite.

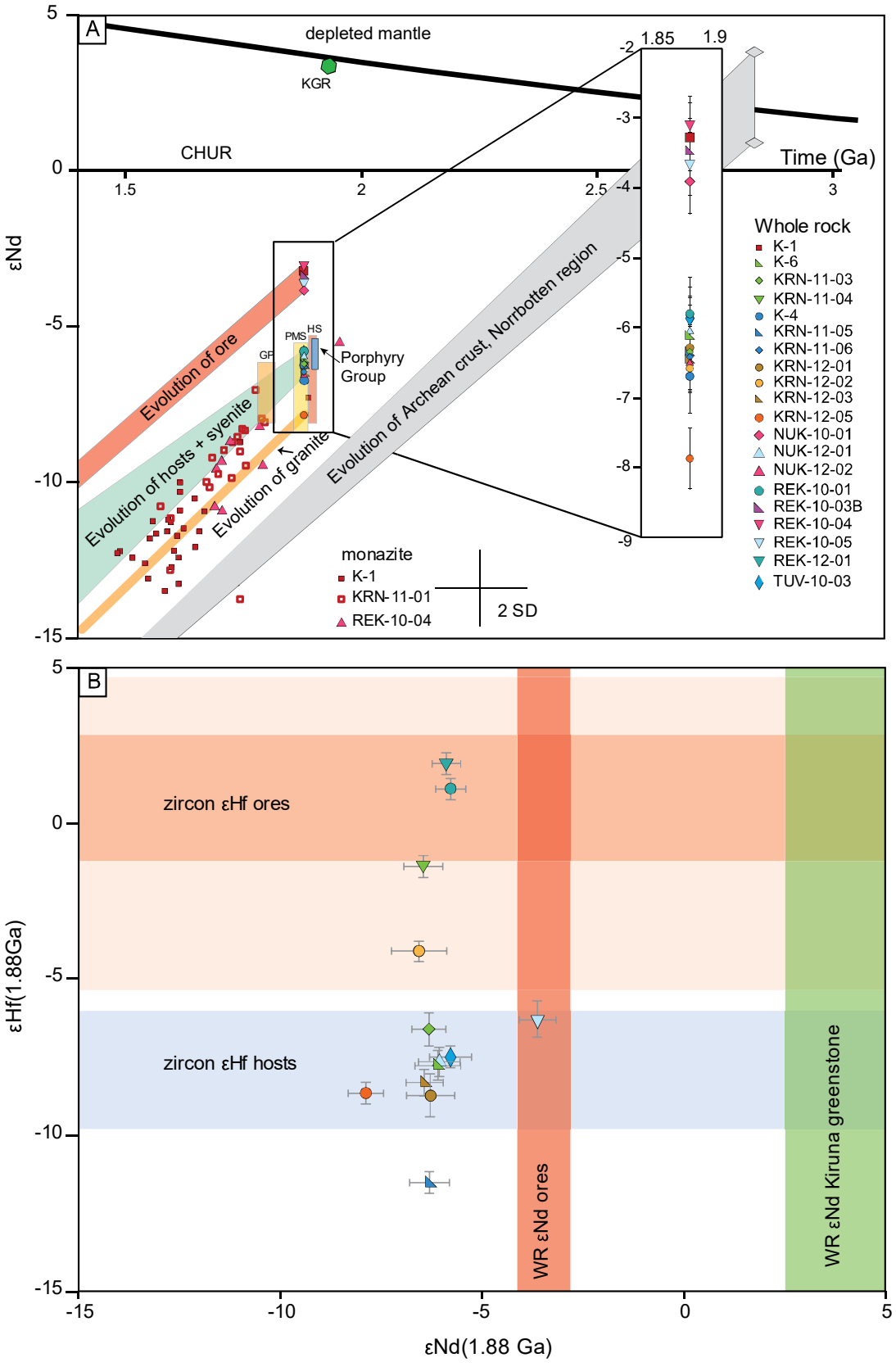
A
depleted mantle
KGR
CHUR
Time (Ga)
1.5
2
2.5
3
1.85
1.9
εNd
5
0
-5
-10
-15
-2
-3
-4
-5
-6
-7
-8
-9
PMS
HS
GP
Porphyry Group
Evolution of ore
Evolution of hosts + syenite
Evolution of granite
Evolution of Archean crust, Norrbotten region
monazite
K-1
KRN-11-01
REK-10-04
2 SD
Whole rock
K-1
K-6
KRN-11-03
KRN-11-04
K-4
KRN-11-05
KRN-11-06
KRN-12-01
KRN-12-02
KRN-12-03
KRN-12-05
NUK-10-01
NUK-12-01
NUK-12-02
REK-10-01
REK-10-03B
REK-10-04
REK-10-05
REK-12-01
TUV-10-03
B
zircon εHf ores
zircon εHf hosts
WR εNd ores
WR εNd Kiruna greenstone
εHf(1.88Ga)
εNd(1.88 Ga)
-15
-10
-5
0
5

Figure 3-10 on previous page. εNd_i composition vs. time for a) whole rock (WR) ores, host rock and altered samples and monazite from the Kiruna area, Norrbotten region, Sweden. The whole rock data is calculated at 1.88 Ga and compared to Svecofennian igneous rocks and Archean crust (Bergman et al 2001, and the reference therein); KGR: Kiruna greenstone group, HS: Haparanda Suite, PMS: Perthite Monzonite Suite, GP: Granite Pegmatite. Insert shows the εNd results of this study with 2σ uncertainties. εNd of monazite analyses is calculated at the individual U-Pb grain age, average 2 SD of all analyses is shown. Depleted mantle curve is that of DePaolo (1981); b) WR εNd vs. εHf, calculated at 1.88 Ga using the algorithm of Ickert (2013). WR εNd of ore samples from this study (red) and the Kiruna greenstone group (green, Skiöld and Cliff, 1984) are plotted as comparison. The orange box represents the range of values of εHf_i of ore zircon (darker most samples, light orange whole range), while the blue box shows the range of in situ εHf_i of zircon from host samples of this study (Westhues et al., 2017).

Determination of the whole rock Lu-Hf isotopic compositions was only successful for host rock samples, likely due to very low Hf contents of the ore samples; results are presented in Figure 3-10b and Table 3-4. Most host rocks have εHf_i values (calculated at 1.88 Ga) within a tight range of -6.6 to -8.7, very similar to the in situ results of zircon from these samples. The hanging wall of the Kiirunavaara deposits (KRN-11-05) has the most negative εHf_i (-11.5) of the set. Less negative values can be observed from the altered footwall sample KRN-11-04 and the aplite intrusion KRN-12-02. The highest εHf_i value is found for the Rektorn porphyry, the highly altered hanging wall of the Rektorn ore (REK-12-01). This sample also shows a large range of the in situ εHf_i in its zircon (Westhues et al., 2017), which was explained as a result of the high degree of metasomatic alteration by hydrothermal fluids. The εHf_i of the sample from the footwall of the Rektorn deposit (REK-10-05), which has a different εNd_i compared to most host rocks, is only slightly different from the range of the host rocks.

3.6 Discussion

3.6.1 Hydrothermal zircon features

Numerous studies suggest that zircon may not only be magmatic in origin, but can also be formed in late-magmatic to hydrothermal environments (e.g., Rubin et al., 1989; Claoué-Long et al., 1990; Hoskin, 2005; Schaltegger, 2007; Yang et al., 2014). Complex internal textures in BSE and CL images, a potential characteristic property for hydrothermal zircon grains, can be found in numerous grains from this study. Only few samples show more typical magmatic zircon features (well developed growth zoning, euhedral shapes),

including grains from the host rock hanging wall (Fig. 3-4a), the granitic intrusion, and most grains from the aplite dikes within the syenite intrusion at Kiirunavaara. However, some grains found with those dikes show complex secondary overgrowth rims, which are atypical of magmatic zircon growth. All zircon crystals separated from the syenite intrusion at Kiruna show secondary features such as fractured cores, vein-like structures, patchy zones, resorption textures, or chaotic areas (Fig. 3-4c). These complex textures have been attributed to post-crystallization hydrothermal alteration, recrystallization, or growth, by Schaltegger (2007) and (Geisler et al., 2007).

Zircon grains from the Kiirunavaara ore likely reveal the most intriguing hydrothermal textures in this study. Cores with partly magmatic features (growth zonation) have rims so rich in Fe- and P-rich inclusions that they appear sponge-like in BSE images (Fig. 3-4d). Also, the zircon grains from the Nukutus ore are characterized by several growth phases, with some enrichment of Fe and P-rich inclusions in the later ones. These texturally complex grains of the aplite, the syenite, and the ores further show enrichment in Ca, Fe, Y and/or P in their EMPA X-ray maps (Fig. 3-4b-d), which is likewise associated with metasomatic alteration by hydrothermal fluids (e.g., Schaltegger, 2007).

Unaltered igneous zircon typically contains less than 1 wt. % of the REE, and 0.5-3% HfO_2 (Hoskin and Schaltegger, 2003). Chondrite normalized REE diagrams for igneous zircon show patterns with enrichment of HREE relative to LREE and a steep slope from La to Lu, often including positive Ce and negative Eu anomalies. Patterns like this can be observed for several of the Kiruna zircon crystal analysed with magmatic textures, for instance for the Kiirunavaara hanging wall (KRN-11-05, Fig. 3-5a). However, numerous

zircon grains contain higher total REE and have a distinctly different pattern, for instance enrichment in LREE (Fig. 3-5e). This is a common feature and proposed diagnostic for zircon which has been altered by, or formed from, hydrothermal activity (e.g., Whitehouse and Kamber, 2002; Hoskin, 2005; Rayner et al., 2005).

In hydrothermally altered zircon, enrichment of the LREE is often accompanied by a significant increase elements such as Ca, Al, Fe, P, Y, U, Th and Ti, as well as a decrease in the Zr and Si contents (Geisler et al., 2003; Hoskin, 2005; Rayner et al., 2005; Toscano et al., 2014). One of the explanations for elemental changes in hydrothermal zircon could be the development of micro- and nano-scale pores, which contain inclusions of U, Th, and Y phases (Geisler et al., 2003; Schaltegger, 2007), although that doesn't explain the elevated concentrations of all the elements listed above. Even though many zircon crystals from this study contain several inclusions (e.g., apatite, monazite, see above), the observed REE patterns high in LREE from zircon in this study are probably not the result of large inclusions, as would be evident from BSE images and the time-resolved LA analyses (Fig. 3-6a-c). Elemental plots, such as the Th vs. chondrite normalized (La/Sm) plot (Whitehouse and Kamber, 2002), further show no clear correlation between LREE enrichment and geochemical indicators of potential inclusions (Voisey, 2015). Instead, the LREE enrichment can either be related to unresolvable micro-inclusions of LREE phases or an overall enrichment of these elements in the crystal substituting for Zr and Si.

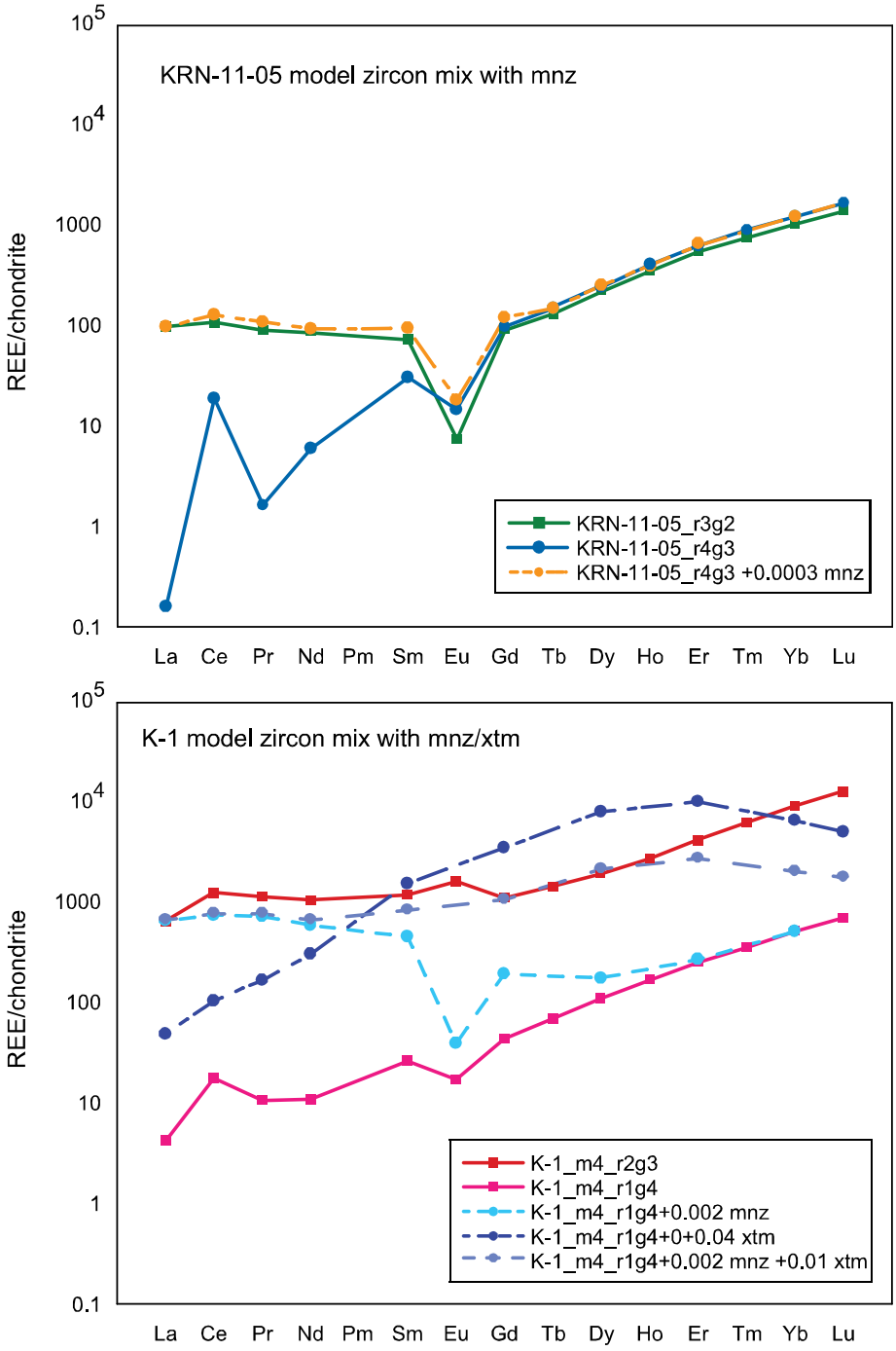

Figure 3-11. REE patterns of grains from each KRN-11-05 and K-1, one with patterns typical for zircon (low in LREE, high in HREE) and one with elevated REE contents. Mixes of the "normal" zircon REE compositions with different amount of monazite and/or xenotime added have been modeled to achieve REE patterns similar to grains with elevated REE content. Solid lines represent measured REE patterns, dashed lines are calculated. Average monazite and xenotime concentrations are from Bea (1996).

In Figure 3-11, the REE contents for one zircon grain from KRN-11-05 and K-1, respectively, with a typical REE distribution, are modeled to mix with different amounts of monazite and xenotime. Also plotted is a REE pattern from a grain for each sample that shows elevated REE contents for comparison. For KRN-11-05, only a low concentration of monazite (0.003 %) is sufficient to model a pattern elevated in LREE that closely matches that observed in a high REE grain. In this case, micro-inclusions of monazite, non-resolvable in the LA signal, seem a likely interpretation of the elevated LREE patterns observed in some grains, as the one shown here. In the ore zircon K-1, the REE pattern seems more complex and is not easily explained by a simple incorporation of monazite; the HREE of such a mix would be lower than observed in other grains. Similarly, inclusions of xenotime would also result in a different pattern than observed, with lower LREE to match the HREE levels and a different shape of the overall pattern. Adding both monazite and xenotime in small concentrations results in similar levels for most REE elements, however, the calculated pattern does not match the observed pattern completely. Therefore, for the zircon grains from K-1, an overall enrichment of LREE seems more likely as explanation for the observed REE patterns.

The TEM images of selected zircon grains from this sample confirm this interpretation for K-1; both core and rim region of these crystals consists exclusively of zircon and show no evidence for LREE-rich mineral inclusion on the nano- or micro-scale (Fig. 3-6d). Some core regions that showed elevated LREE contents have a mosaic structure and a strong microporosity. The LREE may reside in these pore spaces, potentially along the walls of the pores. Other grains have no microporosity, but show a faint zonation with

elevated Y contents. The LREE may further reside in the complex amorphous regions of the zircon. In contrast, grain R2G1 with low LREE does not show the mosaic structure and the accompanying porosity, nor does it not contain any pores or inclusions.

The microporosity in the core regions and the large voids the rims regions of some grains are highly unusual in zircon and are a strong evidence for the influence of hydrothermal fluids (Geisler et al., 2003). The close succession of partially amorphous and crystalline zircon on nanometer scale is evidence for dissolution-reprecipitation. The porosity may be related to the high contents of LREE measured by LA-ICPMS for these zircon grains. It is very likely that these grains were overprinted by a fluid with relatively high concentrations of Ca, Fe, Mn La, Ce, and Y. This observation is probably also responsible for the low quality of U-Pb analyses done within the rim region of this sample K-1 (Westhues et al., 2016). However, the core regions (as in grain R2G1) consist of massive zircon, giving confidence in the concordant U-Pb dates reported for the zircon core regions of this sample.

The FTIR results show that all the zircon crystals analyzed have significantly high water contents, up to 3.61 wt. % (see Fig. 3-3). The nature of where this water resides in the zircon structure is uncertain but it likely resides in the interstitial site (Finch and Hanchar, 2003). It is also possible that OH^- resides in cracks and pore spaces within a zircon crystal in the form of hydrous silicates, or exists as fluid inclusions containing true molecular H_2O (Woodhead et al., 1991). The voids recorded by TEM (Fig. 3-6d) could be remnants of fluid alteration influencing the zircon grains.

The radiation damage accumulated in the zircon grains in this study (Table 3-5) was calculated using the U and Th contents and age of samples (Westhues et al., 2016) following Holland and Gottfried (1955) and Murakami et al. (1991), with the adjustment suggested by Nasdala et al. (2001). All zircon grains from KRN-11-05, KRN-12-05, and KRN-12-02 with magmatic appearance did not accumulate enough alpha decays to have significant radiation damage since their initial crystallization (or even the subsequent greenschist facies metamorphism). Several grains of the ore zircon and from the syenite KRN-12-03 have experienced significant radiation damage, which may have provided pathways for fluids to alter the zircon, especially in the rims of the zircon grains in this study. The elevated water contents in the zircon crystals can explain the low totals of the EPMA analyses, and, more importantly, these results reinforce the importance of a fluid phase in at least part of the zircon growth history at Kiruna. It is evident that the Kiirunavaara ore zircons have been the most influenced by hydrothermal activity.

3.6.2 Secondary event in the Mesoproterozoic

Monazite from three ore samples have younger concordia ages, in comparison to zircon, ranging from 1628 ±12 Ma (K-1) to 1738 ±19 Ma (REK-10-04). The continuous range of concordant dates from 1515 to 1905 Ma, as found in monazite from KRN-11-01 and from 1651 to 1853 Ma in REK-10-02 may reflect the partial resetting of pre-existing monazite grains. The older grain regions observed in REK-10-04 makes this scenario very likely. This could suggest that also other monazites are a result of resetting the U-Pb system, more completely in these cases. Dates from this time frame have been reported earlier, partly with large errors, from whole rock Rb-Sr studies (Skiöld, 1979; Welin, 1980; Skiöld

and Öhlander, 1989), from zircon from an albite diabase (Skiöld, 1986), and from monazite from a felsic dike (Bergman et al., 2001). Combing these new data with these older observations suggest a later event affecting the immediate Kiruna area. This is in contrast to a study by Romer et al. (1994), who used the Saarijärvi syenite, about 15 km south of Kiruna, as a possible minimum age for a regional hydrothermal alteration event. The syenite, part of the Granite-Pegmatite association, the youngest suite of Proterozoic intrusions in the Norrbotten region, postdates the metamorphism in the area and appears largely unaltered. Two titanite fractions and two highly discordant zircon fractions from this intrusion yield a Discordia line through zero, with an upper intercept of 1792 ± 4 Ma. However, Romer et al. (1994) report chlorite in the Saarijärvi syenite, which could suggest that at least some alteration, maybe less pronounced, is present in this rock and might not be a suitable minimum age constraint. The new U-Pb results from monazite reinstate the earlier suggestion by Cliff and Rickard (1992) of an isotopic reequilibration at Kiruna. With our new data, a possible second event in the area may be placed around ca. 1600 to 1650 Ma in the immediate Kiruna area. Interestingly, several of the ore zircon grains, especially in their rims, have accumulated significant radiation damage approximately in this time frame (see Table 5). This may have been a time when water entered the structure of those zircon grains. This time period further overlaps with the intrusion of Rapakivi granites into the Svecokarelian craton (ca. 1650 to 1500 Ma) and the Gothian orogeny (ca. 1690 to 1550 Ma) (e.g., Åhäll et al., 2000). Even though documented further south, these events may have been a regional heat and fluid generating influence in other parts of Sweden. The second metasomatic event may have caused redistribution of monazite, explaining the

partial resetting of the U-Pb system in some of the grains studied. Whether this is a regional influence, or localized around the ore deposits, cannot be answered here beyond all doubt. However, a localized metasomatic event close to the ore deposits is the preferred interpretation: It can explain the stronger alteration of the footwall of Kiirunavaara from andesite to trachyandesite in contrast to the less altered appearance of the ca. 1792 Ma Saarijärvi syenite further away from the deposits.

3.6.3 Source regions based on Nd and Hf isotopes

Ore samples and altered host rock samples have distinctly different whole rock εNd_i values compared to the unaltered host rocks and intrusions; possibly indicating different source regions of ore and host rocks. A similar difference in whole rock εNd_i values between ore and host rocks has been reported for the Olympic Dam IOCG deposit (Johnson and McCulloch, 1995), and interpreted there as a mantle-derived influence on the ore. Also in Kiruna, host rock samples are closer related to the Nd signal of the Archean crust, while the extensively altered host rock and ore samples are shifted towards the depleted mantle signature. However, instead of showing a direct mantle influence, this could be related to the nearby Kiruna greenstones that have a depleted mantle signature (Skiöld and Cliff, 1984). Fluids circulating through this unit might be influenced by this signature, which is then recorded in the ores and altered samples.

The whole rock REE patterns suggest that the high-P ore from Kiirunavaara is especially highly influenced by its apatite content (close resemblance to apatite REE pattern). It is therefore likely that also the whole rock εNd_i values are influenced by the apatite in the samples.

Similar to the whole rock Sm-Nd results, the whole rock Lu-Hf system of host rocks analyzed suggest a source region related to Archean crust, also recorded by the Hf signature of zircon (Fig. 3-10, data from Westhues et al., 2017). Determining the whole rock Hf signature of the ores was unsuccessful, likely due to very low Hf contents, but zircon grains from these ore samples have been shown to be isotopically distinct from those within the host rocks. These zircon grains show a stronger mantle influence, very similar to what is recorded by whole rock Sm-Nd; all isotope systems point towards a mantle influence for the ores. One possible source for this mantle signature are the Kiruna greenstones, as has been suggested by Westhues et al. (Westhues et al., 2017) in chapter four.

The Sm-Nd composition of monazite in the ore samples is significantly different from that of the whole rock in showing mostly crustal influence. This monazite is younger than most of the ore, and probably records the Sm-Nd isotopic composition of later hydrothermal fluids. The Sm-Nd signature of the whole rock samples of ore (and altered samples) has apparently not been effected by these younger hydrothermal fluids and probably records the original Sm-Nd composition at 1880 Ma of these samples. Therefore, the difference between ore samples and whole rocks is not a result of a younger isotopic shift, and shows a real difference between host rocks and ore.

3.7 Conclusions

This comprehensive geochemical study of whole rock, zircon, and monazite grains from the Kiirunavaara iron oxide apatite ore, its host rocks, and some related intrusions, show strong evidence for metasomatic alteration by hydrothermal fluids in the study area. This is particularly true for zircon crystals from the Kiirunavaara IOA ores, which show

distinctive hydrothermal features. This evidence supports the idea that fluids rich in Fe may have influenced the ore and indicates the possible involvement of high temperature hydrothermal fluids for the formation of ‘Kiruna type” iron ores. These fluids may have originated as a late-stage magmatic fluid exsolved from the adjacent intrusions, since zircon grains from the Kiirunavaara syenite intrusion show hydrothermal textural and chemical features, as well. Samarium-Nd and Lu-Hf isotopic data show distinct differences between host rocks (crustal influence) and ore (closer to depleted mantle signature). This suggests that the ores are sourced from a region with depleted mantle signature, such as the nearby Kiruna greenstones.

Monazite records secondary alteration phases up to ca. 250 million years later that seem to have mostly influenced the ore samples, but can be found in some other isotopic systems, as well. This event may be connected to another period of heat and hydrothermal fluid influx in the area, potentially related to the craton-wide emplacement of Rapakivi granites. During later alteration phases, apatite and monazite recrystallized and were redistributed and iron ore was potentially further concentrated. The Sm-Nd isotopic composition of monazite dated suggests that these fluids have a significant crustal component, unlike the whole rock signature of the ore that reflects a more depleted mantle signature. We interpret this depleted mantle signature of the ores as its original signature, related to the main ore formation.

3.8 Acknowledgements

This paper represents one of three parts of the PhD research of the senior author. Many thanks are due to LKAB (Kiirunavaara operations) for financial and logistical

support, especially K. Holme for making the project possible, and many others for fruitful discussions and help during sampling, including, but not limited to, U.B. Anderson, H. Rutanen, and C. Debras. Olof Martinsson is thanked for introduction to the study area and assistance during field work. The project was financially supported by a NSERC discovery grant to JMH, and MUN, SEG, and MAC funding to the senior author. Numerous people are thanked for discussions and assistance in the labs including M. Wilson, S.J. Piercey, G. Layne, G.R. Dunning, S. Strong, P. King, R. Lam, S. Jantzi, C.M. Fisher, S.E. Phillips S.G. Broughm, and L. Hewa at MUN, K. Lindén at the Swedish Museum of Natural History, and J. Anderson, A. Hallberg, S. Bergman, J.A. Perdåhl and others at the Geological Survey of Sweden.

3.9 Bibliography – Chapter three

Åhäll, K.-I., Connelly, J. N., and Brewer, T. S., 2000, Episodic rapakivi magmatism due to distal orogenesis?: Correlation of 1.69–1.50 Ga orogenic and inboard, "anorogenic" events in the Baltic Shield: Geology, v. 28, p. 823-826.

Allaz, J., Selleck, B., Williams, M. L., and Jercinovic, M. J., 2013, Microprobe analysis and dating of monazite from the Potsdam Formation, New York: A progressive record of chemical reaction and fluid interaction: American Mineralogist, v. 98, p. 1106-1119.

Anders, E., and Grevesse, N., 1989, Abundances of the elements: Meteoritic and solar: Geochimica Et Cosmochimica Acta, v. 53, p. 197-214.

Bea, F., 1996, Residence of REE, Y, Th and U in granites and crustal protoliths; Implications for the chemistry of crustal melts: Journal of Petrology, v. 37, p. 521-552.

Bergman, S., Kübler, L., and Martinsson, O., 2001, Description of regional geological and geophysical maps of northern Norrbotten County (east of the Caledonian Orogen), Sveriges Geologiska Undersökning, Ba 56, 110 pp.

Billström, K., Eilu, P., Martinsson, O., Niiranen, T., Broman, C., Weihed, P., Wanhainen, C., and Ojala, J., 2010, IOCG and related deposits of the Northern Fennoscandian Shield, *in* Porter, T. M., ed., Hydrothermal iron oxide copper-gold and related deposits: a global perspective, 4: Adelaide, PGC Publishing, p. 415-426.

Bindeman, I. N., and Valley, J. W., 2001, Low-$\delta^{18}O$ rhyolites from Yellowstone: Magmatic evolution based on analyses of zircons and individual phenocrysts: Journal of Petrology, v. 42, p. 1491-1517.

Bouvier, A., Vervoort, J. D., and Patchett, P. J., 2008, The Lu-Hf and Sm-Nd isotopic composition of CHUR: Constraints from unequilibrated chondrites and implications for the bulk composition of terrestrial planets: Earth and Planetary Science Letters, v. 273, p. 48-57.

Chen, H., Clark, A. H., and Kyser, T. K., 2010, The Marcona magnetite deposit, Ica, south-central Peru: A product of hydrous, iron oxide-rich melts?: Economic Geology, v. 105, p. 1441-1456.

Claoué-Long, J. C., King, R. W., and Kerrich, R., 1990, Archaean hydrothermal zircon in the Abitibi greenstone belt: constraints on the timing of gold mineralisation: Earth and Planetary Science Letters, v. 98, p. 109-128.

Cliff, R. A., and Rickard, D., 1992, Isotope systematics of the Kiruna magnetite ores, Sweden: Part 2. Evidence for a secondary event 400 m.y. after ore formation: Economic Geology, v. 87, p. 1121-1129.

Cliff, R. A., Rickard, D., and Blake, K., 1990, Isotope systematics of the Kiruna magnetite ores, Sweden: Part 1. Age of the ore: Economic Geology, v. 85, p. 1770 - 1776.

Corfu, F., and Davis, D. W., 1991, Comment on "Archean hydrothermal zircon in the Abitibi greenstone belt: constraints on the timing of gold mineralization" by J.C. Claoué-Long, R.W. King and R. Kerrich: Earth and Planetary Science Letters, v. 104, p. 545-552.

Depaolo, D. J., 1981, Neodymium isotopes in the Colorado front range and crust-mantle evolution in the Proterozoic: Nature, v. 291, p. 193-196.

Finch, R. J., and Hanchar, J. M., 2003, Structure and chemistry of zircon and zircon-group minerals, *in* Hanchar, J. M., and Hoskin, P. W. O., eds., Zircon, 53. Reviews in Mineralogy & Geochemistry, p. 1-25.

Fisher, C. M., McFarlane, C. R. M., Hanchar, J. M., Schmitz, M. D., Sylvester, P. J., Lam, R., and Longerich, H. P., 2011, Sm-Nd isotope systematics by laser ablation-multicollector-inductively coupled plasma mass spectrometry: Methods and potential natural and synthetic reference materials: Chemical Geology, v. 284, p. 1-20.

Frietsch, R., 1978, On the magmatic origin of iron ores of the Kiruna type: Economic Geology, v. 73, p. 478-485.

Frietsch, R., and Perdahl, J. A., 1995, Rare earth elements in apatite and magnetite in Kiruna-type iron ores and some other iron ore types: Ore Geology Reviews, v. 9, p. 489-510.

Frietsch, R., Tuisku, P., Martinsson, O., and Perdahl, J. A., 1997, Early Proterozoic Cu-(Au) and Fe ore deposits associated with regional Na-Cl metasomatism in northern Fennoscandia: Ore Geology Reviews, v. 12, p. 1-34.

Gasser, D., Jerabek, P., Faber, C., Stunitz, H., Menegon, L., Corfu, F., Erambert, M., and Whitehouse, M. J., 2015, Behaviour of geochronometers and timing of metamorphic reactions during deformation at lower crustal conditions: phase equilibrium modelling and U-Pb dating of zircon, monazite, rutile and titanite from

the Kalak Nappe Complex, northern Norway: Journal of Metamorphic Geology, v. 33, p. 513-534.

Geisler, T., Rashwan, A. A., Rahn, M. K. W., Poller, U., Zwingmann, H., Pidgeon, R. T., Schleicher, H., and Tomaschek, F., 2003, Low-temperature hydrothermal alteration of natural metamict zircons from the Eastern Desert, Egypt: Mineralogical Magazine, v. 67, p. 485-508.

Geisler, T., Schaltegger, U., and Tomaschek, F., 2007, Re-equilibration of Zircon in Aqueous Fluids and Melts: Elements, v. 3, p. 43-50.

Groves, D. I., Bierlein, F. P., Meinert, L. D., and Hitzman, M. W., 2010, Iron oxide copper-gold (IOCG) deposits through Earth history: Implications for origin, lithospheric setting, and distinction from other epigenetic iron oxide deposits: Economic Geology, v. 105, p. 641-654.

Hanchar, J. M., and van Westrenen, W., 2007, Rare earth element behavior in zircon-melt systems: ELEMENTS, v. 3, p. 37-42.

Harlov, D. E., Andersson, U. B., Forster, H. J., Nystrom, J. O., Dulski, P., and Broman, C., 2002, Apatite-monazite relations in the Kiirunavaara magnetite-apatite ore, northern Sweden: Chemical Geology, v. 191, p. 47-72.

Hitzman, M. W., Oreskes, N., and Einaudi, M. T., 1992, Geological characteristics and tectonic setting of Proterozoic iron oxide (Cu-U-Au-Ree) deposits: Precambrian Research, v. 58, p. 241-287.

Holland, H. D., and Gottfried, D., 1955, The effect of nuclear radiation on the structure of zircon: Acta Crystallographica, v. 8, p. 291-300.

Hoskin, P. W. O., 2005, Trace-element composition of hydrothermal zircon and the alteration of Hadean zircon from the Jack Hills, Australia: Geochimica Et Cosmochimica Acta, v. 69, p. 637-648.

Hoskin, P. W. O., and Schaltegger, U., 2003, The composition of zircon and igneous and metamorphic petrogenesis: Reviews in Mineralogy and Geochemistry, v. 53, p. 27-62.

Ickert, R. B., 2013, Algorithms for estimating uncertainties in initial radiogenic isotope ratios and model ages: Chemical Geology, v. 340, p. 131-138.

Janots, E., Berger, A., Gnos, E., Whitehouse, M., Lewin, E., and Pettke, T., 2012, Constraints on fluid evolution during metamorphism from U–Th–Pb systematics in Alpine hydrothermal monazite: Chemical Geology, v. 326–327, p. 61-71.

Johnson, J. P., and McCulloch, M. T., 1995, Sources of mineralising fluids for the Olympic Dam Deposit (South Australia); Sm-Nd isotopic constraints: Chemical Geology, v. 121, p. 177-199.

Kirkland, C., Whitehouse, M., and Slagstad, T., 2009, Fluid-assisted zircon and monazite growth within a shear zone: a case study from Finnmark, Arctic Norway: Contributions to Mineralogy and Petrology, v. 158, p. 637-657.

Liu, X.-C., Wu, Y.-B., Fisher, C. M., Hanchar, J. M., Beranek, L., Gao, S., and Wang, H., 2017, Tracing crustal evolution by U-Th-Pb, Sm-Nd, and Lu-Hf isotopes in detrital monazite and zircon from modern rivers: Geology, v. 45, p. 103-106.

Longerich, H. P., Jenner, G. A., Fryer, B. J., and Jackson, S. E., 1990, Inductively coupled plasma-mass spectrometric analysis of geological samples: A critical evaluation based on case studies: Chemical Geology, v. 83, p. 105-118.

Ludwig, K. R., 2003, User's manual for Isoplot 3.00, A geochronological toolkit for Microsoft Excel: Berkley Geochronology Center Special Publication, v. 4, p. 71.

McFarlane, C. R. M., and McCulloch, M. T., 2007, Coupling of in-situ Sm-Nd systematics and U-Pb dating of monazite and allanite with applications to crustal evolution studies: Chemical Geology, v. 245, p. 45-60.

Murakami, T., Chakoumakos, B. C., Ewing, R. C., Lumpkin, G. R., and Weber, W. J., 1991, Alpha-decay event damage in zircon: American Mineralogist, v. 76, p. 1510-1532.

Nasdala, L., Wenzel, M., Vavra, G., Irmer, G., Wenzel, T., and Kober, B., 2001, Metamictisation of natural zircon: accumulation versus thermal annealing of radioactivity-induced damage: Contributions to Mineralogy and Petrology, v. 141, p. 125-144.

Nyström, J. O., and Henríquez, F., 1994, Magmatic features of iron ores of the Kiruna type in Chile and Sweden; ore textures and magnetite geochemistry: Economic Geology, v. 89, p. 820-839.

Öhlander, B., Skiöld, T., Elming, S. Å., Claesson, S., and Nisca, D. H., 1993, Delineation and character of the Archaean-Proterozoic boundary in northern Sweden: Precambrian Research, v. 64, p. 67-84.

Parák, T., 1975, Kiruna iron ores are not 'intrusive-magmatic ores of the Kiruna type': Economic Geology, v. 70, p. 1242-1258.

Patchett, P. J., and Tatsumoto, M., 1980, A routine high-precision method for Lu-Hf isotope geochemistry and chronology: Contributions to Mineralogy and Petrology, v. 75, p. 263-267.

Pettke, T., Audetat, A., Schaltegger, U., and Heinrich, C. A., 2005, Magmatic-to-hydrothermal crystallization in the W-Sn mineralized Mole Granite (NSW, Australia) - Part II: Evolving zircon and thorite trace element chemistry: Chemical Geology, v. 220, p. 191-213.

Phillips, S. E., 2015, High-spatial-resolution Sm-Nd & U-Pb and Lu-Hf & U-Pb isotope geochemistry of monazite and zircon in the Old Woman - Piute batholith, California: Unpub. M.Sc. thesis, Memorial University, 164 pp.

Rayner, N., Stern, R. A., and Carr, S. D., 2005, Grain-scale variations in trace element composition of fluid-altered zircon, Acasta Gneiss Complex, northwestern Canada: Contributions to Mineralogy and Petrology, v. 148, p. 721-734.

Romer, R. L., Martinsson, O., and Perdahl, J. A., 1994, Geochronology of the Kiruna Iron-Ores and Hydrothermal Alterations: Economic Geology and the Bulletin of the Society of Economic Geologists, v. 89, p. 1249-1261.

Rossman, G. R., 2006, Analytical Methods for Measuring Water in Nominally Anhydrous Minerals: Reviews in Mineralogy and Geochemistry, v. 62, p. 1-28.

Rubin, J. N., Henry, C. D., and Price, J. G., 1989, Hydrothermal zircons and zircon overgrowths, Sierra-Slanca Peaks, Texas: American Mineralogist, v. 74, p. 865-869.

Rubin, J. N., Henry, C. D., and Price, J. G., 1993, The mobility of zirconium and other "immobile" elements during hydrothermal alteration: Chemical Geology, v. 110, p. 29-47.

Schaltegger, U., 2007, Hydrothermal zircon: ELEMENTS, v. 3, p. 51-79.

Skiöld, T., 1979, U-Pb zircon and Rb-Sr whole-rock and mineral ages of Proterozoic intrusives on mapsheet Lannavaara, north-eastern Sweden: Geologiska Föreningen i Stockholm Förhandlingar, v. 101, p. 131-137.

Skiöld, T., 1986, On the age of the Kiruna Greenstones, northern Sweden: Precambrian Research, v. 32, p. 35-44.

Skiöld, T., and Cliff, R. A., 1984, Sm-Nd and U-Pb dating of Early Proterozoic mafic-felsic volcanism in northernmost Sweden: Precambrian Research, v. 26, p. 1-13.

Skiöld, T., and Öhlander, B., 1989, Chronology and geochemistry of late Svecofennian processes in northern Sweden: Geologiska Föreningen i Stockholm Förhandlingar, v. 111, p. 347-354.

Söderlund, U., Patchett, P. J., Vervoort, J. D., and Isachsen, C. E., 2004, The ^{176}Lu decay constant determined by Lu–Hf and U–Pb isotope systematics of Precambrian mafic intrusions: Earth and Planetary Science Letters, v. 219, p. 311-324.

Stacey, J. S., and Kramers, J. D., 1975, Approximation of terrestrial lead isotope evolution by a two-stage model: Earth and Planetary Science Letters, v. 26, p. 207-221.

Steiger, R., and Jäger, E., 1977, Subcommission on geochronology: Convention on the use of decay constants in geo- and cosmochronology: Earth and Planetary Science Letters, v. 36, p. 359-362.

Toscano, M., Pascual, E., Nesbitt, R. W., Almodóvar, G. R., Sáez, R., and Donaire, T., 2014, Geochemical discrimination of hydrothermal and igneous zircon in the Iberian Pyrite Belt, Spain: Ore Geology Reviews, v. 56, p. 301-311.

Vervoort, J. D., and Blichert-Toft, J., 1999, Evolution of the depleted mantle: Hf isotope evidence from juvenile rocks through time: Geochimica Et Cosmochimica Acta, v. 63, p. 533-556.

Vervoort, J. D., Patchett, P. J., Söderlund, U., and Baker, M., 2004, Isotopic composition of Yb and the determination of Lu concentrations and Lu/Hf ratios by isotope dilution using MC-ICPMS: Geochemistry, Geophysics, Geosystems, v. 5, p. Q11002.

Voisey, C. R., 2015, Trace element geochemistry of zircon crystals from the Kiruna iron oxide apatite ore district in the Norrbotten region of northern Sweden: Unpub. B. Sc. (Hons.) thesis, Memorial University of Newfoundland, 107 pp.

Welin, E., 1980, Tabulation of recalculated radiometric ages published 1960–1979 for rocks and minerals in Sweden: Geologiska Föreningen i Stockholm Förhandlingar, v. 101, p. 309-320.

Westhues, A., Hanchar, J. M., LeMessurier, M. J., and Whitehouse, M. J., 2017, Evidence for hydrothermal alteration and source regions for the Kiruna iron oxide–apatite ore (northern Sweden) from zircon Hf and O isotopes: Geology, v. 45, p. 571-574.

Westhues, A., Hanchar, J. M., Whitehouse, M. J., and Martinsson, O., 2016, New constraints on the timing of host rock emplacement, hydrothermal alteration, and

iron oxide-apatite mineralization in the Kiruna district, Norrbotten, Sweden: Economic Geology v. 111, p. 1595-1618.

Whitehouse, M. J., and Kamber, B. S., 2002, On the overabundance of light rare earth elements in terrestrial zircons and its implication for Earth's earliest magmatic differentiation: Earth and Planetary Science Letters, v. 204, p. 333-346.

Williams, M. L., Jercinovic, M. J., Goncalves, P., and Mahan, K., 2006, Format and philosophy for collecting, compiling, and reporting microprobe monazite ages: Chemical Geology, v. 225, p. 1-15.

Williams, M. L., Jercinovic, M. J., Harlov, D. E., Budzyń, B., and Hetherington, C. J., 2011, Resetting monazite ages during fluid-related alteration: Chemical Geology, v. 283, p. 218-225.

Woodhead, J. A., Rossman, G. R., and Thomas, A. P., 1991, Hydrous species in zircon: American Mineralogist, v. 76, p. 1533-1546.

Yang, W.-B., Niu, H.-C., Shan, Q., Sun, W.-D., Zhang, H., Li, N.-B., Jiang, Y.-H., and Yu, X.-Y., 2014, Geochemistry of magmatic and hydrothermal zircon from the highly evolved Baerzhe alkaline granite: implications for Zr–REE–Nb mineralization: Mineralium Deposita, v. 49, p. 451-470.

Table 3-1. Summary of sample locations, mineralogy, alteration, zircon U-Pb ages (Chapter two, Westhues et al., 2016), zircon Lu-Hf and oxygen isotopic signatures (Chapter four, Westhues et al., 2017).

sample	Latitude	Longitude	mine level	Rock type + mineralogy	dominant alteration	U-Pb age zircon (Ma)*	n	MSWD	average εHf ± 2SD	average $\delta^{18}O$ ± 2SD
K-6	N 67° 49' 42.2"	E 20° 12' 12.2"	1065 m	KRN basalt/andesite (FW) *Kfs, Ab, ±act-tt-qz*	Na-Fe-Ca					
KRN-11-03	N 67° 50' 13.1"	E 20° 12' 17.4"	1365 m	KRN basalt/andesite (FW) *Kfs, plag ±act-tt-qz*	Na-Fe-Ca	1884.1 ±3.7[a]	4	0.69	-2.56 ±4.61	5.98 ±0.80
K-4	N 67° 51' 11.4"	E 20° 12' 43.2"	1060 m	KRN rhyodacite (HW) *Kfs, qz ±hbl-tt*	Na	1879.5 ±7.1				
KRN-11-05	N 67° 50' 35.6"	E 20° 12' 37.4"	1065 m	KRN hanging wall rhyodacite (HW) *Kfs, qz ±hbl-tt*	Na	1880.5 ± 4.5	8	0.95	-6.94 ±0.46	3.40 ±0.38
KRN-11-06	N 67° 50' 35.8"	E 20° 12' 32.4"	1076 m	KRN rhyodacite (HW), altered *Kfs (ser, Fe incl.), qz ±hbl-tt*	Na ±K	1880.1 ± 2.7	18	0.97	-7.51 ±1.52	2.86 ±0.25
KRN-12-01	N 67° 50' 57.8"	E 20° 10' 24.7"	Surface	KRN syenite *Kfs (ser), act, tt ±Ab-qz*	Na-Ca-Fe ±K	1879.7 ±6.9[b]	6	1.14		
KRN-12-02	N 67° 50' 57.8"	E 20° 10' 24.7"	Surface	KRN aplite *qz, Kfs, Ab ±hbl-tt-mag*	Na	1880.6 ±3.7	18	0.99	-7.06 ±0.67	2.95 ±0.12
KRN-12-03	N 67° 50' 23.4"	E 20° 10' 49.7"	Surface	KRN syenite *Kfs (Fe incl.), act, tt ± Ab-qz*	Na-Ca-Fe	1896 ±19[b]	12	4.5	-5.74 ±1.43	3.82 ±0.28
KRN-12-05	N 67° 50' 30.1"	E 20° 10' 50.1"	1365 m	KRN granite *Kfs, qz ±Ab-bt-tt*	K-Na ±Fe	1874.1 ±3.8	24	1.3	-8.68 ±1.20	3.43 ±0.37
REK-10-05	N 67° 52' 18.0"	E 20° 14' 08.1"	Surface	REK rhyodacite (FW) *qz, ap, fsp (ser), ±bt-rt-mag-hm*	Na-Ca-Fe					
REK-12-02	N 67° 52' 17.6"	E 20° 14' 08.9"	Surface	REK rhyodacite (FW) *qz, ap, fsp (ser), ±bt-rt-mag-hm*	Ca-K-Fe					
NUK-12-01	N 67° 53' 53.1"	E 20° 15' 31.1"	Surface	NUK footwall rhyodacite *qz, Kfs, ±bt-rt-act-mag*	K ±Fe	1881.7 ± 2.2	24	1.1	-7.39 ±0.59	3.44 ±0.32
REK-10-01	N 67° 52' 17.8"	E 20° 14' 15.1"	Surface	Rektorn porphyry (HW) *Kfs (Fe incl., ser), qz, ±Fe oxide*	K-Fe	1873.7 ±9.1	3	0.97		
REK-10-02	N 67° 52' 17.8"	E 20° 14' 15.1"	Surface	Rektorn porphyry (HW) *Kfs (Fe incl., ser), qz, Fe oxide*	K-Na					
REK-10-03B	N 67° 52' 17.4"	E 20° 14' 07.4"	Surface	REK ap-rich vein (HW) *ap (Fe incl.), mag, Kfs*	Ca-Fe					
REK-12-01	N 67° 52' 17.8"	E 20° 14' 13.6"	Surface	Rektorn porphyry (HW) *Kfs (Fe incl., ser), qz, Fe oxide*	K-Fe	1876.2 ±6.8	13	1.8	-1.17 ±2.92	5.30 ±0.85
TUV-10-03	N 67° 51' 13.9"	E 20° 18' 57.0"	Surface	TUV host rhyodacite *Kfs, qz ±act-tt*	Na-K					

Continued on following page.

Table 3-1 - continued. Summary of sample locations, mineralogy, alteration, zircon U-Pb ages (Chapter two, Westhues et al., 2016), zircon Lu-Hf and oxygen isotopic signatures (Chapter four, Westhues et al., 2017).

sample	Latitude	Longitude	Underground level	Rock type + mineralogy	dominant alteration	U-Pb age zircon (Ma)*	n	MSWD	average εHf ± 2SD	average $\delta^{18}O$ ± 2SD
K-1	N 67° 51' 0.6"	E 20° 12' 23.8"	767 m	KRN D-ore *mag, act, ap ±fsp-qz*		1874.1 ±7.1	4	1.7	7.17 ±2.93	6.81 ±0.82
KRN-11-01	N 67° 51' 15.7"	E 20° 12' 20.7"	816 m	KRN D-ore *mag, act, ap*						
REK-10-04	N 67° 52' 17.4"	E 20° 14' 07.4"	Surface	REK ore *ap, mag ±cal-qz*						
NUK-10-01	N 67° 53' 51.0"	E 20° 15' 31.9"	Surface	NUK ore *ap, mag*						
NUK-12-02	N 67° 53' 50.8"	E 20° 15' 33.9"	Surface	NUK ore + host *mag, ap – qz, ser ±ap, mag*		1877.1 ±3.5	21	1.3	1.06 ±0.71	6.98 ±0.38
TUV-10-01	N 67° 51' 15.1"	E 20° 18' 54.1"	Surface	TUV ore *mag, act, ap*						

KRN: Kiirunavaara, REK: Rektorn, NUK: Nukutus, TUV: Tuolluvaara; FW: footwall; HW: hanging wall; *Concordia age unless: [a] $^{206}Pb/^{207}Pb$ weighted mean age, [b] upper intercept age. Minerals: Ab: albite, act: actinolite, ap: apatite, bt: biotite, cal: calcite, hm: hematite, Kfs: K-feldspar, mag: magnetite, qz: quartz, rt: rutile, tt: titanite

Table 3-2. Results of EPMA quantitative zircon analyses as averages of n number of analyses in different zircon grains.

Sample	KRN-11-05	KRN-12-05	KRN-12-03	KRN-12-02	NUK-12-02	K-1	SynZirc std
n	6	6	5	5	8	11	4
FeO wt.%	0.00	0.00	0.36	0.17	0.01	0.30	n.d.
Y_2O_3 wt.%	0.16	0.27	0.45	0.34	0.12	0.19	n.d.
P_2O_5 wt.%	0.08	0.11	0.10	0.10	0.10	0.13	0.04
SiO_2 wt.%	31.81	31.69	31.27	31.63	31.49	31.25	32.02
HfO_2 wt.%	0.67	0.69	0.69	0.63	0.80	0.73	n.d.
ZrO_2 wt.%	66.60	66.22	64.30	65.33	66.11	64.78	67.77
CaO wt.%	0.00	0.00	0.36	0.30	0.00	0.11	n.d.
Total wt.%	**99.32**	**98.97**	**97.53**	**98.49**	**98.62**	**97.49**	**99.82**

n.d.: not detected

Table 3-3. LA-ICPMS results zircon analyses, sorted by sample, Kiruna hanging wall, granite and aplite.

	KRN-11-05 – metavolcanic host rock						KRN-12-05 - granite						KRN-12-02 - aplite				
	r3-g2 l	r3-g2 d	r4-g4	r4-g3	r2-g4	r3-g1	r4-g1	r4-g1 R	r4-g4	r3-g7	r1-g1	r2-g1	r4-g1	r3-g1 R	r3-g1 C	r2-g2	r3-g5
Al	n.d.	126	n.d.	32	n.d.	n.d.	n.d.	n.d.	n.d.	n.d.	n.d.	n.d.	n.d.	1299	162	n.d.	42
P	671	101	103	144	134	99	141	160	264	281	252	125	136	140	248	164	183
Ca	1980	101	5	n.d.	27	n.d.	n.d.	n.d.	210	718	65	n.d.	n.d.	5970	650	n.d.	12
Sc	371	394	335	368	383	384	347	424	391	367	399	364	373	325	383	375	403
Ti	4.7	15.3	3.7	3.6	3.1	4.6	4.1	3.4	6.4	2.1	5.3	2.6	5.1	49.6	3.5	3.7	7.0
V	1.2	2.4	1.8	2.2	1.3	1.7	1.5	1.6	2.4	1.7	1.5	1.2	1.3	33.7	3.4	1.6	1.3
Mn	4.1	19.4	2.4	2.1	0.3	1.6	3.4	2.0	2.5	2.5	0.6	0.6	n.d.	566.8	31.0	4.7	1.8
Fe	13	362	33	246	n.d.	530	141	21	n.d.	2	8	7	1	3700	730	7	131
Rb	n.d.	1.18	0.21	0.32	0.23	0.75	0.61	n.d.	0.41	0.08	0.24	0.09	n.d.	0.99	0.23	n.d.	n.d.
Sr	0.69	3.95	0.44	0.13	0.16	0.19	0.96	0.25	0.47	0.39	0.15	0.17	n.d.	91.30	2.40	n.d.	n.d.
Y	547	495	1140	557	461	683	1000	824	892	642	1037	703	737	590	1446	781	1141
Nb	1.4	1.7	3.3	5.3	1.2	1.1	2.1	4.1	5.9	4.7	3.2	2.0	2.7	29.8	9.7	3.5	7.2
Ba	n.d.	2.38	0.08	0.28	n.d.	0.11	0.26	0.20	0.29	0.12	n.d.	n.d.	n.d.	29.30	2.09	0.21	0.48
La	22.40	4.13	3.55	0.14	1.41	0.11	2.28	1.88	4.23	4.84	0.06	n.d.	n.d.	30.13	5.57	0.17	0.70
Ce	63.40	21.90	23.90	9.00	10.27	5.96	24.23	20.80	38.30	26.80	43.40	11.36	16.14	175.4	35.80	19.63	34.30
Pr	7.75	2.29	1.75	0.21	0.51	0.13	1.36	0.63	2.90	1.89	0.20	0.10	0.08	18.11	2.77	0.22	0.59
Nd	39.00	17.90	12.00	2.55	2.70	1.66	11.14	4.30	20.20	9.58	3.04	1.75	1.55	105.8	16.10	2.66	5.32
Sm	10.40	11.01	7.61	3.61	2.51	3.36	12.12	3.76	8.60	3.92	5.27	3.11	3.24	57.50	10.58	5.22	7.21
Eu	0.41	1.38	0.69	0.77	0.12	0.23	1.71	0.25	1.31	0.24	0.94	0.36	0.20	21.46	1.14	0.36	0.65
Gd	17.80	15.87	26.80	15.70	9.81	15.09	44.00	15.40	20.30	12.23	25.90	15.81	15.15	116.0	36.90	18.62	29.90
Tb	4.65	3.89	8.80	4.67	3.31	5.36	13.54	5.86	5.99	4.22	8.13	5.26	5.52	32.03	11.78	5.96	9.95
Dy	53.20	42.40	107.0	49.70	40.44	62.50	147.3	70.4	78.5	53.6	93.3	63.3	67.2	364.2	142.2	71.8	108.8
Ho	19.17	16.47	41.80	18.70	15.78	24.00	54.50	28.35	31.10	22.44	35.60	25.21	26.48	142.9	52.6	27.88	40.7
Er	85.80	77.00	183.0	83.3	73.8	104.8	232.0	130.4	148.0	104.7	159.8	113.2	114.6	667.1	234.0	123.3	181.5
Tm	18.03	16.59	37.10	18.40	15.20	21.39	44.70	27.83	31.30	22.55	32.35	22.95	24.23	143.3	45.10	25.21	35.57
Yb	162.6	154.7	332.0	180.1	139.5	189.8	383.0	245.5	280.0	207.9	298.5	211.6	214.8	1236	401.0	222.7	312.7
Lu	33.38	32.9	63.6	37.9	28.55	38.3	74.0	48.1	54.7	40.37	58.80	42.73	42.56	226.1	74.9	44.05	61.2
Hf	5610	5735	6134	6520	5678	5274	4436	6569	7220	6839	5760	4560	5163	6718	5588	4884	4980
Ta	0.46	0.39	1.87	0.20	0.41	0.34	0.54	1.11	1.54	1.45	0.63	0.62	0.85	3.73	1.02	0.71	0.97
Pb	6.1	5.7	16.8	6.5	5.2	7.6	13.5	8.8	17.9	12.0	13.3	5.6	9.7	34.3	15.3	9.0	13.1
Th	37.8	51.2	99.0	72.1	30.6	43.2	78.3	52.2	90.2	60.9	77.7	31.9	55.3	612.9	103	54.8	80.2
U	59.9	106.9	137.0	112.2	59.0	74.5	105.8	105.1	172.0	129.9	63.1	59.2	87.4	1107	162.0	83.0	102.6

continued on following pages. rX-gY: row X, grain Y. R: rim, C: core, l: light in BSE, d: dark in BSE. n.d.: not detected.

Table 3-3 - continued. LA-ICPMS results zircon analyses, sorted by sample, Kiruna syenite and Nukutus ore.

	KRN-12-03 - syenite					NUK-12-02 – Nukutus ore							
	r4-g2 C	r4-g2 R	r3-g2	r2-g2 C	r2-g2 R	r1-g3	r1-g5	r2-g2 C	r2-g2 R	r3-g3 C	r3-g3 R a	r3-g3 R b	r4-g1
Al	10	1190	814	697	449	n.d.	n.d.	300	10	157	56	62	7
P	62	170	245	128	87	223	142	369	85	121	1050	212	139
Ca	2	3870	4850	1280	1590	122	n.d.	740	10	45	1600	31	n.d.
Sc	307	467	352	435	299	371	438	346	341	403	523	379	395
Ti	6.7	44.8	26.8	83.8	25.3	6.4	9.0	9.7	1.9	17.7	8.0	12.2	19.5
V	1.5	10.9	15.0	9.5	8.6	3.2	2.1	2.5	1.8	1.9	3.2	3.1	1.9
Mn	28.4	523.0	720.0	191.0	214.0	12.4	0.6	61.4	0.8	3.3	8.3	17.5	2.8
Fe	204	4550	3670	1680	1844	146	3	1067	29	261	169	208	125
Rb	n.d.	1.37	n.d.	0.85	0.85	0.10	0.57	0.66	0.12	1.42	0.06	0.12	0.09
Sr	n.d.	65.70	114.6	29.10	18.20	0.46	0.13	3.81	0.08	1.70	4.35	8.50	0.13
Y	370	2820	430	1480	809	733	477	872	222	597	542	360	757
Nb	1.1	5.4	6.4	5.8	3.2	1.3	0.9	1.3	0.8	0.7	1.4	1.6	0.8
Ba	1.52	61.40	32.60	56.20	21.5	0.48	0.09	4.40	0.23	1.17	3.50	4.10	0.51
La	4.19	177.0	55.80	129.1	41.3	0.99	n.d.	36.50	2.40	143.0	67.00	117.0	0.50
Ce	28.03	544.0	259.0	506.0	162	12.76	5.91	103.0	9.70	318.0	155.0	270.0	8.05
Pr	2.04	45.40	22.00	50.20	16.5	0.69	n.d.	12.00	0.60	34.20	15.50	26.80	0.43
Nd	11.89	224.0	132.0	274.0	92.0	3.57	0.67	53.4	2.80	102.0	62.0	96.00	3.51
Sm	5.89	123.0	101.0	132.0	51.0	4.02	3.10	19.40	1.25	15.50	9.70	16.60	4.80
Eu	1.62	40.40	34.80	33.40	12.0	0.55	0.21	2.82	0.14	2.39	0.79	2.99	0.68
Gd	13.25	200.0	241.0	180.0	71.7	16.60	9.91	34.80	4.54	20.40	16.40	13.70	21.90
Tb	2.92	34.90	50.60	23.40	11.1	5.79	3.49	9.53	1.61	5.47	4.20	3.10	6.45
Dy	32.65	307.0	465.0	163.0	101.0	64.80	42.00	93.30	18.00	57.40	49.80	34.00	73.30
Ho	13.12	102.8	157.6	49.60	34.80	24.26	16.56	31.30	7.35	20.81	18.55	12.26	26.29
Er	59.7	434.0	635.0	194.0	145.0	110.4	73.30	130.0	34.70	91.20	82.40	58.30	111.3
Tm	12.84	86.70	116.8	37.60	29.80	22.86	15.78	27.36	7.54	17.35	18.69	13.15	22.72
Yb	115.9	739.0	868.0	311.0	240.0	205.7	142.2	240.2	72.50	153.7	172.9	124.6	200.9
Lu	21.47	131.0	124.2	55.60	43.1	41.23	28.10	48.03	15.66	29.90	34.50	26.10	38.90
Hf	3940	7081	5383	7974	5508	6337	6869	5730	6536	6258	9510	7019	6092
Ta	0.40	1.24	1.59	1.17	1.03	0.55	0.34	0.77	0.40	0.20	0.58	0.54	0.30
Pb	21.6	70.1	105.9	56.4	36.0	20.9	11.5	17.1	5.9	9.7	13.0	10.5	14.9
Th	118.9	1024	2085	1095	413.0	114.4	64.1	148.7	31.3	56.0	70.3	72.9	80.2
U	196.1	848.0	685.0	260.0	238	264.9	175.8	347.0	124.3	124.2	230.6	190.1	179.1

continued on following page. rX-gY: row X, grain Y, m: mount #. R: rim, C: core. n.d.: not detected.

Table 3-3 - continued. LA-ICPMS results zircon analyses, sorted by sample, Kiruna ore.

	K-1 – mount 4							K-1 – mount 2							
	r1g4	r1g8	r3g6	r2g6	r1g7	r2g3	r1g6	r1g1	r2g1	r3g1	r3g2	r3g2b	r4g2	r5g3	r5g2
Al	136	1400	n.d.	639	2900	2090	3480	1560	129	1150	1600	3770	1324	681	630
P	58	947	153	285	107	608	6400	301	78	359	837	1740	500	167	361
Ca	n.d.	2860	100	725	n.d.	3410	18100	2650	33	1560	2220	4730	1470	943	520
Sc	259	796	429	430	399	947	673	386	444	455	632	927	558	415	445
Ti	2.9	39.7	6.5	11.0	18.4	76.3	319.0	51.0	3.7	56.7	35.3	51.9	58.3	18.5	10.0
V	0.9	37.6	1.8	6.7	13.8	83.2	135.7	20.5	2.1	9.8	19.7	25.9	15.7	10.1	2.3
Mn	22.2	1540	75.9	543.0	74.0	2320	1156	1584	88.7	920	1380	2218	1090	709	49.8
Fe	285	6340	266	2950	3600	10350	25000	6950	655	4710	6020	10770	5320	3390	1600
Rb	1.19	10.10	6.17	7.01	23.10	22.1	18.40	5.87	0.48	3.54	4.82	5.90	1.90	0.47	0.63
Sr	0.68	47.1	1.30	15.0	0.71	65.1	42.4	46.3	1.24	47.0	42.6	83.70	34.10	17.50	1.17
Y	277	2930	443	1480	561	1580	1410	920	357	1640	1530	372	148	1066	1055
Nb	0.7	36.7	1.7	8.7	3.0	66.5	22.4	15.5	1.8	9.6	17.3	22.6	13.1	6.0	2.6
Ba	0.16	10.71	0.44	4.35	1.38	19.6	12.80	10.22	0.80	71.0	15.9	24.70	10.30	5.08	0.44
La	0.98	81.7	1.89	30.5	1.85	129.0	74.60	73.9	0.98	50.0	84.3	353.0	107.00	25.10	9.20
Ce	10.50	415.0	22.8	174.0	15.81	665.0	378.0	402.0	14.76	306.0	493.0	1274.	504.00	117.9	43.4
Pr	0.94	52.2	1.43	22.5	0.97	84.70	47.20	51.00	0.73	39.90	60.90	162.6	58.80	16.14	3.30
Nd	4.90	252.0	7.33	108.7	5.93	412.0	236.0	251.0	3.89	193.0	304.0	765.0	279.0	75.0	16.70
Sm	3.79	95.3	7.51	44.9	6.71	160.0	110.6	96.70	2.86	80.10	132.1	277.5	106.30	27.70	9.30
Eu	0.96	51.00	2.32	19.6	0.44	78.80	48.20	53.20	0.73	44.20	68.7	141.8	55.0	12.46	0.91
Gd	8.56	127.0	12.26	63.4	12.65	208.0	198.0	131.3	7.40	108.0	224.0	385.0	150.0	41.80	29.80
Tb	2.47	29.10	3.57	16.50	4.46	48.10	54.3	32.20	2.56	27.70	55.8	93.0	38.20	11.70	9.06
Dy	26.10	273.0	36.3	154.0	51.40	433.0	502.0	284.0	29.40	240.0	479.0	772.0	351.0	108.7	101.2
Ho	9.26	93.8	14.06	49.1	20.04	142.0	162.0	84.20	11.30	69.90	141.0	222.3	101.0	36.60	37.18
Er	39.20	420.0	63.4	208.0	89.70	631.0	682.0	342.2	54.00	287.0	554.0	881.0	407.0	153.9	161.8
Tm	8.43	99.7	14.96	45.3	18.41	143.0	142.7	69.70	12.57	60.20	113.5	189.0	84.10	33.80	33.44
Yb	81.60	1032	145.6	421.0	165.7	1419	1375	596.0	123.8	566.0	1051	1808	764.0	318.0	298.2
Lu	16.64	224.0	32.2	87.1	33.29	305.0	276.0	110.8	28.01	110.0	211.0	365.7	143.0	62.70	61.7
Hf	3730	6591	6690	6320	6298	7197	6279	6929	7160	4895	6850	6370	6740	6690	6656
Ta	0.22	6.04	0.74	1.31	0.85	16.0	1.76	4.25	0.50	2.85	6.36	6.15	2.37	1.01	1.12
Pb	7.5	2050	19.2	58.9	20.5	693.0	96.3	85.0	13.8	245.0	191.0	720.0	114.0	30.3	15.6
Th	42.9	1255	129.0	420.0	75.2	6740	846.0	622.0	75.7	1230	1224	3640	1104	239.0	72.1
U	129.1	1426	328.2	564.0	189.7	2110	797.0	1485	288.1	687.0	1337	2000	1037	740.0	121.0

rX-gY: row X, grain Y. R: rim, C: core.

Table 3-4. Whole rock tracer radiogenic isotope compositions and calculated initial ε values, following Ickert (2013).

Sample	Type	t (Ga)	$^{176}Lu/^{177}Hf$	2σ	$^{176}Hf/^{177}Hf$	2σ	$^{147}Sm/^{144}Nd$	2σ	$^{143}Nd/^{144}Nd$	2σ	εHf_t	2σ	εNd_t	2σ
K-1	KRN ore	1.88					0.1002	0.0002	0.511277	0.000007			-3.30	0.49
K-6	KRN FW	1.88	0.021034	0.000042	0.282118	0.000006	0.1190	0.0002	0.511366	0.000007	-7.75	0.47	-6.11	0.57
KRN-11-03	KRN FW	1.88	0.025042	0.000050	0.282295	0.000007	0.0838	0.0002	0.510920	0.000007	-6.54	0.52	-6.33	0.42
KRN-11-03[1]	*KRN FW*	1.88	*0.025169*	*0.000050*	*0.282298*	*0.000008*					*-6.60*	*0.52*		
KRN-11-04	KRN FW alt	1.88	0.007022	0.000014	0.281796	0.000005	0.0973	0.0002	0.511079	0.000007	-1.39	0.35	-6.47	0.48
K-4	KRN HW	1.88					0.1172	0.0002	0.511316	0.000006			-6.66	0.55
KRN-11-05	KRN HW	1.88	0.008725	0.000017	0.281572	0.000005	0.1016	0.0002	0.511140	0.000007	-11.50	0.36	-6.32	0.49
KRN-11-06	KRN HW alt	1.88					0.1115	0.0002	0.511259	0.000007			-6.38	0.54
KRN-11-06[1]	*KRN HW alt*	1.88					0.1112	0.0002	0.511259	0.000007			-6.31	0.53
KRN-10-03	KRN dike	1.88					0.1195	0.0002	0.511435	0.000007			-4.88	0.57
KRN-12-01	KRN intr.	1.88	0.040405	0.000081	0.282783	0.000007	0.1271	0.0003	0.511456	0.000007	-8.71	0.69	-6.29	0.60
KRN-12-02	KRN intr.	1.88	0.007288	0.000015	0.281730	0.000004	0.1481	0.0003	0.511702	0.000007	-4.10	0.33	-6.57	0.69
KRN-12-03	KRN intr.	1.88	0.011764	0.000024	0.281771	0.000008	0.0947	0.0002	0.511049	0.000006	-8.31	0.43	-6.43	0.46
KRN-12-05	KRN intr.	1.88	0.007412	0.000015	0.281606	0.000004	0.0867	0.0002	0.510876	0.000007	-8.63	0.33	-7.89	0.43
NUK-10-01	NUK ap vein	1.88					0.0938	0.0002	0.511167	0.000007			-3.89	0.46
NUK-12-01	NUK FW	1.88	0.014185	0.000028	0.281876	0.000009	0.1061	0.0002	0.511208	0.000007	-7.64	0.47	-6.08	0.51
REK-09-01	REK ore	1.88					0.1108	0.0002	0.511275	0.000007			-5.90	0.53
REK-10-01	REK porph	1.88	0.001110	0.000002	0.281623	0.000005	0.0666	0.0001	0.510735	0.000008	-0.06	0.33	-5.78	0.37
REK-10-03B	REK peg vein	1.88					0.0924	0.0002	0.511171	0.000009			-3.48	0.47
REK-10-04	REK ore	1.88					0.0789	0.0002	0.511024	0.000006			-3.08	0.40
REK-10-05	REK FW	1.88	0.036451	0.000073	0.282709	0.000005	0.0908	0.0002	0.511143	0.000007	-6.31	0.62	-3.64	0.45
REK-12-01	REK porph	1.88	0.000977	0.000002	0.281674	0.000005	0.0655	0.0001	0.510715	0.000007	1.92	0.34	-5.90	0.35
HEN-10-01	HEN FW	1.88					0.0980	0.0002	0.511111	0.000010			-6.01	0.50
TUV-10-01	TUV ore	1.88					0.1753	0.0004	0.511753	0.000007			-12.18	0.81
TUV-10-03	TUV host	1.88	0.009108	0.000018	0.281700	0.000004	0.1079	0.0002	0.511244	0.000007	-7.47	0.34	-5.80	0.52

[1] duplicate analyses for quality control; KRN: Kiirunavaara, REK: Rektorn, NUK: Nukutus, TUV: Tuolluvaara; FW: footwall; HW: hanging wall, intr.: intrusion, porph: porphyry, peg: pegmatite

Table 3-5. Radiation damage calculation for zircon grains from samples KRN-12-03, K-1 and NUK-12-02 (Holland and Gottfried, 1955; Murakami et al., 1991), using Th and U concentrations from LA-ICPMS analyses and sample ages from Westhues et al. (2016). Dα = accumulated dose in a-decay events per milligram; accumulated radiation damage in zircon divided by Murakami et al. (1991) into three stages: (I) dominantly crystalline with only isolated point defects, (II) fewer crystalline and more aperiodic regions, and (III) completely aperiodic. In accordance with Nasdala et al. (2001), more realistic thresholds are used for the calculations here: Stage I: Dα < $1.5*10^5$, stage II: Dα ~ 1.5 to 4 $*10^5$, and stage III: Dα > 4 $*10^5$. Time when Dα ~ $1.5*10^5$ (stage II) was reached is approximated iteratively.

sample	grain	U (ppm)	Th (ppm)	Th/U	Dα today	Current stage	Time (Ma) when stage II was reached
KRN-12-03	r4g1	87.4	55.3	0.63	7.39E+14	I	
KRN-12-03	r3g1_rim	1107	612.9	0.55	9.23E+15	III	1520
KRN-12-03	r3g1_core	162	103	0.64	4.64E+14	I	
KRN-12-03	r2g3	83	54.8	0.66	2.39E+14	I	
KRN-12-03	r3g5	102.6	80.2	0.78	3.03E+14	I	
KRN-12-03	r4g2_core	196.1	118.9	0.61	5.59E+14	I	
KRN-12-03	r4g2_rim	848	1024	1.21	7.91E+15	III	1470
KRN-12-03	r3g2	685	2085	3.04	8.30E+15	III	1500
KRN-12-03	r2g2_core	260	1095	4.21	3.61E+15	III	1040
KRN-12-03	r2g2_rim	238	413	1.74	2.41E+15	II	630
K-1	r1g4	129.1	42.9	0.33	1.03E+15	I	
K-1	r1g8	1426	1255	0.88	1.26E+16	III	1620
K-1	r3g6	328.2	129	0.39	2.66E+15	II	730
K-1	r2g6	564	420	0.74	4.86E+15	III	1230
K-1	r1g7	189.7	75.2	0.40	1.54E+15	II	40
K-1	r2g3	2110	6740	3.19	2.60E+16	III	1760
K-1	r1g6	797	846	1.06	7.26E+15	III	1430
K-1	r1g1	1485	622	0.42	1.21E+16	III	1610
K-1	r2g1	288.1	75.7	0.26	2.27E+15	II	560
K-1	r3g1	687	1230	1.79	7.02E+15	III	1430
K-1	r3g2a	1337	1224	0.92	1.19E+16	III	1600
K-1	r3g2b	2000	3640	1.82	2.05E+16	III	1720
K-1	r4g2	1037	1104	1.06	9.45E+15	III	1540
K-1	r5g3	740	239	0.32	5.91E+15	III	1330
K-1	r5g2	121	72.1	0.60	1.02E+15	I	
K-1	r5g2	472	266	0.56	3.94E+15	III	1080
NUK-12-02	r1g3	264.9	114.4	0.43	2.16E+15	II	500
NUK-12-02	r1g5	175.8	64.1	0.36	1.41E+15	I	
NUK-12-02	r2g2_core	347	148.7	0.43	2.83E+15	II	780
NUK-12-02	r2g2_rim	124.3	31.26	0.25	9.79E+14	I	
NUK-12-02	r3g3_core	124.2	56	0.45	1.02E+15	I	
NUK-12-02	r3g3_dark rim	230.6	70.3	0.30	1.84E+15	II	280
NUK-12-02	r3g3_light rim	190.1	72.9	0.38	1.54E+15	I	
NUK-12-02	r4g1	179.1	80.2	0.45	1.46E+15	I	

4 Evidence for hydrothermal alteration and source regions for the Kiruna iron oxide apatite ore from zircon Hf and O isotopes

4.1 Abstract

Zircon grains from the Kiruna iron oxide apatite (IOA) ore bodies in northern Sweden are distinct in their Hf and O isotopic ratios compared to zircon grains from adjacent metavolcanic host rocks and related intrusions. Here, we combine these two isotopic systems on previously dated zircon grains to improve our understanding of these ore deposits with a long-debated origin. Contrasting theories for the formation of the Kiruna iron ores suggest either: 1) emplacement through immiscible silicate-iron oxide melts; or 2) transportation and deposition of iron by hydrothermal fluids.

Zircon from the metavolcanic host rocks and intrusions have oxygen isotopic ratios ($\delta^{18}O$ ~3‰) that lie below typical magmatic compositions, which is evidence that roof rocks altered by meteoric water were digested into the magma. In contrast, the ores show an influence of a fluid that is higher in $\delta^{18}O$ (~7‰). Based on these findings, we propose the involvement of episodic magmatic-hydrothermal fluids in the ore genesis of the Kiruna iron ore deposits: 1) the first related to a deep-seated magmatism and to regional-scale metasomatic alteration; and 2) a later fluid event related to shallow intrusions and responsible for the ore formation. Distinct differences in the Hf isotopic ratios for host rocks and intrusions (εHf_i = −6 to −10, Archean crust) and ore (εHf_i = −5 to +3, depleted mantle) further allow us to screen possible fluid sources for their involvement in the ore process.

4.2 Introduction

The Hf and O isotopic systems can be combined for zircon analysis and used to decipher the origin and geologic history of a variety of types of rocks (e.g., Kemp et al., 2007; Iizuka et al., 2013). The potential of the Hf isotope system to distinguish between mantle- and crust-derived source regions has been recognized for over 30 years (e.g., Patchett et al., 1982), and zircon retains its Hf isotopic signature from the time it crystallized (Kinny and Maas, 2003). Oxygen isotopes of zircon give insights into magmatic processes, crustal growth, and the degree of rock-hydrothermal fluid interaction (Valley, 2003). Integrating these two isotopic systems with high-resolution in situ U-Pb dating is a powerful approach to understand the petrogenesis of rock units of otherwise elusive origins or to understand crustal evolution (e.g., Hawkesworth and Kemp, 2006; Kemp et al., 2007).

We use this approach to study the world-class iron ore deposits in the vicinity of Kiruna in the Norrbotten region of northern Sweden, the type locality of "Kiruna-type" deposits (e.g., Parák, 1975). The massive 2500 Mt ore body with iron grades of 50 to 60% at Kiirunavaara (the main deposit located in the town of Kiruna, Fig. 4-1) is hosted by Paleoproterozoic (ca. 1880 Ma) alkali altered metavolcanic rocks (Bergman et al., 2001) related to the Svecokarelian orogeny (ca. 1.9 - 1.8 Ga, Billström et al., 2010). During this orogeny, the whole Norrbotten region was intruded by suites of plutonic rocks, some of which are thought to be comagmatic with the metavolcanic rocks (Martinsson, 2004).

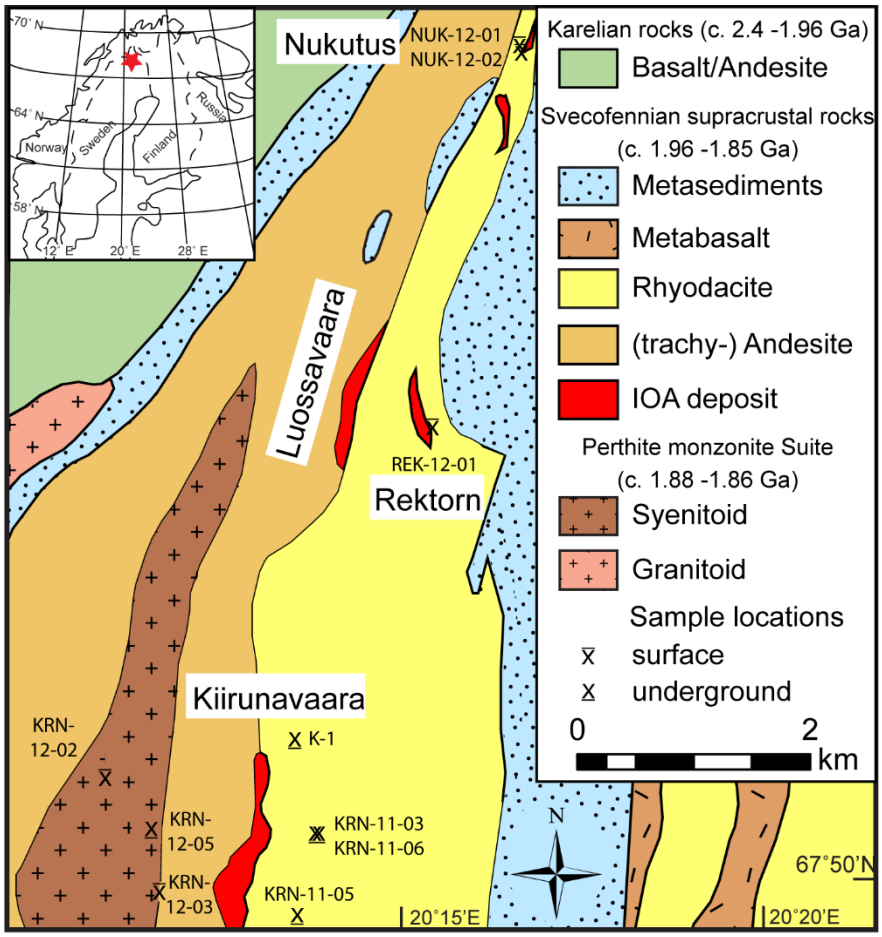

Figure 4-1. Geological map of the Kiruna area, modified from Bergman et al. (2001) and Westhues et al. (2016). Iron ore bodies are hosted by Svecofennian metavolcanic rocks that are underlain by Archean Greenstone Group and intruded by the Paleoproterozoic Perthite Monzonite Suite. Underground sample are projected to the surface, and appear east of the ore body due to its eastward dip.

Different authors have suggested a magmatic (Geijer, 1910; Frietsch, 1978), a sedimentary-exhalative (Parák, 1975), or hydrothermal origin (Hitzman et al., 1992) for these iron deposits. Similarities in the ore mineralogy and the prevalent host rock alteration have led to the suggestion that they are related to the iron oxide copper gold type of deposits (IOCG, e.g. Hitzman et al., 1992) and represent a subgroup, often called iron oxide apatite deposits (IOA, e.g., Williams, 2009). Detailed descriptions of the regional geology can be found in Bergman et al. (2001) and Westhues et al. (2016).

To better understand the genesis of these ores, the Hf and O isotopic compositions were determined in situ on previously dated zircon crystals (Westhues et al., 2016) from the iron ores, their host rocks, and some nearby related plutonic intrusions in the Kiruna area (Appendix C). We chose samples from two ore bodies in the Kiruna area (K-1 from the main ore body at Kiirunavaara, 1874 Ma, and NUK-12-02 from the smaller nearby Nukutus ore body, 1877 Ma) both of which contained abundant zircon crystals. We also included the trachyandesitic footwall (KRN-11–03, 1884 Ma) at Kiirunavaara, which is intruded by a syenite-aplite (KRN-12–03, KRN-12–02, 1880 Ma) and a granite (KRN-12–05, 1874 Ma). The rhyodacite hanging wall at Kiirunavaara (KRN-11–05, KRN-11–06, 1880 Ma), the rhyodacite footwall of the Nukutus deposit (NUK-12–01, 1882 Ma) were also part of this study. Further, the host rock of the Rektorn deposit (REK-12–01, 1876 Ma) was included, which shows a high degree of hydrothermal alteration in appearance and whole rock chemistry and has been interpreted to record extensive metasomatism caused by the infiltration of hydrothermal fluids (Westhues et al., 2016).

4.3 In situ Hf and O isotope results

Zircon grains from the metavolcanic host rocks and intrusions are numerous and show typical magmatic zoning, while zircon is rare in the ore samples and shows distinct core and rim regions (representative CL images in Fig. 4-2 and in Appendix C, Fig. 8-1). The ore zircon grains likely have been overprinted by hydrothermal alteration, as preliminary results of electron microprobe and Fourier transform infrared analyses indicate (Hanchar et al., 2015 and chapter 3). The O isotopic composition ($^{18}O/^{16}O$, reported as $\delta^{18}O_{VSMOW}$, details in Appendix C) was measured on zircon grains that were found to be 95% concordant or higher since zones with discordant U-Pb analyses are likely to have a disturbed $\delta^{18}O$, as well. Lu-Hf ratios were determined subsequently on the same region of the grains from which O was previously measured, and are reported as initial epsilon Hf (εHf_i) values (see Appendix C). Features such as cracks and inclusions of other minerals have been carefully avoided.

Zircon from the oldest sample in this study, the footwall of the Kiirunavaara ore (ca. 1884 Ma), has $\delta^{18}O$ values from 5.1 to 7.1‰ (Fig. 4-2a), which suggests the zircon grew in equilibrium with a mantle melt (Valley et al., 2005). Lower $\delta^{18}O$ values from 2.5 to 4.7 ‰ are found in zircon from the ca. 1880 Ma hanging wall of the Kiirunavaara ore deposit, the host rock of Nukutus ore (ca. 1881 Ma), syenite and aplite (ca. 1880 Ma), and granite intrusions (ca. 1874 Ma). Zircon grains from all these samples, including the Kiirunavaara footwall, have non-radiogenic Hf values (Fig. 4-2b), most analyses fall within a relatively narrow εHf_i range from -8.7 to -5.7.

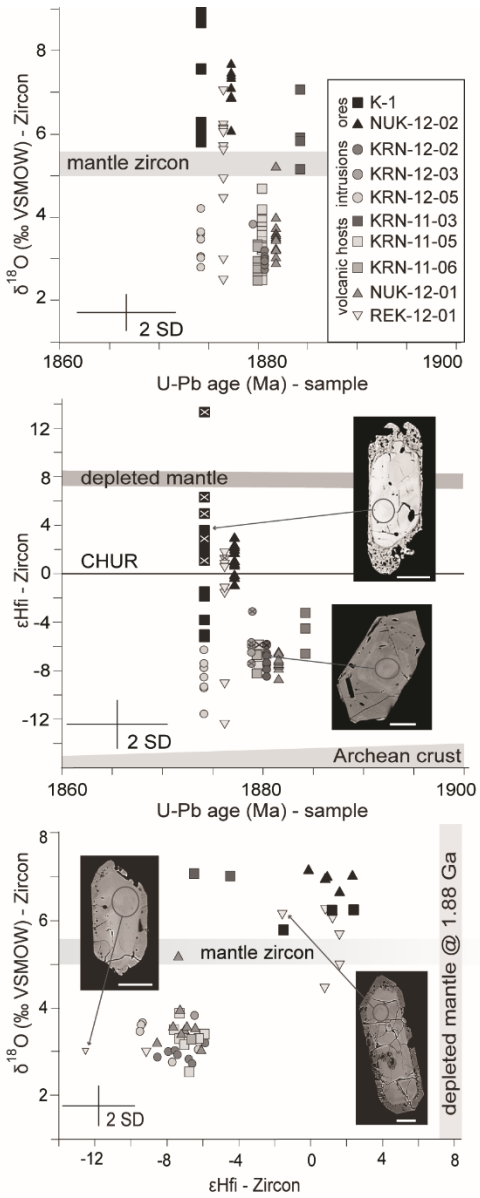

Figure 4-2. Zircon oxygen and Hf isotopic results (details in Appendix C): A) U-Pb age of each sample (concordia or weighted mean) vs. $\delta^{18}O$ (‰, VSMOW) of individual zircon grains. Value of typical mantle zircon (Valley, 2003) is plotted for comparison. B) U-Pb age vs. εHf_i: The εHf_i value has been calculated at the concordia or weighted mean age of each sample. Analyses done in spots with larger than 10% discordance have been marked with an "x". Mantle array is after Vervoort et al. (1999) and values for Archean crust are calculated based on Hf data from Archean gneiss in Scandinavia (Valley, 2001). BSE images of one grain from K-1 (ore) and KRN-11-05 (host) show their distinct textures (scale 50 μm, grey circle represents Hf laser analyses). C) Combing $\delta^{18}O$ (‰, VSMOW) and εHf_i values of individual zircon grains shows a clear contrast between ore zircon grains and zircon from host rocks and intrusions. Exceptions are the zircon grains from the Kiirunavaara footwall with Hf signature similar to other host rocks, but higher $\delta^{18}O$ values. Representative BSE images of the two different zircon populations from sample REK-12-01 and their corresponding results are shown.

Zircon from the main Kiirunavaara ore body (ca. 1874 Ma) and the smaller Nukutus ore body (ca. 1877 Ma) have consistently high $\delta^{18}O$ values ranging from 5.5 to 8.9 ‰. Their Hf isotopic signatures also differ from those of the host rocks, with the Nukutus ore having a narrow range from εHf_i = -1 to +2.9 and the Kiirunavaara ore with a larger range from εHf_i = -5.1 to 13.3. The host rock of the smaller Rektorn deposit (ca. 1876 Ma) shows a high degree of hydrothermal alteration in appearance and whole rock chemistry (see Chapter 3). This sample has been interpreted to record extensive metasomatism caused by the infiltration of hydrothermal fluids (Westhues et al., 2016). Zircon grains from this sample show the largest range of both $\delta^{18}O$ values (2.5 to 7.1 ‰) and εHf_i values; most analyses overlap within the range of the ore zircon (εHf_i =-1.6 to +1.6) and have higher $\delta^{18}O$; these grains are highly fractured and commonly exhibit distinct rims. Two grains with only a few internal zoning features have negative εHf_i and lower $\delta^{18}O$ values (Fig. 4-2c).

4.4 Discussion

4.4.1 Magmatic versus hydrothermal ore genesis based on oxygen isotopes

Considering the undisturbed primary growth zoning of the zircon grains from metavolcanic rocks and related intrusions, their unusually low $\delta^{18}O$ signature is regarded as primary magmatic. The close grouping of the results (Fig. 4-2c) suggests a common process in their formation. Values below the $\delta^{18}O$ composition of typical mantle zircon are generally thought to be related to high-temperature hydrothermally altered rocks (Taylor and Sheppard, 1986; Bindeman and Valley, 2001). Similar low values for magmatic zircon are known from only a few areas, such as the Yellowstone caldera (Bindeman and Valley,

2001). In studies of that region, magmatic activity resulted in a magmatically-driven hydrothermal fluid circulation cell; low $\delta^{18}O$ meteoric water infiltrated and exchanged with the surrounding rocks; then magma assimilating these rocks, and any crystallizing zircon, became lower $\delta^{18}O$. We argue that the low $\delta^{18}O$ ratios of zircon here require similar high T (>600 ºC) magmatic-hydrothermal fluids with low $\delta^{18}O$ values in the Kiruna system.

Evidence in favor of an origin for IOA deposits from immiscible iron oxide melts with a high temperature hydrothermal overprint has been presented for the Chilean iron oxide deposit El Laco (Tornos et al., 2016). Fe-rich spheroidal globules in a silica rich groundmass as evidence for melt immiscibility have yet to be documented at Kiruna. Our low $\delta^{18}O$ values of the zircon grains disagree with a solely immiscible iron oxide-silicate melt system. Magmatic fractionation of magnetite (low $\delta^{18}O$) leaves the residual melt with higher $\delta^{18}O$ (Taylor and Sheppard, 1986). Magnetite from Kiirunavaara, with $\delta^{18}O$ values reported from +2.2 to –0.7 ‰ (Nyström et al., 2008), could theoretically have been in equilibrium with a rhyolite magma with $\delta^{18}O$ values of 4.0–6.9 ‰ (see Appendix C, Table 8-9), not a magma with distinctively low $\delta^{18}O$ ratios. Our data cannot entirely exclude the existence of an immiscible iron oxide melt at Kiruna, or the magnetite floatation model proposed for the Los Colorados IOA deposit, Chile (Knipping et al., 2015). However, the magnetite $\delta^{18}O$ values reported cannot be achieved by fractionation of the ore from the metavolcanic host rocks or the intrusions.

The ore zircon grains from Kiruna and Nukutus instead have $\delta^{18}O$ values above the typical mantle range. Even though fewer analyses are available due to low zircon numbers in these samples, the results overlap between two separate ore deposits. If the ratio from

the ore zircon is regarded as magmatic, this difference to host rock zircon could reflect step-wise emplacement of magmas with different $\delta^{18}O$ values (e.g., Lackey et al., 2008). However, textural and geochemical evidence shows that the ore zircon grains have experienced post-crystallization hydrothermal alteration (Hanchar et al., 2015). Watson and Cherniak (1997) demonstrated that the original $\delta^{18}O$ can be disturbed under wet conditions and high temperatures. The two different zircon populations of the altered Rektorn host rock are evidence of this process (Fig. 2c): Few grains record the original magmatic ratio, whereas most overlap with the $\delta^{18}O$ ratios of the ore zircon grains. We suggest that these grains record the $\delta^{18}O$ ratio of the hydrothermal fluid that altered the zircon. Unlike the meteoric fluid involved in the formation of the host rock zircon grains with low $\delta^{18}O$ values, this fluid was high in $\delta^{18}O$ (6‰ or higher). Magnetite $\delta^{18}O$ values reported from Kiruna (-0.7 to +2.2 ‰, Nyström et al., 2008) can be achieved by crystallizing it from fluids at high T (>600 ºC) ranging from 4.5 to 7.4 ‰ (see Appendix C, Table 8-9), in good agreement with the isotopic composition recorded in the ore zircon here. A study from the Grängesberg IOA deposit in Central Sweden indicates that similar magmatic-hydrothermal fluids with $\delta^{18}O$ values > 5 ‰ could be responsible for magnetite crystallization there (Jonsson et al., 2013), and comparable $\delta^{18}O$ compositions for fluids depositing magnetite are found in IOCG deposits (e.g., Dreher et al., 2008). Whereas zircon has preserved the original magmatic ratio (low $\delta^{18}O$) in hanging wall and intrusions, whole rock O isotopic analyses reflect the highly altered major minerals (e.g., feldspars), ranging from 6.4‰ for the syenite intrusion to 8.3‰ for the hanging wall of Kiirunavaara ore body (Blake, 1992). These whole rock ratios can be achieved by fluids with temperatures ranging from 600 to

800 ºC, but not with lower temperature processes (see calculations in Appendix C, Table 8-10). We propose that a magmatic-hydrothermal fluid, recorded by zircon in ore and altered host rock, is responsible for transporting dissolved iron (+ Cl, F, P, rare earth elements) at Kiruna and altered the surrounding host rocks.

4.4.2 Hf isotopes and source regions

Similar to a study on zircon grains from the Adirondack IOA deposits (Valley et al., 2010), the Hf isotopic compositions show strong contrasts between zircon from ore and from host rocks. In Kiruna, the relatively tight cluster formed by the zircon from the host rocks and intrusions (Fig. 4-b) has a εHf_i composition similar to an Archean crust (Patchett et al., 1982), suggesting crustal melting within the Archean basement. The zircon grains from the ore bodies and the altered host rock of the Rektorn deposit, however, have Hf isotopic ratios that are either related to a direct influence of the depleted mantle, or the incorporation of material with such a Hf isotopic ratio. In the Kiruna area, a possible source are the rocks of the Archean Kiruna greenstone belt (e.g., Bergman et al., 2001), mostly mafic volcanic rocks formed during a period of rifting, that lie stratigraphically below the succession that contains the ore (Fig. 4-1). No whole-rock or mineral Hf data exist for the greenstone belt rocks, but they are expected to have an depleted mantle signature, similar to their Nd isotopic composition (Skiöld and Cliff, 1984). This unit is depleted in Fe especially in the Kiruna area and has previously been suggested to be a source of the Fe in the Kiruna ores (Parák, 1985).

4.4.3 Model for the formation of the Kiruna iron ores

Recent models for the formation of IOCG deposits (e.g., Porter, 2010) suggest episodic alteration, with deep sodic-calcic ± iron and shallow iron-potassic-calcic and Cu-rich alteration, to explain zonation observed in this endmember (Hitzman et al., 1992). Albitization of the adjacent rocks may be essential for the liberation of Fe and K (Dilles and Einaudi, 1992; Oliver et al., 2004). Based on the oxygen isotopic ratios of the zircon analyzed in this study, we propose a similar episodic nature of alteration with two fluids of different $\delta^{18}O$ composition for the Kiruna IOA deposits (Fig. 4-3a, b): 1) The footwall recorded the isotopic composition of the magma at ca.1884 Ma ($\delta^{18}O$ of ~6‰, εHf_i –2.5 to –6), indicating melting of Archean crustal material; 2) The magmatism drove a regional-scale high T hydrothermal fluid alteration system and the input of meteoric water lowered the $\delta^{18}O$ of the surrounding rocks; 3); some altered rocks became incorporated into the magma, lowering its overall $\delta^{18}O$; 4) These low $\delta^{18}O$ values were recorded in the zircon from the rhyodacite hanging wall (average $\delta^{18}O$ ~3.4 ‰), the syenite ($\delta^{18}O$ ~3.0‰) and the granite ($\delta^{18}O$ ~3.4 ‰). 5) A second, more localized hydrothermal fluid system infiltrated after 1880 Ma, probably related to the 1874 Ma granite intrusion. This magmatic-hydrothermal fluid transported dissolved iron at temperatures from 600 to 800 ºC (see Appendix C, Table 8-10). The overlap in the Hf isotopic ratio of zircon from 1884 to 1874 Ma indicates melting of the Archean crust as a common source for the metavolcanic host rocks and the intrusions. The distinct Hf ratios of the ore zircon grains indicate that the iron was not sourced from the adjacent host rock or intrusions. More likely, the nearby mafic Archean Kiruna greenstone group was a major source of the iron. The iron was deposited

in the large Kiirunavaara deposit at 1874 Ma, between the two volcanic units, and in the smaller deposits such as Nukutus and Rektorn.

4.5 Conclusions

The combination of Hf and O isotopes in zircon grains, a powerful tool for providing insights into complex rock histories, has been applied to the long-debated Kiruna iron ore system. The oxygen isotope data presented here argues for the involvement of high temperature magmatic-hydrothermal fluids of different isotopic composition in: a) the alteration of the host rocks; and b) the formation of the ore bodies. Zircon grains from two different ore bodies have Hf isotopic compositions with a depleted mantle influence that is not present in host rocks and nearby intrusions. Combining these findings, we suggest an interpretation that involves two stages of magmatic-hydrothermal fluids and a source for the iron ores that differs isotopically from their host rocks, potentially the Archean Kiruna Greenstone Group underlying the succession hosting the ore.

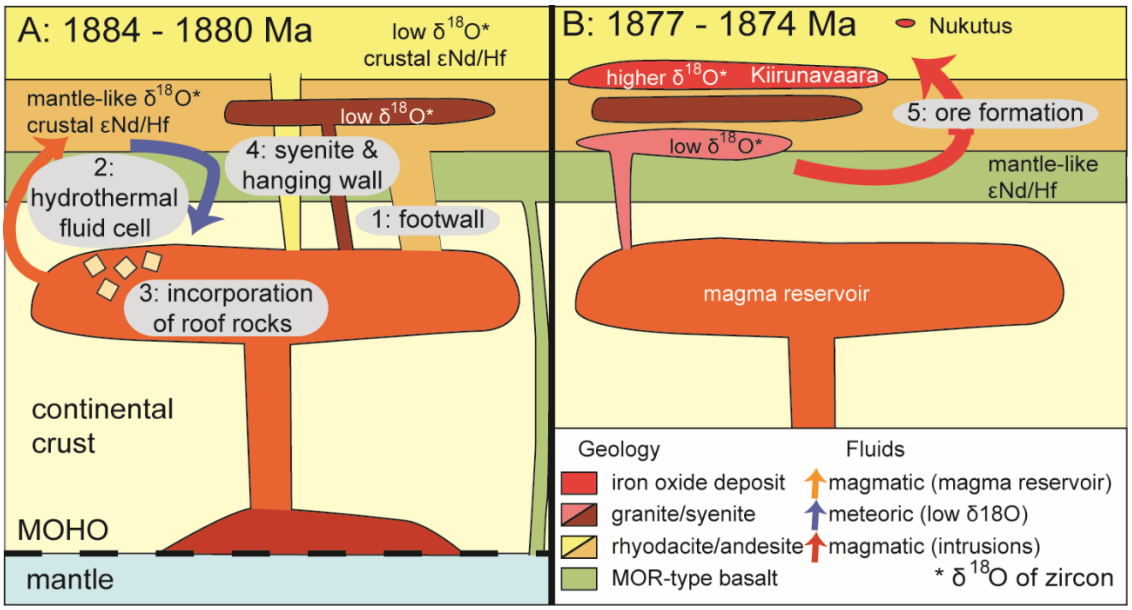

Figure 4-3. Schematic diagram illustrating the possible formation of the Kiruna iron ore deposits by magmatic-hydrothermal processes at 1884-1880 Ma (A) and 1877 -1874 Ma (B) based on the new Hf and oxygen data, not to scale. 1-5 represent steps in the evolution in a magmatic-hydrothermal scenario, see text for details.

4.6 Acknowledgements

Funded by NSERC Canada Discovery Grant to JMH, and SEG and MAC research grants to AW. We acknowledge the help of O. Martinsson; K. Lindén and others from the NordSIM facility; and R. Lam, P. King and others at MUN. We also thank LKAB, especially K. Holme, and members of the Geological Survey of Sweden. Comments of Garry Davidson, Jade Star Lackey and Adam Simon on an earlier version dramatically improved the manuscript. Brendan Murphy is thanked for editorial handling.

4.7 Bibliography – Chapter four

Bergman, S., Kübler, L., and Martinsson, O., 2001, Description of regional geological and geophysical maps of northern Norrbotten County (east of the Caledonian Orogen), Sveriges Geologiska Undersökning, Ba 56, 110 pp.

Billström, K., Eilu, P., Martinsson, O., Niiranen, T., Broman, C., Weihed, P., Wanhainen, C., and Ojala, J., 2010, IOCG and related deposits of the Northern Fennoscandian Shield, *in* Porter, T. M., ed., Hydrothermal iron oxide copper-gold and related deposits: a global perspective, 4: Adelaide, PGC Publishing, p. 415-426.

Bindeman, I. N., and Valley, J. W., 2001, Low-$\delta^{18}O$ rhyolites from Yellowstone: Magmatic evolution based on analyses of zircons and individual phenocrysts: Journal of Petrology, v. 42, p. 1491-1517.

Blake, K. L., 1992, The petrology, geochemistry and association to ore formation of the host rocks of the Kiirunavaara magnetite-apatite deposit, northern Sweden: Unpub. PhD thesis, University of Wales, 349 pp.

Dilles, J. H., and Einaudi, M. T., 1992, Wall-rock alteration and hydrothermal flow paths about the Ann-Mason porphyry copper deposit, Nevada; a 6-km vertical reconstruction: Economic Geology, v. 87, p. 1963-2001.

Dreher, A., Xavier, R., Taylor, B., and Martini, S., 2008, New geologic, fluid inclusion and stable isotope studies on the controversial Igarapé Bahia Cu–Au deposit, Carajás Province, Brazil: Mineralium Deposita, v. 43, p. 161-184.

Frietsch, R., 1978, On the magmatic origin of iron ores of the Kiruna type: Economic Geology, v. 73, p. 478-485.

Geijer, P., 1910, Igneous rocks and iron ores of Kiirunavaara, Luossavaara and Tuolluvaara: Economic Geology, v. 5, p. 699-718.

Hanchar, J. M., Westhues, A., Voisey, C. M., Whitehouse, M. J., and Rossman, G. R., 2015, U-Pb, Hf, O, trace element, and H_2O, constraints for the Kiruna apatite iron oxide deposits, Sweden: 25th Goldschmidt conference, Prague, Aug 16-21, Abstract 1166.

Hawkesworth, C. J., and Kemp, A. I. S., 2006, Using hafnium and oxygen isotopes in zircons to unravel the record of crustal evolution: Chemical Geology, v. 226, p. 144-162.

Hitzman, M. W., Oreskes, N., and Einaudi, M. T., 1992, Geological characteristics and tectonic setting of Proterozoic iron oxide (Cu-U-Au-Ree) deposits: Precambrian Research, v. 58, p. 241-287.

Iizuka, T., Campbell, I. H., Allen, C. M., Gill, J. B., Maruyama, S., and Makoka, F., 2013, Evolution of the African continental crust as recorded by U–Pb, Lu–Hf and O isotopes in detrital zircons from modern rivers: Geochimica Et Cosmochimica Acta, v. 107, p. 96-120.

Jonsson, E., Troll, V. R., Högdahl, K., Harris, C., Weis, F., Nilsson, K. P., and Skelton, A., 2013, Magmatic origin of giant ˜Kiruna-type" apatite-iron-oxide ores in Central Sweden: Scientific Reports, v. 3.

Kemp, A. I. S., Hawkesworth, C. J., Foster, G. L., Paterson, B. A., Woodhead, J. D., Hergt, J. M., Gray, C. M., and Whitehouse, M. J., 2007, Magmatic and crustal differentiation history of granitic rocks from Hf-O isotopes in zircon: Science, v. 315, p. 980-983.

Kinny, P., and Maas, R., 2003, Lu–Hf and Sm–Nd isotope systems in zircon: Reviews in Mineralogy and Geochemistry, v. 53, p. 327-341.

Knipping, J. L., Bilenker, L. D., Simon, A. C., Reich, M., Barra, F., Deditius, A. P., Lundstrom, C., Bindeman, I., and Munizaga, R., 2015, Giant Kiruna-type deposits form by efficient flotation of magmatic magnetite suspensions: Geology, v. 43, p. 591-594.

Lackey, J. S., Valley, J. W., Chen, J. H., and Stockli, D. F., 2008, Dynamic magma systems, crustal recycling, and alteration in the central Sierra Nevada batholith: the oxygen isotope record: Journal of Petrology, v. 49, p. 1397-1426.

Martinsson, O., 2004, Geology and metallogeny of the northern Norrbotten Fe-Cu-Au province: Society of Economic Geologists, Guidebook Series, v. 33, p. 131-148.

Nyström, J. O., Billström, K., Henríquez, F., Fallick, A. E., and Naslund, H. R., 2008, Oxygen isotope composition of magnetite in iron ores of the Kiruna type in Chile and Sweden: Gff, v. 130, p. 177 - 188.

Oliver, N. H. S., Cleverley, J. S., Mark, G., Pollard, P. J., Fu, B., Marshall, L. J., Rubenach, M. J., Williams, P. J., and Baker, T., 2004, Modeling the role of sodic alteration in the genesis of iron oxide-copper-gold deposits, Eastern Mount Isa block, Australia: Economic Geology, v. 99, p. 1145-1176.

Parák, T., 1975, Kiruna iron ores are not 'intrusive-magmatic ores of the Kiruna type': Economic Geology, v. 70, p. 1242-1258.

Parák, T., 1985, Phosphorus in different types of ore, sulfides in the iron deposits, and the type and origin of ores at Kiruna: Economic Geology, v. 80, p. 646-665.

Patchett, P. J., Kouvo, O., Hedge, C. E., and Tatsumoto, M., 1982, Evolution of continental crust and mantle heterogeneity: Evidence from Hf isotopes: Contributions to Mineralogy and Petrology, v. 78, p. 279-297.

Porter, T. M., 2010, Current understanding of iron oxide associated-alkali altered mineralised systems: Part I - An overview, *in* Porter, T. M., ed., Hydrothermal iron oxide copper-gold and related deposits: a global perspective, 3: Adelaide, PGC Publishing, p. 5-32.

Skiöld, T., and Cliff, R. A., 1984, Sm-Nd and U-Pb dating of Early Proterozoic mafic-felsic volcanism in northernmost Sweden: Precambrian Research, v. 26, p. 1-13.

Taylor, B. E., and Sheppard, S. M. F., 1986, Igneous rocks: 1. Processes of isotopic fractionation and isotopic systematics, *in* Valley, J. W., Taylor, H. P., Jr., and O'Neil, J. R., eds., Stable Isotopes in High Temperature Geological Processes. Reviews in Mineralogy, 16: Washington, DC, United States, Mineralogical Society of America, p. 227-271.

Tornos, F., Velasco, F., and Hanchar, J. M., 2016, Iron-rich melts, magmatic magnetite, and superheated hydrothermal systems: The El Laco deposit, Chile: Geology, v. 44, p. 427-430.

Valley, J. W., 2001, Stable isotope thermometry at high temperatures, *in* Valley, J. W., and Cole, D. R., eds., Stable isotope geochemistry, Reviews in Mineralogy and Geochemistry, 43: Washington, DC, Mineralogical Society of America/Geochemical Society, p. 365-413.

Valley, J. W., 2003, Oxygen isotopes in zircon, *in* Hanchar, J. M., and Hoskin, P. W. O., eds., Zircon, Reviews in Mineralogy and Geochemistry, 53: Washington, DC, Mineralogical Society of America/Geochemical Society, p. 343-385.

Valley, J. W., Lackey, J. S., Cavosie, A. J., Clechenko, C. C., Spicuzza, M. J., Basei, M. A. S., Bindeman, I. N., Ferreira, V. P., Sial, A. N., King, E. M., Peck, W. H., Sinha, A. K., and Wei, C. S., 2005, 4.4 billion years of crustal maturation: oxygen isotope ratios of magmatic zircon: Contributions to Mineralogy and Petrology, v. 150, p. 561-580.

Valley, P. M., Fisher, C. M., Hanchar, J. M., Lam, R., and Tubrett, M., 2010, Hafnium isotopes in zircon: A tracer of fluid-rock interaction during magnetite-apatite ("Kiruna-type") mineralization: Chemical Geology, v. 275, p. 208-220.

Vervoort, J. D., Patchett, P. J., Blichert-Toft, J., and Albarède, F., 1999, Relationships between Lu-Hf and Sm-Nd isotopic systems in the global sedimentary system: Earth and Planetary Science Letters, v. 168, p. 79-99.

Watson, E. B., and Cherniak, D. J., 1997, Oxygen diffusion in zircon: Earth and Planetary Science Letters, v. 148, p. 527-544.

Westhues, A., Hanchar, J. M., Whitehouse, M. J., and Martinsson, O., 2016, New constraints on the timing of host rock emplacement, hydrothermal alteration, and iron oxide-apatite mineralization in the Kiruna district, Norrbotten, Sweden: Economic Geology v. 111, p. 1595-1618.

Williams, P. J., 2009, Classifying IOCG deposits, *in* Corriveau, L., and Mumin, A. H., eds., Exploring for iron oxide copper-gold deposits: Canada and global analogues. Geological Association of Canada, Short Course Notes, 20, p. 89-110.

5 Summary and Outlook

5.1 Implications of results of this project for the origin of the Kiruna IOA deposits

The origin of the massive Kiirunavaara IOA orebody in northern Sweden has been debated for over a century. Results from this PhD project bring new evidence in this long-standing debate, using an array of geochemical methods on whole rock and mineral scale. New zircon U-Pb geochronology, as presented in chapter two (Westhues et al., 2016), the first to date the iron ore directly, suggests an epigenetic origin of the ore, possibly contemporaneous with the intrusion of a granitic body. The metavolcanic footwall and hanging wall of the Kiirunavaara iron ore body have been dated to ca. 1884 and 1880 Ma, respectively. The Kiirunavaara and Nukutus ore bodies have been dated at ca. 1877 to 1874 Ma, in close overlap by the intrusion of a granite at 1874 Ma. Magmatic-hydrothermal fluids (>600°C) provided by the emplacement of this granite and a syenite at ca. 1880 Ma are potential candidates to alter existing ores and mobilize dissolved iron. A magmatic-hydrothermal fluid system can explain many features observed in the iron oxide deposits at Kiruna, for example the intense metasomatic alteration of the host rocks, which was also studied in greater detail in chapter two.

The zircon grains, which the U-Pb geochronology is based on, were studied further and the results are reported in chapter three. Together with monazite and whole rock data, the complex fluid alteration story of the Kiruna area can be demonstrated. The zircon grains from the ore bodies show distinctive hydrothermal features, which are strong evidence for the involvement of high temperature fluids that have already been suggested based on

results of chapter two. Zircon grains from intrusive samples also show hydrothermal textural and chemical features, indicating influences of hydrothermal fluids, potentially late stage magmatic fluids. The isotopic systems Lu-Hf and Sm-Nd, on whole grain and mineral scale, show distinct differences between host rocks (crustal influence) and ores (evidence of depleted mantle influence), suggesting a region with depleted mantle signature, such as the Kiruna greenstones, as potential source for the ores.

Later alteration periods influencing the ores are recorded by monazite at ca. 1738 and 1628 Ma, up to 250 million years after the formation of host rocks and ores. Earlier studies reported disturbances in Sm-Nd, Sr and Pb isotopic systems in the Kiruna area up to 1500 Ma (Cliff and Rickard, 1992). In the Malmberget region, ca. 1890-1870 Ma old volcanic and plutonic rocks are intruded by granites with ages of ca. 1800 Ma that are related to the amphibolite-grade metamorphism (e.g., Skiöld, 1987). Monazite, titanite, and apatite from late stage veins give distinct younger ages: ca. 1740 Ma for monazite, 1620-1613 Ma for titanite, and 1620-1600 for apatite (Romer, 1996). These authors interpret these ages to be related to hydrothermal activity, similar to our interpretations, which may be related to tectonic reactivation of older structures. The relation of these events to the iron ore formation remains unclear, but some of the iron oxide could have been remobilized at those times.

In chapter four, oxygen and Hf isotope ratios of zircon show further interesting differences between ore and host rocks (Westhues et al., 2017). Zircon grains from the host rocks have unusually low $\delta^{18}O$ signatures, which are only known from a few other localities worldwide, such as the Yellowstone caldera (e.g., Bindeman and Valley, 2001). These data

are strong arguments for the involvement of high temperature magmatic-hydrothermal fluids in the formation and alteration of the host rocks of the IOA deposits in Kiruna. The Hf isotopic data further shows a depleted mantle signature in zircon from two distinct ore bodies that is not present in the host rocks, which have a clear crustal influence instead. The depleted mantle signature is also recorded in the whole rock Sm-Nd data of ore samples, as presented in chapter three. The combination of isotopic information from Sm-Nd and Lu-Hf data suggests a source of the ores different from their host rocks, which could lie in the underlying Archean Kiruna Greenstone. The oxygen and hafnium data are used to propose a model for the formation of the Kiruna IOA ores that involves two stages of magmatic-hydrothermal fluids at temperatures.

In conclusion, the data presented here are in favor of an epigenetic ore formation process for the Kiruna IOA deposits involving hydrothermal fluids that were active only shortly after the host rock were formed. It should be emphasized that these fluids are suggested to be at high temperatures (> 600 ºC) at the magmatic-to-hydrothermal transition, possibly exsolved from the nearby intrusions, in contrast to a low temperature sedimentary-exhalative origin suggested earlier (Parák, 1975). A purely magmatic origin seems unlikely for the Kiruna iron oxide ores in comparison with the chemical composition of nelsonites (see chapter two) and existing experimental data on the silicate – iron liquid immiscibility gap (Philpotts, 1967; Charlier and Grove, 2012). The strong evidence for the influence of metasomatism in Kiruna, such as the distinctively low oxygen composition, is best explained by invoking magmatic-hydrothermal fluids.

5.2 Comparisons with IOA and IOCG deposits worldwide, open questions, and suggested further research

The results of this PhD project highlight the importance of hydrothermal processes in the formation of the Kiruna IOA deposits, as summarized above. However, for the El Laco deposit, a recent model combines a magmatic origin with an hydrothermal overprint to explain many of the observed features (Tornos et al., 2016). Unequivocal evidence for melt immiscibility, such as Fe-rich spheroidal globules in a silica rich groundmass as are presented for El Laco(Velasco et al., 2016), have not been found in our Kiruna samples and are not reported elsewhere. Nevertheless, the existence of an immiscible iron oxide melt at Kiruna at some stage during the formation cannot be excluded beyond doubt, but hydrothermal fluids are the preferred mechanism for the formation of these large deposits. One remaining question is therefore whether the assumption that El Laco represents a younger analogue of a Kiruna-type deposit is correct. While the IOA deposits at Kiruna are epigenetic, show brecciated contacts to their volcanic host rocks, and have formed at some depth, El Laco formed at the surface and shows a strong resemblance to lava flows.

Other deposits classified as IOA, such as Pea Ridge and related deposits in Missouri, USA (Nuelle et al., 1992; Aleinikoff et al., 2016; Slack et al., 2016) or in the Great Bear magmatic zone, Canada (Corriveau et al., 2016) show more convincing similarities with Kiruna. These include brecciation and veining of the ore into its host rocks, the presence of actinolite as a gangue mineral and large-scale alteration of the host rocks. Interestingly, similar to the interpretations for Kiruna, at least two fluid phases have been shown to be active at Pea Ridge (Johnson et al., 2016), and episodic hydrothermal fluids have also been

reported for the Carajás IOCG Province, Brazil (Moreto et al., 2015). Multiple fluid phases may represent another unifying feature and could potentially be of importance in the genesis of these massive and large deposits. Instead of a hydrothermal overprint or minor redistribution of the ore, these events could be responsible for upgrading the iron ores to their present size. Further research is suggested to focus on these late stage overprints, using for instance radiogenic and stable isotopic systems in combination with detailed dating (U-Pb, Re-Os) of later phases in a systematic manner among several IOA districts.

There are only few fluid inclusion studies available for Kiruna, which would help to understand the salinities and temperatures of the active hydrothermal fluids in these deposits and could be compared with results from other IOA and IOCG districts. A recent study of fluid inclusions and thermometry at the Pea Ridge IOA deposit (Hofstra et al., 2016), for instance, showed the importance of magmatic-hydrothermal fluids in the formation of the iron oxide apatite mineralization there. Further, multi-element analysis of fluid inclusion by LA-ICPMS is becoming a more widely available technique (Wagner et al., 2016) and would provide vital clues on the composition of the hydrothermal fluids involved in the formation of IOA deposits. Additional temperature constraints, in addition to our estimates based on oxygen isotopes (Chapter four), and pressure/depth constraints, which are interesting for understanding the precipitation mechanism of IOA deposits, could be studied using geothermobarometers, such as Ti-in-zircon (Ferry and Watson, 2007) or Zr-in-titanite (Hayden et al., 2008).

Another open question is the relation between IOCG deposits sensu stricto and IOA deposits, which may represent end members of iron oxide-alkali altered systems with

differences in mineralization (mainly content of Cu and Au) due to varying depth and/or timing of mineralization, or supply of reduced sulphur as "trap" for Cu sulphides. There is a range of deposits like Kiruna in Northern Sweden with regional alteration, large tonnages of magnetite-apatite mineralization and minor Cu-sulfides to deposits like Olympic Dam with high Cu grades in a similar alteration environment. Most authors agree that both IOCG and IOA deposits are temporally related to magmatism (e.g., Williams, 2009; Dill, 2010; Groves et al., 2010). In many provinces with iron oxide-alkali altered systems, large batholitic complexes that are broadly coeval with the mineralization are present (Porter, 2010). Our new U-Pb data for Kiruna show that at least some of these intrusions are contemporaneous with the ore formation and likely related to their formation. This could be tested for other IOA and IOCG deposits as well.

The most recent models for the formation of IOCG deposits (e.g., Porter, 2010; Williams et al., 2010) invoke episodic alteration involving two or more hydrothermal fluids, usually an early sodic-calcic±iron and a later iron-potassic-calcic alteration stage. In our model presented in chapter four, we suggest that at least two hydrothermal fluid phases were active in the Kiruna area. The sodic alteration predates the major iron oxide (and IOCG sensu stricto) mineralization and may be responsible for removing base and ferrous metals from the host (Williams, 1994; Oliver et al., 2004). The availability of sulfur (deep-sourced magmatic and/or surface derived), crucial for precipitating Cu-sulfides, may explain the difference in IOCG and IOA deposits (Perring et al., 2000; Barton and Johnson, 2004). The question of whether IOA deposits represent incompletely developed IOCG

deposits will remain a topic for further research. A progressive development from barren iron oxide apatite mineralization to IOCG deposits sensu stricto is possible.

Another remaining question concerns the tectonic setting of IOCG and IOA deposits. First suggestions for the tectonic setting of IOCG placed them in a continental regime in areas of extension and rifting (Hitzman et al., 1992). Extensional fractures may act as pathways for the altering and mineralizing fluids of magmatic-hydrothermal character. IOA deposits like Kiirunavaara in Northern Sweden are supposed to have formed in a late-stage magmatic continental arc setting (e.g., Martinsson, 2004). Also, numerous IOCG and IOA deposits are found in the Coastal Cordillera of northern Chile and southern Peru in a subduction-related magmatic arc setting (e.g., Sillitoe, 2003). More recently, the observed magmatic features in IOCG provinces are attributed to anorogenic settings rather than (late-stage) extensional subduction zone settings, and Groves et al. (2010) connect the distribution of the major IOCG sensu stricto to the stability phases of supercontinents (Proterozoic Columbia and Rodinia, Pangea). Our zircon oxygen isotope data in chapter four shows similarities with the Yellowstone caldera region (e.g., Bindeman and Valley, 2001) and highlights the magmatic-hydrothermal processes active at Kiruna. It would be interesting to see if other IOA deposits, such as Pea Ridge in Missouri, show similar unusual oxygen isotopic composition in their zircon grains and how these results impact the current tectonic settings suggested for IOA deposits.

In conclusion, the data presented in this PhD thesis highlights the importance of magmatic-hydrothermal processes at the Kiruna IOA deposits, which is in agreement with recent studies at other IOA districts, such as the deposits in Missouri, or in the Great Bear

magmatic zone (e.g., Slack et al., 2016). However, there are still open questions regarding the relation of IOA deposits, IOCG deposits sensu stricto and the magmatic dominated El Laco deposit, which will remain a topic for further research.

5.3 Bibliography - Summary

Aleinikoff, J. N., Selby, D., Slack, J. F., Day, W. C., Pillers, R. M., Cosca, M. A., Seeger, C. M., Fanning, C. M., and Samson, I. M., 2016, U-Pb, Re-Os, and Ar/Ar geochronology of rare earth element (REE)-rich breccia pipes and associated host rocks from the Mesoproterozoic Pea Ridge Fe-REE-Au deposit, St. Francois Mountains, Missouri: Economic Geology, v. 111, p. 1883-1914.

Barton, M. D., and Johnson, D. A., 2004, Footprints of Fe-oxide(-Cu-Au) systems, SEG 2004: Predictive Mineral Discovery Under Cover. Centre for Global Metallogeny, Spec. Pub, 33, The University of Western Australia, p. 112-116.

Bindeman, I. N., and Valley, J. W., 2001, Low-$\delta^{18}O$ rhyolites from Yellowstone: Magmatic evolution based on analyses of zircons and individual phenocrysts: Journal of Petrology, v. 42, p. 1491-1517.

Charlier, B., and Grove, T., 2012, Experiments on liquid immiscibility along tholeiitic liquid lines of descent: Contributions to Mineralogy & Petrology, v. 164, p. 27-44.

Cliff, R. A., and Rickard, D., 1992, Isotope systematics of the Kiruna magnetite ores, Sweden: Part 2. Evidence for a secondary event 400 m.y. after ore formation: Economic Geology, v. 87, p. 1121-1129.

Corriveau, L., Montreuil, J.-F., and Potter, E. G., 2016, Alteration facies linkages among iron oxide copper-gold, iron oxide-apatite, and affiliated deposits in the Great Bear Magmatic Zone, Northwest Territories, Canada: Economic Geology, v. 111, p. 2045-2072.

Dill, H. G., 2010, The "chessboard" classification scheme of mineral deposits: Mineralogy and geology from aluminum to zirconium: Earth-Science Reviews, v. 100, p. 1-420.

Ferry, J. M., and Watson, E. B., 2007, New thermodynamic models and revised calibrations for the Ti-in-zircon and Zr-in-rutile thermometers: Contributions to Mineralogy and Petrology, v. 154, p. 429-437.

Groves, D. I., Bierlein, F. P., Meinert, L. D., and Hitzman, M. W., 2010, Iron oxide copper-gold (IOCG) deposits through Earth history: Implications for origin, lithospheric setting, and distinction from other epigenetic iron oxide deposits: Economic Geology, v. 105, p. 641-654.

Hayden, L. A., Watson, E. B., and Wark, D. A., 2008, A thermobarometer for sphene (titanite): Contributions to Mineralogy and Petrology, v. 155, p. 529-540.

Hitzman, M. W., Oreskes, N., and Einaudi, M. T., 1992, Geological characteristics and tectonic setting of Proterozoic iron oxide (Cu-U-Au-Ree) deposits: Precambrian Research, v. 58, p. 241-287.

Hofstra, A. H., Meighan, C. J., Song, X., Samson, I., Marsh, E. E., Lowers, H. A., Emsbo, P., and Hunt, A. G., 2016, Mineral thermometry and fluid inclusion studies of the Pea Ridge iron oxide-apatite–rare earth element deposit, Mesoproterozoic St. Francois Mountains Terrane, southeast Missouri, USA: Economic Geology, v. 111, p. 1985-2016.

Johnson, C. A., Day, W. C., and Rye, R. O., 2016, Oxygen, hydrogen, sulfur, and carbon isotopes in the Pea Ridge magnetite-apatite deposit, southeast Missouri, and sulfur

isotope comparisons to other iron deposits in the region: Economic Geology, v. 111, p. 2017-2032.

Martinsson, O., 2004, Geology and metallogeny of the northern Norrbotten Fe-Cu-Au province: Society of Economic Geologists, Guidebook Series, v. 33, p. 131-148.

Moreto, C. P. N., Monteiro, L. V. S., Xavier, R. P., Creaser, R. A., DuFrane, S. A., Tassinari, C. C. G., Sato, K., Kemp, A. I. S., and Amaral, W. S., 2015, Neoarchean and Paleoproterozoic iron oxide-copper-gold events at the Sossego deposit, Carajás Province, Brazil: Re-Os and U-Pb geochronological evidence: Economic Geology, v. 110, p. 809-835.

Nuelle, L. M., Day, W. C., Sidder, G. B., and Seeger, C. M., 1992, Geology and mineral paragenesis of the Pea Ridge iron ore mine, Washington County, Missouri - Origins of the rare-earth-element- and gold bearing breccia pipes: USGS Bulletin, v. 1989 A, p. A1-A11.

Oliver, N. H. S., Cleverley, J. S., Mark, G., Pollard, P. J., Fu, B., Marshall, L. J., Rubenach, M. J., Williams, P. J., and Baker, T., 2004, Modeling the role of sodic alteration in the genesis of iron oxide-copper-gold deposits, Eastern Mount Isa block, Australia: Economic Geology, v. 99, p. 1145-1176.

Parák, T., 1975, Kiruna iron ores are not 'intrusive-magmatic ores of the Kiruna type': Economic Geology, v. 70, p. 1242-1258.

Perring, C. S., Pollard, P. J., Dong, G., Nunn, A. J., and Blake, K. L., 2000, The Lightning Creek sill complex, Cloncurry district, northwest Queensland: A source of fluids for Fe oxide Cu-Au mineralization and sodic-calcic alteration: Economic Geology and the Bulletin of the Society of Economic Geologists, v. 95, p. 1067-1089.

Philpotts, A. R., 1967, Origin of certain iron-titanium oxide and apatite rocks: Economic Geology, v. 62, p. 303-315.

Porter, T. M., 2010, Current understanding of iron oxide associated-alkali altered mineralised systems: Part I - An overview, *in* Porter, T. M., ed., Hydrothermal iron oxide copper-gold and related deposits: a global perspective, 3: Adelaide, PGC Publishing, p. 5-32.

Romer, R. L., 1996, U-Pb systematics of stilbite-bearing low-temperature mineral assemblages from the Malmberget iron ore, northern Sweden: Geochimica Et Cosmochimica Acta, v. 60, p. 1951-1961.

Sillitoe, R. H., 2003, Iron oxide-copper-gold deposits: an Andean view: Mineralium Deposita, v. 38, p. 787-812.

Skiöld, T., 1987, Aspects of the Proterozoic geochronology of northern Sweden: Precambrian Research, v. 35, p. 161-167.

Slack, J. F., Corriveau, L., and Hitzman, M. W., 2016, A special issue devoted to Proterozoic iron oxide-apatite (±REE) and iron oxide copper-gold and affiliated deposits of southeast Missouri, USA, and the Great Bear magmatic zone, Northwest Territories, Canada: Preface: Economic Geology, v. 111, p. 1803-1814.

Tornos, F., Velasco, F., and Hanchar, J. M., 2016, Iron-rich melts, magmatic magnetite, and superheated hydrothermal systems: The El Laco deposit, Chile: Geology, v. 44, p. 427-430.

Velasco, F., Tornos, F., and Hanchar, J. M., 2016, Immiscible iron- and silica-rich melts and magnetite geochemistry at the El Laco volcano (northern Chile): Evidence for a magmatic origin for the magnetite deposits: Ore Geology Reviews, v. 79, p. 346-366.

Wagner, T., Fusswinkel, T., Wälle, M., and Heinrich, C. A., 2016, Microanalysis of fluid inclusions in crustal hydrothermal systems using laser ablation methods: Elements, v. 12, p. 323-328.

Westhues, A., Hanchar, J. M., LeMessurier, M. J., and Whitehouse, M. J., 2017, Evidence for hydrothermal alteration and source regions for the Kiruna iron oxide–apatite ore (northern Sweden) from zircon Hf and O isotopes: Geology, v. 45, p. 571-574.

Westhues, A., Hanchar, J. M., Whitehouse, M. J., and Martinsson, O., 2016, New constraints on the timing of host rock emplacement, hydrothermal alteration, and iron oxide-apatite mineralization in the Kiruna district, Norrbotten, Sweden: Economic Geology v. 111, p. 1595-1618.

Williams, P. J., 1994, Iron mobility during synmetamorphic alteration in the Selwyn Range area, NW Queensland: implications for the origin of ironstone-hosted Au-Cu deposits: Mineralium Deposita, v. 29, p. 250-260.

Williams, P. J., 2009, Classifying IOCG deposits, *in* Corriveau, L., and Mumin, A. H., eds., Exploring for iron oxide copper-gold deposits: Canada and global analogues. Geological Association of Canada, Short Course Notes, 20, p. 89-110.

Williams, P. J., Kendrick, M. A., and Xavier, R. P., 2010, Sources of ore fluid components in the IOCG deposits, *in* Porter, T. M., ed., Hydrothermal iron oxide copper-gold and related deposits: a global perspective, 3: Adelaide, PGC Publishing, p. 107-116.

6 Appendix A – Detailed sample description and U-Pb geochronology data for zircon and titanite, chapter two

6.1 Detailed sample description and petrography

6.1.1 Metavolcanic host rocks

Kiirunavaara footwall: The samples K-6 and KRN-11-03 (taken at 1065 and 1365 m mining level - m below former summit of Kiirunavaara, respectively) have a grey fine-grained matrix containing phenocrysts up to 0.5 cm in size. They are occasionally crosscut by light and dark veins, the latter being rich in magnetite. In thin section, large phenocrysts are identified as plagioclase and K-feldspar; both phases show varying degrees of alteration (Fig. 6-1, row 1). CL reveals a strong albitization of original K-feldspar (bright blue) to dull, dark blue colors. Other phenocrysts are actinolite, titanite, and opaque phases, mostly magnetite; all three often occur in close spatial relationship. The light veins consist mostly of quartz with larger grain sizes than the surrounding matrix. The veins also contain quite large actinolite and titanite crystals that seem to be partly dissolved by the later quartz.

Kiirunavaara hanging wall: Two varieties of the hanging wall at Kiirunavaara have been sampled at 1060 to 1070 m mining level: a more altered (KRN-11-06) and a less altered type (KRN-11-05 and K-4). Texturally, they all show a comparable fine-grained matrix with phenocrysts up to c. 1 cm in size (Fig. 2-3, main text). The difference is obvious in the color of the hand pieces and thin section: while the less altered samples have grey matrix with white to slightly pink phenocrysts, the altered sample has reddish tints in both matrix and phenocrysts. Large phenocrysts in the less altered samples are all K-feldspars,

smaller ones are titanite, few actinolite, opaque phases and quartz. One titanite grain in a thin section from sample KRN-11-05 is exceptionally large (4x1 mm) compared to other titanite, and shows a rim of biotite. Quartz usually grows in clusters and along fractures and seems to be a later phase. Zircon could be identified in different places throughout the thin section. In the more altered sample KRN-11-06, the mineralogy is very similar to the less altered types; however, feldspar phenocrysts show a higher degree of albitization (only cores of original K-feldspar preserved) and finely distributed iron oxides. Calcite and veins of quartz can be found in places.

Per Geijer host rocks: The footwall of the Per Geijer deposits is part of the same unit as the hanging wall of Kiirunavaara, and has been sampled at Rektorn (REK-12-02) and Nukutusvaara (NUK-12-01). Both have a fine-grained matrix and phenocrysts, but show different appearances from the Kiirunavaara hanging wall. REK-12-02 is from the altered zone close to the ore body contact. It has light grey matrix with slightly pinkish phenocrysts up to 0.5 cm in size. It also contains smaller dark and brownish phenocrysts. In thin section, the pinkish phenocrysts are revealed to be apatite, not feldspars as in the Kiirunavaara hanging wall. Other phenocrysts are quartz, often as accumulations of small grains, biotite, rutile and opaque phases, again probably magnetite and hematite. The matrix shows high degrees of seritization and calcification. Feldspars are rare and only occur in remnants. NUK-12-01 has white to light greyish phenocrysts in a dark grey and partly reddish matrix. In thin section, some of the phenocrysts are rounded and show an almost concentric layering that is made up by quartz in different grain sizes (Fig. 6-1, row 4). A few larger K-feldspar phenocrysts are present that are strongly albitized. Further, some biotite, rutile

and few actinolite are observed. Magnetite occurs in banded structures rather than as angular crystals. Carbonates can be found on the rims of K-feldspar grains.

The hanging wall of Rektorn is a highly altered, probably volcanic rock, which is locally called Rektorn porphyry. It contains quartz and dark phenocrysts (magnetite and hematite) and large reddish minerals. These may have been originally K-feldspar, but are now completely replaced by albite (brownish-red in CL) and quartz (Fig. 2-3, main text). The red coloring in hand piece and PPL and the red color emitted in CL are probably related to micro-inclusions of Fe oxide. The finer grained matrix is made up of K-feldspar and quartz. Fe oxide can occur as rims around the feldspar crystals, but also with quartz, usually as bands made of crystals sized around 100 μm or less. Zircon grains were identified within quartz-magnetite bands.

6.1.2 Syenite and granite intrusions

An intrusion in the trachyandesitic footwall of Kiirunavaara can be found outcropping and extending underground to mining level 800 to 850 m (Fig. 2-4, main text). This body, stratigraphically about one kilometer below the ore body, has been sampled in two locations at surface (KRN-12-01 and KRN-12-03). In previous publications, this intrusive body has been mapped as gabbro/monzonite (e.g., Bergman et al., 2001). Samples in this study, however, have the modal mineralogy of a syenite; therefore, the older name for this unit is used here. The appearance of the two syenite hand samples is quite different and can be related to different degrees of alteration. KRN-12-01 consists of white feldspar that is intensely sericitizied. Green amphibole is quite abundant and gives the whole rock a greenish appearance. The second syenite sample, KRN-12-03, is pinkish-grey. Thin section

reveals that intensely albitized K-feldspar, together with actinolite makes up the majority of this sample (Fig. 6-1, row 2). In this sample, the albitization is expressed as red CL colors on the rims of feldspar grains, probably related to the presence of Fe^{3+}. This would also be in concordance with the reddish overall appearance of this sample. In conclusion, both samples appear to have a similar mineralogy made up of altered K-feldspar, green amphibole, titanite and opaque phases, containing very few quartz, but show different alterations in the two sampled locations.

An aplitic dike (KRN-12-02) occurring within the syenite at KRN-12-01 has been sampled as well. This finer grained aplite has a pinkish appearance, few visible quartz and feldspar grains and dark minerals. The majority of this sample consists of microcrystalline quartz and feldspar; subhedral crystals up to several cm of quartz and K-feldspar (sometimes perthite) are often cracked (Fig. 2-3, main text). This sample shows again albitization with red CL colors, indicating the presence of Fe^{3+}. The sample also contains small grained opaque phases, some titanite, and few amphiboles.

The footwall is further intruded by granitic body that is found in deeper levels of the mine (from about 900 m below the surface and about one kilometer stratigraphically below ore, UB Andersson, pers. comm. 2013). The pinkish-reddish appearance of the granite is dominated by quite large feldspar. Quartz and dark minerals can also be observed. K-feldspar grains can be several mm and up to one cm long, and show strong albitization, expressed as brown-reddish CL colors (Fig. 6-1, row 3). Plagioclase only occurs as few remnants. Quartz is very common, and contains numerous fluid inclusions. Biotite is a minor mineral and contains zircon, which can also be found within feldspar. One cluster of

titanite grains, about 2 mm in diameter, is present in the thin section, as are few opaque phases.

6.1.3 Iron oxide apatite ore

The Kiirunavaara ore occurs in two varieties, called B-ore with less than 0.05% P and D-ore with more than 1% of P. K-1 (D-ore) is quite high in apatite, which occurs as bands between magnetite layers. The magnetite is almost pure, and there are only very few other oxides phases visible (Fig. 2-3, main text). Apatite grains show green to grey colors in CL, which is not typical for magmatic apatite that would usually show bright yellow colors. Actinolite occurs together with apatite between magnetite and contains small magnetite grains. Interstitial plagioclase, K-feldspar, and quartz also occur. Small monazite has been detected close to magnetite, in between quartz grains. In the second D-ore sample KRN-11-01, apatite is distributed more randomly within the magnetite and quartz content is low.

The ore sample from Nukutusvaara (NUK-12-02) is also quite rich in apatite (11.38 wt.% P_2O_5) that is subequal in size to magnetite and randomly distributed within the latter (Fig. 6-1, row 5). Similar to the Kiirunavaara ore, apatite emits green to grey colors in CL. The thin section of this sample shows the contact between the ore and waste rock, which consists of very fine-grained mix of sericite and quartz and contains only few Fe oxides and apatite. In the Rektorn ore sample (REK-10-04), apatite also occurs randomly distributed throughout the Fe oxides, but in smaller grain size than at Nukutusvaara. A vein of quartz and calcite cuts through the ore, containing elongated Fe oxide grains. This later vein may have dissolved and re-precipitated some pre-existing magnetite. Monazite may have been detected within quartz from the vein.

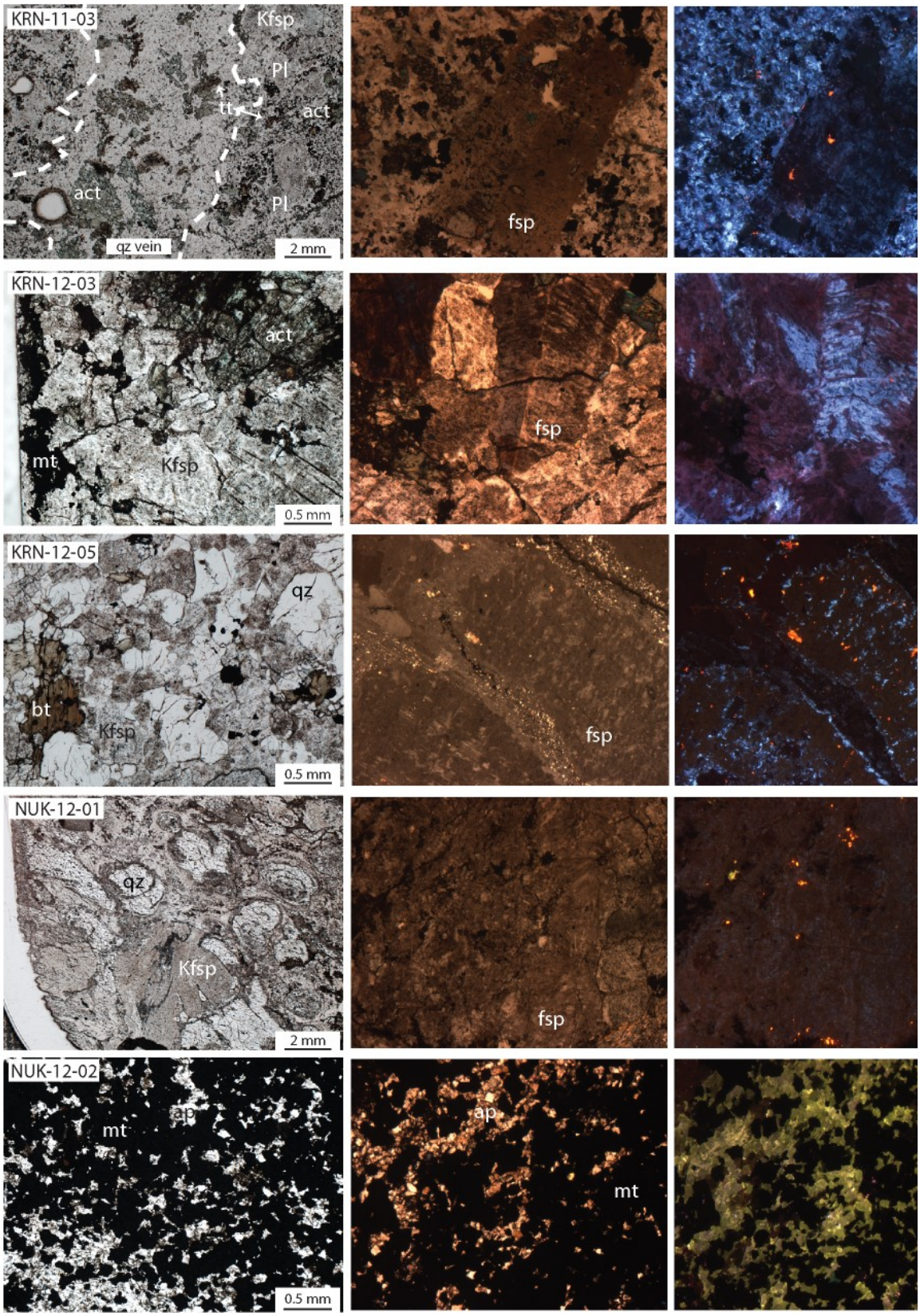
KRN-11-03
Kfsp
Pl
tt
act
act
Pl
qz vein
2 mm
fsp
KRN-12-03
act
mt
Kfsp
0.5 mm
fsp
KRN-12-05
qz
bt
Kfsp
0.5 mm
fsp
NUK-12-01
qz
Kfsp
2 mm
fsp
NUK-12-02
mt
ap
0.5 mm
ap
mt

Figure 6-1 on previous page. Further photomicrographs of thin sections from Kiirunavaara and Per Geijer samples – plain polarized (PPL) overviews of samples (left column), cross polarized (XPL, center) and cathodoluminescence (CL, right) images of altered feldspar crystals. Field of view for XPL and CL is 2.5 mm in x-direction. KRN-11-03 (footwall Kiirunavaara) consist of plagioclase and K-feldspar phenocrysts, actinolite and titanite in fine grained matrix; a crosscutting quartz vein contains no feldspar, and titanite and actinolite are partly dissolved (PPL). Na alteration in this sample is similar to KRN hanging wall (see Fig. 2-3, main text), expressed as dark blue, dull colors in CL for albite that has almost completely replaced K-feldspar. Syenite KRN-12-03 is dominated by large K-feldspars, and further contains actinolite, titanite, and magnetite. Similar to the aplite (KRN-12-02), original K-feldspar (blue) is replaced by reddish albite (starting from the rims). KRN-12-05 (granite) consists mostly of K-feldspar, quartz, and biotite. K-feldspar has only small spots of original material (bright blue) left, while most of the crystal is highly altered (reddish-brown in CL). NUK-12-01 (Nukutusvaara footwall) contains K-feldspar and quartz in fine grained matrix, quartz forms rounded aggregations with concentric layering (PPL). In CL, dark reddish to brown colors prevail, original K-feldspar is only present as small remnants (blue spots throughout crystal). The Nukutusvaara ore (NUK-12-02) consist of magnetite and apatite, the latter showing green to grey colors in CL (untypical of magmatic apatite). All samples also contain varying amount of calcite (bright orange in CL).

6.2 References – Appendix A

Bergman, S., Kübler, L., and Martinsson, O., 2001, Description of regional geological and geophysical maps of northern Norrbotten County (east of the Caledonian Orogen), Sveriges Geologiska Undersökning, Ba 56, 110 pp.

Stacey, J. S., and Kramers, J. D., 1975, Approximation of terrestrial lead isotope evolution by a two-stage model: Earth and Planetary Science Letters, v. 26, p. 207-221.

Table 6-1. Geochronology results for zircon from Kiirunavaara ore and host rock: U-Pb-Th SIMS analytical data.

						Isotopic ratios							Ages (Ma)					
Sample/ spot #	[U] ppm	[Th] ppm	[Pb] ppm	Th/U meas	f_{206}%[1]	$^{207}Pb/^{235}U$	±σ %	$^{238}U/^{206}Pb$	±σ %	$^{207}Pb/^{206}Pb$	±σ %	Disc. %	$^{207}Pb/^{206}Pb$	±σ	$^{207}Pb/^{235}U$	±σ	$^{206}Pb/^{238}U$	±σ
a) K-1 (Kiirunavaara ore)																		
n3911_K1@19	194	121	83	0.63	0.07	5.2863	2.24	3.040	2.19	0.1165	0.51		1904.0	9.1	1866.7	19.3	1833.3	35.0
n3911_K1-r1-g3#1@8	655	591	290	0.90	0.03	5.1305	1.78	3.106	1.75	0.1156	0.30	-1.9	1888.8	5.4	1841.2	15.2	1799.3	27.5
n4721_K-1_@22	550	161	215	0.29	0.01	5.1752	0.90	3.070	0.89	0.1152	0.15	-2.2	1883.5	2.7	1848.5	7.7	1817.6	14.1
n3911_K1@26	299	83	122	0.28	{0.02}	5.4276	2.05	2.924	2.02	0.1151	0.36		1881.4	6.4	1889.2	17.7	1896.3	33.2
n4721_K-1_@10	446	181	181	0.41	0.01	5.2181	0.86	3.034	0.84	0.1148	0.17	-0.7	1877.0	3.1	1855.6	7.4	1836.5	13.5
n4721_K-1_@16	414	140	164	0.34	0.03	5.1531	0.88	3.071	0.86	0.1148	0.18	-1.8	1876.5	3.2	1844.9	7.5	1817.1	13.7
n3911_K-1#1@12	169	105	75	0.62	{0.01}	5.4349	2.17	2.910	2.12	0.1147	0.47		1875.4	8.5	1890.4	18.8	1904.0	35.1
n3911_K1-r2-g1#1@9	551	128	214	0.23	0.02	5.1917	1.93	3.046	1.90	0.1147	0.34		1874.8	6.0	1851.3	16.6	1830.4	30.4
n4721_K-1_@21	416	154	164	0.37	0.02	5.1061	0.93	3.091	0.90	0.1145	0.22	-2.0	1871.7	4.0	1837.1	7.9	1806.8	14.3
n4721_K-1_@17	90	71	39	0.80	0.06	5.1401	1.16	3.067	1.09	0.1143	0.39	-0.3	1869.2	7.1	1842.8	9.9	1819.4	17.4
n4721_K-1_@6	290	87	108	0.30	0.03	4.8799	0.83	3.220	0.80	0.1140	0.22	-5.5	1863.4	4.0	1798.8	7.0	1743.6	12.2
n4721_K-1_@13	252	91	104	0.36	0.15	4.7399	1.17	3.310	1.14	0.1138	0.24	-7.4	1860.9	4.4	1774.3	9.8	1701.6	17.1
n3911_K1@28	965	376	341	0.39	0.03	4.5187	2.43	3.470	2.40	0.1137	0.38	-9.3	1859.6	6.8	1734.4	20.4	1632.5	34.7
n4721_K-1_@4	664	225	242	0.34	0.03	4.6984	0.80	3.324	0.78	0.1133	0.17	-8.0	1852.3	3.1	1767.0	6.7	1695.6	11.7
n4721_K-1_@18	575	197	205	0.34	0.04	4.5851	0.82	3.403	0.80	0.1132	0.19	-10.0	1850.9	3.4	1746.6	6.9	1660.7	11.7
n4721_K-1_@20	424	313	168	0.74	0.16	4.7358	1.39	3.287	1.37	0.1129	0.26	-5.5	1846.3	4.6	1773.6	11.8	1712.5	20.6
n3911_K-1#1@13	208	100	70	0.48	0.07	4.0219	2.14	3.827	2.09	0.1116	0.48	-16.2	1826.4	8.7	1638.6	17.6	1496.3	27.9
n4721_K-1_@24	736	306	247	0.42	0.07	4.1322	0.81	3.697	0.79	0.1108	0.15	-15.2	1812.5	2.8	1660.7	6.6	1543.3	10.9
n4721_K-1_@19	356	335	106	0.94	0.08	3.3707	2.13	4.467	2.10	0.1092	0.31	-26.6	1786.2	5.6	1497.6	16.8	1302.2	24.9
n3911_K1@27	1242	699	381	0.56	0.10	3.5176	4.50	4.244	4.32	0.1083	1.25	-16.7	1770.3	22.6	1531.2	36.2	1364.1	53.3
n3911_K-1#1@11	1206	383	349	0.32	0.10	3.5246	2.76	4.231	2.73	0.1081	0.41	-20.6	1768.4	7.6	1532.7	22.1	1367.8	33.8
n4721_K-1_@3	863	334	246	0.39	0.09	3.4416	0.84	4.312	0.82	0.1076	0.18	-24.6	1759.5	3.3	1513.9	6.6	1344.6	9.9
n3911_K1@23	473	281	141	0.59	0.16	3.2213	3.46	4.591	3.37	0.1073	0.78	-24.3	1753.4	14.3	1462.3	27.2	1270.3	39.0
n4721_K-1_@11	817	425	242	0.52	0.11	3.4158	0.97	4.328	0.96	0.1072	0.17	-24.4	1752.6	3.0	1508.0	7.7	1340.1	11.6
n4721_K-1_@14	3157	1322	884	0.42	0.09	3.2874	1.16	4.445	1.08	0.1060	0.42	-24.5	1731.5	7.6	1478.1	9.0	1308.0	12.8
n3911_K1@25	1526	564	385	0.37	0.11	2.8971	2.24	4.975	2.19	0.1045	0.47	-30.0	1706.0	8.7	1381.1	17.0	1180.8	23.7
n3911_K1@20	1368	354	341	0.26	0.15	2.9435	2.46	4.848	2.44	0.1035	0.30	-27.4	1687.9	5.5	1393.2	18.8	1208.8	26.9
n3911_K1@24	2765	1348	721	0.49	0.13	2.8432	2.92	4.877	2.87	0.1006	0.54	-24.1	1634.6	10.1	1367.0	22.2	1202.3	31.6
n4721_K-1_@5	1577	1819	317	1.15	0.25	1.7631	3.05	7.177	2.98	0.0918	0.64	-40.5	1462.7	12.2	1032.0	20.0	840.9	23.6
n4721_K-1_@9	6367	3009	1170	0.47	0.08	1.8731	1.73	6.723	1.55	0.0913	0.78	-36.6	1453.7	14.7	1071.6	11.5	893.9	13.0
n3911_K1-r1-g2#1@7	337	103	51	0.31	0.19	1.5332	3.60	8.186	3.05	0.0910	1.91	-40.5	1447.2	36.0	943.8	22.4	743.0	21.4
n4721_K-1_@8	277	302	55	1.09	0.24	1.5734	13.53	7.936	12.59	0.0906	4.95	-19.8	1437.2	91.6	959.7	87.7	765.1	91.5
n4721_K-1_@1	1536	3121	294	2.03	0.25	1.3224	6.07	9.255	5.77	0.0888	1.89	-43.4	1399.2	35.8	855.6	35.7	661.4	36.3
n4721_K-1_@23 - R	2166	2569	448	1.19	0.32	1.4897	3.84	8.202	3.79	0.0886	0.59	-44.5	1396.0	11.2	926.2	23.6	741.6	26.6
n4721_K-1_@15 - R	1973	1804	396	0.91	0.39	1.6587	1.51	7.335	1.39	0.0882	0.57	-39.7	1387.6	10.9	992.9	9.6	823.9	10.8
n3911_K-1#1@10 -R	3249	1786	515	0.55	0.25	1.3543	2.26	8.892	1.78	0.0873	1.39	-44.2	1368.0	26.6	869.4	13.3	687.0	11.6
n4721_K-1_@2 - R	2312	896	396	0.39	0.29	1.3991	2.12	8.563	2.00	0.0869	0.72	-45.6	1358.0	13.7	888.6	12.6	712.0	13.5
n4721_K-1_@12 - R	2387	852	437	0.36	0.21	1.5461	3.25	7.737	2.68	0.0868	1.84	-33.9	1355.2	35.1	949.0	20.2	783.6	19.8
n3911_K1@21	3948	4699	794	1.19	0.64	1.3042	5.32	8.705	4.64	0.0823	2.61	-30.2	1253.6	50.3	847.6	31.0	701.0	30.9
n4721_K-1_@7 - R	3823	8813	1252	2.31	1.77	1.3307	5.68	8.101	3.52	0.0782	4.45	-9.6	1151.5	86.0	859.2	33.5	750.4	25.0
n3911_K1@22	2131	1381	331	0.65	0.41	1.1364	10.30	9.258	9.38	0.0763	4.25	-13.1	1102.9	82.7	770.8	57.2	661.2	59.2
n3911_K1-r1-g1#1@5	5560	3268	860	0.59	0.40	1.1286	6.72	9.181	5.85	0.0752	3.31	-17.4	1072.5	65.0	767.1	36.9	666.5	37.2
n3911_K1-r1-g1#1@6 - R	4367	6967	746	1.60	0.26	1.0861	3.24	9.524	2.74	0.0750	1.74	-30.0	1069.1	34.5	746.6	17.3	643.7	16.8

continued on following pages. R: analyses on rim of zircon grain.

Table 6-1. - continued**.** Geochronology results for zircon from Kiirunavaara ore and host rock: U-Pb-Th SIMS analytical data.

Sample/ spot #	[U] ppm	[Th] ppm	[Pb] ppm	Th/U meas	f_{206}%[1]	Isotopic ratios $^{207}Pb/^{235}U$	±σ %	$^{238}U/^{206}Pb$	±σ %	$^{207}Pb/^{206}Pb$	±σ %	Disc. %	Ages (Ma) $^{207}Pb/^{206}Pb$	±σ	$^{207}Pb/^{235}U$	±σ	$^{206}Pb/^{238}U$	±σ
b) KRN-11-03 (Kiirunavaara footwall)																		
n4722_KRN11-03_@6	509	455	231	0.89	0.02	5.2948	1.02	3.010	0.98	0.1156	0.26	-0.2	1889.3	4.7	1868.0	8.7	1849.0	15.9
n4722_KRN11-03_@3	307	131	126	0.43	0.06	5.2962	0.84	3.004	0.81	0.1154	0.24	-0.1	1885.7	4.2	1868.3	7.2	1852.6	13.0
n4722_KRN11-03_@7 - R	350	763	202	2.18	0.02	5.3127	0.84	2.990	0.82	0.1152	0.19		1883.3	3.4	1870.9	7.2	1859.8	13.3
n4722_KRN11-03_@5	426	941	247	2.21	0.05	5.2627	0.81	3.016	0.79	0.1151	0.18	-0.4	1881.5	3.2	1862.8	7.0	1846.1	12.8
n4722_KRN11-03_@9	246	348	115	1.41	0.92	5.0010	1.40	3.170	0.95	0.1150	1.02	-1.8	1879.5	18.3	1819.5	11.9	1767.6	14.8
n4722_KRN11-03_@2	214	105	86	0.49	0.03	5.1044	1.20	3.103	1.17	0.1149	0.27	-2.2	1877.8	4.8	1836.8	10.2	1800.9	18.4
n4722_KRN11-03_@8	429	1152	256	2.69	0.04	5.1769	1.06	3.059	1.05	0.1148	0.18	-1.1	1877.5	3.2	1848.8	9.1	1823.4	16.7
n4722_KRN11-03_@1	248	699	160	2.82	0.05	5.2956	0.87	2.981	0.83	0.1145	0.24		1872.1	4.4	1868.2	7.4	1864.6	13.5
n4722_KRN11-03_@4	527	367	215	0.70	0.10	4.8795	1.04	3.224	0.99	0.1141	0.31	-5.3	1865.9	5.6	1798.7	8.8	1741.4	15.2
n4722_KRN11-03_@10	390	829	211	2.13	0.89	5.0096	2.13	3.140	1.23	0.1141	1.74		1865.4	31.1	1820.9	18.2	1782.3	19.1
c) K-4 (Kiirunavaara hanging wall)																		
n3914-K4@33 - R	389	321	180	0.83	0.02	5.4692	2.34	2.908	2.33	0.1154	0.30		1885.6	5.3	1895.8	20.3	1905.1	38.5
n3914-K4@32	340	272	156	0.80	{0.01}	5.4278	2.22	2.926	2.18	0.1152	0.43		1883.0	7.7	1889.3	19.2	1895.0	35.9
n3914-K4@38 - R	310	220	142	0.71	0.06	5.4889	2.17	2.893	2.14	0.1152	0.35		1882.4	6.3	1898.9	18.8	1914.0	35.5
n3914-K4@34	697	588	311	0.84	0.03	5.2357	2.23	3.031	2.22	0.1151	0.24		1881.3	4.4	1858.5	19.2	1838.1	35.6
n3914-K4@35 - R	108	55	47	0.51	{0.06}	5.4402	2.29	2.916	2.14	0.1150	0.81		1880.4	14.5	1891.2	19.9	1901.0	35.4
n3914-K4@31	367	344	172	0.94	0.05	5.3282	3.51	2.966	3.50	0.1146	0.32		1873.9	5.8	1873.4	30.5	1873.0	57.1
n3914-K4@30	118	65	51	0.55	{0.01}	5.3121	2.38	2.969	2.31	0.1144	0.58		1870.3	10.4	1870.8	20.6	1871.3	37.7
n3914-K4@36	138	96	61	0.69	0.09	5.3417	2.88	2.938	2.81	0.1138	0.64		1861.4	11.5	1875.6	24.9	1888.4	46.2
n3914-K4@37	156	81	68	0.52	{0.04}	5.4449	2.32	2.878	2.26	0.1137	0.49		1858.6	8.8	1891.9	20.1	1922.5	37.7
d) KRN-11-05 (Kiirunavaara hanging wall)																		
n4723_KRN11-5_@12	178	110	76	0.62	{0.02}	5.2811	0.84	3.027	0.79	0.1159	0.27	-1.3	1894.5	4.9	1865.8	7.2	1840.2	12.7
n4723_KRN11-5_@2	157	100	67	0.64	{0.02}	5.2399	1.18	3.047	1.14	0.1158	0.30	-1.2	1892.4	5.3	1859.1	10.1	1829.5	18.2
n4723_KRN11-5_@14	67	35	28	0.53	{0.03}	5.2973	0.94	3.012	0.84	0.1157	0.43	-0.1	1891.4	7.7	1868.4	8.1	1847.9	13.5
n4723_KRN11-5_@1	241	177	103	0.73	0.04	5.1262	1.50	3.112	1.47	0.1157	0.27	-2.7	1890.7	4.9	1840.5	12.8	1796.4	23.2
n4723_KRN11-5_@7	124	69	52	0.55	{0.02}	5.2866	0.88	3.015	0.82	0.1156	0.32	-0.5	1889.5	5.7	1866.7	7.6	1846.3	13.2
n4723_KRN11-5_@28	141	81	60	0.57	{0.01}	5.2909	0.94	3.010	0.89	0.1155	0.29	-0.1	1887.6	5.3	1867.4	8.0	1849.3	14.4
n4723_KRN11-5_@13	57	31	24	0.54	{0.03}	5.2748	1.01	3.018	0.90	0.1155	0.47		1887.3	8.3	1864.8	8.7	1844.7	14.4
n4723_KRN11-5_@25	341	305	156	0.90	0.01	5.3041	0.84	3.001	0.82	0.1155	0.19	-0.2	1887.1	3.4	1869.5	7.2	1853.8	13.2
n4723_KRN11-5_@22	208	146	91	0.70	{0.01}	5.2971	0.87	3.005	0.83	0.1155	0.27	-0.1	1887.1	4.9	1868.4	7.5	1851.6	13.4
n4723_KRN11-5_@27	395	359	178	0.91	0.02	5.2106	0.78	3.054	0.76	0.1154	0.18	-2.0	1886.2	3.2	1854.3	6.7	1826.1	12.2
n4723_KRN11-5_@17	188	72	77	0.38	{0.02}	5.2927	0.82	3.006	0.77	0.1154	0.28	-0.1	1885.9	5.1	1867.7	7.0	1851.3	12.4
n4900-R3-G2b	154	102	69	0.66	{0.01}	5.4257	0.68	2.932	0.48	0.1154	0.47		1885.8	8.5	1888.9	5.8	1891.8	7.9
n4900-R3-G3	366	283	166	0.77	0.01	5.3830	0.53	2.953	0.48	0.1153	0.24		1884.6	4.3	1882.1	4.6	1879.9	7.8
n4723_KRN11-5_@19	232	170	103	0.73	0.02	5.3405	0.84	2.975	0.81	0.1152	0.23		1883.7	4.2	1875.4	7.2	1867.9	13.2
n4723_KRN11-5_@8	276	195	121	0.71	0.04	5.2975	0.92	2.999	0.89	0.1152	0.21		1883.7	3.9	1868.5	7.9	1854.8	14.4
n4723_KRN11-5_@23	130	80	56	0.61	{0.02}	5.2681	0.91	3.016	0.83	0.1152	0.39		1883.7	7.0	1863.7	7.8	1845.9	13.3
n4900-R2-G4	124	72	54	0.58	{0.01}	5.3541	0.62	2.967	0.47	0.1152	0.40		1883.3	7.3	1877.6	5.4	1872.3	7.7
n4723_KRN11-5_@26	169	107	73	0.63	{0.01}	5.3047	0.90	2.994	0.86	0.1152	0.27		1882.9	4.8	1869.6	7.7	1857.7	13.9
n4723_KRN11-5_@20	121	51	50	0.42	{0.02}	5.2709	0.97	3.012	0.90	0.1151	0.36		1881.9	6.5	1864.2	8.3	1848.3	14.4
n4900-R4-G4	226	138	99	0.61	{0.00}	5.3693	0.56	2.953	0.47	0.1150	0.30		1880.1	5.4	1880.0	4.8	1879.8	7.7
n4723_KRN11-5_@4	189	128	81	0.67	0.03	5.1991	0.89	3.049	0.86	0.1150	0.26	-1.0	1879.2	4.7	1852.5	7.6	1828.7	13.7
n4900-R1-G3	125	97	56	0.77	{0.02}	5.2138	0.62	3.040	0.47	0.1149	0.41	-0.7	1878.9	7.3	1854.9	5.3	1833.5	7.5

continued on following page. R: analyses on rim of zircon grain.

Table 6-1. - continued**.** Geochronology results for zircon from Kiirunavaara ore and host rock: U-Pb-Th SIMS analytical data.

Sample/ spot #	[U] ppm	[Th] ppm	[Pb] ppm	Th/U meas	f_{206}%[1]	Isotopic ratios $^{207}Pb/^{235}U$	±σ %	$^{238}U/^{206}Pb$	±σ %	$^{207}Pb/^{206}Pb$	±σ %	Disc[2]	Ages (Ma) $^{207}Pb/^{206}Pb$	±σ	$^{207}Pb/^{235}U$	±σ	$^{206}Pb/^{238}U$	±σ
b) KRN-11-05 (Kiirunavaara hanging wall) continued																		
n4723_KRN11-5_@24	118	68	50	0.57	{0.03}	5.2392	0.87	3.024	0.81	0.1149	0.32	-0.1	1878.1	5.7	1859.0	7.5	1842.0	13.0
n4723_KRN11-5_@11	316	238	137	0.75	0.04	5.1618	0.80	3.068	0.77	0.1149	0.20	-1.8	1877.5	3.7	1846.3	6.8	1818.8	12.2
n4723_KRN11-5_@21	252	262	119	1.04	{0.01}	5.3198	0.79	2.976	0.76	0.1148	0.22		1877.1	3.9	1872.1	6.8	1867.5	12.3
n4723_KRN11-5_@15	147	102	62	0.69	0.05	5.0690	1.14	3.122	1.04	0.1148	0.47	-2.3	1876.3	8.4	1830.9	9.7	1791.3	16.3
n4723_KRN11-5_@9	177	105	75	0.59	0.03	5.2400	0.91	3.020	0.87	0.1148	0.27		1876.1	4.8	1859.1	7.8	1844.1	13.9
n4723_KRN11-5_@16 - R	229	150	99	0.66	{0.02}	5.2698	0.90	3.002	0.87	0.1147	0.23		1875.6	4.2	1864.0	7.7	1853.6	14.0
n4723_KRN11-5_@6	100	56	42	0.56	{0.03}	5.2283	0.96	3.022	0.89	0.1146	0.37		1873.5	6.7	1857.2	8.2	1842.8	14.2
n4900-R3-G1	158	113	71	0.72	{0.01}	5.3659	0.59	2.942	0.47	0.1145	0.36		1871.7	6.4	1879.4	5.1	1886.4	7.8
n4900-R2-G5	103	56	44	0.54	0.06	5.2100	0.67	3.028	0.48	0.1144	0.46		1871.0	8.4	1854.2	5.7	1839.4	7.6
n4900-R4-G1	260	163	106	0.63	0.04	4.9761	0.59	3.170	0.52	0.1144	0.29	-4.6	1870.5	5.3	1815.3	5.0	1767.5	8.0
n4723_KRN11-5_@10	208	137	90	0.66	0.03	5.2566	0.85	3.000	0.79	0.1144	0.33		1870.3	5.9	1861.9	7.3	1854.3	12.7
n4723_KRN11-5_@18	159	114	70	0.72	{0.03}	5.2684	0.86	2.989	0.80	0.1142	0.32		1867.5	5.8	1863.7	7.4	1860.4	13.0
n4723_KRN11-5_@5	198	150	91	0.76	0.03	5.4523	1.28	2.885	1.26	0.1141	0.25	0.4	1865.7	4.5	1893.1	11.1	1918.2	20.9
n4900-R3-G2a	151	44	31	0.29	{0.04}	2.5716	1.34	6.033	1.23	0.1125	0.52	-47.0	1840.6	9.5	1292.6	9.8	988.6	11.3
n4723_KRN11-5_@3	298	187	97	0.63	0.05	3.9038	1.39	3.943	1.33	0.1116	0.39	-19.8	1826.4	7.1	1614.5	11.3	1457.0	17.3
n4900-R4-G3	104	74	31	0.71	{0.02}	2.6997	0.83	4.417	0.47	0.0865	0.68		1349.0	13.1	1328.4	6.2	1315.6	5.6
c) KRN-11-06 (Kiirunavaara hanging wall)																		
n4901-R3-G5	83	41	36	0.50	{0.92}	5.6520	0.98	2.928	0.48	0.1200	0.86		1956.7	15.2	1924.1	8.5	1894.0	7.8
n4901-R2-G4	130	92	58	0.71	{0.04}	5.4192	0.62	2.944	0.48	0.1157	0.40		1890.9	7.1	1887.9	5.3	1885.1	7.8
n4724_KRN11-6_@12	88	48	37	0.55	{0.04}	5.2473	0.99	3.038	0.87	0.1156	0.48	-0.6	1889.4	8.6	1860.3	8.5	1834.5	13.9
n4724_KRN11-6_@15	110	64	47	0.58	0.10	5.2887	0.93	3.012	0.86	0.1155	0.35	-0.1	1888.2	6.3	1867.0	8.0	1848.1	13.8
n4901-R1-G4	233	172	103	0.74	{0.03}	5.2858	0.59	3.013	0.51	0.1155	0.30	-0.8	1888.0	5.3	1866.6	5.1	1847.4	8.2
n4901-R1-G2	168	117	74	0.70	{0.01}	5.3481	0.59	2.974	0.47	0.1154	0.35		1885.4	6.3	1876.6	5.0	1868.6	7.7
n4901-R4-G2	85	41	36	0.49	{0.01}	5.3199	0.71	2.987	0.47	0.1153	0.53		1884.0	9.5	1872.1	6.1	1861.4	7.7
n4724_KRN11-6_@3	173	123	76	0.71	0.03	5.2962	0.87	2.998	0.83	0.1152	0.27		1882.7	4.9	1868.3	7.5	1855.3	13.3
n4724_KRN11-6_@17	84	44	35	0.52	{0.04}	5.2407	0.97	3.029	0.87	0.1151	0.42	-0.1	1882.1	7.5	1859.3	8.3	1838.9	14.0
n4724_KRN11-6_@9	184	105	78	0.57	0.03	5.2795	0.86	3.006	0.80	0.1151	0.32		1881.6	5.7	1865.6	7.3	1851.2	12.8
n4724_KRN11-6_@8	150	139	68	0.92	0.02	5.2130	0.90	3.043	0.85	0.1151	0.29	-0.9	1880.9	5.2	1854.7	7.7	1831.5	13.5
n4901-R2-G5	100	67	44	0.66	{0.02}	5.3349	0.71	2.973	0.47	0.1150	0.53		1880.4	9.6	1874.5	6.1	1869.1	7.7
n4724_KRN11-6_@7	353	265	156	0.75	0.01	5.2742	0.82	3.006	0.79	0.1150	0.23		1879.9	4.2	1864.7	7.0	1851.1	12.7
n4724_KRN11-6_@11	164	126	73	0.77	{0.03}	5.2677	0.84	3.004	0.79	0.1148	0.29		1876.0	5.3	1863.6	7.2	1852.6	12.7
n4724_KRN11-6_@13	196	125	84	0.64	0.02	5.2414	0.89	3.019	0.83	0.1148	0.32		1876.0	5.8	1859.4	7.6	1844.5	13.4
n4724_KRN11-6_@10	166	101	71	0.61	{0.02}	5.2030	0.88	3.040	0.84	0.1147	0.28	-0.5	1875.3	5.0	1853.1	7.6	1833.4	13.4
n4724_KRN11-6_@6	165	116	68	0.70	0.03	4.9738	0.87	3.176	0.83	0.1146	0.28	-4.6	1873.4	5.1	1814.9	7.4	1764.4	12.8
n4724_KRN11-6_@2	117	71	45	0.60	{0.01}	4.7125	1.01	3.351	0.96	0.1145	0.34	-9.1	1872.3	6.1	1769.5	8.5	1683.6	14.2
n4724_KRN11-6_@5	203	140	85	0.69	0.03	5.0701	0.89	3.114	0.85	0.1145	0.25	-2.7	1871.9	4.5	1831.1	7.6	1795.4	13.4
n4901-R2-G1	72	35	29	0.49	{0.01}	5.1032	0.73	3.092	0.48	0.1144	0.55	-1.3	1871.0	9.8	1836.6	6.2	1806.5	7.6
n4724_KRN11-6_@14	162	111	63	0.68	0.08	4.6976	0.99	3.358	0.94	0.1144	0.31	-9.4	1870.5	5.5	1766.8	8.3	1680.4	14.0
n4724_KRN11-6_@4	178	112	67	0.63	0.02	4.5205	0.88	3.486	0.83	0.1143	0.28	-12.8	1868.7	5.1	1734.8	7.3	1625.9	12.0
n4724_KRN11-6_@16	251	227	99	0.90	0.05	4.5258	0.75	3.477	0.71	0.1141	0.24	-12.7	1866.0	4.4	1735.7	6.3	1629.7	10.2
n4724_KRN11-6_@1	139	99	55	0.71	{0.03}	4.7600	1.05	3.303	0.96	0.1140	0.42	-7.1	1864.3	7.5	1777.9	8.8	1705.1	14.4
n4724_KRN11-6_@18	82	53	32	0.65	{0.04}	4.7753	1.11	3.292	0.99	0.1140	0.51	-6.5	1864.3	9.1	1780.6	9.3	1710.0	14.8

[1]Percentage of common ^{206}Pb in measured ^{206}Pb, estimated from ^{204}Pb counts. Figures in parentheses are given when no correction was applied and indicate a value calculated assuming a present-day Stacey & Kramers (1975) model terrestrial Pb-isotope composition. All other ratios are common Pb corrected. [2]Age discordance at closest approach of error ellipse to concordia (2σ level). R: analyses on rim of zircon grain.

Table 6-2. Geochronology results for zircon from Kiirunavaara intrusions: U-Pb-Th SIMS analytical data.

Sample/ spot #	[U] ppm	[Th] ppm	[Pb] ppm	Th/U meas	f_{206}%[1]	Isotopic ratios $^{207}Pb/^{235}U$	±σ %	$^{238}U/^{206}Pb$	±σ %	$^{207}Pb/^{206}Pb$	±σ %	Disc	Ages (Ma) $^{207}Pb/^{206}Pb$	±σ	$^{207}Pb/^{235}U$	±σ	$^{206}Pb/^{238}U$	±σ
a) KRN-12-01 (Kiirunavaara syenite)																		
n4728_KRN12-1_@9	160	155	73	0.97	0.05	5.2083	0.80	3.035	0.75	0.1146	0.27	-0.4	1874.1	4.9	1854.0	6.8	1836.1	12.0
n4728_KRN12-1_@5	573	1178	277	2.06	0.17	4.4143	0.84	3.498	0.83	0.1120	0.17	-11.4	1831.9	3.0	1715.0	7.0	1620.9	11.8
n4728_KRN12-1_@10	576	836	233	1.45	0.22	3.9960	4.70	3.834	4.64	0.1111	0.75	-11.8	1817.8	13.5	1633.4	38.9	1494.0	62.2
n4728_KRN12-1_@6	1240	2138	445	1.72	0.51	3.3043	0.88	4.468	0.86	0.1071	0.17	-26.8	1750.1	3.1	1482.1	6.9	1302.1	10.2
n4728_KRN12-1_@2	2892	2292	815	0.79	0.25	3.1045	0.79	4.700	0.74	0.1058	0.26	-29.2	1728.7	4.8	1433.8	6.1	1243.6	8.4
n4728_KRN12-1_@3	2031	6657	627	3.28	0.60	2.2169	0.96	6.150	0.94	0.0989	0.20	-40.9	1603.2	3.8	1186.4	6.8	971.2	8.5
n4728_KRN12-1_@8	1048	319	160	0.30	0.99	1.6563	4.41	7.724	4.17	0.0928	1.45	-41.0	1483.4	27.3	992.0	28.3	784.8	30.9
n4728_KRN12-1_@4	2329	2982	486	1.28	0.67	1.8463	4.27	6.856	3.82	0.0918	1.90	-31.7	1463.5	35.7	1062.1	28.5	877.7	31.4
n4728_KRN12-1_@1	1285	3861	301	3.01	1.20	1.5458	0.83	7.905	0.79	0.0886	0.27	-45.9	1396.2	5.3	948.8	5.2	767.8	5.7
n4728_KRN12-1_@7	1054	1810	172	1.72	2.03	1.2692	4.85	8.890	4.19	0.0818	2.44	-31.7	1241.5	47.2	832.0	27.9	687.2	27.4
b) KRN-12-02 (Kiirunavaara aplite)																		
n4727_KRN12-2_@9	85	54	37	0.64	{0.02}	5.3951	0.83	2.980	0.75	0.1166	0.34	-0.2	1904.6	6.1	1884.1	7.1	1865.5	12.2
n4727_KRN12-2_@19	168	123	75	0.73	0.02	5.3984	0.84	2.958	0.80	0.1158	0.25		1892.7	4.6	1884.6	7.2	1877.3	13.1
n4727_KRN12-2_@3	149	79	64	0.53	{0.02}	5.3834	0.90	2.959	0.86	0.1155	0.27		1888.0	4.8	1882.2	7.8	1877.0	14.1
n4899-R4-G1b	88	38	37	0.43	{0.01}	5.3914	0.68	2.952	0.48	0.1154	0.48		1886.4	8.6	1883.5	5.8	1880.9	7.9
n4727_KRN12-2_@2	155	80	66	0.52	0.01	5.3667	0.79	2.965	0.74	0.1154	0.26		1886.3	4.7	1879.6	6.8	1873.5	12.1
n4727_KRN12-2_@12	211	109	89	0.52	{0.01}	5.3214	0.82	2.990	0.78	0.1154	0.25		1885.8	4.5	1872.3	7.1	1860.2	12.7
n4727_KRN12-2_@7	197	127	86	0.64	0.02	5.3504	0.79	2.973	0.76	0.1154	0.23		1885.6	4.1	1877.0	6.8	1869.2	12.3
n4727_KRN12-2_@15	199	133	88	0.67	0.02	5.3685	0.77	2.962	0.74	0.1153	0.23		1884.8	4.2	1879.8	6.6	1875.4	12.0
n4727_KRN12-2_@1a	129	80	56	0.62	0.04	5.3288	0.79	2.983	0.73	0.1153	0.29		1884.1	5.2	1873.5	6.7	1864.0	11.8
n4727_KRN12-2_@8	146	86	63	0.59	{0.01}	5.2949	0.78	3.000	0.74	0.1152	0.27		1883.3	4.8	1868.0	6.7	1854.4	11.9
n4727_KRN12-2_@13	164	127	74	0.78	0.01	5.3254	0.81	2.982	0.76	0.1152	0.27		1882.9	4.9	1873.0	6.9	1864.0	12.3
n4899-R2-G2	132	70	57	0.53	{0.00}	5.3742	0.62	2.952	0.47	0.1151	0.39		1880.9	7.1	1880.7	5.3	1880.7	7.7
n4727_KRN12-2_@16	163	112	72	0.69	0.02	5.3756	0.79	2.951	0.73	0.1151	0.30		1880.8	5.4	1881.0	6.8	1881.2	12.0
n4727_KRN12-2_@6	150	93	63	0.62	0.05	5.3190	0.81	2.981	0.76	0.1150	0.26		1879.7	4.7	1871.9	6.9	1864.9	12.4
n4727_KRN12-2_@5	106	87	46	0.82	0.04	5.0477	0.90	3.140	0.84	0.1149	0.33	-3.7	1879.0	6.0	1827.4	7.7	1782.4	13.0
n4899-R4-G1a	208	151	94	0.73	{0.00}	5.3797	0.57	2.946	0.47	0.1149	0.31		1878.7	5.6	1881.6	4.9	1884.2	7.7
n4899-R1-G1	137	60	58	0.44	{0.00}	5.3916	0.61	2.938	0.48	0.1149	0.39		1878.3	7.0	1883.5	5.3	1888.3	7.8
n4727_KRN12-2_@14	205	90	86	0.44	0.01	5.3370	0.77	2.967	0.73	0.1149	0.22		1877.7	4.0	1874.8	6.6	1872.1	11.9
n4899-R1-G4	174	113	78	0.65	{0.01}	5.4247	0.58	2.919	0.47	0.1148	0.34		1877.4	6.2	1888.8	5.0	1899.1	7.8
n4899-R3-G5	151	87	66	0.58	{0.01}	5.3689	0.60	2.948	0.47	0.1148	0.37		1876.4	6.7	1879.9	5.2	1883.1	7.7
n4899-R2-G1	185	124	79	0.67	0.04	5.0548	0.63	3.094	0.50	0.1134	0.39	-1.0	1854.9	7.0	1828.5	5.4	1805.5	7.9
n4899-R3-G1a	377	279	147	0.74	0.49	4.5172	1.00	3.444	0.94	0.1128	0.34	-10.1	1845.6	6.2	1734.1	8.4	1643.3	13.7
n4899-R4-G4b	204	101	73	0.49	0.08	4.3633	0.77	3.535	0.62	0.1119	0.45	-11.5	1829.8	8.1	1705.4	6.3	1606.0	8.9
n4899-R4-G5a	3372	3665	1043	1.09	0.23	3.2517	0.65	4.589	0.63	0.1082	0.14	-29.9	1769.7	2.6	1469.6	5.0	1270.9	7.3
n4899-R4-G4a	327	150	103	0.46	0.08	3.7322	0.67	3.980	0.48	0.1077	0.48	-17.7	1761.2	8.7	1578.3	5.4	1445.1	6.2
n4727_KRN12-2_@10	3148	2618	780	0.83	0.40	2.6013	0.77	5.423	0.73	0.1023	0.25	-36.0	1666.4	4.5	1301.0	5.7	1091.0	7.3
n4899-R1-G3	3270	2821	783	0.86	0.33	2.4728	0.53	5.654	0.48	0.1014	0.22	-38.1	1649.8	4.1	1264.1	3.9	1049.9	4.7
n4727_KRN12-2_@4	1625	1071	353	0.66	0.47	2.3441	0.90	5.933	0.87	0.1009	0.26	-40.2	1640.2	4.8	1225.8	6.5	1004.1	8.1
n4899-R4-G3	1189	785	251	0.66	1.72	2.1025	0.74	6.309	0.51	0.0962	0.53	-38.9	1551.9	10.0	1149.6	5.1	948.4	4.5
n4727_KRN12-2_@18	2518	1952	419	0.78	0.62	1.5538	1.24	8.002	1.07	0.0902	0.64	-45.9	1429.3	12.2	952.0	7.7	759.1	7.6
n4899-R4-G5b	1333	960	196	0.72	0.91	1.3806	0.60	8.776	0.48	0.0879	0.36	-50.2	1379.7	6.8	880.7	3.5	695.6	3.2
n4727_KRN12-2_@17	1398	1132	187	0.81	1.33	1.2346	3.13	9.559	2.52	0.0856	1.85	-43.1	1329.0	35.5	816.4	17.7	641.4	15.4
n4727_KRN12-2_@11	1473	909	187	0.62	1.08	1.0742	1.28	10.026	1.07	0.0781	0.70	-44.3	1149.6	13.9	740.8	6.8	612.9	6.3
n4899-R3-G1b	2114	1278	200	0.60	0.92	0.6995	0.75	13.497	0.47	0.0685	0.58	-45.0	882.9	12.0	538.5	3.1	460.8	2.1

continued on following pages. R: analyses on rim of zircon grain.

Table 6-2. – continued. Geochronology results for zircon from Kiirunavaara intrusions: U-Pb-Th SIMS analytical data.

Sample/ spot #	[U] ppm	[Th] ppm	[Pb] ppm	Th/U meas	f_{206}%[1]	Isotopic ratios $^{207}Pb/^{235}U$	±σ %	$^{238}U/^{206}Pb$	±σ %	$^{207}Pb/^{206}Pb$	±σ %	Disc	Ages (Ma) $^{207}Pb/^{206}Pb$	±σ	$^{207}Pb/^{235}U$	±σ	$^{206}Pb/^{238}U$	±σ
c) KRN-12-03 (Kiirunavaara syenite)																		
n4898-R4-G2	225	124	96	0.55	0.03	5.2786	0.56	3.010	0.47	0.1152	0.31	-0.4	1883.6	5.5	1865.4	4.8	1849.2	7.6
n4726_KRN12-3_@7	483	865	246	1.79	0.32	4.8317	0.95	3.279	0.93	0.1149	0.17	-8.0	1878.4	3.1	1790.4	8.0	1715.9	14.1
n4726_KRN12-3_@6	2782	24383	2098	8.77	0.21	4.6513	0.77	3.352	0.75	0.1131	0.16	-8.7	1849.2	2.9	1758.5	6.5	1683.2	11.2
n4898-R2-G2	141	502	64	3.57	1.65	3.4749	1.53	4.457	1.04	0.1123	1.13	-26.5	1837.3	20.3	1521.5	12.2	1305.0	12.2
n4726_KRN12-3_@3	273	609	114	2.23	1.17	3.7413	1.75	4.099	1.70	0.1112	0.39	-22.1	1819.6	7.0	1580.3	14.1	1407.2	21.6
n4726_KRN12-3_@13	66	329	53	4.96	0.41	4.3931	0.96	3.487	0.82	0.1111	0.49	-9.3	1817.7	8.9	1711.1	8.0	1625.3	11.8
n4726_KRN12-3_@8	3954	4481	1285	1.13	0.38	3.4970	0.99	4.292	0.88	0.1089	0.45	-24.3	1780.3	8.2	1526.5	7.8	1350.2	10.7
n4726_KRN12-3_@1	3194	8405	1242	2.63	0.64	3.3439	1.52	4.466	1.51	0.1083	0.19	-26.9	1771.1	3.5	1491.4	12.0	1302.6	17.8
n4726_KRN12-3_@11	685	1559	241	2.28	0.45	2.8720	0.86	5.038	0.73	0.1049	0.46	-32.4	1713.3	8.4	1374.6	6.5	1167.2	7.8
n4898-R1-G3	1468	2818	299	1.92	1.80	1.6360	1.52	8.274	1.34	0.0982	0.72	-52.8	1589.7	13.3	984.2	9.6	735.5	9.3
n4898-R2-G3	2956	15385	914	5.20	1.49	1.8317	4.39	7.364	4.24	0.0978	1.13	-44.0	1583.1	21.0	1056.9	29.2	820.9	32.7
n4898-R4-G4	832	1848	228	2.22	0.77	2.1285	2.32	6.330	2.23	0.0977	0.65	-39.0	1581.1	12.1	1158.1	16.1	945.5	19.6
n4726_KRN12-3_@5	1193	4433	342	3.72	0.99	1.8754	1.64	7.044	1.61	0.0958	0.32	-45.2	1544.1	6.0	1072.4	11.0	855.7	12.9
n4726_KRN12-3_@10	866	2411	214	2.78	0.92	1.7229	1.54	7.396	1.39	0.0924	0.66	-43.6	1476.0	12.4	1017.1	9.9	817.5	10.7
n4898-R3-G2	1209	2872	208	2.37	2.22	1.1867	1.73	10.240	1.63	0.0881	0.57	-55.7	1385.3	10.9	794.4	9.6	600.7	9.4
n4726_KRN12-3_@16	875	2931	202	3.35	1.13	1.3979	1.49	8.461	1.43	0.0858	0.42	-45.7	1333.2	8.1	888.1	8.9	720.2	9.8
n4726_KRN12-3_@2	2223	4674	249	2.10	6.57	0.7658	3.83	14.468	1.91	0.0804	3.32	-44.6	1205.6	64.0	577.3	17.0	430.9	7.9
n4898-R3-G4	1178	3251	194	2.76	2.43	0.9530	1.02	11.479	0.71	0.0793	0.74	-51.8	1180.6	14.5	679.6	5.1	538.4	3.7
n4726_KRN12-3_@9	1368	3866	234	2.83	2.22	1.0016	5.26	10.786	4.83	0.0784	2.10	-38.5	1155.8	41.2	704.6	27.1	571.6	26.4
n4726_KRN12-3_@15	1132	3364	175	2.97	2.21	0.8553	2.78	12.052	1.63	0.0748	2.26	-38.2	1062.1	44.7	627.6	13.1	513.9	8.1
n4726_KRN12-3_@17	1292	2545	175	1.97	1.20	0.8281	0.95	12.155	0.73	0.0730	0.61	-47.3	1014.1	12.4	612.6	4.4	509.6	3.6
n4898-R2-G1	2419	15343	344	6.34	5.01	0.5421	1.22	18.480	0.65	0.0727	1.03	-60.0	1004.3	20.8	439.8	4.4	339.7	2.2
n4726_KRN12-3_@14	1550	5383	196	3.47	3.17	0.6198	1.16	16.082	0.83	0.0723	0.81	-56.6	994.2	16.4	489.7	4.5	388.9	3.1
n4898-R1-G4	1953	4275	238	2.19	2.18	0.6707	0.93	14.473	0.48	0.0704	0.80	-49.9	940.2	16.3	521.1	3.8	430.7	2.0
n4726_KRN12-3_@12	2527	5214	271	2.06	3.49	0.6027	1.03	15.550	0.76	0.0680	0.70	-49.7	867.7	14.4	478.9	4.0	401.8	3.0
n4726_KRN12-3_@18	2664	12442	347	4.67	4.63	0.5413	4.09	16.441	3.62	0.0645	1.91	-34.4	759.5	39.8	439.3	14.7	380.6	13.4
n4726_KRN12-3_@4	1519	20585	369	13.55	39.07	0.9829	58.21	8.633	6.50	0.0615	57.85		658.3	911.7	695.1	345.7	706.5	43.6
c) KRN-12-05 (Kiirunavaara granite)																		
n4725_KRN12-5_@18	82	136	48	1.67	1.57	5.9428	6.62	2.762	3.59	0.1190	5.56		1941.9	96.2	1967.5	59.2	1992.0	61.8
n4725_KRN12-5_@11 R	111	48	46	0.44	{0.04}	5.3350	0.91	2.998	0.84	0.1160	0.34	-0.1	1895.4	6.2	1874.5	7.8	1855.6	13.5
n4725_KRN12-5_@15	91	73	40	0.81	{0.02}	5.3148	1.54	3.002	1.49	0.1157	0.38		1891.4	6.8	1871.2	13.2	1853.2	24.0
n4725_KRN12-5_@21	144	62	59	0.43	{0.01}	5.2730	1.54	3.021	1.50	0.1155	0.37		1888.2	6.7	1864.5	13.2	1843.3	24.0
n4897-R1-G1	86	107	43	1.24	{0.00}	5.3491	0.68	2.978	0.47	0.1155	0.49		1888.1	8.8	1876.7	5.9	1866.5	7.7
n4897-R4-G5	142	94	63	0.66	{0.01}	5.3838	0.61	2.954	0.47	0.1153	0.38		1885.2	6.9	1882.3	5.2	1879.7	7.7
n4725_KRN12-5_@9	88	37	37	0.42	{0.03}	5.3587	0.98	2.967	0.90	0.1153	0.37		1884.9	6.7	1878.3	8.4	1872.3	14.7
n4725_KRN12-5_@13	96	51	40	0.52	0.04	5.2697	1.53	3.017	1.49	0.1153	0.36		1884.6	6.4	1864.0	13.1	1845.6	23.9
n4725_KRN12-5_@17	133	82	57	0.62	{0.01}	5.2946	1.52	3.002	1.49	0.1153	0.30		1884.0	5.3	1868.0	13.0	1853.6	24.0
n4725_KRN12-5_@12	168	81	70	0.48	{0.02}	5.2611	0.93	3.020	0.89	0.1152	0.27	-0.3	1883.4	4.9	1862.6	8.0	1844.0	14.2
n4725_KRN12-5_@14	65	90	32	1.40	{0.03}	5.2764	1.56	3.010	1.49	0.1152	0.45		1882.9	8.1	1865.0	13.4	1849.0	24.0
n4725_KRN12-5_@23	133	70	56	0.53	0.03	5.3124	1.53	2.989	1.50	0.1151	0.29		1882.2	5.3	1870.9	13.2	1860.6	24.3
n4897-R5-G2	190	110	72	0.58	{0.01}	4.5680	1.31	3.472	1.25	0.1150	0.40	-12.2	1880.3	7.1	1743.4	11.0	1631.6	18.0
n4725_KRN12-5_@4	189	96	78	0.51	0.02	5.2260	0.85	3.034	0.81	0.1150	0.26	-0.7	1880.0	4.6	1856.9	7.3	1836.3	13.0
n4897-R3-G7	201	170	93	0.85	0.03	5.3956	0.58	2.938	0.48	0.1150	0.33		1879.7	6.0	1884.1	5.0	1888.2	7.8
n4725_KRN12-5_@22	189	475	117	2.52	0.02	5.3399	1.58	2.969	1.56	0.1150	0.25		1879.6	4.6	1875.3	13.6	1871.3	25.4
n4725_KRN12-5_@20	121	285	72	2.36	0.04	5.3103	1.53	2.983	1.49	0.1149	0.38		1878.4	6.8	1870.5	13.2	1863.4	24.1

continued on following page. R: analyses on rim of zircon grain.

Table 6-2 – continued**.** Geochronology results for zircon from Kiirunavaara intrusions: U-Pb-Th SIMS analytical data.

						Isotopic ratios							Ages (Ma)					
Sample/ spot #	**[U] ppm**	**[Th] ppm**	**[Pb] ppm**	**Th/U meas**	**f_{206}%[1]**	**$^{207}Pb/^{235}U$**	**±σ %**	**$^{238}U/^{206}Pb$**	**±σ %**	**$^{207}Pb/^{206}Pb$**	**±σ %**	**Disc[2]**	**$^{207}Pb/^{206}Pb$**	**±σ**	**$^{207}Pb/^{235}U$**	**±σ**	**$^{206}Pb/^{238}U$**	**±σ**
c) KRN-12-05 (Kiirunavaara granite) continued																		
n4725_KRN12-5_@2	127	100	56	0.79	{0.03}	5.2681	1.75	3.007	1.71	0.1149	0.37		1878.3	6.6	1863.7	15.0	1850.6	27.5
n4725_KRN12-5_@16	181	149	82	0.82	0.02	5.3106	1.53	2.981	1.51	0.1148	0.25		1877.3	4.5	1870.6	13.1	1864.6	24.5
n4725_KRN12-5_@19	201	119	86	0.59	0.02	5.2688	1.53	3.002	1.50	0.1147	0.28		1875.4	5.1	1863.8	13.1	1853.4	24.2
n4725_KRN12-5_@5	95	130	47	1.36	0.07	5.2343	0.90	3.019	0.82	0.1146	0.37		1873.8	6.7	1858.2	7.7	1844.4	13.1
n4725_KRN12-5_@6	165	150	76	0.91	{0.02}	5.2883	0.88	2.987	0.84	0.1146	0.27		1873.2	4.9	1867.0	7.6	1861.4	13.6
n4725_KRN12-5_@7	174	113	75	0.65	0.03	5.2522	0.87	3.008	0.83	0.1146	0.27		1873.1	4.8	1861.1	7.4	1850.4	13.3
n4897-R4-G2	88	130	46	1.48	{0.01}	5.3803	0.88	2.936	0.47	0.1146	0.74		1873.1	13.3	1881.7	7.5	1889.6	7.7
n4897-R4-G1	122	74	53	0.61	0.06	5.3176	0.64	2.970	0.47	0.1146	0.43		1872.9	7.7	1871.7	5.5	1870.7	7.7
n4897-R2-G1	103	73	46	0.70	{0.02}	5.3530	0.75	2.947	0.47	0.1144	0.59		1870.8	10.5	1877.4	6.5	1883.3	7.7
n4897-R1-G5	142	89	62	0.63	{0.01}	5.2933	0.61	2.980	0.47	0.1144	0.38		1870.3	6.9	1867.8	5.2	1865.5	7.7
n4897-R4-G4	155	92	60	0.59	0.03	4.6964	1.00	3.347	0.92	0.1140	0.40	-8.5	1864.4	7.2	1766.6	8.4	1685.0	13.7
n4725_KRN12-5_@10	211	163	89	0.77	0.03	4.9379	0.82	3.175	0.78	0.1137	0.25	-3.9	1859.6	4.6	1808.8	6.9	1765.0	12.0
n4725_KRN12-5_@8	721	338	202	0.47	0.10	3.2816	2.22	4.763	2.21	0.1134	0.20	-34.0	1853.9	3.6	1476.7	17.5	1228.6	24.8
n4897-R2-G5	563	326	201	0.58	0.16	4.2825	1.02	3.645	1.00	0.1132	0.23	-15.6	1851.7	4.2	1690.0	8.5	1562.8	13.9
n4725_KRN12-5_@3	537	477	240	0.89	0.04	5.0288	1.02	3.080	1.01	0.1123	0.16		1837.3	2.9	1824.2	8.7	1812.8	15.9
n4725_KRN12-5_@1	1546	2900	237	1.88	0.24	0.9964	0.86	10.389	0.83	0.0751	0.23	-44.9	1070.7	4.7	702.0	4.4	592.4	4.7

[1]Percentage of common ^{206}Pb in measured ^{206}Pb, estimated from ^{204}Pb counts. Figures in parentheses are given when no correction was applied and indicate a value calculated assuming a present-day Stacey & Kramers (1975) model terrestrial Pb-isotope composition. All other ratios are common Pb corrected. [2]Age discordance at closest approach of error ellipse to concordia (2σ level).

Table 6-3. Geochronology results for zircon from Nukutus, Rektorn and Tuolluvaara: U-Pb-Th SIMS analytical data.

Sample/ spot #	[U] ppm	[Th] ppm	[Pb] ppm	Th/U meas	f_{206}%[1]	Isotopic ratios $^{207}Pb/^{235}U$	±σ %	$^{238}U/^{206}Pb$	±σ %	$^{207}Pb/^{206}Pb$	±σ %	Disc[2]	Ages (Ma) $^{207}Pb/^{206}Pb$	±σ	$^{207}Pb/^{235}U$	±σ	$^{206}Pb/^{238}U$	±σ
a) NUK-12-02 (Nukutus ore)																		
n4729_NUK12-2_@10	713	224	596	0.31	1.80	11.7582	6.44	1.454	5.73	0.1240	2.94	58.9	2014.2	51.2	2585.3	62.2	3374.5	152.4
n4896-R4-G2a	190	42	75	0.22	1.12	5.4027	0.75	3.027	0.49	0.1186	0.56	-2.9	1935.3	10.1	1885.3	6.4	1840.2	7.8
n4896-R1-G4	731	1017	453	1.39	0.41	6.8221	1.27	2.386	1.18	0.1180	0.47	16.7	1926.8	8.5	2088.6	11.3	2256.7	22.4
n4729_NUK12-2_@21	255	145	109	0.57	{0.01}	5.3766	0.99	2.978	0.96	0.1161	0.26		1897.5	4.6	1881.1	8.5	1866.4	15.5
n4896-R1-G1	364	169	130	0.47	0.10	4.4612	0.81	3.583	0.76	0.1159	0.28	-16.5	1894.4	4.9	1723.8	6.8	1586.8	10.8
n4896-R4-G5	113	36	46	0.32	{0.02}	5.3699	0.67	2.971	0.47	0.1157	0.47		1890.9	8.4	1880.1	5.7	1870.3	7.7
n4729_NUK12-2_@28	206	79	77	0.38	0.02	4.8692	0.89	3.276	0.85	0.1157	0.25	-8.6	1890.9	4.4	1796.9	7.5	1717.1	12.8
n4729_NUK12-2_@22 - R	362	125	134	0.35	0.08	4.8602	0.97	3.282	0.93	0.1157	0.28	-8.5	1890.5	5.1	1795.4	8.2	1714.6	14.1
n4896-R1-G5	292	95	118	0.33	{0.00}	5.3325	0.55	2.991	0.48	0.1157	0.27	-0.3	1890.3	4.8	1874.1	4.7	1859.5	7.7
n4729_NUK12-2_@19	184	70	70	0.38	0.04	4.9970	1.15	3.189	1.12	0.1156	0.28	-5.5	1888.7	4.9	1818.8	9.8	1758.4	17.3
n4896-R4-G1	245	87	101	0.35	{0.00}	5.3895	0.58	2.956	0.50	0.1155	0.31		1888.3	5.5	1883.2	5.0	1878.5	8.1
n4896-R1-G3	601	227	245	0.38	0.02	5.3084	0.51	2.999	0.47	0.1155	0.19	-0.7	1887.3	3.5	1870.2	4.4	1854.9	7.6
n4729_NUK12-2_@7 - R	496	162	203	0.33	0.01	5.4049	0.75	2.945	0.73	0.1154	0.16		1886.6	2.8	1885.6	6.4	1884.7	12.0
n4729_NUK12-2_@9	224	103	94	0.46	{0.01}	5.3365	0.79	2.982	0.76	0.1154	0.23		1886.5	4.1	1874.7	6.8	1864.1	12.3
n4896-R4-G2b	46	16	17	0.35	0.19	4.8714	0.94	3.267	0.51	0.1154	0.78	-6.2	1886.3	14.1	1797.3	7.9	1721.7	7.7
n4729_NUK12-2_@25	309	82	117	0.26	0.08	5.0366	1.05	3.159	1.02	0.1154	0.28	-4.5	1885.8	5.1	1825.5	9.0	1773.1	15.8
n4729_NUK12-2_@26	324	157	130	0.48	0.10	5.0873	0.83	3.127	0.80	0.1154	0.22	-4.1	1885.8	3.9	1834.0	7.1	1788.7	12.5
n4729_NUK12-2_@6	181	86	77	0.48	{0.01}	5.4300	0.78	2.929	0.73	0.1154	0.26		1885.4	4.7	1889.6	6.7	1893.5	12.1
n4729_NUK12-2_@24	435	144	178	0.33	0.00	5.3828	0.75	2.955	0.73	0.1153	0.17		1885.3	3.1	1882.1	6.5	1879.3	12.0
n4729_NUK12-2_@12	440	232	186	0.53	0.01	5.3165	0.77	2.991	0.74	0.1153	0.19		1884.8	3.4	1871.5	6.6	1859.6	12.0
n4896-R3-G6	180	69	74	0.39	{0.00}	5.3268	0.61	2.985	0.50	0.1153	0.36		1884.8	6.5	1873.2	5.3	1862.7	8.1
n4729_NUK12-2_@16	489	177	203	0.36	0.01	5.4127	0.76	2.937	0.74	0.1153	0.16		1884.6	2.9	1886.9	6.5	1889.0	12.1
n4896-R4-G4	380	111	147	0.29	0.06	5.0834	0.57	3.127	0.48	0.1153	0.30	-4.1	1884.3	5.4	1833.3	4.8	1788.8	7.5
n4729_NUK12-2_@17	244	93	100	0.38	{0.01}	5.3445	0.77	2.974	0.73	0.1153	0.22		1884.1	4.0	1876.0	6.6	1868.7	11.9
n4896-R2-G6a	329	423	113	1.29	1.02	3.4352	3.48	4.625	3.37	0.1152	0.88	-30.4	1883.6	15.7	1512.5	27.7	1261.7	38.7
n4729_NUK12-2_@8	259	87	105	0.34	0.02	5.3250	0.85	2.984	0.82	0.1152	0.22		1883.4	4.0	1872.9	7.3	1863.4	13.4
n4729_NUK12-2_@30	320	111	122	0.35	0.06	4.9746	0.76	3.193	0.73	0.1152	0.21	-6.0	1883.0	3.7	1815.0	6.4	1756.3	11.3
n4729_NUK12-2_@29	595	172	238	0.29	0.01	5.3058	0.74	2.993	0.73	0.1152	0.14		1882.4	2.5	1869.8	6.4	1858.5	11.8
n4729_NUK12-2_@3	351	140	147	0.40	0.21	5.4246	0.77	2.927	0.73	0.1151	0.25		1882.1	4.5	1888.7	6.7	1894.8	12.0
n4729_NUK12-2_@5	292	109	111	0.37	0.14	4.8861	0.88	3.248	0.85	0.1151	0.23	-7.3	1881.7	4.1	1799.9	7.4	1730.1	12.8
n4896-R2-G2a	285	146	122	0.51	{0.00}	5.3636	0.58	2.959	0.47	0.1151	0.34		1881.6	6.1	1879.1	5.0	1876.7	7.7
n4729_NUK12-2_@14	268	137	110	0.51	0.03	5.1463	0.79	3.083	0.75	0.1151	0.25	-2.5	1881.3	4.5	1843.8	6.8	1810.7	11.9
n4896-R3-G3	247	118	103	0.48	{0.00}	5.2902	0.56	2.999	0.48	0.1151	0.30		1881.2	5.4	1867.3	4.8	1854.8	7.7
n4729_NUK12-2_@23	105	29	35	0.27	0.52	4.3030	1.01	3.687	0.89	0.1151	0.47	-17.4	1881.0	8.5	1693.9	8.3	1546.9	12.3
n4729_NUK12-2_@18	207	50	76	0.24	0.08	4.9067	0.78	3.233	0.74	0.1151	0.26	-6.9	1880.8	4.7	1803.4	6.6	1737.2	11.2
n4729_NUK12-2_@15	431	234	185	0.54	0.01	5.3537	0.91	2.963	0.88	0.1150	0.24		1880.6	4.2	1877.5	7.9	1874.7	14.4
n4896-R2-G6b	237	40	67	0.17	0.25	3.7602	0.69	4.218	0.53	0.1150	0.45	-27.8	1880.5	8.2	1584.3	5.6	1371.4	6.5
n4729_NUK12-2_@27 - R	200	85	83	0.43	{0.01}	5.3501	0.81	2.964	0.77	0.1150	0.23		1880.3	4.2	1876.9	6.9	1873.9	12.5
n4729_NUK12-2_@13	235	92	95	0.39	0.01	5.2360	0.82	3.029	0.79	0.1150	0.23	-0.6	1880.2	4.1	1858.5	7.0	1839.2	12.6
n4896-R3-G1	336	140	140	0.42	{0.00}	5.3537	0.55	2.962	0.48	0.1150	0.28		1880.1	5.1	1877.5	4.7	1875.2	7.8
n4729_NUK12-2_@1	361	196	157	0.54	0.03	5.4181	0.91	2.924	0.89	0.1149	0.18		1878.2	3.3	1887.7	7.9	1896.4	14.7
n4896-R4-G3	216	82	89	0.38	{0.00}	5.3065	0.57	2.976	0.47	0.1145	0.32		1872.7	5.8	1869.9	4.9	1867.4	7.7
n4896-R2-G2b	188	59	74	0.32	{0.01}	5.1438	0.59	3.067	0.47	0.1144	0.35	-1.3	1870.6	6.2	1843.4	5.0	1819.3	7.5
n4729_NUK12-2_@11	276	77	106	0.28	0.28	5.0368	1.11	3.122	1.06	0.1140	0.32	-2.0	1864.8	5.7	1825.5	9.5	1791.3	16.7
n4729_NUK12-2_@4	32	2	7	0.07	3.19	2.8082	2.43	5.534	1.48	0.1127	1.93	-36.2	1843.5	34.4	1357.7	18.4	1070.9	14.7
n4729_NUK12-2_@2 - R	1030	297	345	0.29	0.17	4.3130	0.77	3.554	0.76	0.1112	0.13	-12.2	1818.4	2.3	1695.8	6.4	1598.5	10.8
n4729_NUK12-2_@20	1355	448	255	0.33	0.38	2.0688	0.92	6.261	0.87	0.0939	0.31	-37.4	1506.8	5.9	1138.5	6.3	955.3	7.7

continued on following pages. R: analyses on rim of zircon grain.

Table 6-3 – continued. Geochronology results for zircon from Nukutus, Rektorn and Tuolluvaara: U-Pb-Th SIMS analytical data.

						Isotopic ratios							Ages (Ma)					
Sample/ spot #	[U] ppm	[Th] ppm	[Pb] ppm	Th/U meas	f_{206}%[1]	$^{207}Pb/^{235}U$	±σ %	$^{238}U/^{206}Pb$	±σ %	$^{207}Pb/^{206}Pb$	±σ %	Disc[2]	$^{207}Pb/^{206}Pb$	±σ	$^{207}Pb/^{235}U$	±σ	$^{206}Pb/^{238}U$	±σ
b) NUK-12-01 (Nukutus footwall)																		
n4719_NUK12-01_@24	60	40	39	0.67	6.35	7.7931	13.86	2.138	9.99	0.1208	9.61		1968.7	162.0	2207.4	133.1	2473.5	208.5
NUK12-1_zr_@40	238	192	98	0.81	{0.05}	5.0391	0.70	3.166	0.66	0.1157	0.23	-5.8	1891.2	4.1	1825.9	6.0	1769.2	10.3
n4719_NUK12-01_@14	148	112	63	0.76	0.06	5.1612	1.42	3.089	1.33	0.1156	0.49	-1.6	1889.9	8.9	1846.2	12.2	1807.8	21.0
n4719_NUK12-01_@15	246	192	109	0.78	{0.02}	5.2741	0.87	3.022	0.84	0.1156	0.23	-0.9	1889.2	4.2	1864.7	7.5	1842.7	13.5
n4719_NUK12-01_@21	329	699	187	2.12	{0.01}	5.2988	0.87	3.006	0.85	0.1155	0.20	-0.3	1888.0	3.6	1868.7	7.5	1851.3	13.7
n4719_NUK12-01_@22	141	86	60	0.61	{0.03}	5.3071	0.92	3.000	0.86	0.1155	0.31		1887.3	5.5	1870.0	7.9	1854.5	13.9
n4719_NUK12-01_@11	147	93	63	0.63	{0.02}	5.2950	0.96	3.005	0.89	0.1154	0.36		1886.4	6.5	1868.1	8.2	1851.6	14.3
NUK12-1_zr_@39	195	131	85	0.67	{0.01}	5.3134	0.70	2.993	0.66	0.1153	0.24		1885.0	4.4	1871.0	6.0	1858.4	10.7
n4719_NUK12-01_@28	102	88	46	0.86	0.03	5.2393	1.14	3.035	1.04	0.1153	0.47	0.0	1884.7	8.5	1859.0	9.7	1836.1	16.6
NUK12-1_zr_@45	243	189	107	0.78	{0.03}	5.2784	0.72	3.011	0.69	0.1153	0.22	-0.5	1884.0	3.9	1865.4	6.2	1848.8	11.1
n4719_NUK12-01_@19	100	54	42	0.54	{0.02}	5.3179	1.00	2.988	0.93	0.1153	0.37		1883.9	6.6	1871.7	8.6	1860.8	15.1
n4719_NUK12-01_@8	134	85	58	0.63	{0.03}	5.3237	0.94	2.985	0.85	0.1153	0.39		1883.9	7.0	1872.7	8.1	1862.6	13.8
n4719_NUK12-01_@26	186	144	89	0.77	1.34	5.5833	1.17	2.844	0.80	0.1152	0.85		1882.8	15.2	1913.5	10.1	1942.0	13.4
n4719_NUK12-01_@29	205	178	88	0.87	0.06	5.0765	1.02	3.127	0.97	0.1151	0.33	-3.3	1881.9	6.0	1832.2	8.7	1788.7	15.1
n4719_NUK12-01_@10	191	144	94	0.75	2.47	5.8025	4.09	2.736	1.90	0.1151	3.63		1881.8	63.9	1946.8	36.1	2008.5	32.8
n4719_NUK12-01_@23	120	73	50	0.61	{0.03}	5.2090	0.90	3.047	0.83	0.1151	0.35	-0.9	1881.6	6.4	1854.1	7.7	1829.7	13.3
n4719_NUK12-01_@16	183	133	80	0.73	{0.02}	5.2563	0.90	3.019	0.85	0.1151	0.27	-0.2	1881.3	4.9	1861.8	7.7	1844.4	13.7
n4719_NUK12-01_@25	135	123	56	0.91	0.20	5.1050	1.08	3.107	1.02	0.1150	0.35	-2.4	1880.3	6.3	1836.9	9.2	1798.9	16.1
n4719_NUK12-01_@20	162	111	69	0.69	0.07	5.1883	0.96	3.054	0.91	0.1149	0.30	-1.0	1878.8	5.4	1850.7	8.2	1825.8	14.5
NUK12-1_zr_@42	173	106	74	0.62	{0.03}	5.2991	0.71	2.989	0.66	0.1149	0.26		1878.2	4.7	1868.7	6.1	1860.2	10.7
n4719_NUK12-01_@12	312	207	126	0.67	0.24	4.9701	0.95	3.185	0.89	0.1148	0.31	-4.9	1877.1	5.6	1814.3	8.0	1760.0	13.8
n4719_NUK12-01_@27	152	98	65	0.64	0.04	5.2346	0.94	3.024	0.89	0.1148	0.30		1877.1	5.4	1858.3	8.1	1841.5	14.3
n4719_NUK12-01_@17	184	131	81	0.71	{0.02}	5.2843	0.94	2.994	0.90	0.1148	0.27		1876.0	4.9	1866.3	8.1	1857.6	14.6
NUK12-1_zr_@43	277	213	120	0.77	0.09	5.1962	0.74	3.045	0.70	0.1147	0.26	-0.9	1875.8	4.7	1852.0	6.3	1830.9	11.1
NUK12-1_zr_@41	132	72	56	0.55	{0.03}	5.3017	0.73	2.982	0.66	0.1147	0.30		1874.6	5.4	1869.1	6.2	1864.2	10.7
NUK12-1_zr_@44	307	274	122	0.89	0.06	4.7370	0.72	3.337	0.69	0.1147	0.21	-9.6	1874.4	3.8	1773.8	6.0	1689.6	10.2
n4719_NUK12-01_@18	163	117	73	0.72	0.86	5.3914	1.12	2.921	0.97	0.1142	0.55		1867.6	9.9	1883.5	9.6	1897.9	16.0
n4719_NUK12-01_@9	169	120	79	0.71	1.62	5.4828	1.13	2.850	0.94	0.1133	0.62	1.8	1853.5	11.2	1897.9	9.7	1938.8	15.8
n4719_NUK12-01_@13	234	99	76	0.42	0.27	3.8907	1.08	3.878	1.03	0.1094	0.31	-17.2	1790.0	5.6	1611.8	8.7	1478.8	13.6
c) REK-10-01 (Rektorn hanging wall)																		
n3916_REK1@51	129	50	54	0.39	{0.04}	5.3888	2.11	2.961	2.02	0.1157	0.58		1890.9	10.4	1883.1	18.2	1876.0	33.0
n3916-REK1@55 - R	496	186	191	0.38	0.04	4.9025	2.18	3.210	2.15	0.1141	0.33	-3.0	1866.3	6.0	1802.7	18.5	1748.2	33.1
n3916_REK1@48	389	218	140	0.56	0.13	4.3831	2.48	3.589	2.45	0.1141	0.41	-12.5	1865.5	7.4	1709.1	20.7	1584.5	34.5
n3916_REK1@50	287	149	113	0.52	0.09	4.8206	1.91	3.238	1.87	0.1132	0.40	-3.2	1851.4	7.3	1788.5	16.2	1735.0	28.5
n3916_REK1@47	1447	357	214	0.25	1.29	1.8136	2.35	8.533	2.30	0.1122	0.46	-61.6	1836.1	8.4	1050.4	15.5	714.4	15.6
n3916-REK1@56	558	308	207	0.55	0.32	4.4815	3.89	3.435	3.78	0.1117	0.90	-3.2	1826.5	16.2	1727.5	32.8	1647.1	55.2
n3916_REK1@49 - R	1214	325	312	0.27	0.22	3.1703	2.78	4.714	2.69	0.1084	0.69	-28.1	1772.3	12.5	1449.9	21.7	1240.3	30.5
n3916-REK1@54	235	63	62	0.27	0.15	3.2030	2.35	4.597	2.29	0.1068	0.56	-25.9	1745.3	10.2	1457.9	18.4	1268.8	26.4
n3916_REK1@46	807	278	209	0.34	1.96	2.7851	8.48	4.645	6.98	0.0938	4.82		1504.6	88.4	1351.6	65.4	1257.0	80.2
n3916_REK1@53	5005	1696	777	0.34	0.34	1.5948	7.97	7.644	7.28	0.0884	3.24	-26.1	1391.4	61.0	968.2	51.0	792.6	54.5
n3916_REK1@52	867	53	57	0.06	1.23	0.5887	3.32	16.674	2.96	0.0712	1.51	-51.1	962.9	30.5	470.0	12.6	375.5	10.8
d) REK-10-02 (Rektorn hanging wall)																		
n3915-REK2@42	342	136	144	0.40	{0.01}	5.4482	2.36	2.911	2.33	0.1150	0.32		1880.0	5.8	1892.5	20.4	1903.9	38.6
n3915-REK2@39	868	637	376	0.73	0.16	5.1387	2.34	3.060	2.32	0.1140	0.29		1864.7	5.3	1842.5	20.1	1823.0	36.9
n3915-REK2@40	888	403	313	0.45	0.59	4.4212	2.23	3.539	2.20	0.1135	0.31	-11.3	1855.7	5.6	1716.3	18.6	1604.4	31.4
n3915-REK2@43 - R	38	3	[6]	0.07	4.92	2.0730	14.97	6.546	10.77	0.0984	10.39		1594.3	182.4	1139.9	108.1	916.5	92.7

continued on following pages. R: analyses on rim of zircon grain.

Table 6-3 continued. Geochronology results for zircon from Nukutus, Rektorn and Tuolluvaara: U-Pb-Th SIMS analytical data.

						Isotopic ratios							Ages (Ma)					
Sample/ spot #	[U] ppm	[Th] ppm	[Pb] ppm	Th/U meas	f_{206}%[1]	$^{207}Pb/^{235}U$	±σ %	$^{238}U/^{206}Pb$	±σ %	$^{207}Pb/^{206}Pb$	±σ %	Disc[2]	$^{207}Pb/^{206}Pb$	±σ	$^{207}Pb/^{235}U$	±σ	$^{206}Pb/^{238}U$	±σ
d) REK-10-02 (Rektorn hanging wall) continued																		
n3915-REK2@44	2286	216	341	0.09	2.46	1.7080	3.14	7.534	3.00	0.0933	0.91	-43.3	1494.6	17.1	1011.5	20.3	803.4	22.7
n3915-REK2@41	2172	1070	278	0.49	2.90	1.2287	6.14	9.690	4.43	0.0864	4.26	-30.6	1346.1	80.0	813.7	35.0	633.1	26.8
n3915-REK2@45	1	12	1	8.97	12.29	2.4461	41.80	4.574	8.86	0.0811	40.85		1224.9	643.8	1256.3	357.4	1274.7	103.3
e) REK-12-01 (Rektorn hanging wall)																		
REK12-1_zr_@28	119	36	49	0.30	{0.02}	5.4323	0.75	2.946	0.69	0.1161	0.31		1896.4	5.6	1890.0	6.5	1884.1	11.2
REK12-1_zr_@22	485	198	201	0.41	{0.01}	5.3569	0.69	2.978	0.67	0.1157	0.17		1890.9	3.0	1878.0	5.9	1866.3	10.9
REK12-1_zr_@29	239	103	100	0.43	{0.02}	5.3575	0.70	2.970	0.66	0.1154	0.22		1886.2	3.9	1878.1	6.0	1870.8	10.8
REK12-1_zr_@15	173	70	71	0.41	{0.02}	5.3211	0.71	2.989	0.66	0.1154	0.27		1885.5	4.9	1872.3	6.1	1860.4	10.7
REK12-1_zr_@27	200	118	86	0.59	{0.02}	5.3307	0.72	2.982	0.66	0.1153	0.29		1884.4	5.3	1873.8	6.2	1864.2	10.7
REK12-1_zr_@24	302	128	125	0.42	{0.01}	5.3091	0.73	2.993	0.70	0.1152	0.20		1883.7	3.6	1870.3	6.2	1858.3	11.3
REK12-1_zr_@18	435	164	178	0.38	{0.02}	5.3259	0.72	2.983	0.70	0.1152	0.17		1883.6	3.1	1873.0	6.2	1863.5	11.3
REK12-1_zr_@33	740	311	305	0.42	{0.01}	5.2928	0.67	2.994	0.66	0.1149	0.13		1878.7	2.3	1867.7	5.8	1857.8	10.7
REK12-1_zr_@30	495	194	204	0.39	{0.01}	5.3313	0.68	2.972	0.66	0.1149	0.16		1878.5	2.8	1873.9	5.8	1869.8	10.8
REK12-1_zr_@35	318	203	139	0.64	{0.01}	5.3586	0.70	2.950	0.67	0.1147	0.20		1874.6	3.6	1878.3	6.0	1881.6	10.9
REK12-1_zr_@21	148	85	62	0.58	{0.02}	5.1661	0.74	3.055	0.68	0.1145	0.29	-0.9	1871.3	5.3	1847.1	6.3	1825.6	10.9
REK12-1_zr_@25 - R	439	108	167	0.25	0.04	5.0551	0.73	3.117	0.71	0.1143	0.18	-3.0	1868.4	3.3	1828.6	6.2	1793.9	11.1
REK12-1_zr_@26	492	239	198	0.49	0.03	5.0427	0.68	3.123	0.66	0.1142	0.16	-3.2	1867.6	3.0	1826.5	5.8	1790.7	10.3
REK12-1_zr_@31	556	182	199	0.33	0.15	4.6332	0.71	3.396	0.69	0.1141	0.17	-10.8	1865.8	3.0	1755.3	6.0	1664.0	10.2
REK12-1_zr_@16	74	28	29	0.38	{0.04}	5.0307	0.79	3.115	0.66	0.1137	0.42	-1.6	1858.8	7.6	1824.5	6.7	1794.6	10.4
REK12-1_zr_@34	437	187	156	0.43	0.05	4.4621	0.70	3.478	0.67	0.1126	0.19	-11.6	1841.2	3.4	1724.0	5.8	1629.0	9.7
REK12-1_zr_@32	605	143	110	0.24	0.45	2.2744	1.15	6.812	1.12	0.1124	0.24	-54.0	1838.0	4.4	1204.4	8.1	883.0	9.3
REK12-1_zr_@20	840	359	284	0.43	0.11	4.2874	1.38	3.609	1.38	0.1122	0.15	-13.5	1835.9	2.8	1690.9	11.5	1576.5	19.3
REK12-1_zr_@19 - R	211	81	59	0.38	0.40	3.3711	1.77	4.568	1.72	0.1117	0.39	-30.3	1827.2	7.1	1497.7	13.9	1276.1	20.0
REK12-1_zr_@17 - R	1177	388	381	0.33	0.05	4.0999	1.09	3.739	1.04	0.1112	0.33	-15.7	1818.8	5.9	1654.3	8.9	1527.8	14.2
REK12-1_zr_@36 - R	334	214	102	0.64	0.21	3.5799	1.09	4.271	0.82	0.1109	0.71	-24.5	1814.2	12.8	1545.1	8.7	1356.1	10.1
REK12-1_zr_@23	1776	699	547	0.39	0.06	3.8201	0.68	3.964	0.67	0.1098	0.13	-20.3	1796.4	2.3	1597.0	5.5	1450.2	8.7
REK12-1_zr_@14	1056	510	293	0.48	0.34	3.2975	2.04	4.517	2.03	0.1080	0.22	-26.7	1766.3	3.9	1480.5	16.0	1289.3	23.7
f) TUV-10-01 (Tuolluvaara ore)																		
n3912_TUV1#1@14	841	4963	288	5.90	0.75	1.3910	3.67	8.366	3.43	0.0844	1.33	-38.0	1301.7	25.6	885.1	21.9	727.9	23.6
n3912_TUV1#1@15	1177	5134	266	4.36	1.33	1.0915	3.17	10.914	2.96	0.0864	1.14	-53.4	1347.1	21.8	749.2	17.0	565.1	16.1
n3912_TUV1@29	1069	3925	256	3.67	0.62	1.2454	2.47	8.998	2.27	0.0813	0.99	-40.6	1228.3	19.3	821.3	14.0	679.3	14.6

[1]Percentage of common ^{206}Pb in measured ^{206}Pb, estimated from ^{204}Pb counts. Figures in parentheses are given when no correction was applied and indicate a value calculated assuming a present-day Stacey & Kramers (1975) model terrestrial Pb-isotope composition. All other ratios are common Pb corrected. [2]Age discordance at closest approach of error ellipse to concordia (2σ level).

Table 6-4. Geochronology results for titanite from Kiirunavaara, Tuolluvaara, and secondary standard Khan: U-Pb-Th SIMS analytical data.

						Isotopic ratios							Ages (Ma)					
Sample/ spot #	[U] ppm	[Th] ppm	[Pb] ppm	$^{206}Pb/^{204}Pb$ meas.	f_{206}%[1]	$^{207}Pb/^{235}U$	±σ %	$^{238}U/^{206}Pb$	± σ %	$^{207}Pb/^{206}Pb$	± σ %	Disc.[2]	$^{207}Pb/^{206}Pb$	± σ	$^{207}Pb/^{235}U$	± σ	$^{206}Pb/^{238}U$	± σ
f) K-6 (Kiirunavaara footwall)																		
n3918_ttn_K6@7	13	13	13	3706	0.41	5.4792	3.01	2.917	2.68	0.1159	1.38		1894.1	24.7	1897.3	26.2	1900.3	44.2
n3918_ttn_K6@6	9	9	11	2963	0.52	5.4206	3.13	2.947	2.69	0.1158	1.60		1893.0	28.4	1888.1	27.2	1883.7	44.0
n3918_ttn_K6@1	12	12	13	1064	1.44	5.3419	3.24	2.969	2.68	0.1150	1.82		1880.2	32.4	1875.6	28.1	1871.5	43.7
n3918_ttn_K6@5	13	13	16	20690	0.07	5.3980	2.92	2.937	2.68	0.1150	1.17		1879.5	20.9	1884.5	25.4	1889.1	44.0
n3918_ttn_K6@2	11	11	13	7167	0.21	5.3803	3.02	2.931	2.68	0.1144	1.40		1870.3	25.0	1881.7	26.2	1892.1	44.1
n3918_ttn_K6@8	19	19	27	3830	0.40	5.3204	2.98	2.948	2.68	0.1138	1.31		1860.5	23.4	1872.2	25.8	1882.6	43.9
n3918_ttn_K6@4	10	10	11	1151	1.34	5.2531	3.28	2.981	2.68	0.1136	1.89		1857.1	33.8	1861.3	28.4	1865.0	43.5
n3918_ttn_K6@3	11	11	13	1772	0.87	5.2353	3.25	2.977	2.68	0.1130	1.85		1849.0	33.0	1858.4	28.1	1866.8	43.6
n3918_ttn_K6@9	7	7	14	125	12.32	4.9459	7.46	2.632	2.69	0.0944	6.96	2.62	1516.4	125.9	1810.1	65.1	2076.0	47.9
b) TUV-10-03 (Tuolluvaara host)																		
n3919_ttn_TUV3@23	38	38	15	8876	0.18	4.6812	2.81	3.192	2.68	0.1084	0.85		1772.2	15.5	1763.9	23.8	1756.9	41.3
n3919_ttn_TUV3@16	17	17	9	5348	0.29	4.4456	3.19	3.335	2.69	0.1075	1.71		1758.0	31.0	1720.9	26.8	1690.5	40.1
n3919_ttn_TUV3@19	7	7	3	2617	0.59	4.1264	4.12	3.592	2.69	0.1075	3.12		1757.5	56.0	1659.5	34.2	1583.2	37.8
n3919_ttn_TUV3@17	5	5	2	1733	0.90	4.1576	4.25	3.525	2.73	0.1063	3.26		1736.8	58.6	1665.7	35.4	1609.9	38.9
n3919_ttn_TUV3@10	31	31	13	9616	0.16	4.3016	2.88	3.345	2.68	0.1044	1.06		1703.3	19.3	1693.7	24.0	1685.9	39.9
n3919_ttn_TUV3@15	23	23	11	>1e6	* 0.00	4.1975	2.92	3.423	2.68	0.1042	1.16		1700.3	21.1	1673.5	24.2	1652.2	39.2
n3919_ttn_TUV3@13	49	49	20	64827	0.02	4.2806	2.77	3.355	2.68	0.1042	0.71		1699.7	13.0	1689.6	23.1	1681.6	39.8
n3919_ttn_TUV3@11	27	27	12	4183	0.37	4.2693	2.95	3.359	2.68	0.1040	1.25		1697.1	22.9	1687.5	24.6	1679.7	39.7
n3919_ttn_TUV3@20	60	60	23	>1e6	* 0.00	4.2424	2.76	3.377	2.68	0.1039	0.69		1695.2	12.6	1682.3	23.0	1671.9	39.6
n3919_ttn_TUV3@21	39	39	17	>1e6	* 0.00	4.1769	2.79	3.410	2.68	0.1033	0.78		1684.1	14.4	1669.5	23.1	1657.9	39.3
n3919_ttn_TUV3@18	31	31	12	10895	0.14	4.1806	2.87	3.396	2.68	0.1030	1.04		1678.3	19.1	1670.2	23.8	1663.8	39.4
n3919_ttn_TUV3@12	47	47	21	8260	0.19	4.0654	2.83	3.483	2.68	0.1027	0.89		1673.7	16.4	1647.4	23.3	1626.9	38.7
n3919_ttn_TUV3@22	21	21	10	>1e6	* 0.00	4.1935	2.93	3.367	2.69	0.1024	1.17		1668.4	21.6	1672.8	24.3	1676.2	39.8
n3919_ttn_TUV3@14	18	18	10	31381	* 0.05	3.9557	2.93	3.482	2.68	0.0999	1.19		1622.0	22.0	1625.2	24.1	1627.6	38.7
c) secondary standard Khan titanite																		
KHAN_110831_@6	55782	55782	5842	4729	0.38	0.6348	3.36	12.357	2.80	0.0569	1.85		487.5	40.4	499.1	13.3	501.6	13.5
KHAN_110831_@3	307	307	31	3311	0.54	0.6218	2.86	12.772	2.70	0.0576	0.94		514.6	20.5	491.0	11.2	485.9	12.6
KHAN_110831_@4	231	231	24	3503	0.51	0.6444	2.85	12.333	2.68	0.0576	0.96		516.0	20.9	505.0	11.4	502.6	13.0
KHAN_110831_@2	3375	3375	333	2688	0.67	0.6068	3.07	13.113	2.75	0.0577	1.37		518.7	29.8	481.5	11.8	473.8	12.6
KHAN_110831_@1	193	193	20	3470	0.52	0.6278	2.78	12.679	2.68	0.0577	0.75		519.7	16.3	494.8	10.9	489.4	12.6
KHAN_110831_@7	35886	35886	3720	3905	0.46	0.6496	4.01	12.495	2.71	0.0589	2.96		562.3	63.1	508.3	16.2	496.3	13.0
KHAN_110831_@5	429	429	44	400	4.48	0.6568	7.19	12.712	2.69	0.0606	6.67		623.3	137.6	512.6	29.4	488.2	12.6

[1]Percentage of common ^{206}Pb in measured ^{206}Pb, estimated from ^{204}Pb counts. Asterixis in front of values implies possibly insignificant common Pb (hence, inappropriate / over-correction). Ratios are common Pb corrected assuming a 1900 Ma (K-6), 1800 Ma (TUV-10-03) and 500 Ma (Khan) Stacey & Kramers (1975) model terrestrial Pb-isotope composition. [2]Age discordance at closest approach of error ellipse to concordia (2σ level).

7 Appendix B – Detailed analytical methods for chapter three, LA-ICPMS trace element data and U-Pb geochronology for monazite

7.1 Detailed analytical procedures

7.1.1 Sample preparation and whole rock geochemistry

Samples have been crushed using standard techniques and a split of each sample was further pulverized by shatter box for analysis of major and trace element geochemistry and tracer radiogenic isotopes (Sm-Nd and Lu-Hf). Trace element concentrations were analysed at the CREAIT facility at Memorial University of Newfoundland (MUN) inductively coupled plasma mass spectrometry (ICP-MS) PerkinElmer ELAN DRCII using the techniques of Longerich et al. (Longerich et al., 1990). The remainder of each sample was used for heavy mineral separation using standard techniques including heavy liquid and magnetic separation. Zircon and monazite were handpicked from the heavy mineral fraction under a binocular microscope and mounted in epoxy. Back-scatter electron (BSE) of all mounted mineral grains have been taken prior to all in situ analyses (laser ablation, U-Th-Pb geochronology) to select the locations for the spot analysis using the FEI Quanta 400 scanning electron microscope (SEM) at Memorial University of Newfoundland.

7.1.2 Sm-Nd whole rock analyses

Twenty-five representative samples were selected for Sm-Nd analyses on whole rock scale, which were done following an established “in house” protocol described briefly below. A mixed $^{150}Nd/^{149}Sm$ spike was added to the whole rock powders, which were then

dissolved in a 3:1 mixture of 29M HF – 15M HNO_3 in Savilex© Teflon beakers on a hotplate. After five to six days, the samples were evaporated to dryness and redissolved in 6M HCl for another two days. This solution was again dried down and brought up in 2.5M HCl. Sm and Nd were separated by conventional two-step column procedure. Bulk REE were separated using cation exchange resin Bio-Rad AG-50W-X8 and the resulting solution was brought up in 0.18M HCl after evaporation. Sm and Nd were then isolated using Eichrom© Ln resin. All reagents used were distilled.

Determinations of Sm and Nd isotopic compositions and contents were carried out using a multicollector Finnigan Mat 262 mass spectrometer in static and dynamic mode at MUN. $^{146}Nd/^{144}Nd = 0.7219$ and $^{152}Sm/^{147}Sm = 1.783$ were used to correct for instrumental mass bias. Standard JNdi-1 was analysed repeatedly during the data acquisition, resulting in an average $^{143}Nd/^{144}Nd + 0.512100\pm7$ (n=79, 2SD), and all sample$^{143}Nd/^{144}Nd$ ratios were adjusted to the reported value of this standard of $^{143}Nd/^{144}Nd = 0.512115\pm7$ (Tanaka et al., 2000). For quality control, the USGS BCR-2 standard was measured repeatedly during whole period and averaged at 0.512636±13 (n=12, 2SD), which is in excellent agreement with the reported value (Raczek et al., 2003). The uncertainties on Nd isotopic compositions are given at 2 standard error of the mean (2SE) and are typically <0.002%. Errors on the $^{147}Sm/^{144}Nd$ ratio are estimated to be less than 0.2%. The average total blank measured at the MUN TIMS laboratory was less than 200 pg for Nd and was considered negligible. Decay constant was 6.54 10^{-12} y^{-1} for ^{147}Sm by Steiger and Jäger (1977), and the εNd values were calculated using a $^{147}Sm/^{144}Nd$ ratio of 0.1967 and a $^{143}Nd/^{144}Nd$ ratio

of 0.512638 for the present day chondrite uniform reservoir (CHUR). The algorithm of Ickert (2010) was applied for determining initial εNd (εNd_i) and uncertainties.

7.1.3 Lu-Hf whole rock analyses

Representative samples were selected for whole rock ^{176}Lu-^{176}Hf analyses and analyzed following methods described by Patchett and Tatsumoto (1980), Vervoort and Blichert-Toft (1999), and Vervoort et al. (2004) and adjusted for the laboratory at MUN as described below and in Phillips (2015). In brief, whole rock powders were digested in a 3:1 mixture of 29M HF – 15M HNO_3 with mixed ^{176}Lu-^{180}Hf spikes in steel-jacketed PTFE dissolution vessels (Parr type). Exceptions are Hf-poor samples such as most ore samples, which have been spiked and digested in 3:1 HF-HNO_3 in Savilex© Teflon beakers on a hotplate. Following Vervoort et al. (2004), spikes with different ^{176}Lu-^{180}Hf compositions were used according to the Lu/Hf ratio of each sample. After 5-6 days of digestion, all samples were evaporated to dryness in Savilex© Teflon beakers and then completely dissolved in 6M HCl for about 2 days. The evaporated samples were dissolved in 1M HCl - 0.1M HF for a first column separation of the high field strength elements (HFSE, including Hf) from the heavy REE (HREE, including Lu and Yb), using Bio-rad AG 50W-X12. The HFSE split was brought up in 2.5M HCl after evaporation for removing Ti from the samples using 0.09Hcit - 0.45M HNO_3 + 1wt% H_2O_2 on columns with Ln spec resin. Hf was then eluted in 6M HCl - 0.4M HF and dried down for a Hf clean-up column using AG 50W-X12 resin. Lu was separated from Yb in Ln spec columns, using 2.5M HCl to remove most Yb and 6.2M HCl to elute Lu (see Vervoort et al., 2004, for details).

The Lu-Hf isotopic composition of the whole rock samples was determined using the Thermo-Finnigan Neptune multi-collector (MC) ICP-MS system in static mode at MUN. Lu and Hf splits were injected to the MC-ICPMS as 2% HNO_3 solutions using nebulizers with an average flow rate of 50 µl/min. In between samples, the nebulizer and spray chamber were cleaned by introducing 0.1% HF (Hf) or 2N HCl (Lu) into the inlet system for several minutes before equilibration with 2% HNO_3. Hf was measured over 75 cycles and Lu over 30 cycles of ~8 seconds integration time

Hf and Lu data reduction was done using the excel macros based on "LAMTOOL-Hf", provided by Jan Košler of the University of Bergen. A 202 ppb solution of JMC-475 Hf standard was measured regularly during each Hf session after about every fifth sample. Mass bias correction of Hf was done using $^{179}Hf/^{177}Hf$ (0.7325, Patchett and Tatsumoto, 1980) applying the exponential law ratio-by-ratio for each single analysis. During the two days of analyses for this study, the standard averaged $^{176}Hf/^{177}Hf = 0.282154 \pm 12$ (2SD, n=22). Session bias factors were determined using the mass bias corrected Hf isotopic composition of the JMC-475 Hf standard adjusted to the accepted values of $^{176}Hf/^{177}Hf$=0.282160, $^{178}Hf/^{177}Hf = 1.467170$ and $^{180}Hf/^{177}Hf = 1.886660$ (Blichert-Toft et al., 1997; Söderlund et al., 2004). Sample Hf analyses were further corrected for the ^{176}Yb interference on ^{176}Hf and the ^{180}W interference on ^{180}Hf using $^{176}Yb/^{173}Yb = 0.796310$ (Vervoort et al., 2004) and $^{180}W/^{182}W = 0.004501$ (Lee and Halliday, 1995).

Mixed Lu/Yb solutions were measured regularly after every fifth Lu analysis and at the beginning and end of each session. The small ^{176}Hf interference on ^{176}Lu was corrected for both standard solution and sample Lu analyses using the natural $^{176}Hf/^{177}Hf$ ratio of

0.282160 (Blichert-Toft et al., 1997) and the ^{177}Hf mass. Mass bias effects for Yb and the ^{176}Yb interference on ^{176}Lu are corrected using the protocol of Vervoort et al. (2004) and their natural ratios for $^{173}Yb/^{171}Yb$ ratio of 1.132338 and $^{176}Yb/^{173}Yb$ of 0.79631 and the measured ^{173}Yb mass. The Lu mass bias for the mixed Lu/Yb solutions is corrected using the natural $^{176}Lu/^{175}Lu$ ratio of 0.02655 and used to establish an empirically relationship of $\beta_{Yb} \sim 1.1\ \beta_{Lu}$ for the Neptune at MUN. This calculated β_{Lu} was then used to correct the interference corrected Lu sample analyses for mass bias (Vervoort et al., 2004). The USGS standard BCR-2 has been monitored during the course of the study and has a $^{176}Hf/^{177}Hf$ of 0.282867 ±8 (2SE) compared to the value of 0.282862 of Vervoort et al. (2004).

The values of Bouvier et al. (2008) of $^{176}Hf/^{177}Hf = 0.282785$ and $^{176}Lu/^{177}Hf = 0.0336$ for the CHUR have been used to calculate εHf values. Initial $^{176}Hf/^{177}Hf$ ($^{176}Hf/^{177}Hf_i$) have been calculated with the decay constant of Söderlund et al. (2004) for 1.88 Ga. The algorithm of Ickert (2010) was applied for determining initial εHf (εHf_i) and uncertainties.

7.1.4 Electron Probe Micro-Analyzer (EPMA)

Selected zircon grains from Kiirunavaara as well as from the Nukutusvaara ore deposit were analyzed in situ using the JEOL JXA-8230 EPMA at the Memorial University of Newfoundland. A total of 48 zircon analyses spot analyses were done by wavelength dispersive spectroscopy (WDS) with an accelerating voltage of 15 kV and a beam current of 20nA. Elements measured were Zr *Kα*, Si *Kα*, Hf *Mα*, Ca *Kα*, Y *Lα*, P *Kα*, and Fe *Kα,* all parameters for the analyses can be found in Table 7-1. The undoped pure synthetic zircon standard “SynZirc” (Hanchar et al., 2001) was used to apply correction factors for

the interferences of Si *Kα* on Hf *Mα*, and Zr *Lα* on P *Kα*, respectively. The standard was also analysed throughout the measurement session to ensure accurate data acquisition. Hf was used to normalize the LA-ICPMS analyses done in the same spots subsequently.

High resolution EPMA WDS X-ray maps of 10 zircon grains and 8 monazite grains were done using a voltage of 15 kV and a current of 250nA. Elements mapped in zircon were Hf *Mα*, Ca *Kα*, Y *Lα*, P*Kα*, and Fe*Kα* with a 1.0 μm step size and a 200 ms dwell time. Monazite maps of Ca *Kα*, Nd *Lα*, Th *Mα*, U*Mα* and La*Lα* were acquired from 8 monazite grains with a dwell time of 200 ms and a step size of 0.5 μm.

7.1.5 Transmission Electron Microscopy (TEM) and Fourier Transform Infrared (FTIR) analyses

Four zircon grains from the Kiirunavaara ore K-1 were studied by transmission electron microscopy (TEM) at the GFZ Potsdam. Foils for the TEM analyses were cut from zircon grains within one mount close to the LA-ICPMS trace element pit using a focused ion beam (Wirth, 2004). The FEI Tecnai G2 F20 X-Twin TEM at the GFZ is equipped with a high angle annular dark field (HAADF) detector, an EDAX energy dispersive X-ray spectroscopy system and a Gatan Tridiem energy filter.

Representative zircon crystals that were not previously mounted from K-1, NUK-12-01, KRN-12-03 and KRN-11-05 were analyzed by Fourier transform infrared spectroscopy (FTIR) at the California Institute of Technology. Infrared spectra were obtained on individual zircons using a Thermo-Nicolet iS50 FTIR with a CaF_2 beamsplitter, an incandescent silicon nitride source, and a MCT-A detector that is part of a Continuum infrared microscope with a 15× ReflAchromat objective. The zircons were oriented on a

(100) face and examined in an approximately 60 × 100 μm area. The infrared spectrum used in FTIR analysis detects OH molecule vibrations, either derived from OH ions bounded to a mineral species or from actual water molecules themselves. All results for these analyses have been reported as if they were water molecules for analytical convenience as is the convention in that area of research. The results were calibrated using grossular and a rhyolite glass as an approximation (Rossman, 2006) in the lack of a OH or H_2O -bearing zircon standard.

7.1.6 Trace element composition using Laser Ablation Inductively Coupled Plasma Mass Spectrometry (LA-ICPMS)

In situ LA-ICP-MS trace element geochemical analyses of the zircon grains were done using the Thermo-Finnigan ELEMENT XR coupled with a GeoLas 193 nm Excimer laser system at Memorial University of Newfoundland with a repetition rate of 8 Hz, and a fluence of 3 J/cm^2. Background was measured for ca. 30 seconds before the laser was fired for ca. 60 seconds, resulting in about 480 pulses per analyses. Carrier and auxiliary gas were helium and argon, respectively. For calibration, National Institute of Standards in Technology (NIST) 610 (~500 ppm) and 612 (~50 ppm) glasses (Pearce et al., 1997) were used as primary and secondary standard, respectively. Additional secondary standards used to assess the precision and accuracy of the analyses included JK-91500 (Wiedenbeck et al., 2004) and USGS BCR-2G (Pearce et al., 2007). All the standards were monitored throughout the measurement session to identify instrumental drift, mass bias, and mass fractionation. Spot sizes varied from 59 μm (JK-91500), 49 μm (NIST 612, BCR-2G) to 40

μm (NIST 610). Samples were analyses with a 40 μm spot size in the same locations as for EPMA analyses.

The LA-ICPMS data were reduced using Iolite software (Paton et al., 2011) using the EPMA determined Hf concentration as internal standard. Each analysis was carefully monitored for inclusions, which were excluded from data reduction. Iolite allows selection of representative signal intervals, background subtraction, and internal standard correction for ablation yield differences, instrument sensitivity drift during the analytical session. Long term averages of secondary standards glass BCR-2G and zircon JK-91500 and recommended values for NIST-612 (Pearce et al., 1997) have been compared with analyses from this study and show generally good correlations (see Table 7-2 to 7-5).

7.1.7 In situ dating of monazite by Secondary Ion Mass Spectrometry (SIMS)

The high spatial resolution U-Th-Pb mineral analyses were done using the Cameca ims1280 large-format high mass resolution ion microprobe at the Swedish Museum of Natural History (NordSIM facility). Analytical methods for monazite follow those described by Kirkland et al. (2009) for analyses done in 2011 (samples starting with n3911 and n3917). For all other analyses done in 2013, the adjustment as described in Gasser et al. (2015) have been applied. All SIMS U-Pb data for monazite grain analyses are presented in Table 7-6, sorted for each sample by decreasing $^{207}Pb/^{206}Pb$ ages.

Monazite standards used for calibrating U-Pb ratio were 270 Ma Trebilcock (Tomascak et al., 1996) and 1822 Ma KM03-72 (MacLachlan et al., 2004). Trebilcock monazite from a granitic pegmatite in southwestern Maine has 5600 ppm U and 1850 ppm Pb on average (average of three analyses from Tomascak et al., 1996). The latter reference

material KM03-72, kindly provided by G. Dunning, originates from a pelitic migmatite from the Rottenstone Domain, Trans-Hudson Orogen, Saskatchewan. Average U and Pb concentration are ca. 2500 and ca. 4400 ppm, respectively (averages of three analyses by G. Dunning, pers. comm.).

7.1.8 In situ Sm-Nd analyses of monazite by Laser Ablation Inductively Coupled Plasma Mass Spectrometry (LA-ICPMS)

Sm-Nd in monazite have been measured using the LA-MC-ICPMS (Finnigan Neptune) interfaced with a New Wave 213 nm laser at Washington State University following the methods discussed in Fisher et al. (2011). The operating parameters are summarized in Table 7-7. Unknowns were measured with a spot size of 20 μm, while the LREE and JNdi glass standards were analysed with spot sizes of 80 and 60 μm, respectively, due to their low Sm and Nd concentrations. Data reduction implements the correction procedures discussed in Fisher et al. (2011) in a customized scheme for Iolite (Paton et al., 2011). The Sm mass bias is corrected using the natural $^{147}Sm/^{149}Sm$ of Dubois (1992) and the interference of ^{144}Sm on ^{144}Nd is then corrected using the measured ^{149}Sm and the natural ratio of $^{144}Sm/^{149}Sm$ (e.g., Fisher et al., 2011; Iizuka et al., 2011). The mass bias for Nd is calculated using the natural $^{146}Nd/^{144}Nd$ ratio of 0.7219 (Wasserburg et al., 1981). The accuracy of the $^{147}Sm/^{144}Nd$ is ensured by bracketing the sample analyses with analyses of the LREE glass and allows correcting for mass bias, instrumental drift, elemental differences between Sm and Nd and laser induced fractionation.

7.2 Reference – Appendix B

Blichert-Toft, J., Chauvel, C., and Albarède, F., 1997, Separation of Hf and Lu for high-precision isotope analysis of rock samples by magnetic sector-multiple collector ICP-MS: Contributions to Mineralogy and Petrology, v. 127, p. 248-260.

Bouvier, A., Vervoort, J. D., and Patchett, P. J., 2008, The Lu-Hf and Sm-Nd isotopic composition of CHUR: Constraints from unequilibrated chondrites and implications for the bulk composition of terrestrial planets: Earth and Planetary Science Letters, v. 273, p. 48-57.

Chen, H., Clark, A. H., and Kyser, T. K., 2010, The Marcona magnetite deposit, Ica, south-central Peru: A product of hydrous, iron oxide-rich melts?: Economic Geology, v. 105, p. 1441-1456.

Dubois, J. C., Retali, G., and Cesario, J., 1992, Isotopic analysis of rare earth elements by total vaporization of samples in thermal ionization mass spectrometry: International Journal of Mass Spectrometry and Ion Processes, v. 120, p. 163-177.

Fisher, C. M., McFarlane, C. R. M., Hanchar, J. M., Schmitz, M. D., Sylvester, P. J., Lam, R., and Longerich, H. P., 2011, Sm-Nd isotope systematics by laser ablation-multicollector-inductively coupled plasma mass spectrometry: Methods and potential natural and synthetic reference materials: Chemical Geology, v. 284, p. 1-20.

Gasser, D., Jerabek, P., Faber, C., Stunitz, H., Menegon, L., Corfu, F., Erambert, M., and Whitehouse, M. J., 2015, Behaviour of geochronometers and timing of metamorphic reactions during deformation at lower crustal conditions: phase equilibrium modelling and U-Pb dating of zircon, monazite, rutile and titanite from the Kalak Nappe Complex, northern Norway: Journal of Metamorphic Geology, v. 33, p. 513-534.

Hanchar, J. M., Finch, R. J., Hoskin, P. W. O., Watson, E. B., Cherniak, D. J., and Mariano, A. N., 2001, Rare earth elements in synthetic zircon: Part 1. Synthesis, and rare earth element and phosphorus doping: American Mineralogist, v. 86, p. 667-680.

Iizuka, T., Eggins, S. M., McCulloch, M. T., Kinsley, L. P. J., and Mortimer, G. E., 2011, Precise and accurate determination of $^{147}Sm/^{144}Nd$ and $^{143}Nd/^{144}Nd$ in monazite using laser ablation-MC-ICPMS: Chemical Geology, v. 282, p. 45-57.

Kirkland, C., Whitehouse, M., and Slagstad, T., 2009, Fluid-assisted zircon and monazite growth within a shear zone: a case study from Finnmark, Arctic Norway: Contributions to Mineralogy and Petrology, v. 158, p. 637-657.

Lee, D.-C., and Halliday, A. N., 1995, Precise determinations of the isotopic compositions and atomic weights of molybdenum, tellurium, tin and tungsten using ICP magnetic sector multiple collector mass spectrometry: International Journal of Mass Spectrometry and Ion Processes, v. 146–147, p. 35-46.

Longerich, H. P., Jenner, G. A., Fryer, B. J., and Jackson, S. E., 1990, Inductively coupled plasma-mass spectrometric analysis of geological samples: A critical evaluation based on case studies: Chemical Geology, v. 83, p. 105-118.

MacLachlan, K., Rayner, N., Dunning, G., and Leugner, C., 2004, New results and ideas from the Rottenstone Domain project, Summary of Investigations 2004, 2,

Saskatchewan Geological Survey, Sask. Industry Resources, Misc. Rep. 2004-4.2, Paper A-3, p. 21.

Patchett, P. J., and Tatsumoto, M., 1980, A routine high-precision method for Lu-Hf isotope geochemistry and chronology: Contributions to Mineralogy and Petrology, v. 75, p. 263-267.

Paton, C., Hellstrom, J., Paul, B., Woodhead, J., and Hergt, J., 2011, Iolite: Freeware for the visualisation and processing of mass spectrometric data: Journal of Analytical Atomic Spectrometry, v. 26, p. 2508-2518.

Pearce, N. J. G., Denton, J. S., Perkins, W. T., Westgate, J. A., and Alloway, B. V., 2007, Correlation and characterisation of individual glass shards from tephra deposits using trace element laser ablation ICP-MS analyses: current status and future potential: Journal of Quaternary Science, v. 22, p. 721-736.

Pearce, N. J. G., Perkins, W. T., Westgate, J. A., Gorton, M. P., Jackson, S. E., Neal, C. R., and Chenery, S. P., 1997, A compilation of new and published major and trace element data for NIST SRM 610 and NIST SRM 612 glass reference materials: Geostandards Newsletter, v. 21, p. 115-144.

Phillips, S. E., 2015, High-spatial-resolution Sm-Nd & U-Pb and Lu-Hf & U-Pb isotope geochemistry of monazite and zircon in the Old Woman - Piute batholith, California: Unpub. M.Sc. thesis, Memorial University, 164 pp.

Raczek, I., Jochum, K. P., and Hofmann, A. W., 2003, Neodymium and strontium isotope data for USGS reference materials BCR-1, BCR-2, BHVO-1, BHVO-2, AGV-1, AGV-2F GSP-1, GSP-2 and eight MPI-DING reference glasses: Geostandards Newsletter-the Journal of Geostandards and Geoanalysis, v. 27, p. 173-179.

Rossman, G. R., 2006, Analytical Methods for Measuring Water in Nominally Anhydrous Minerals: Reviews in Mineralogy and Geochemistry, v. 62, p. 1-28.

Söderlund, U., Patchett, P. J., Vervoort, J. D., and Isachsen, C. E., 2004, The ^{176}Lu decay constant determined by Lu–Hf and U–Pb isotope systematics of Precambrian mafic intrusions: Earth and Planetary Science Letters, v. 219, p. 311-324.

Steiger, R., and Jäger, E., 1977, Subcommission on geochronology: Convention on the use of decay constants in geo- and cosmochronology: Earth and Planetary Science Letters, v. 36, p. 359-362.

Tanaka, T., Togashi, S., Kamioka, H., Amakawa, H., Kagami, H., Hamamoto, T., Yuhara, M., Orihashi, Y., Yoneda, S., Shimizu, H., Kunimaru, T., Takahashi, K., Yanagi, T., Nakano, T., Fujimaki, H., Shinjo, R., Asahara, Y., Tanimizu, M., and Dragusanu, C., 2000, JNdi-1: a neodymium isotopic reference in consistency with LaJolla neodymium: Chemical Geology, v. 168, p. 279-281.

Tomascak, P. B., Krogstad, E. J., and Walker, R. J., 1996, U-Pb Monazite Geochronology of Granitic Rocks from Maine: Implications for Late Paleozoic Tectonics in the northern Appalachians: The Journal of Geology, v. 104, p. 185-195.

Vervoort, J. D., and Blichert-Toft, J., 1999, Evolution of the depleted mantle: Hf isotope evidence from juvenile rocks through time: Geochimica Et Cosmochimica Acta, v. 63, p. 533-556.

Vervoort, J. D., Patchett, P. J., Söderlund, U., and Baker, M., 2004, Isotopic composition of Yb and the determination of Lu concentrations and Lu/Hf ratios by isotope

dilution using MC-ICPMS: Geochemistry, Geophysics, Geosystems, v. 5, p. Q11002.

Wasserburg, G. J., Jacousen, S. B., DePaolo, D. J., McCulloch, M. T., and Wen, T., 1981, Precise determination of Sm/Nd ratios, Sm and Nd isotopic abundances in standard solutions: Geochimica Et Cosmochimica Acta, v. 45, p. 2311-2323.

Wiedenbeck, M., Hanchar, J. M., Peck, W. H., Sylvester, P., Valley, J., Whitehouse, M., Kronz, A., Morishita, Y., Nasdala, L., Fiebig, J., Franchi, I., Girard, J. P., Greenwood, R. C., Hinton, R., Kita, N., Mason, P. R. D., Norman, M., Ogasawara, M., Piccoli, P. M., Rhede, D., Satoh, H., Schulz-Dobrick, B., Skår, O., Spicuzza, M. J., Terada, K., Tindle, A., Togashi, S., Vennemann, T., Xie, Q., and Zheng, Y. F., 2004, Further Characterisation of the 91500 Zircon Crystal: Geostandards and Geoanalytical Research, v. 28, p. 9-39.

Wirth, R., 2004, Focused Ion Beam (FIB): A novel technology for advanced application of micro- and nanoanalysis in geosciences and applied mineralogy: European Journal of Mineralogy, v. 16, p. 863-876.

Table 7-1. Electron probe micro-analyser elements measured and associated crystals, standards and parameters used.

Oxide	Crystal	Standard	Peak Position	Lower Background (mm)	Upper Background (mm)	Spot size	Count time (s)
FeO	LIFL	Magnetite	134.608	7.5	4.0	focused	10 on, 5 off
Y_2O_3	PETL	YP5O14	206.556	2.0	2.0	20 µm	240 on, 120 off
P_2O_5	PETL	YP5O14	197.163	6.5	4.0	20 µm	240 on, 120 off
SiO_2	TAP	Syn-Zirc	77.419	3.3	4.1	focused	240 on, 120 off
HfO_2	TAP	Syn-Haf	81.915	11.0	6.0	focused	240 on, 120 off
ZrO_2	PETH	Syn-Zirc	194.394	4.0	6.0	focused	240 on, 120 off
CaO	PETH	Apatite	107.577	3.0	3.0	focused	240 on, 120 off

Table 7-2. LA-ICPMS results (in ppm) for secondary glass standard BCR2G.

	#1	#2	#3	#4	#5	#6	#7	#8	#9	#10	#11	#12	#13
Al	6.35E+04	6.52E+04	5.86E+04	5.65E+04	5.72E+04	6.50E+04	4.70E+04	5.16E+04	5.94E+04	5.94E+04	6.25E+04	6.34E+04	5.14E+04
Si	2.00E+05	2.18E+05	2.06E+05	2.09E+05	2.10E+05	2.30E+05	1.61E+05	1.75E+05	2.01E+05	2.02E+05	2.18E+05	2.17E+05	1.75E+05
P	919	1003	910	950	940	1030	752	800	940	990	1030	1030	840
Ca	3.99E+04	4.16E+04	3.95E+04	3.90E+04	3.65E+04	4.29E+04	3.08E+04	3.42E+04	4.04E+04	3.86E+04	4.11E+04	4.21E+04	3.42E+04
Sc	25.7	26.4	24.3	23.9	24	26.9	19.7	21.7	25.4	23.7	26	27.3	22.2
Ti	9590	1.05E+04	9.10E+03	9.30E+03	9.30E+03	1.08E+04	7800	8.40E+03	1.00E+04	9.80E+03	1.04E+04	1.03E+04	8.50E+03
V	333	353	313	329	317	367	262	285	337	328	351	348	290
Mn	1270	1450	1280	1280	1340	1460	1010	1120	1310	1310	1390	1390	1120
Fe	7.88E+04	8.04E+04	7.47E+04	7.90E+04	7.68E+04	8.40E+04	5.99E+04	6.68E+04	7.90E+04	7.50E+04	8.10E+04	7.90E+04	6.37E+04
Co	27.7	30.8	27.9	28.7	30	33	22.6	24.5	30.8	29.6	32	31.7	25.7
Zn	118	129	110	109	116	121	78	94	117	116	117	124	96
Rb	39.4	43.7	41.5	38.8	38.7	42.5	30	32.6	40.6	38.9	41.1	40.7	33.9
Sr	264	278	251	254	250	285	205	228	268	262	268	275	229
Y	26.3	27.4	24.7	24.4	24.4	28.4	20	22.1	25.9	25.7	26.7	26.7	22
Zr	133	146	135	127	127	122	106	115	137	131	141	141	118
Nb	8.46	8.91	7.79	8.4	8.1	9.2	6.76	6.95	8.6	8.2	9.2	9.2	7.18
Ba	512	533	475	502	494	562	384	435	514	500	520	527	446
La	21.1	21.4	19.3	18.9	18.8	22.1	15.9	17.1	20.3	19.9	20.8	20.8	17.6
Ce	42.8	42.2	38.3	38.1	37.8	44	31.2	33.9	40.4	40	43.3	42.1	35.1
Pr	5.09	5.23	4.67	4.73	4.84	5.15	3.78	3.93	4.97	4.75	4.9	5.25	4.3
Nd	23.4	22.4	21.1	20.5	21.2	21.7	17.6	17.2	21.5	21.6	23.2	23.1	18.1
Sm	7.08	6.26	6.72	4.89	4.56	5.65	3.98	3.89	5.33	4.82	5.32	5.48	4.39
Eu	1.69	1.64	1.55	1.59	1.44	1.5	1.1	1.31	1.6	1.34	1.64	1.63	1.38
Gd	5.41	5.81	5.09	4.72	4.69	4.99	3.55	3.64	4.97	4.37	5.61	5.2	3.62
Tb	0.84	0.84	0.79	0.74	0.74	0.80	0.51	0.54	0.79	0.68	0.77	0.83	0.63
Dy	4.96	5.22	4.67	4.78	4.61	4.73	3.98	3.92	4.91	4.72	4.35	5.12	4.03
Ho	1.01	1.07	0.97	1.01	0.99	1.05	0.68	0.78	0.94	0.82	1.02	1.00	0.93
Er	2.84	2.9	2.61	2.45	2.34	2.65	1.67	2.25	2.62	2.59	2.71	2.96	2.26
Tm	0.37	0.40	0.34	0.37	0.38	0.40	0.26	0.27	0.4	0.33	0.43	0.38	0.24
Yb	2.74	2.9	2.34	2.31	2.44	2.68	1.69	1.95	2.63	2.27	2.79	3.03	1.82
Lu	0.40	0.39	0.37	0.35	0.37	0.42	0.26	0.28	0.37	0.36	0.37	0.36	0.28
Hf	3.66	3.81	3.26	3.22	2.97	4.30	2.30	3.30	4.10	3.60	3.52	3.3	3.1
Ta	0.57	0.60	0.57	0.56	0.54	0.66	0.45	0.39	0.67	0.59	0.56	0.48	0.47
Pb	7.92	9.31	7.94	8.9	7.74	8.70	6.28	7.20	7.50	8.00	8.60	5.10	7.01
Th	4.72	4.74	4.5	3.97	4.23	4.52	3.57	3.8	4.75	4.67	4.14	5.17	3.54
U	1.52	1.40	1.23	1.48	1.14	1.41	0.57	1.18	1.23	1.19	1.31	1.31	1.08

Table 7-3. LA-ICPMS results (in ppm) for secondary glass standard NIST-612.

	612_1	612_2	612_3	612_4	612_5	612_6	612_7	612_8	612_9	612_10	612_11	612_12	612_13	612_14
Al	9610	9630	9800	9590	10190	9850	10050	1.23E+04	1.05E+04	9530	9640	9690	9600	9570
Si	2.79E+05	2.81E+05	2.87E+05	2.76E+05	3.01E+05	2.91E+05	2.98E+05	3.69E+05	3.23E+05	2.72E+05	2.78E+05	2.97E+05	2.78E+05	2.79E+05
P	27.9	33.8	31.1	26.6	32	29.5	33.8	34	29	29.2	32.4	30.7	31.8	36.5
Ca	7.23E+04	7.27E+04	7.22E+04	7.41E+04	7.75E+04	7.43E+04	7.59E+04	9.30E+04	8.01E+04	7.34E+04	7.05E+04	7.31E+04	7.35E+04	7.46E+04
Sc	32.7	32.9	32.4	32.6	33.5	33.4	32.7	33.4	33.9	32.8	32.1	33.9	32.6	33.4
Ti	50.8	51.5	37.3	32.5	32.3	33.1	35.3	27.2	37	32.6	31	31.6	34.6	31
V	31.64	32.55	32.1	32.2	33.3	32.4	34.1	38	35.7	32.5	31.7	33.1	32.2	31.9
Mn	33.9	35.2	35.4	35.4	39.1	36.4	37.7	37.6	38.4	34.8	35.1	36.4	35.7	36.1
Fe	-28	-19	28	32	59	47	47	130	37	31	36	41	39	31.6
Co	30	31.9	29.1	28.1	31.8	29.5	30.5	36.7	31.4	28.8	29	29.4	28.9	29.4
Zn	34.2	35.1	35.6	33.2	33.6	32.3	34.2	37.1	32	33.8	32.7	32.7	31.9	34.6
Rb	44.7	44.3	32.4	33.3	33.1	29.5	30.7	34.7	31.5	27.7	27	27.7	26.4	27.6
Sr	68.2	68.9	68.3	67.7	71.3	67.3	69.7	86.2	76.2	67.3	67.8	68.2	66.1	70
Y	33.42	33.6	33.2	33.2	33.8	33.3	34.1	38.8	34.4	33.4	32.6	33.3	32	33.2
Zr	27.6	29.4	29.8	28.5	27.6	28.8	30.1	17.9	18.6	29.2	28.8	52	27.3	29.5
Nb	29.98	30.3	30.5	29.3	31.1	30.2	30.9	37.5	31.7	29.9	29.4	30.3	29.6	30.4
Ba	33.4	32.8	32.2	32.3	32.2	33.5	34.7	41.8	35.2	31.7	32.2	31.8	33.5	33.2
La	33.14	32.73	33.2	32.4	33.7	32.5	34.1	41.3	35.1	32.5	31.6	33.3	32.6	33.5
Ce	34.2	32.99	33	33.8	33.8	33.5	34.8	41	34.6	32.7	32.3	32.2	32.8	34.7
Pr	32.07	31.79	31.8	32	32.9	31.7	32.7	40.1	34.7	31.3	31.2	31.7	31.4	32.1
Nd	31.1	30.66	31.1	31	31.3	31	32.1	37.2	33.2	31	30.3	31.2	29.9	32.6
Sm	38.6	37	35.6	37.7	36.9	35	36.8	41.8	36.8	33.4	31.2	33.2	32.4	33.9
Eu	31.84	32.46	32.7	33.2	33.1	32.9	32.17	39.2	34.9	31.7	31.4	32.3	31.9	32.2
Gd	33.55	33.1	32.7	33.3	33.4	32.2	34.6	44.7	37.4	32.7	33.8	33.3	32.7	33.8
Tb	33.9	33.72	33.8	34.3	33.9	33.6	33.8	41.7	35.2	32.9	32.5	33.6	33.3	33.8
Dy	31.21	30.2	31.5	31.1	31.9	31.4	31.4	37.8	34.3	31.3	29.1	31.1	30.6	31.4
Ho	34	33.57	34.7	34.4	34.6	33.8	34.7	43.3	35.2	33.7	32.9	34.5	33.2	35.1
Er	32.4	32.3	32.7	32.2	32.5	32	32.9	39.9	34.4	31.9	30.2	31.3	31.4	32.5
Tm	32.59	31.91	32.1	33.13	32.4	31.25	32.1	38	34.2	31.7	30.5	31.8	31.7	31.8
Yb	33.5	34.2	33.9	33.9	34.1	33.2	34.4	41	35.4	33.2	31.2	34	32.9	33.9
Lu	32.45	32.14	32.5	32.87	32.6	31.8	32.8	40.2	33.7	31.6	31.4	32.2	31.9	33.1
Hf	33.1	32.3	33.1	32.3	31.8	32.9	33	35	32.4	32.3	31.5	32.8	32	33.4
Ta	33.32	33.55	33.8	33.34	34.1	33.1	34.2	41.7	34.8	32.7	32.2	33	32.9	33
Pb	32.55	33.68	32.8	33.5	33.4	32.4	32.5	43.7	38.1	33.1	31.5	32.8	33.3	34.9
Th	33.33	33.76	33.8	33.31	33.2	32.3	34	42.8	33.9	32.8	32.7	32.5	32.7	33.5
U	33.6	32.91	32.7	31.9	33	31.5	33.3	40.4	33.5	33	31.8	32	33	32.4

Table 7-4. LA-ICPMS results (in ppm) for secondary standard zircon 91500.

	JK91500_1	JK91500_2	JK91500_3	JK91500_4	JK91500_5	JK91500_6
Al	3.2	-0.1	3.8	-11.3	10.7	-10.6
Si	1.40E+05	1.51E+05	1.50E+05	1.37E+05	1.41E+05	1.42E+05
P	21.1	24.2	19.9	17.7	13.3	16.9
Ca	7	31	5	-58	21	48
Sc	628	656	660	601	612	608
Ti	5.7	5.1	4.9	5.1	4.8	5.6
V	0.85	0.65	0.99	1.1	0.86	1.55
Mn	-0.2	0.8	0	1.24	0.35	-0.16
Fe	9	-7	8.2	-11	4.8	-3.5
Co	-0.13	-0.04	-0.12	-0.13	-0.3	-0.45
Zn	1.43	2.7	2.15	0.25	2.36	0.72
Rb	0.17	0.49	0.23	0.072	-0.05	0.03
Sr	0.2	0.13	0.212	0.087	0.169	0.091
Y	138.1	144.1	136	135.2	131.6	129.3
Zr	4.73E+05	4.87E+05	4.61E+05	4.72E+05	4.56E+05	4.57E+05
Nb	1.083	1.248	1.04	0.97	1.1	1.07
Ba	0.04	0.19	0.15	0.19	-0.06	0.1
La	0.0034	0.024	0.012	0.045	0.014	0.008
Ce	2.54	2.85	2.72	2.68	2.42	2.46
Pr	0.017	0.027	0.021	0.0061	0.026	0.03
Nd	0.175	0.22	0.204	0.192	0.164	0.24
Sm	0.88	2.25	0.56	0.64	0.57	0.43
Eu	0.336	0.341	0.199	0.269	0.256	0.216
Gd	2.37	2.4	2.04	1.73	2.16	2.35
Tb	0.94	0.846	0.84	0.81	0.802	0.82
Dy	10.5	10.6	10.3	10.8	10.19	10.5
Ho	4.71	5.18	4.49	4.77	4.63	4.69
Er	23.89	24.4	22.9	23.35	23.67	23.84
Tm	5.81	6.5	5.76	5.69	5.96	5.76
Yb	59.5	69.2	61.1	62.5	62.9	64.8
Lu	12.69	14	13.11	12.82	12.88	12.81
Hf	5730	6100	5670	6040	5957	5815
Ta	0.46	0.484	0.447	0.531	0.496	0.499
Pb	2.72	3.43	2.66	2.56	2.9	2.71
Th	30.5	35.7	29.4	30.9	29.63	29.1
U	83.9	97.4	89.4	81.2	84.8	82.4

Table 7-5. Average LA-ICPMS results for secondary standards glass BCR2G, NIST-612, and zircon 91500, in comparison with long-term MUN averages (BCR-2G, 91500) and recommended value of NIST-612 (Pearce et al., 1997).

	BCR-2G	BCR-2G (MUN)	NIST-612	NIST-612 (recomm.)	JK91500	JK91500 (MUN)
Sc	24.4	31.27	33.0	37.9	627.5	-
V	324	407	33.1	41.4	1.0	-
Mn	1287	1448	36.2	37.37	0.4	-
Co	28.8	36	30.3	39.8	-	-
Zn	111	129	33.8	38.8	1.6	
Rb	38.6	-	32.2	31.01	0.2	
-	255	326	70.2	73.6	0.1	0.1
Y	25	32	33.7	39.0	135.7	149.1
Zr	129	166	28.9	34.8	4.68E+05	
Nb	8.2	12	30.8		1.1	0.8
Ba	493	641	33.6	33.6	0.1	0.1
La	19.5	24.6	33.7	33.5	0.0	0.0
Ce	39.2	51.2	34.0	33.9	2.6	2.9
Pr	4.7	6.4	32.7	35.9	0.0	0.0
Nd	21.0	27.8	31.7	33.52	0.2	0.2
Sm	5.26	6.3	35.7	35.6	0.9	0.4
Eu	1.49	1.97	33.0	32.68	0.3	0.2
Gd	4.74	6.24	34.4	36.03	2.2	2.3
Tb	0.73	0.94	34.3	38.46	0.8	0.9
Dy	4.62	6.1	31.7	35.02	10.5	11.8
Ho	0.94	1.23	34.8	38.9	4.7	5.0
Er	2.53	3.43	32.8	35.05	23.7	26.3
Tm	0.35	0.49	32.5	39.2	5.9	6.9
Yb	2.43	3.38	34.2	37.4	63.3	72.1
Lu	0.35	0.48	32.9	39.5	13.1	14.4
Hf	3.42	4.57	32.7	26.43	5885.3	5895.0
Ta	0.55	0.76	34.0		0.5	0.5
Pb	7.71	11.37	34.2	36.9	2.8	3.5
Th	4.33	5.8	33.9	37.1	30.9	32.3
U	1.23	1.62	33.2	35.4	86.5	89.6

Table 7-6. Geochronology results for monazite from Kiirunavaara and Rektorn ore and host rock: U-Pb-Th SIMS analytical data.

						Isotopic ratios							Ages (Ma)					
Sample/	**[U]**	**[Th]**	**[Pb]**	**Th/U**	**f_{206}%[1]**	**$^{207}Pb/^{235}U$**	**±σ**	**$^{238}U/^{206}Pb$**	**±σ**	**$^{207}Pb/^{206}Pb$**	**±σ**	**Disc**	**$^{207}Pb/^{206}Pb$**	**±σ**	**$^{207}Pb/^{235}U$**	**±σ**	**$^{206}Pb/^{238}U$**	**±σ**
spot #	**ppm**	**ppm**	**ppm**	**calc**			**%**		**%**		**%**	**%**						
a) K-1 (Kiirunavaara ore)																		
n4721_mnz_K-1_@24	54.4	6317.7	383.2	116.18	{0.00}	3.65378	4.13	3.5169	3.29	0.093196	2.50		1491.9	46.5	1561.3	33.5	1613.2	47.1
n4721_mnz_K-1_@13	41.2	4658.8	316.9	113.16	{0.00}	3.77448	4.41	3.4057	3.24	0.093232	2.99		1492.6	55.5	1587.3	36.0	1659.6	47.6
n4721_mnz_K-1_@18	56.3	5767.4	377.6	102.48	{0.00}	3.70555	4.13	3.5163	3.36	0.094502	2.40		1518.2	44.6	1572.6	33.6	1613.4	48.2
n3911_mnz_K1@13	59.0	2351.5	42.8	39.89	0.16	4.09681	5.65	3.1987	5.24	0.095043	2.11	0.3	1528.9	39.3	1653.7	47.2	1753.6	81.0
n4721_mnz_K-1_@30	29.2	3431.5	219.7	117.43	{0.00}	3.72244	4.97	3.5496	3.63	0.095831	3.39		1544.5	62.4	1576.2	40.6	1600.0	51.7
n3911_mnz_K1@11	31.6	1684.1	29.4	53.30	0.34	4.07606	6.65	3.2447	6.10	0.095922	2.67		1546.2	49.3	1649.5	55.7	1731.8	93.2
n4721_mnz_K-1_@23	45.9	4717.9	312.9	102.70	{0.00}	3.81038	4.41	3.4731	3.37	0.095980	2.85		1547.4	52.5	1594.9	36.1	1631.2	48.8
n4721_mnz_K-1_@6	62.5	4767.4	310.2	76.26	{0.00}	3.94514	4.16	3.3614	3.49	0.096179	2.26		1551.3	41.8	1623.0	34.2	1678.9	51.8
n4721_mnz_K-1_@26	62.8	5244.2	337.3	83.46	{0.00}	3.77478	4.32	3.5216	3.63	0.096411	2.34		1555.8	43.3	1587.4	35.3	1611.3	52.0
n4721_mnz_K-1_@2	41.1	4122.6	256.3	100.21	{0.00}	3.83856	4.58	3.4720	3.55	0.096661	2.89		1560.6	53.3	1600.9	37.6	1631.6	51.3
n4721_mnz_K-1_@4	34.3	3789.1	240.7	110.62	{0.00}	3.82540	4.86	3.4978	3.67	0.097045	3.19		1568.1	58.6	1598.1	39.9	1621.0	52.8
n4721_mnz_K-1_@25	54.3	2908.9	211.0	53.52	{0.00}	3.90907	5.63	3.4408	5.01	0.097552	2.56		1577.8	47.2	1615.6	46.6	1644.7	73.1
n4721_mnz_K-1_@15	50.6	4523.7	309.3	89.38	{0.00}	3.90995	4.83	3.4463	3.93	0.097729	2.81		1581.2	51.7	1615.7	39.8	1642.4	57.2
n3911_mnz_K1@4	61.1	2333.8	43.9	43.9	{0.00}	4.17854	5.59	3.2348	5.36	0.098033	1.59		1587.0	29.5	1669.8	46.9	1736.5	82.2
n4721_mnz_K-1_@12	58.3	9043.5	576.1	155.14	{0.00}	3.88533	4.73	3.4870	4.04	0.098260	2.45		1591.4	45.1	1610.6	38.9	1625.4	58.4
n4721_mnz_K-1_@01	33.4	2866.9	205.0	85.84	{0.00}	3.98283	5.05	3.4029	3.64	0.098298	3.50		1592.1	64.0	1630.7	41.9	1660.8	53.5
n4721_mnz_K-1_@20	61.6	4575.7	280.8	74.26	{0.00}	3.81056	3.87	3.5599	3.05	0.098385	2.38		1593.7	43.8	1595.0	31.6	1595.9	43.3
n4721_mnz_K-1_@29	35.7	4662.5	306.8	130.77	{0.00}	3.97380	4.97	3.4228	4.05	0.098647	2.87		1598.7	52.7	1628.9	41.1	1652.3	59.4
n4721_mnz_K-1_@14	52.0	3634.8	241.4	69.87	{0.00}	3.86394	4.23	3.5243	3.43	0.098764	2.48		1600.9	45.5	1606.2	34.7	1610.2	49.0
n3911_mnz_K1@14	55.3	1576.4	29.7	28.51	{0.14}	4.30121	5.18	3.1682	4.89	0.098832	1.70		1602.2	31.4	1693.6	43.6	1768.4	76.1
n3911_mnz_K1@15	58.3	1846.4	34.5	31.68	0.31	4.17462	5.71	3.2723	5.37	0.099077	1.93		1606.8	35.5	1669.1	47.9	1719.0	81.6
n4721_mnz_K-1_@10	36.0	3718.4	244.8	103.21	{0.00}	3.95958	4.79	3.4609	3.68	0.099389	3.07		1612.7	56.1	1626.0	39.6	1636.2	53.3
n4721_mnz_K-1_@17	34.9	2797.9	182.0	80.18	{0.00}	3.87136	4.48	3.5447	3.29	0.099528	3.04		1615.3	55.5	1607.7	36.8	1602.0	46.8
n3911_mnz_K1@8	61.8	2519.6	46.6	40.75	0.17	4.30107	4.98	3.1912	4.69	0.099546	1.67		1615.6	30.7	1693.6	41.9	1757.2	72.6
n4721_mnz_K-1_@8	51.5	8481.5	618.6	164.71	{0.00}	4.13768	4.42	3.3177	3.56	0.099560	2.62		1615.9	48.1	1661.8	36.8	1698.3	53.4
n4721_mnz_K-1_@05	33.4	4237.6	290.3	126.71	{0.00}	3.88423	5.93	3.5346	4.76	0.099574	3.55		1616.1	64.7	1610.4	49.1	1606.0	68.0
* n4721_mnz_K-1_@27	41.0	5147.0	337.1	125.55	{0.00}	4.09702	4.57	3.3534	3.44	0.099643	3.01		1617.4	55.0	1653.7	38.0	1682.4	51.1
n4721_mnz_K-1_@22	29.6	3150.1	220.8	106.52	{0.00}	4.14325	6.38	3.3169	4.17	0.099672	4.83		1618.0	87.3	1662.9	53.5	1698.7	62.5
n4721_mnz_K-1_@19	38.1	2967.7	191.8	77.83	{0.00}	3.89344	5.07	3.5307	4.07	0.099701	3.01		1618.5	55.1	1612.3	41.8	1607.6	58.2
n3911_mnz_K1@6	49.2	1708.5	32.9	34.70	{0.00}	4.20499	5.29	3.2799	4.97	0.100030	1.80		1624.6	33.2	1675.0	44.4	1715.5	75.4
n3911_mnz_K1@2	30.6	1060.6	21.2	34.71	{0.16}	4.30485	6.60	3.2082	5.98	0.100167	2.78		1627.2	50.9	1694.3	55.9	1749.1	92.3

continued on following pages.

Table 7-6 continued. Geochronology results for monazite from Kiirunavaara and Rektorn ore and host rock: U-Pb-Th SIMS analytical data.

						Isotopic ratios							Ages (Ma)					
Sample/	**[U]**	**[Th]**	**[Pb]**	**Th/U**	**f_{206}%[1]**	**$^{207}Pb/^{235}U$**	**±σ**	**$^{238}U/^{206}Pb$**	**±σ**	**$^{207}Pb/^{206}Pb$**	**±σ**	**Disc**	**$^{207}Pb/^{206}Pb$**	**±σ**	**$^{207}Pb/^{235}U$**	**±σ**	**$^{206}Pb/^{238}U$**	**±σ**
spot #	**ppm**	**ppm**	**ppm**	**calc**			**%**		**%**		**%**	**%**						
a) K-1 (Kiirunavaara ore) continued																		
n3911_mnz_K1@1	32.3	1409.8	25.9	43.59	{0.18}	4.28433	5.98	3.2261	5.60	0.100245	2.10		1628.6	38.6	1690.4	50.5	1740.6	86.0
n4721_mnz_K-1_@21	46.3	2845.5	187.3	61.39	{0.00}	4.05976	4.27	3.4228	3.41	0.100781	2.57		1638.5	47.0	1646.3	35.4	1652.3	49.9
n3911_mnz_K1@3	34.5	1726.8	33.6	50.09	{0.00}	4.35895	7.17	3.2060	6.86	0.101354	2.10		1649.1	38.4	1704.6	61.0	1750.1	106.0
n4721_mnz_K-1_@7	52.8	3730.1	269.8	70.64	{0.00}	4.01765	4.08	3.4811	3.16	0.101435	2.58		1650.5	47.2	1637.8	33.7	1627.8	45.6
n3911_mnz_K1@7	31.3	1177.3	22.5	37.57	{0.00}	4.30103	8.66	3.2523	8.34	0.101453	2.32		1650.9	42.4	1693.6	73.9	1728.3	127.7
n3911_mnz_K1@16	44.3	1204.8	23.0	27.17	{0.12}	4.39057	7.23	3.1870	6.84	0.101486	2.36		1651.5	43.2	1710.6	61.7	1759.2	106.1
n4721_mnz_K-1_@09	46.7	3900.8	251.5	83.45	{0.00}	4.03125	4.07	3.4720	3.15	0.101512	2.59		1651.9	47.2	1640.5	33.7	1631.6	45.6
n3911_mnz_K1@12	43.9	1410.1	27.1	32.14	{0.00}	4.42109	5.72	3.1787	5.36	0.101925	1.99		1659.5	36.5	1716.3	48.5	1763.3	83.2
n3911_mnz_K1@10	55.9	1931.4	35.9	34.57	{0.13}	4.44667	5.13	3.1789	4.86	0.102520	1.65		1670.2	30.2	1721.1	43.5	1763.2	75.4
n3911_mnz_K1@9	53.6	1324.5	25.5	24.73	{0.00}	4.40357	5.57	3.2617	5.14	0.104171	2.12		1699.7	38.6	1713.0	47.1	1723.9	78.3
n4721_mnz_K-1_@3	48.0	3642.5	238.5	75.96	{0.00}	4.13231	4.05	3.5146	3.07	0.105335	2.64		1720.2	47.8	1660.7	33.7	1614.1	44.0
n4721_mnz_K-1_@11	31.5	2779.3	177.9	88.30	{0.00}	4.12692	5.10	3.5548	3.86	0.106400	3.33		1738.6	59.8	1659.6	42.5	1597.9	54.8
n4721_mnz_K-1_@16	40.5	5032.5	324.0	124.15	{0.00}	4.15951	5.12	3.5403	4.24	0.106803	2.87		1745.6	51.6	1666.1	42.8	1603.7	60.5
b) KRN-11-01 (Kiirunavaara ore)																		
n4730_mnz_KRN11-1_@15	45.1	7792.0	490.7	172.94	{0.28}	3.64970	4.59	3.5650	3.74	0.094367	2.67		1515.5	49.6	1560.4	37.3	1593.9	53.0
n4730_mnz_KRN11-1_@12	41.7	3795.0	232.8	91.07	{0.00}	3.49803	4.19	3.7910	3.11	0.096178	2.81		1551.3	51.9	1526.8	33.6	1509.2	41.9
n4730_mnz_KRN11-1_@11	20.8	929.5	60.2	44.60	{0.00}	3.70734	5.39	3.6262	3.78	0.097503	3.85		1576.9	70.4	1573.0	44.1	1570.0	52.8
n4730_mnz_KRN11-1_@10	63.1	995.4	83.2	15.76	{0.00}	3.83173	3.99	3.5467	3.24	0.098563	2.33		1597.1	42.9	1599.4	32.7	1601.2	46.1
n4730_mnz_KRN11-1_@26	28.2	3240.2	222.1	114.92	{0.00}	4.15175	4.94	3.2754	3.93	0.098625	3.00		1598.3	55.0	1664.6	41.3	1717.6	59.5
n4730_mnz_KRN11-1_@16	16.4	3451.5	235.2	210.61	{0.00}	3.84784	6.23	3.5371	4.46	0.098710	4.35		1599.9	79.0	1602.8	51.5	1605.0	63.7
n4730_mnz_KRN11-1_@6	41.8	2143.4	149.6	51.32	{0.00}	4.21592	4.39	3.3274	3.17	0.101742	3.04		1656.1	55.3	1677.1	36.7	1693.9	47.4
n4730_mnz_KRN11-1_@3	42.1	2475.4	171.8	58.79	{0.00}	4.04868	4.46	3.4999	3.54	0.102770	2.72		1674.7	49.5	1644.0	37.0	1620.1	50.9
n4730_mnz_KRN11-1_@24	14.8	1150.0	89.0	77.65	{0.00}	4.61226	6.11	3.0834	4.49	0.103144	4.14		1681.4	74.6	1751.5	52.3	1810.8	71.3
n4730_mnz_KRN11-1_@8	15.5	2592.4	180.9	167.45	{0.33}	4.35944	5.82	3.2714	4.13	0.103433	4.10		1686.6	73.8	1704.7	49.3	1719.4	62.7
n4730_mnz_KRN11-1_@20	22.9	4194.4	301.4	183.01	{0.00}	4.52920	4.88	3.1714	3.63	0.104178	3.26		1699.8	59.0	1736.3	41.5	1766.8	56.4
n4730_mnz_KRN11-1_@22	14.3	3284.8	234.7	229.61	{0.00}	4.65295	6.95	3.1072	5.57	0.104858	4.16		1711.8	74.6	1758.8	59.8	1798.7	88.0
n4730_mnz_KRN11-1_@5	32.2	3461.0	244.2	107.57	{0.00}	4.36268	4.72	3.3437	3.65	0.105799	3.00		1728.2	54.1	1705.3	39.8	1686.7	54.4
n4730_mnz_KRN11-1_@09	15.3	3484.0	224.0	227.18	{0.21}	3.94068	7.62	3.7040	6.38	0.105862	4.17		1729.3	74.7	1622.1	63.7	1540.7	88.0
n4730_mnz_KRN11-1_@19	55.1	3026.5	227.6	54.88	{0.00}	4.78126	5.15	3.0538	4.69	0.105895	2.12		1729.9	38.4	1781.6	44.2	1826.1	75.0

continued on following pages.

Table 7-6 continued. Geochronology results for monazite from Kiirunavaara and Rektorn ore and host rock: U-Pb-Th SIMS analytical data.

						Isotopic ratios							Ages (Ma)					
Sample/ spot #	[U] ppm	[Th] ppm	[Pb] ppm	Th/U calc	f_{206}%[1]	$^{207}Pb/^{235}U$	±σ %	$^{238}U/^{206}Pb$	±σ %	$^{207}Pb/^{206}Pb$	±σ %	Disc %	$^{207}Pb/^{206}Pb$	±σ	$^{207}Pb/^{235}U$	±σ	$^{206}Pb/^{238}U$	±σ
b) KRN-11-01 (Kiirunavaara ore) continued																		
n4730_mnz_KRN11-1_@17	18.1	727.8	56.1	40.20	{0.00}	4.81074	5.70	3.0568	4.25	0.106655	3.80		1743.0	68.0	1786.8	49.1	1824.5	68.0
n4730_mnz_KRN11-1_@18	14.3	6453.9	479.3	451.50	{0.00}	4.48662	9.73	3.2812	6.90	0.106770	6.86		1745.0	120.6	1728.5	84.2	1714.9	104.8
n4730_mnz_KRN11-1_@13	21.1	3586.8	243.1	169.75	{0.00}	4.38842	5.22	3.3578	3.79	0.106870	3.60		1746.7	64.5	1710.2	44.1	1680.5	56.2
n4730_mnz_KRN11-1_@2	32.4	1471.7	106.1	45.38	{0.00}	4.39654	4.85	3.3588	3.92	0.107100	2.87		1750.6	51.6	1711.7	41.0	1680.0	58.2
n4730_mnz_KRN11-1_@04	24.4	2341.3	156.6	96.12	{0.00}	4.71403	4.78	3.1369	3.55	0.107248	3.20		1753.2	57.5	1769.7	40.9	1783.8	55.6
n4730_mnz_KRN11-1_@01	44.8	3727.0	283.5	83.27	{0.00}	4.62056	5.33	3.2102	3.52	0.107577	4.01		1758.8	71.6	1753.0	45.5	1748.1	54.1
n4730_mnz_KRN11-1_@27	44.2	2072.5	152.6	46.90	{0.00}	4.61717	4.29	3.2484	3.55	0.108780	2.41		1779.1	43.3	1752.4	36.5	1730.1	54.1
n4730_mnz_KRN11-1_@21	42.0	4020.9	290.3	95.73	{0.00}	4.60122	4.11	3.2677	3.34	0.109046	2.39		1783.5	42.9	1749.5	34.9	1721.1	50.7
n4730_mnz_KRN11-1_@23	5.2	6222.5	424.3	1202.76	{0.00}	4.41021	10.25	3.4237	6.68	0.109511	7.78		1791.3	135.4	1714.3	88.6	1651.9	98.0
n4730_mnz_KRN11-1_@7	19.9	1156.2	88.3	58.04	{0.00}	4.85169	5.11	3.1159	3.73	0.109641	3.49		1793.5	62.3	1793.9	44.0	1794.3	58.7
n4730_mnz_KRN11-1_@14	6.6	3026.5	204.0	460.63	{0.00}	4.70817	10.47	3.4168	6.35	0.116672	8.32		1905.8	142.4	1768.7	91.7	1654.9	93.3
c) REK-10-04 (Rektorn ore)																		
n4731_mnz_REK10-4_@02	2410.1	27461.1	539.1	11.39	{0.04}	0.38419	3.07	19.3372	2.93	0.053881	0.92		366.1	20.5	330.1	8.7	325.0	9.3
n3917_mnz_REK4@22	32.1	1227.9	23.6	38.29	{0.23}	4.75573	6.38	3.0073	6.00	0.103727	2.17		1691.9	39.5	1777.1	55.0	1850.6	97.2
n4731_mnz_REK10-4_@4	70.4	12003.0	981.2	170.46	{0.00}	4.26738	3.90	3.3560	3.31	0.103870	2.07		1694.4	37.6	1687.1	32.6	1681.2	49.1
n4731_mnz_REK10-4_@01	45.6	8385.9	608.8	183.74	{0.00}	4.34643	4.18	3.3175	3.46	0.104579	2.35		1706.9	42.7	1702.2	35.1	1698.4	51.9
n3917_mnz_REK4@17	48.4	3815.5	72.1	78.80	{0.25}	4.71946	5.41	3.0569	5.12	0.104632	1.75		1707.9	31.9	1770.7	46.4	1824.5	81.8
n4731_mnz_REK10-4_@6	85.5	2160.2	191.0	25.27	{0.00}	4.38708	3.55	3.2944	3.04	0.104820	1.83		1711.2	33.3	1709.9	29.8	1708.9	45.8
n3917_mnz_REK4@19	53.1	4033.3	78.9	75.92	0.34	4.88609	6.32	2.9650	6.03	0.105073	1.90		1715.6	34.4	1799.9	54.7	1873.5	98.8
n4731_mnz_REK10-4_@9	68.0	4309.8	297.4	63.36	{0.00}	4.45441	5.06	3.2690	4.44	0.105609	2.42		1724.9	43.8	1722.5	42.8	1720.5	67.4
n3917_mnz_REK4@20	56.4	730.0	15.6	12.95	{0.13}	4.89940	6.12	2.9877	5.90	0.106166	1.64		1734.6	29.8	1802.2	53.0	1861.1	96.1
n4731_mnz_REK10-4_@5	44.9	3286.9	239.9	73.23	{0.00}	4.72173	3.74	3.1125	3.09	0.106589	2.10		1741.9	38.0	1771.1	31.8	1796.0	48.6
n4731_mnz_REK10-4_@07	11.5	1170.9	46.8	101.98	{0.42}	4.34239	7.25	3.4670	6.75	0.109191	2.64		1786.0	47.3	1701.5	61.6	1633.7	98.1
n4731_mnz_REK10-4_@3	132.1	22153.0	1744.1	167.70	{0.00}	4.69749	3.12	3.2072	2.78	0.109268	1.42		1787.2	25.6	1766.8	26.5	1749.5	42.8
n3917_mnz_REK4@23	18.6	1056.6	21.2	56.66	{0.40}	5.14488	8.07	2.9376	7.51	0.109614	2.94		1793.0	52.6	1843.5	71.0	1888.7	124.2
n4731_mnz_REK10-4_@8	7.5	4029.0	273.7	536.11	{0.00}	5.03081	8.95	3.2897	5.78	0.120031	6.84		1956.7	117.3	1824.5	78.8	1711.0	87.4
n3917_mnz_REK4@18	38.8	9091.5	148.8	234.23	2.94	7.96905	6.33	2.6112	5.84	0.150919	2.45		2356.4	41.3	2227.5	58.8	2090.1	105.1

Continued on following page.

Table 7-6 continued. Geochronology results for monazite from Kiirunavaara and Rektorn ore and host rock: U-Pb-Th SIMS analytical data.

						Isotopic ratios							Ages (Ma)					
Sample/	**[U]**	**[Th]**	**[Pb]**	**Th/U**	**f_{206}%[1]**	**^{207}Pb**	**±σ**	**^{238}U**	**±σ**	**^{207}Pb**	**±σ**	**Disc**	**^{207}Pb**	**±σ**	**^{207}Pb**	**±σ**	**^{206}Pb**	**±σ**
spot #	**ppm**	**ppm**	**ppm**	**calc**		**^{235}U**	**%**	**^{206}Pb**	**%**	**^{206}Pb**	**%**	**%**	**^{206}Pb**		**^{235}U**		**^{238}U**	
d) REK-12-02 (Rektorn host rhyodacite)																		
n4732_mnz_REK12-2_@4	67.8	4779.6	346.9	70.47	{0.00}	3.70188	4.10	3.7798	3.48	0.101482	2.18		1651.4	39.9	1571.8	33.4	1513.2	47.0
n4732_mnz_REK12-2_@5	42.7	4549.4	302.9	106.59	{0.08}	4.44073	4.11	3.2857	3.13	0.105823	2.66		1728.7	48.0	1720.0	34.6	1712.8	47.2
n4732_mnz_REK12-2_@2	16.4	7554.2	585.9	460.52	{0.00}	4.34683	5.55	3.3579	3.92	0.105863	3.93		1729.4	70.5	1702.3	46.9	1680.4	58.2
n4732_mnz_REK12-2_@7	38.5	2383.8	176.5	61.94	{0.00}	4.35441	4.48	3.4010	3.71	0.107409	2.52		1755.9	45.4	1703.7	37.7	1661.6	54.5
n4732_mnz_REK12-2_@03	31.0	1114.7	89.4	35.97	{0.00}	4.71524	4.29	3.1863	3.33	0.108965	2.71		1782.2	48.6	1770.0	36.6	1759.6	51.4
n4732_mnz_REK12-2_@01	53.5	3070.5	245.5	57.38	{0.00}	4.80472	4.56	3.1296	4.03	0.109059	2.14		1783.8	38.4	1785.7	39.1	1787.4	63.3
n4732_mnz_REK12-2_@6	12.4	1822.6	140.2	147.00	{0.00}	4.40463	6.76	3.4479	5.18	0.110144	4.34		1801.8	77.0	1713.2	57.5	1641.7	75.5
n4732_mnz_REK12-2_@08	13.7	7795.8	571.1	569.84	{0.00}	4.71359	6.31	3.2605	4.33	0.111464	4.59		1823.4	81.1	1769.7	54.3	1724.5	65.8
n4732_mnz_REK12-2_@9	17.5	6650.5	533.1	381.02	{1.29}	4.73042	6.12	3.3028	4.50	0.113313	4.15		1853.2	73.2	1772.6	52.6	1705.0	67.7

[1]Percentage of common ^{206}Pb in measured ^{206}Pb, estimated from ^{204}Pb counts. Figures in parentheses are given when no correction was applied and indicate a value calculated assuming a present-day Stacey & Kramers (1975) model terrestrial Pb-isotope composition. All other ratios are common Pb corrected. [2]Age discordance at closest approach of error ellipse to concordia (2σ level). R: analyses on rim of zircon grain.

Table 7-7. Cup configuration and instrument operation parameters for Sm-Nd monazite LA-MC-ICPMS laser analyses at Washington State University.

a) Cup configuration and interferences

L4	L3	L2	L1	Axial	H1	H2	H3	H4
^{142}Nd	^{143}Nd	^{144}Nd ^{144}Sm	^{145}Nd	^{146}Nd	^{147}Sm	^{149}Sm	^{153}Eu	^{157}Gd $^{141}Pr^{16}O$

b) Instrument Operating Parameters

MC-ICPMS		*Laser ablation*	
Model	ThermoFinnigan Neptune	Type	213 nm Nd:YAG
Forward Power	1200 W	Model	New wave UP-213
		Repetition rate	8 Hz
Gas flows-laser ablation		Laser fluence	~7 J/cm^2
Cool/plasma (Ar)	15 l/min	Spot size	20 μm
Auxiliary (Ar)	0.80 l/min		
Sample/nebulizer (Ar)	07-0.8 l/min		
Sample cell gas (He)	~1 l/min		
Nitrogen	5 ml/min		

8 Appendix C– Sample preparation and analytical methods for chapter four, detailed in situ oxygen and Lu-Hf data for zircon

8.1 Samples, sample preparation, and detailed results

Samples were collected in collaboration with the operating mining company LKAB (Luossavaara-Kiirunavaara Aktiebolag) from three different ore bodies (e.g., Kiirunavaara, Rektorn, Nukutus) within the vicinity of Kiruna (see Fig. 4-1, main text), the metavolcanic host rocks of those deposits, and igneous intrusions spatially and temporally related to the Kiirunavaara ore body (see Table 8-1 for locations and mineralogy).

Zircon grains were separated from the samples in this study using standard crushing and separation techniques and were then mounted in epoxy and polished to reveal the crystal centers. Zircon grains were imaged by back-scattered electrons (BSE) and cathodoluminescence (CL) using a FEI Quanta 400 secondary electron microscope (SEM) at Memorial University of Newfoundland (MUN) prior to the in situ analyses. Subsequent CL images were taken with a JEOL JSM-7100F field emission SEM at MUN after all analyses were completed to precisely verify where in situ analyses were done. Representative CL and BSE images can be found in Figure 8-2.

Determination of the zircon oxygen isotopic compositions ($^{18}O/^{16}O$) was done at the NordSIM facility of the Swedish Museum for Natural History, using a Cameca IMS1280 ion microprobe, after the zircon grains had been previously dated with the same instrument. The methodology follows that of Whitehouse and Nemchin (2009) and Heinonen et al. (2015), using a rastered 20 keV Cs+ primary beam (ca. 1.5 nA) in Gaussian focussed mode

to sputter a ca. 15 μm sample area. Charge compensation was provided by a normal incidence electron gun. Runs were fully automated and included a 60 s pre-sputter period (rastered area 20 μm), and within-run centering of the field aperture, entrance slit, and mass, using the ^{16}O signal. Data were acquired for 64 s using two Faraday detectors in the multicollector system. The mounts were gently repolished to remove spots from prior U-Th-Pb analyses to then the oxygen analyses were made in the same locations where concordant ages were previously obtained. The oxygen isotope data were normalized to reference zircon samples Temora-2 and 91500 that were measured repeatedly throughout the sessions, assuming a $\delta^{18}O$ value of 8.20‰ and 9.86‰, respectively (Black et al., 2004; Wiedenbeck et al., 2004). Temora-2 was used as primary standard in the 2013 session, because the 91500 piece used showed impurities (see Fig. 8-2 and Table 8-2). Minor linear drift corrections (0.004 and 0.001 %/run in 2013 and 2014, respectively) were applied to the data sets where applicable based on minimising the external error on the standards. $\delta^{18}O$ compositions are reported relative to Vienna standard mean ocean water (V-SMOW). Errors for $\delta^{18}O$ represent the sum of counting statistics error for individual spot and the external error obtained based on all standards analysed during the session, which were added in quadrature.

Hf isotopes were later measured at MUN by laser ablation multi-collector inductively coupled mass spectrometry (LA-MC-ICPMS) using a Thermo Finnigan Neptune MC-ICPMS and a GeoLas 193nm excimer laser system, following the methods of Fisher et al. (2011). Helium was used as the carrier gas in the ablation cell and flowed at a rate of 1 litre/min with an auxiliary Ar gas flow of 0.8-0.9 litres/min and Ar make up gas flow of

0.825 litres/min. The laser spot size used was 40 μm, except for standard zircon Plešovice (49 μm), with a repetition rate of 10 Hz and fluence of 5 J/cm^2. The cup configuration for the MC-ICPMS can be found in Table 8-3. Before each analysis, the gas background (blank) was measured for 30 seconds, and then the laser fired for approximately 60 seconds resulting in ~600 pulses. The integration time used for each data acquisition point was approximately 1 second. Hf data reduction was done following the methods of Fisher et al. (2011) and is summarized in the following. The Lu-Hf isotope data was processed using the Excel macro MCTool-Hf, which is based on macros from "LAMTOOL-Hf", provided by Jan Košler of the University of Bergen. Mass bias effects for Hf and Yb were corrected using $^{179}Hf/^{177}Hf$ and $^{173}Yb/^{171}Yb$ (1.1302, Segal et al., 2003), respectively, with β_{Yb} being calculated ratio-by-ratio during single analysis. The $^{176}Yb/^{173}Yb$ ratio (Segal et al., 2003) and ^{173}Yb mass were used for the interference correction of ^{176}Yb on ^{176}Hf. The second interference on ^{176}Hf by ^{176}Lu was corrected using the measured ^{175}Lu mass, assuming $\beta_{Lu} = \beta_{Yb}$, and using $^{176}Lu/^{175}Lu$ of 0.02656 by Chu et al. (2002). Outliers for the Hf ratios were rejected based on the 2SD criteria with uncertainties based on the 2SD of the mean and only analyses with a minimum of 20 valid cycles (~1 cycle integrated per second) were used. Analyses with less than 20 cycles and where the invariant $^{178}Hf/^{177}Hf$ ratio, which monitors the effectiveness of mass bias correction, is different from natural Hf isotopic composition, were not used in the data reduction calculations. Standards used were the synthetic zircon MUNZirc-3 (B-142) and MUNZirc-4 (B-144) (Fisher et al., 2011) and natural zircon samples FC-1 and Temora-2 (Woodhead and Hergt, 2005). These were monitored throughout the measurement sessions and compared to accepted Hf isotopic

ratios as found in Table 8-4. LA-MC-ICPMS results of the zircon standards from this study can be found in Figure 8-3 and Table 8-5. Epsilon Hf (εHf) values are reported as deviation from the chondritic uniform reservoir (CHUR) using the values from Bouvier et al. (2008) of $^{176}Hf/^{177}Hf = 0.282785$ and $^{176}Lu/^{177}Hf = 0.0336$. Initial $^{176}Hf/^{177}Hf$ ($^{176}Hf/^{177}Hf_i$) have been calculated for the best age estimate for each sample, using the decay constant of Söderlund et al. (2004). Initial εHf (εHf_i) and uncertainties have been calculated following the algorithm of Ickert (2010).

Three-hundred and nine U-Pb analyses were done on the zircon grains from the ten samples in this study, over three measurement sessions in 2011, 2013 and 2014 on four different grain mounts (Westhues et al., 2016). While measuring the oxygen isotopic composition in 2013, the primary Cs^+ beam became charged (probably due to minute amounts of water vapor caught in bubbles in the epoxy) and the electron gun drilled explosively into and across the epoxy mount. During this unfortunate event, 87 zircon grains were destroyed, and 59 grains were not measured following the explosion due to their proximity to the damaged region in the epoxy mount. Of the remaining 163 zircon grains, 99 oxygen analyses were done on the most concordant grains (Table 8-6). Lu-Hf ratios were determined in the same spots as oxygen analyses, but also in other dated spots to identify differences between concordant and discordant areas of the zircon, totaling 128 Lu/Hf analyses (8-7). Analyses for Hf isotopic composition of samples placed in discordant areas of the dated zircon grains overlap with those done in concordant areas for samples KRN-11-05, KRN-12-02, -03, -05 and NUK-12-02. The highest εHf_i values from K-1 are obtained from analyses with U-Pb results with a discordance of greater than 5%. Table 8-

8 gives a comprehensive summary of SIMS U-Pb dates and oxygen analyses, and LA-MC-ICPMS Lu-Hf ratios for the individual grains.

Table 8-9 shows calculation of theoretical oxygen isotopic compositions for rhyolite and dacite magmas in equilibrium with magnetite from Kiruna (values from Nyström et al., 2008). Mineral-rock oxygen fractionation values (1000lnα) are from Zhao and Zheng (2003): magnetite-andesite = -4.7 ‰, magnetite-dacite = -4.3 ‰, and mineral-water oxygen fractionation values (1000lnα) at different temperatures are from Zheng (Zheng, 1991): magnetite-water (800 ºC) = - 5.3 ‰ and magnetite-water (400 ºC) = -7.9 ‰. Table 8-10 shows calculations of theoretical oxygen isotopic compositions of fluids in equilibrium with whole rock oxygen data of metavolcanic and intrusive rocks from Kiruna (Blake, 1992) at different temperatures, water-rock oxygen fractionation values (1000lnα) from Zhao and Zheng (2003).

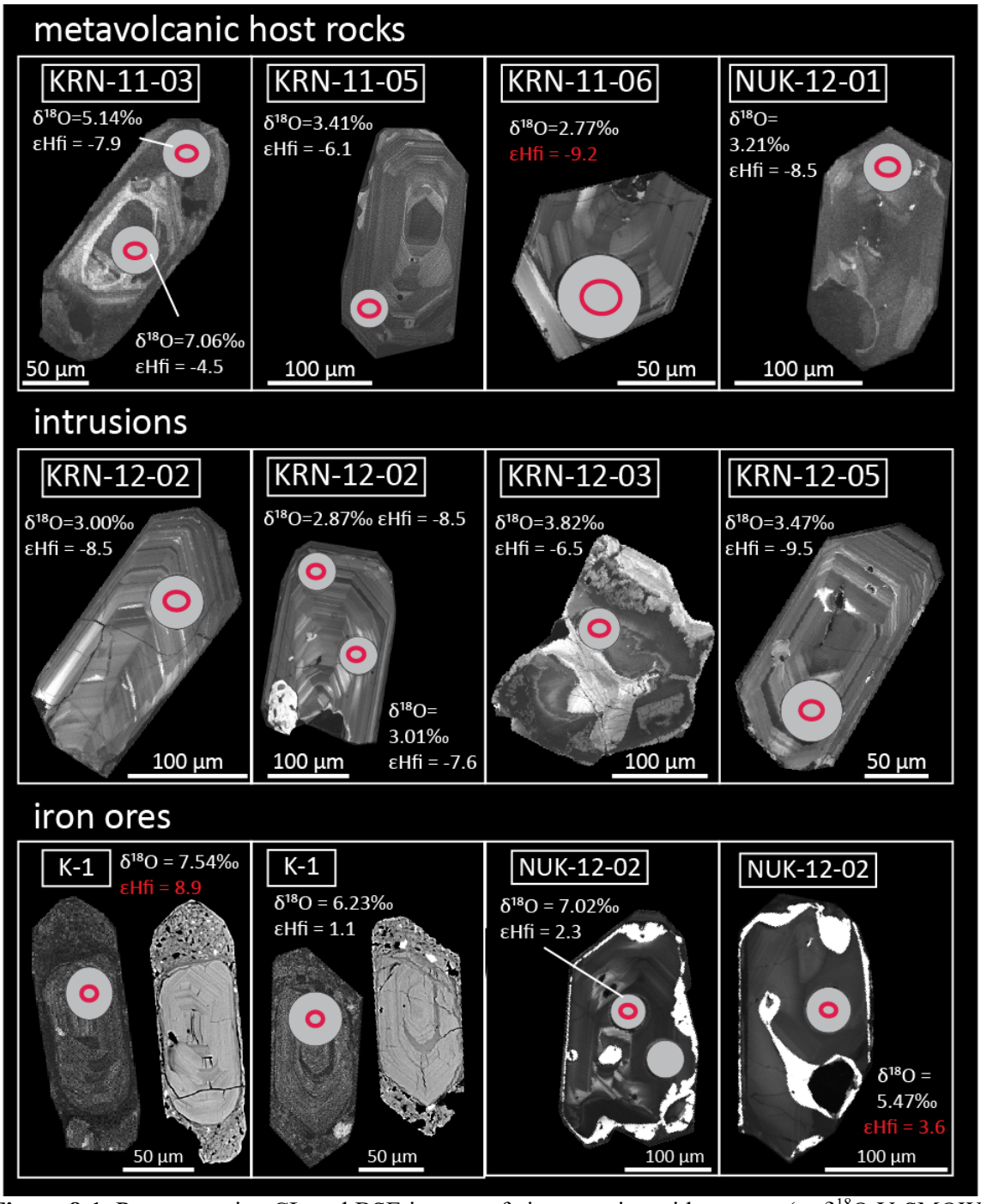

Figure 8-1. Representative CL and BSE images of zircon grains with oxygen (as $\delta^{18}O$ V-SMOW) and Lu-Hf (as initial εHf) isotopic compositions; εHf values in red have not been used due to analytical problems (see Table 8-7). Red ellipses in CL images show locations of NordSIM oxygen analyses, grey spots in CL images show subsequent Lu-Hf LA-MC-ICPMS analyses. For ore sample K-1, BSE images have been included, since they show the differences between core and rims regions particularly well.

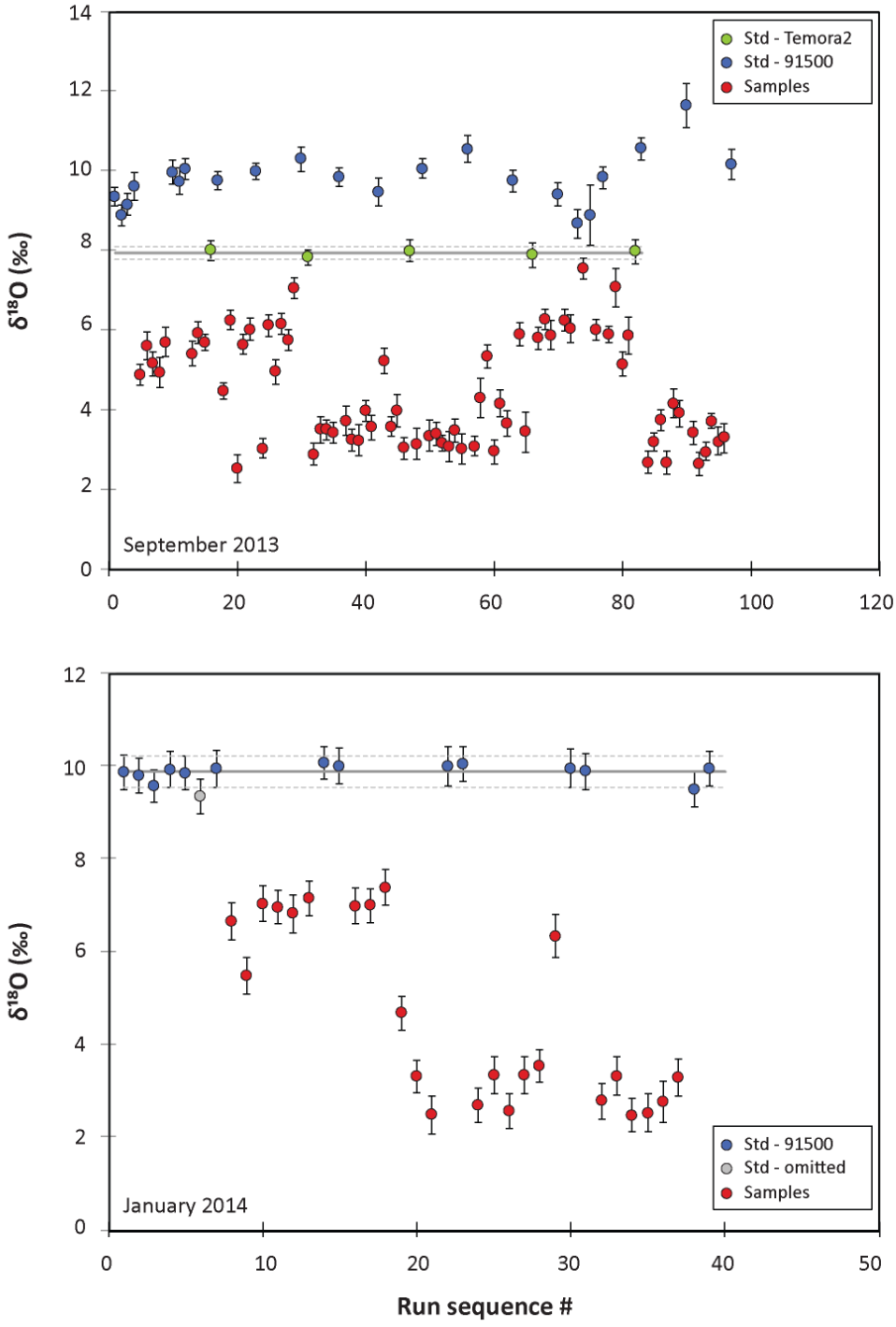

Figure 8-2. Oxygen analyses session overview for September 2013 (upper part) and January 2014 (lower part). While the piece of geostandard zircon 91500 (Wiedenbeck et al., 2004) used in 2014 has very consistent results, however, the piece used in 2013, that was mounted in the same epoxy mount as the Kiruna zircon crystals showed impurities in the oxygen composition. Therefore, the geostandard zircon Temora-2 (Eiler, 2001) was used instead a primary standard.

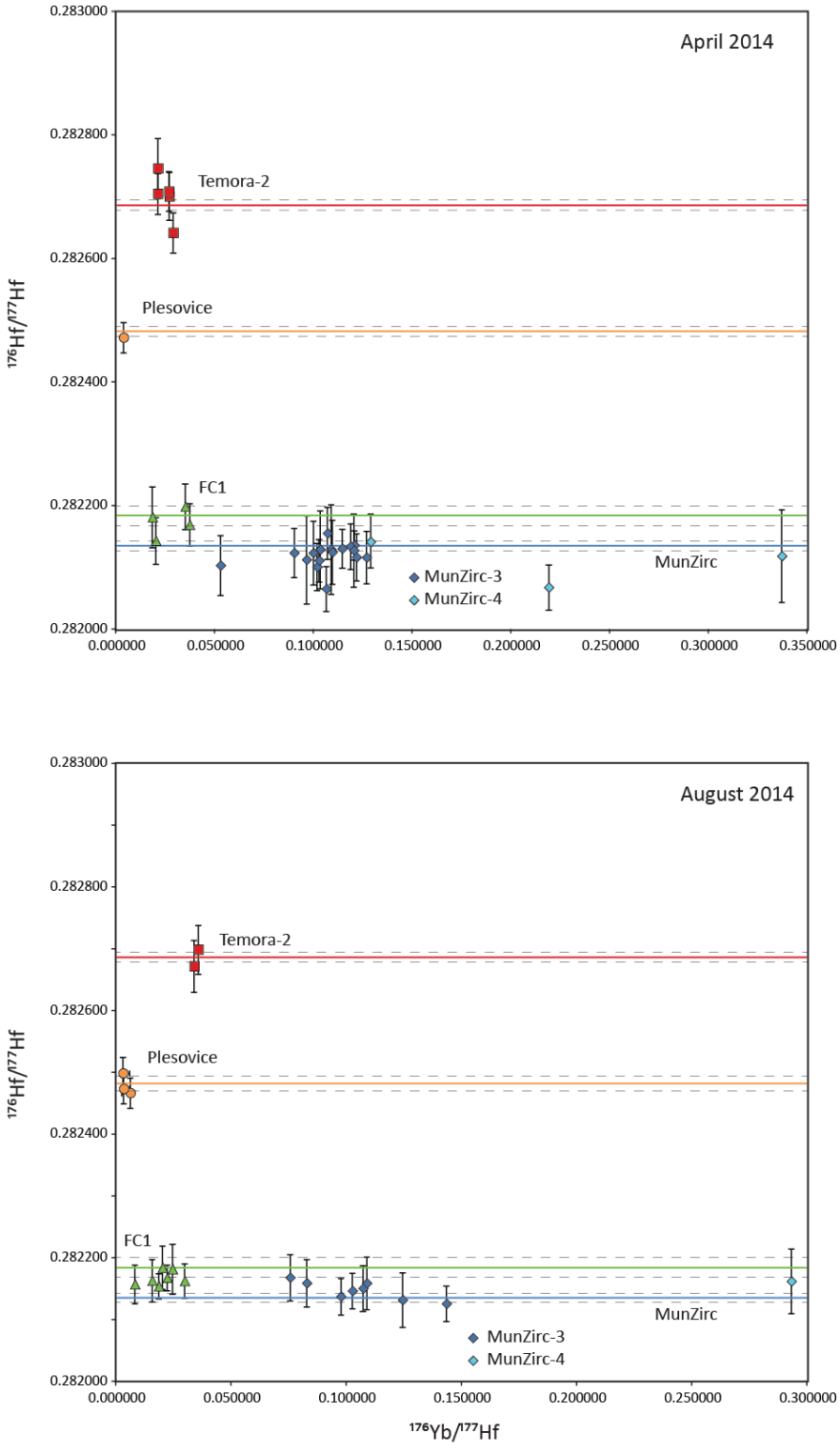

Figure 8-3. Plot of $^{176}Hf/^{177}Hf$ vs. $^{176}Yb/^{177}Hf$ for zircon standard measurements from this study. Bold lines represent accepted values and dashed lines the reported uncertainties as found in Table 8-4.

Table 8-1. Sample list with GPS locations, rock types, and mineralogy; sorted by location.

Sample	Latitude	Longitude	Underground level	Rock type + mineralogy
K-1	N 67° 51' 0.6"	E 20° 12' 23.8"	767 m	D-ore*: mag, ap, act ±fsp-qz*
KRN-11-03	N 67° 50' 13.1"	E 20° 12' 17.4"	1365 m	(trachy-) andesite(FW): *Ab, Kfs ±act-tt-qz*
KRN-11-05	N 67° 50' 35.6"	E 20° 12' 37.4"	1065 m	rhyodacite (HW): *Kfs, qz ±hbl-tt*
Drill core end	N 67° 50' 35.6"	E 20° 12' 36.9"	1066 m	
KRN-11-06	N 67° 50' 35.8"	E 20° 12' 32.4"	1076 m	rhyodacite (HW): *Kfs (ser, Fe incl.), qz ±hbl-tit*
Drill core end	N 67° 50' 35.7"	E 20° 12' 34.2"	1077 m	
KRN-12-02	N 67° 50' 57.8"	E 20° 10' 24.7"	Surface	aplite: *qz, Kfs, Ab ±hbl-tt-mag*
KRN-12-03	N 67° 50' 23.4"	E 20° 10' 49.7"	Surface	syenite: *Kfs (Fe incl.), act, tt ± Ab-qz*
KRN-12-05	N 67° 50' 30.1"	E 20° 10' 50.1"	1365 m	granite: K*fs, qz ±Ab-bt-tt*
NUK-12-02	N 67° 53' 50.8"	E 20° 15' 33.9"	Surface	ore + host: *mag, ap – qz, ser ±ap, mag*
NUK-12-01	N 67° 53' 53.1"	E 20° 15' 31.1"	Surface	rhyodacite (FW): *qz, Kfs, ±bt-rt-act-mag*
REK-12-01	N 67° 52' 17.8"	E 20° 14' 13.6"	Surface	Rektorn porphyry (HW) K*fs (Fe incl., ser), qz, Fe ox*

Notes: KRN/K: Kiirunavaara, REK: Rektorn, NUK: Nukutusvaara, TUV: Tuolluvaara; FW: footwall; HW: hanging wall, ser.: seritization
Mineral abbreviations: Ab: albite, act: actinolite, ap: apatite, bt: biotite, cal: calcite, hm: hematite, Kfs: K-feldspar, mag: magnetite, qz: quartz, rt: rutile, tt: titanite.

Table 8-2. SIMS oxygen ratio analyses for zircon standards.

Sample ID	Seq # run	^{16}O cps (x 10^9)	$^{16}O_{samp/av.std}$	$^{18}O/^{16}O$ *drift corrected*	± abs	$\delta^{18}O$ *standards*	± ‰	$\delta^{18}O$ *rejected**	± ‰
a) September 2013: standard Temora-2, δ18O (std, ‰) = 7.93, extl. error (‰, 1SD) = 0.08, drift corr. (‰/run) = 0.004									
915ox_AW-mt4_@1	1	2.63	1.00	0.00201930	0.00000018			9.35	0.12
915ox_AW-mt4_@02	2	2.66	1.01	0.00201834	0.00000021			8.87	0.13
915ox_AW-mt4_@03	3	2.68	1.02	0.00201888	0.00000023			9.14	0.14
915ox_AW-mt4_@04	4	2.68	1.02	0.00201978	0.00000032			9.59	0.18
915ox_AW-mt4_@05	10	2.68	1.02	0.00202051	0.00000026			9.96	0.15
915ox_AW-mt4_@06	11	2.68	1.02	0.00202005	0.00000030			9.73	0.17
915ox_AW-mt4_@07	12	2.69	1.02	0.00202070	0.00000021			10.05	0.13
Tem_ox_AW-mt4_@1	16	2.70		0.00201660	0.00000019	8.00	0.12		
915ox_AW-mt4_@08	17	2.68	1.02	0.00202009	0.00000019			9.74	0.12
915ox_AW-mt4_@09	23	2.66	1.01	0.00202055	0.00000015			9.97	0.11
915ox_AW-mt4_@10	30	2.65	1.01	0.00202117	0.00000027			10.28	0.15
Tem_ox_AW-mt4_@2	31	2.65		0.00201624	0.00000013	7.82	0.10		
915ox_AW-mt4_@11	36	2.62	1.00	0.00202028	0.00000017			9.84	0.11
915ox_AW-mt4_@12	42	2.58	0.98	0.00201949	0.00000032			9.44	0.18
Tem_ox_AW-mt4_@3	47	2.63		0.00201657	0.00000022	7.98	0.13		
915ox_AW-mt4_@13	49	2.61	1.00	0.00202070	0.00000020			10.05	0.13
915ox_AW-mt4_@14	56	2.72	1.04	0.00202168	0.00000029			10.54	0.16
915ox_AW-mt4_@15	63	2.78	1.06	0.00202009	0.00000023			9.74	0.14
Tem_ox_AW-mt4_@4	66	2.66		0.00201637	0.00000027	7.88	0.15		
915ox_AW-mt4_@16	70	2.60	0.99	0.00201940	0.00000025			9.40	0.15
915ox_AW-mt4_@17	77	2.50	0.95	0.00202024	0.00000023			9.82	0.14
Tem_ox_AW-mt4_@5	82	2.48		0.00201653	0.00000026	7.97	0.15		
915ox_AW-mt4_@18	83	2.49	0.95	0.00202169	0.00000024			10.55	0.14
915ox_AW-mt4_@19	90	2.65	1.01	0.00202388	0.00000054			11.64	0.28
915ox_AW-mt4_@20	97	2.51	0.96	0.00202092	0.00000035			10.16	0.19
b) January 2014 a: standard 91500, δ18O (std, ‰) = 9.86, extl. error (‰, 1SD) = 0.17, drift corr. (‰/run) = 0.001									
915ox_mt-Kiruna6_@1	1	2.67		0.00202018	0.00000017	9.84	0.19		
915ox_mt-Kiruna6_@2	2	2.63		0.00202004	0.00000016	9.77	0.18		
915ox_mt-Kiruna6_@3	3	2.60		0.00201960	0.00000013	9.55	0.18		
915ox_mt-Kiruna6_@4	4	2.52		0.00202031	0.00000019	9.90	0.19		
915ox_mt-Kiruna6_@5	5	2.69		0.00202016	0.00000013	9.83	0.18		
915ox_mt-Kiruna6_@06	6	2.78	1.15	0.00201915	0.00000017			9.32	0.19
915ox_mt-Kiruna6_@07	7	2.63		0.00202037	0.00000022	9.93	0.20		
915ox_mt-Kiruna6_@08	14	2.55		0.00202061	0.00000012	10.06	0.18		
915ox_mt-Kiruna6_@09	15	2.55		0.00202046	0.00000021	9.98	0.20		
915ox_mt-Kiruna6_@10	22	2.42		0.00202046	0.00000027	9.98	0.21		
915ox_mt-Kiruna6_@11	23	2.41		0.00202053	0.00000016	10.01	0.18		
915ox_mt-Kiruna6_@12	30	2.23		0.00202035	0.00000025	9.93	0.21		
915ox_mt-Kiruna6_@13	31	2.19		0.00202023	0.00000019	9.86	0.19		
915ox_mt-Kiruna6_@14	38	1.95		0.00201944	0.00000018	9.47	0.19		
915ox_mt-Kiruna6_@15	39	1.92		0.00202035	0.00000019	9.92	0.19		
c) January 2014 b: chosen standard 91500, δ18O (std, ‰) = 9.86, extl. error (‰, 1SD) = 0.18, drift corr. (‰/run) = 0.001									
915ox_mt-Kiruna6_@14-b	1	1.95		0.00201952	0.00000018	9.53	0.20		
915ox_mt-Kiruna6_@15-b	2	1.92		0.00202048	0.00000019	10.01	0.21		
915ox_mt-Kiruna6_@16	9	1.71		0.00202017	0.00000017	9.86	0.20		
915ox_mt-Kiruna6_@17	10	1.68		0.00202059	0.00000016	10.07	0.20		
915ox_mt-Kiruna6_@18	17	1.53		0.00202030	0.00000029	9.93	0.23		
915ox_mt-Kiruna6_@19	18	1.46		0.00202050	0.00000021	10.03	0.21		
915ox_mt-Kiruna6_@20	23	1.19		0.00201996	0.00000023	9.76	0.22		
915ox_mt-Kiruna6_@21	24	1.15		0.00201986	0.00000029	9.71	0.23		

* all 91500 analyses for session a) were rejected due to impurities in the oxygen isotopic value of the used standard piece.

Table 8-3. Neptune MC-ICPMS cup configuration.

L4	L3	L2	L1	C	H1	H2	H3	H4
^{171}Yb	^{173}Yb	^{174}Hf+Yb	^{175}Lu	^{176}Hf+Yb+Lu	177Hf	^{178}Hf	^{179}Hf	empty

Table 8-4. Accepted ^{176}Hf/^{177}Hf isotopic composition of zircon standards used in this study.

Standard	^{176}Hf/^{177}Hf	2SE	Source
Plešovice	0.282482	0.000012	Slama et al 2008
MunZirc	0.282135	0.000007	Fisher et al 2011
FC-1	0.282184	0.000016	Woodhead and Hergt 2004
Temora-2	0.282686	0.000008	Woodhead and Hergt 2004

8.2 References – Appendix C

Black, L. P., Kamo, S. L., Allen, C. M., Davis, D. W., Aleinikoff, J. N., Valley, J. W., Mundil, R., Campbell, I. H., Korsch, R. J., Williams, I. S., and Foudoulis, C., 2004, Improved $^{206}Pb/^{238}U$ microprobe geochronology by the monitoring of a trace-element-related matrix effect; SHRIMP, ID–TIMS, ELA–ICP–MS and oxygen isotope documentation for a series of zircon standards: Chemical Geology, v. 205, p. 115-140.

Blake, K. L., 1992, The petrology, geochemistry and association to ore formation of the host rocks of the Kiirunavaara magnetite-apatite deposit, northern Sweden: Unpub. PhD thesis, University of Wales, 349 pp.

Bouvier, A., Vervoort, J. D., and Patchett, P. J., 2008, The Lu-Hf and Sm-Nd isotopic composition of CHUR: Constraints from unequilibrated chondrites and implications for the bulk composition of terrestrial planets: Earth and Planetary Science Letters, v. 273, p. 48-57.

Chen, H., Clark, A. H., and Kyser, T. K., 2010, The Marcona magnetite deposit, Ica, south-central Peru: A product of hydrous, iron oxide-rich melts?: Economic Geology, v. 105, p. 1441-1456.

Chu, N.-C., Taylor, R. N., Chavagnac, V., Nesbitt, R. W., Boella, R. M., Milton, J. A., German, C. R., Bayon, G., and Burton, K., 2002, Hf isotope ratio analysis using multi-collector inductively coupled plasma mass spectrometry: an evaluation of isobaric interference corrections: Journal of Analytical Atomic Spectrometry, v. 17.

Eiler, J. M., 2001, Oxygen isotope variations of basaltic lavas and upper mantle rocks, *in* Valley, J. W., and Cole, D. R., eds., Stable isotope geochemistry, Reviews in Mineralogy and Geochemistry, 43: Washington, DC, Mineralogical Society of America/Geochemical Society, p. 319-364.

Fisher, C. M., Hanchar, J. M., Samson, S. D., Dhuime, B., Blichert-Toft, J., Vervoort, J. D., and Lam, R., 2011, Synthetic zircon doped with hafnium and rare earth elements: A reference material for in situ hafnium isotope analysis: Chemical Geology, v. 286, p. 32-47.

Segal, I., Halicz, L., and Platzner, I. T., 2003, Accurate isotope ratio measurements of ytterbium by multiple collection inductively coupled plasma mass spectrometry applying erbium and hafnium in an improved double external normalization procedure: Journal of Analytical Atomic Spectrometry, v. 18, p. 1217-1223.

Söderlund, U., Patchett, P. J., Vervoort, J. D., and Isachsen, C. E., 2004, The ^{176}Lu decay constant determined by Lu–Hf and U–Pb isotope systematics of Precambrian mafic intrusions: Earth and Planetary Science Letters, v. 219, p. 311-324.

Westhues, A., Hanchar, J. M., Whitehouse, M. J., and Martinsson, O., 2016, New constraints on the timing of host rock emplacement, hydrothermal alteration, and iron oxide-apatite mineralization in the Kiruna district, Norrbotten, Sweden: Economic Geology v. 111, p. 1595-1618.

Whitehouse, M. J., and Nemchin, A. A., 2009, High precision, high accuracy measurement of oxygen isotopes in large lunar zircon by SIMS: Chemical Geology, v. 261, p. 32-42.

Wiedenbeck, M., Hanchar, J. M., Peck, W. H., Sylvester, P., Valley, J., Whitehouse, M., Kronz, A., Morishita, Y., Nasdala, L., Fiebig, J., Franchi, I., Girard, J. P., Greenwood, R. C., Hinton, R., Kita, N., Mason, P. R. D., Norman, M., Ogasawara, M., Piccoli, P. M., Rhede, D., Satoh, H., Schulz-Dobrick, B., Skår, O., Spicuzza, M. J., Terada, K., Tindle, A., Togashi, S., Vennemann, T., Xie, Q., and Zheng, Y. F., 2004, Further Characterisation of the 91500 Zircon Crystal: Geostandards and Geoanalytical Research, v. 28, p. 9-39.

Woodhead, J. D., and Hergt, J. M., 2005, A preliminary appraisal of seven natural zircon reference materials for in situ Hf isotope determination: Geostandards and Geoanalytical Research, v. 29, p. 183-195.

Zhao, Z.-F., and Zheng, Y.-F., 2003, Calculation of oxygen isotope fractionation in magmatic rocks: Chemical Geology, v. 193, p. 59-80.

Zheng, Y.-F., 1991, Calculation of oxygen isotope fractionation in metal oxides: Geochimica Et Cosmochimica Acta, v. 55, p. 2299-2307.

Table 8-5. LA-MC-ICPMS Lu-Hf isotopic analyses of zircon standards measured in this study. Strike-through data were not used due to analytical problems.

File name	Sample	$^{176}Hf/^{177}Hf$	2SE	$^{176}Lu/^{177}Hf$	2SE	$^{176}Yb/^{177}Hf$	2SE	$^{178}Hf/^{177}Hf$	2SE	Mean Hf, V	spot size
14ap02a01	Plešovice	0.282472	0.000016	0.000114	0.000001	0.003951	0.000025	1.467219	0.000029	4.56	49 µm
14au11b01	Plešovice	0.282466	0.000024	0.000182	0.000010	0.006299	0.000206	1.467203	0.000033	4.15	49 µm
14au11c01	Plešovice	0.282498	0.000026	0.000086	0.000000	0.003144	0.000014	1.467177	0.000041	3.86	49 µm
14au11d01	Plešovice	0.282473	0.000024	0.000096	0.000002	0.003449	0.000074	1.467195	0.000045	4.14	49 µm
	average	**0.282477**									
	2SD	0.000029									
	n	4									
14ap02a02	b142	0.282135	0.000024	0.005893	0.000051	0.120784	0.001161	1.467200	0.000038	3.05	40 µm
14ap02a13	b142	0.282133	0.000037	0.006064	0.000166	0.118967	0.003733	1.467267	0.000047	2.42	40 µm
14ap02a23	b142	0.282100	0.000038	0.005232	0.000023	0.101962	0.000553	1.467422	0.000055	2.72	40 µm
14ap02a32	b142	0.282111	0.000034	0.005328	0.000044	0.102955	0.000800	1.467461	0.000056	2.36	40 µm
14ap02a42	b142	0.282065	0.000036	0.005288	0.000058	0.106638	0.000999	1.467586	0.000041	2.66	40 µm
14ap02a51	b142	0.282123	0.000040	0.004480	0.000228	0.090383	0.005342	1.467238	0.000044	3.46	40 µm
14ap02a62	b142	0.282116	0.000042	0.006288	0.000016	0.127038	0.000153	1.467249	0.000045	2.66	40 µm
~~14ap02b01~~[1]	~~b142~~	~~0.280060~~	~~0.000089~~	~~0.005514~~	~~0.000058~~	~~0.106362~~	~~0.001488~~	~~1.474455~~	~~0.000410~~	~~2.58~~	40 µm
14ap02b11	b142	0.282116	0.000038	0.006085	0.000107	0.121915	0.002331	1.467236	0.000050	2.51	40 µm
14ap02c01	b142	0.282129	0.000073	0.005402	0.000112	0.109095	0.002107	1.467241	0.000055	2.38	40 µm
14ap02c12	b142	0.282127	0.000059	0.005864	0.000075	0.120535	0.001403	1.467240	0.000055	2.72	40 µm
14ap02c22	b142	0.282112	0.000071	0.004795	0.000072	0.096656	0.001232	1.467250	0.000050	2.65	40 µm
14ap02c31	b142	0.282155	0.000042	0.005245	0.000070	0.107201	0.001432	1.467266	0.000060	2.43	40 µm
14ap02c42	b142	0.282130	0.000031	0.005682	0.000015	0.114715	0.000634	1.467284	0.000051	2.48	40 µm
14ap02c51	b142	0.282128	0.000063	0.005162	0.000109	0.103533	0.002156	1.467309	0.000056	2.55	40 µm
14ap02c60	b142	0.282124	0.000052	0.005339	0.000036	0.109652	0.000325	1.467249	0.000046	2.39	40 µm
14ap02c69	b142	0.282123	0.000052	0.004959	0.000068	0.100149	0.001335	1.467300	0.000040	2.88	40 µm
14ap02c80	b142	0.282103	0.000048	0.002827	0.000153	0.053069	0.002790	1.467247	0.000067	3.35	40 µm
14au11b02	b142	0.282150	0.000037	0.005509	0.000181	0.107322	0.004136	1.467180	0.000032	3.89	40 µm
14au11b14	b142	0.282146	0.000029	0.005448	0.000036	0.102706	0.000725	1.467176	0.000053	1.99	40 µm
14au11c02	b142	0.282158	0.000043	0.005372	0.000042	0.108964	0.000813	1.467203	0.000058	2.36	40 µm
14au11c12	b142	0.282167	0.000037	0.004022	0.000029	0.075713	0.000604	1.467215	0.000050	2.13	40 µm
14au11c18	b142	0.282131	0.000044	0.006085	0.000125	0.124507	0.002323	1.467201	0.000041	2.50	40 µm
14au11d04	b142	0.282137	0.000030	0.004990	0.000022	0.097753	0.000343	1.467199	0.000033	3.91	40 µm
14au11d30	b142	0.282125	0.000029	0.006928	0.000070	0.143510	0.001506	1.467192	0.000031	4.13	40 µm
14au11b03	b142	0.282158	0.000039	0.004615	0.000005	0.082890	0.000306	1.467162	0.000047	2.58	40 µm
	average	**0.282128**									
	2SD	0.000044									
	n	25									
14ap02a03	b144	0.282118	0.000075	0.017130	0.000100	0.337272	0.001766	1.467178	0.000076	2.08	40 µm
14ap02c02	b144	0.282067	0.000037	0.011588	0.000022	0.219313	0.000108	1.467188	0.000042	2.56	40 µm
14ap02c81	b144	0.282142	0.000044	0.006970	0.000368	0.129117	0.007390	1.467190	0.000059	2.85	40 µm
14au11b04	b144	0.282161	0.000052	0.014605	0.000098	0.293235	0.002633	1.467205	0.000049	2.41	40 µm
	average	**0.282122**									
	2SD	0.000082									
	n	4									

Continued on next page. All ratios are corrected as described in appendix C; uncertainties are expressed at 95% confidence limit. [1]Invariant ratio off, [2]not enough data points.

Table 8-5 – continued**.** LA-MC-ICPMS Lu-Hf isotopic analyses of zircon standards measured in this study. Strike-through data were not used due to analytical problems.

File name	Sample	$^{176}Hf/^{177}Hf$	2SE	$^{176}Lu/^{177}Hf$	2SE	$^{176}Yb/^{177}Hf$	2SE	$^{178}Hf/^{177}Hf$	2SE	Mean Hf, V	spot size
14ap02b13	FC1	0.282169	0.000034	0.001474	0.000058	0.037445	0.001561	1.467252	0.000048	2.01	40 µm
~~14ap02c03~~[2]	~~FC1~~	~~0.282221~~	~~0.000050~~	~~0.001292~~	~~0.000055~~	~~0.035390~~	~~0.001317~~	~~1.467232~~	~~0.000093~~	~~3.36~~	40 µm
~~14ap02c13~~[2]	~~FC1~~	~~0.282222~~	~~0.000072~~	~~0.001442~~	~~0.000077~~	~~0.037735~~	~~0.002172~~	~~1.467288~~	~~0.000107~~	~~1.64~~	40 µm
14ap02c32	FC1	0.282198	0.000037	0.001333	0.000005	0.035174	0.000156	1.467224	0.000061	2.22	40 µm
14ap02c52	FC1	0.282143	0.000038	0.000797	0.000020	0.020327	0.000529	1.467240	0.000052	1.79	40 µm
14ap02c82	FC1	0.282181	0.000049	0.000735	0.000003	0.018566	0.000094	1.467192	0.000043	2.13	40 µm
14au11b25	FC1	0.282181	0.000040	0.000957	0.000001	0.024664	0.000045	1.467164	0.000062	2.43	40 µm
14au11c03	FC1	0.282157	0.000031	0.000326	0.000005	0.008283	0.000147	1.467250	0.000056	2.59	40 µm
14au11c13	FC1	0.282163	0.000034	0.000593	0.000018	0.015808	0.000534	1.467185	0.000052	2.11	40 µm
14au11c19	FC1	0.282183	0.000035	0.000749	0.000034	0.020283	0.000993	1.467200	0.000055	1.93	40 µm
14au11d02	FC1	0.282162	0.000028	0.001105	0.000029	0.029904	0.000859	1.467211	0.000042	3.38	40 µm
14au11d12	FC1	0.282167	0.000021	0.000872	0.000001	0.022303	0.000022	1.467163	0.000040	3.74	40 µm
14au11d28	FC1	0.282154	0.000020	0.000722	0.000007	0.018701	0.000208	1.467209	0.000042	3.84	40 µm
	average	**0.282169**									
	2SD	0.000042									
	n	11									
14ap02a04	Temora-2	0.282700	0.000039	0.001121	0.000027	0.027092	0.000908	1.467226	0.000051	2.03	40 µm
14ap02a14	Temora-2	0.282708	0.000032	0.001118	0.000038	0.026914	0.000916	1.467389	0.000051	1.91	40 µm
14ap02a33	Temora-2	0.282704	0.000033	0.000931	0.000013	0.021331	0.000362	1.467349	0.000053	2.15	40 µm
14ap02a52	Temora-2	0.282745	0.000049	0.000864	0.000110	0.021358	0.002885	1.467287	0.000072	1.80	40 µm
~~14ap02b02~~[1]	~~Temora-2~~	~~0.282595~~	~~0.000038~~	~~0.001150~~	~~0.000036~~	~~0.028210~~	~~0.000966~~	~~1.467792~~	~~0.000076~~	~~1.81~~	40 µm
14ap02b12	Temora-2	0.282641	0.000033	0.001195	0.000013	0.029107	0.000466	1.467252	0.000050	1.81	40 µm
14au11b05	Temora-2	0.282698	0.000040	0.001439	0.000039	0.035829	0.001346	1.467210	0.000055	1.59	40 µm
14au11b15	Temora-2	0.282671	0.000042	0.001383	0.000006	0.034008	0.000133	1.467217	0.000064	1.77	40 µm
	average	**0.282696**									
	2SD	0.000065									
	n	7									

All ratios are corrected as described in appendix C; uncertainties are expressed at 95% confidence limit. [1]Invariant ratio off, [2]not enough data points.

Table 8-6. SIMS oxygen ratio analyses for zircon of Kiruna, northern Sweden; $\delta^{18}O$ relative to V-SMOW.

sample + mount	oxygen analyses	grain	^{16}O cps (x 10^9)	$^{16}O_{samp/av.std}$	$^{18}O/^{16}O$ *drift corrected*	± abs	$\delta^{18}O$ zrc	± ‰
K-1 ore								
mount 4	n4721ox_K1_@4	R1G2 C	2.60	0.99	0.00201307	0.00000023	**6.23**	**0.14**
	n4721ox_K1_@6	R1G4 C	2.61	1.00	0.00201267	0.00000032	**6.04**	**0.18**
	n4721ox_K1_@10	R1G7	2.65	1.01	0.00201217	0.00000023	**5.79**	**0.14**
	n4721ox_K1_@13	R2G3	2.63	1.00	0.00201793	0.00000034	**8.66**	**0.18**
	n4721ox_K1_@16	R2G6	2.61	1.00	0.00201312	0.00000023	**6.26**	**0.14**
	n4721ox_K1_@17	R2G7	2.56	0.98	0.00201233	0.00000032	**5.87**	**0.18**
	n4721ox_K1_@18	R2G8	2.60	0.99	0.00201569	0.00000021	**7.54**	**0.13**
	n4721ox_K1_@21	R3G3	2.67	1.02	0.00201835	0.00000074	**8.88**	**0.37**
	n4721ox_K1_@22	R3G5 C	2.53	0.96	0.00201262	0.00000021	**6.01**	**0.13**
KRN-11-03 footwall								
mount 4	n4722ox_KRN11-03_@3	R2G1	2.49	0.95	0.00201236	0.00000015	**5.88**	**0.11**
	n4722ox_KRN11-03_@5	R2G3	2.54	0.97	0.00201232	0.00000044	**5.86**	**0.23**
	n4722ox_KRN11-03_@6	R3G2 C	2.69	1.02	0.00201472	0.00000046	**7.06**	**0.24**
	n4722ox_KRN11-03_@7	R3G2 C	2.45	0.93	0.00201087	0.00000026	**5.14**	**0.15**
KRN-11-05 hanging wall								
mount 4	n4723ox_KRN11-05_@6	R1G9	2.48	0.95	0.00200594	0.00000025	**2.67**	**0.14**
	n4723ox_KRN11-05_@7	R2G1	2.53	0.96	0.00200694	0.00000017	**3.17**	**0.11**
	n4723ox_KRN11-05_@9	R2G3	2.50	0.95	0.00200804	0.00000021	**3.72**	**0.13**
	n4723ox_KRN11-05_@10	R2G4	2.50	0.95	0.00200593	0.00000025	**2.67**	**0.14**
	n4723ox_KRN11-05_@13	R3G1	2.51	0.96	0.00200890	0.00000032	**4.15**	**0.18**
	n4723ox_KRN11-05_@14	R3G2	2.57	0.98	0.00200838	0.00000029	**3.89**	**0.16**
	n4723ox_KRN11-05_@16	R3G3 C	2.52	0.96	0.00200742	0.00000025	**3.41**	**0.15**
	n4723ox_KRN11-05_@17	R3G4	2.54	0.97	0.00200586	0.00000026	**2.63**	**0.15**
	n4723ox_KRN11-05_@18	R3G5	2.54	0.97	0.00200643	0.00000013	**2.92**	**0.10**
	n4723ox_KRN11-05_@19	R3G7	2.53	0.96	0.00200788	0.00000013	**3.64**	**0.10**
	n4723ox_KRN11-05_@20	R4G1	2.56	0.97	0.00200694	0.00000030	**3.17**	**0.16**
	n4723ox_KRN11-05_@21	R4G2	2.56	0.98	0.00200719	0.00000037	**3.30**	**0.20**
mount 6	n4900ox-R1-G3	R1-G3	2.52	1.04	0.00200982	0.00000016	**4.66**	**0.18**
	n4900ox-R2-G4	R2-G4	2.40	0.99	0.00200544	0.00000025	**2.47**	**0.21**
	n4900ox-R2-G5	R2-G5	2.43	1.00	0.00200708	0.00000012	**3.29**	**0.17**
	n4900ox-R3-G1	R3-G1	2.45	1.01	0.00200584	0.00000019	**2.67**	**0.19**
	n4900ox-R3-G2a	R3-G2 a	2.41	0.99	0.00200714	0.00000021	**3.32**	**0.20**
	n4900ox-R3-G2b	R3-G2 b	2.40	0.99	0.00200559	0.00000018	**2.54**	**0.19**
	n4900ox-R3-G3	R3-G3	2.37	0.98	0.00200716	0.00000022	**3.33**	**0.20**
	n4900ox-R4-G3	R4-G3	2.29	0.94	0.00201314	0.00000032	**6.32**	**0.23**
	n4900ox-R4-G4	R4-G4	2.34	0.97	0.00200756	0.00000013	**3.53**	**0.18**

Continued on next page. C: analyses in core, R: analyses in rim; a, b two analyses in similar zone of the same grain.

Table 8-6 - continued. SIMS oxygen ratio analyses for zircon of Kiruna, northern Sweden; $\delta^{18}O$ relative to V-SMOW.

sample + mount	oxygen analyses	grain	^{16}O cps (x 10^9)	$^{16}O_{samp/av.std}$	$^{18}O/^{16}O$ *drift corrected*	± abs	$\delta^{18}O$ zrc	± ‰
KRN-11-06 altered hanging wall								
mount 6	n4901ox-R1-G2	R1G2	2.12	0.88	0.00200603	0.00000019	**2.77**	**0.19**
	n4901ox-R1-G4	R1G4	1.87	1.19	0.00200629	0.00000016	**2.92**	**0.20**
	n4901ox-R2-G1	R2G1	2.00	0.82	0.00200704	0.00000024	**3.27**	**0.20**
	n4901ox-R2-G4	R2G4	2.08	0.86	0.00200711	0.00000025	**3.31**	**0.21**
	n4901ox-R2-G5	R2G5	2.01	0.83	0.00200553	0.00000024	**2.51**	**0.20**
	n4901ox-R3-G5	R3G5	2.04	0.84	0.00200543	0.00000017	**2.46**	**0.19**
	n4901ox-R4-G2	R4G2	2.01	0.83	0.00200598	0.00000030	**2.74**	**0.22**
KRN-12-02 intrusion								
mount 6	n4899ox-R1-G1	R1G1	1.62	1.03	0.00200612	0.00000025	**2.84**	**0.22**
	n4899ox-R1-G4	R1G4	1.60	1.02	0.00200685	0.00000020	**3.20**	**0.21**
	n4899ox-R2-G1	R2G1	1.72	1.09	0.00200589	0.00000024	**2.72**	**0.22**
	n4899ox-R2-G2	R2G2	1.70	1.08	0.00200646	0.00000015	**3.00**	**0.20**
	n4899ox-R3-G5	R3G5	1.81	1.15	0.00200631	0.00000023	**2.93**	**0.21**
	n4899ox-R4-G1a	R4G1 a	1.75	1.11	0.00200619	0.00000019	**2.87**	**0.21**
	n4899ox-R4-G1b	R4G1 b	1.78	1.13	0.00200648	0.00000013	**3.01**	**0.19**
KRN-12-03 intrusion								
mount 6	n4898ox-R4-G2	R4G2	1.58	1.01	0.00200808	0.00000042	**3.82**	**0.28**
KRN-12-05 intrusion								
mount 6	n4897ox-R1-G1	R1G1	1.26	0.80	0.00200651	0.00000025	**3.03**	**0.22**
	n4897ox-R1-G5	R1G5	1.31	0.83	0.00200653	0.00000023	**3.04**	**0.21**
	n4897ox-R2-G1	R2G1	1.22	0.78	0.00200599	0.00000039	**2.77**	**0.26**
	n4897ox-R3-G7	R3G7	1.36	0.87	0.00200771	0.00000020	**3.63**	**0.21**
	n4897ox-R4-G1	R4G1	1.60	1.02	0.00200739	0.00000024	**3.47**	**0.22**
	n4897ox-R4-G2	R4G2	1.55	0.99	0.00200885	0.00000021	**4.20**	**0.21**
	n4897ox-R4-G5	R4G5	1.53	0.97	0.00200765	0.00000031	**3.60**	**0.24**
REK-12-01 altered host rock								
mount 4	n4732ox_REK12-1_@15	R1G2	2.71	1.03	0.00200953	0.00000014	**4.47**	**0.10**
	n4732ox_REK12-1_@18	R1G4 C	2.64	1.01	0.00201308	0.00000019	**6.24**	**0.12**
	n4732ox_REK12-1_@21	R2G1	2.65	1.01	0.00200562	0.00000031	**2.51**	**0.17**
	n4732ox_REK12-1_@22	R2G3	2.70	1.03	0.00201187	0.00000020	**5.63**	**0.13**
	n4732ox_REK12-1_@24	R2G5 C	2.58	0.99	0.00201262	0.00000023	**6.01**	**0.14**
	n4732ox_REK12-1_@27	R3G1	2.67	1.02	0.00200663	0.00000019	**3.02**	**0.12**
	n4732ox_REK12-1_@28	R3G4	2.67	1.02	0.00201280	0.00000023	**6.10**	**0.14**
	n4732ox_REK12-1_@29	R4G4	2.65	1.01	0.00201049	0.00000026	**4.94**	**0.15**
	n4732ox_REK12-1_@30	R4G6	2.59	0.99	0.00201288	0.00000021	**6.14**	**0.13**
	n4732ox_REK12-1_@33	R5G3	2.65	1.01	0.00201206	0.00000021	**5.73**	**0.13**
	n4732ox_REK12-1_@35	R5G5	2.67	1.02	0.00201470	0.00000021	**7.05**	**0.13**

Continued on next page. C: analyses in core, R: analyses in rim; a, b two analyses in similar zone of the same grain

Table 8-6 - continued. SIMS oxygen ratio analyses for zircon of Kiruna, northern Sweden; $\delta^{18}O$ relative to V-SMOW.

sample + mount	oxygen analyses	grain	^{16}O cps (x 10^9)	$^{16}O_{samp/av.std}$	$^{18}O/^{16}O$ *drift corrected*	± abs	$\delta^{18}O$ zrc	± ‰
NUK-12-01 footwall								
mount 4	n4719ox_NUK12-1_@8	R2G1	2.63	1.00	0.00200801	0.00000033	**3.71**	**0.18**
	n4719ox_NUK12-1_@11	R2G4	2.62	1.00	0.00200705	0.00000023	**3.23**	**0.13**
	n4719ox_NUK12-1_@16	R3G2	2.49	0.95	0.00200702	0.00000037	**3.21**	**0.20**
	n4719ox_NUK12-1_@17	R3G3	2.63	1.00	0.00200854	0.00000022	**3.97**	**0.13**
	n4719ox_NUK12-1_@19	R3G6	2.61	1.00	0.00200770	0.00000027	**3.55**	**0.15**
	n4719ox_NUK12-1_@21	R3G8	2.63	1.00	0.00201102	0.00000028	**5.21**	**0.16**
	n4719ox_NUK12-1_@22	R3G9	2.58	0.98	0.00200773	0.00000019	**3.57**	**0.12**
	n4719ox_NUK12-1_@27	R4G5	2.59	0.99	0.00200853	0.00000038	**3.97**	**0.21**
	n4719ox_NUK12-1_@29	R4G8	2.47	0.94	0.00200665	0.00000023	**3.03**	**0.14**
	n4719ox_NUK12-1_@39	R1G1	2.64	1.00	0.00200634	0.00000023	**2.87**	**0.14**
	n4719ox_NUK12-1_@41	R1G3	2.63	1.00	0.00200757	0.00000030	**3.49**	**0.17**
	n4719ox_NUK12-1_@42	R1G4	2.63	1.00	0.00200758	0.00000019	**3.49**	**0.12**
	n4719ox_NUK12-1_@43	R1G5	2.67	1.02	0.00200744	0.00000022	**3.42**	**0.13**
NUK-12-02 ore								
mount 6	n4896ox-R1-G3	R1G3	2.50	1.03	0.00201410	0.00000023	**6.80**	**0.20**
	n4896ox-R1-G5	R1G5	2.53	1.04	0.00201477	0.00000019	**7.13**	**0.19**
	n4896ox-R2-G2a	R2G2	2.57	1.06	0.00201453	0.00000020	**6.97**	**0.20**
	n4896ox-R2-G2b	R2G2 R	2.51	1.03	0.00201438	0.00000014	**6.64**	**0.20**
	n4896ox-R3-G1	R3G1	2.67	1.10	0.00201145	0.00000022	**7.02**	**0.19**
	n4896ox-R3-G3	R3G3	2.50	1.03	0.00201446	0.00000014	**6.94**	**0.18**
	n4896ox-R3-G6	R3G6	2.52	1.04	0.00201443	0.00000022	**5.47**	**0.20**
	n4896ox-R4-G1	R4G1	2.61	1.07	0.00201377	0.00000022	**6.98**	**0.18**
	n4896ox-R4-G5	R4G5	2.48	1.02	0.00201523	0.00000021	**7.37**	**0.19**

C: analyses in core, R: analyses in rim; a, b two analyses in similar zone of the same grain.

Table 8-7. LA-MC-ICPMS Lu-Hf isotopic analyses of zircon from Kiruna, Sweden. Strike-through data were not used due to analytical problems.

sample	grain	analyses	$^{176}Hf/^{177}Hf$	2SE	$^{176}Lu/^{177}Hf$	2SE	$^{176}Yb/^{177}Hf$	2SE	$^{178}Hf/^{177}Hf$	2SE	$\varepsilon_{Hf}(0)$	2SE	$^{176}Hf/^{177}Hf_i$	$\varepsilon_{Hf}(i)$	2SE	Assigned age (Ma)	Mean Hf (V)
K-1	**ore**																
mount 2	R2G1[1]	~~14ap02b03~~	~~0.281641~~	~~0.000034~~	~~0.000768~~	~~0.000021~~	~~0.017172~~	~~0.000438~~	~~1.467554~~	~~0.000058~~	~~-40.5~~	~~1.2~~	~~0.281613~~	~~0.9~~	~~1.2~~	~~1874.1~~	~~2.2~~
	R1G3[2]	~~14ap02b04~~	~~0.281517~~	~~0.000192~~	~~0.005458~~	~~0.001155~~	~~0.140501~~	~~0.029576~~	~~1.467707~~	~~0.000106~~	~~-44.8~~	~~6.8~~	~~0.281323~~	~~-9.4~~	~~7.0~~	~~1874.1~~	~~2.6~~
	R1G1, D	14ap02b05	0.281737	0.000045	0.003032	0.000068	0.083703	0.002437	1.467263	0.000065	-37.0	1.6	0.281630	1.5	1.6	1874.1	3.1
	R3G1	14ap02b06	0.281493	0.000057	0.001408	0.000365	0.037606	0.010444	1.467307	0.000063	-45.7	2.0	0.281443	-5.2	2.1	1874.1	2.6
	R3G3[2], D	~~14ap02b07~~	~~0.281713~~	~~0.000042~~	~~0.001542~~	~~0.000270~~	~~0.039188~~	~~0.007515~~	~~1.467233~~	~~0.000101~~	~~-37.9~~	~~1.5~~	~~0.281658~~	~~2.5~~	~~1.6~~	~~1874.1~~	~~2.8~~
	R5G2	14ap02b08	0.281547	0.000046	0.001873	0.000393	0.048459	0.010343	1.467223	0.000069	-43.8	1.6	0.281481	-3.8	1.7	1874.1	2.6
	R6G1, D	14ap02b09	0.281706	0.000037	0.001878	0.000450	0.043268	0.010283	1.467223	0.000047	-38.2	1.3	0.281639	1.8	1.5	1874.1	2.4
	R7G2[2]	~~14ap02b10~~	~~0.281664~~	~~0.000105~~	~~0.001208~~	~~0.000388~~	~~0.031035~~	~~0.010299~~	~~1.467261~~	~~0.000097~~	~~-39.6~~	~~3.7~~	~~0.281621~~	~~1.1~~	~~3.8~~	~~1874.1~~	~~4.0~~
mount 4	R1G2C, D	14ap02c61	0.281700	0.000043	0.0022548	0.001104	0.061994	0.034377	1.467207	0.000081	-38.4	1.5	0.281619	1.1	2.1	1874.1	2.7
	R1G4C[2],D	~~14ap02e62~~	~~0.281689~~	~~0.000050~~	~~0.001133~~	~~0.000243~~	~~0.028177~~	~~0.006368~~	~~1.467211~~	~~0.000106~~	~~-38.8~~	~~1.8~~	~~0.281648~~	~~2.1~~	~~1.8~~	~~1874.1~~	~~2.9~~
	R1G7	14ap02c63	0.281574	0.000047	0.000889	0.000019	0.023140	0.000535	1.467226	0.000059	-42.8	1.7	0.281543	-1.6	1.7	1874.1	2.8
	R2G8[2], D	~~14ap02e64~~	~~0.281423~~	~~0.000215~~	~~0.002368~~	~~0.000972~~	~~0.061788~~	~~0.026720~~	~~1.467318~~	~~0.000101~~	~~-48.2~~	~~7.6~~	~~0.281339~~	~~-8.9~~	~~7.7~~	~~1874.1~~	~~3.1~~
	R2G7[2]	~~14ap02e65~~	~~0.281525~~	~~0.000072~~	~~0.001922~~	~~0.000433~~	~~0.049978~~	~~0.011856~~	~~1.467314~~	~~0.000037~~	~~-44.6~~	~~2.6~~	~~0.281456~~	~~-4.7~~	~~2.6~~	~~1874.1~~	~~2.9~~
	R3G5C[2]	~~14ap02e66~~	~~0.281709~~	~~0.000040~~	~~0.000688~~	~~0.000047~~	~~0.016992~~	~~0.001571~~	~~1.467250~~	~~0.000091~~	~~-38.1~~	~~1.4~~	~~0.281684~~	~~3.4~~	~~1.5~~	~~1874.1~~	~~3.1~~
	R3G3[2]	~~14ap02e67~~	~~0.281662~~	~~0.000049~~	~~0.003577~~	~~0.000373~~	~~0.083593~~	~~0.008592~~	~~1.467288~~	~~0.000098~~	~~-39.7~~	~~1.7~~	~~0.281535~~	~~-1.9~~	~~1.8~~	~~1874.1~~	~~2.8~~
	R2G3[2], D	~~14ap02e68~~	~~0.281535~~	~~0.000076~~	~~0.002610~~	~~0.001605~~	~~0.069058~~	~~0.041860~~	~~1.467280~~	~~0.000034~~	~~-44.2~~	~~2.7~~	~~0.281442~~	~~-5.2~~	~~3.4~~	~~1874.1~~	~~2.7~~
	R1G2R[2],D	14au11c04	0.281796	0.000051	0.001973	0.000411	0.048079	0.009894	1.467175	0.000074	-35.0	1.8	0.281726	4.9	1.9	1874.1	2.3
	R1G4R[2],D	~~14au11c05~~	~~0.281973~~	~~0.000108~~	~~0.008912~~	~~0.000639~~	~~0.216515~~	~~0.014856~~	~~1.467230~~	~~0.000095~~	~~-28.7~~	~~3.8~~	~~0.281656~~	~~2.4~~	~~3.9~~	~~1874.1~~	~~1.6~~
	R1G6[2], D	~~14au11c06~~	~~0.282064~~	~~0.000205~~	~~0.007507~~	~~0.000599~~	~~0.196103~~	~~0.013059~~	~~1.467191~~	~~0.000202~~	~~-25.5~~	~~7.3~~	~~0.281796~~	~~7.4~~	~~7.3~~	~~1874.1~~	~~1.6~~
	R1G8[2], D	~~14au11c07~~	~~0.281676~~	~~0.000080~~	~~0.001163~~	~~0.000161~~	~~0.028221~~	~~0.003605~~	~~1.467188~~	~~0.000078~~	~~-39.2~~	~~2.8~~	~~0.281635~~	~~1.6~~	~~2.9~~	~~1874.1~~	~~2.9~~
	R1G7b	14au11c08	0.281708	0.000056	0.002503	0.000167	0.067408	0.004532	1.467207	0.000093	-38.1	2.0	0.281618	1.1	2.0	1874.1	1.5
	R2G6	14au11c09	0.281740	0.000066	0.002436	0.000911	0.063260	0.024041	1.467119	0.000134	-37.0	2.3	0.281653	2.3	2.6	1874.1	2.4
	R2G4C, D	14au11c10	0.281875	0.000074	0.003076	0.000572	0.076833	0.014048	1.467148	0.000082	-32.2	2.6	0.281765	6.3	2.8	1874.1	2.2
	R2G4R, D	14au11c11	0.282191	0.000070	0.006440	0.000055	0.150980	0.001360	1.467177	0.000101	-21.0	2.5	0.281962	13.3	2.5	1874.1	1.6
	R3G6, D	14au11c14	0.281701	0.000062	0.000987	0.000131	0.024324	0.003568	1.467263	0.000083	-38.3	2.2	0.281666	2.8	2.2	1874.1	1.9
	mean		**0.281731**						**1.467212**					**2.0**			
	2SD		**0.000359**						**0.000104**					**9.6**			
KRN-11-03	**footwall**																
mount 4	R2G1[2]	~~14ap02e70~~	~~0.281705~~	~~0.000106~~	~~0.001262~~	~~0.000036~~	~~0.028687~~	~~0.002201~~	~~1.467115~~	~~0.000117~~	~~-38.2~~	~~3.7~~	~~0.281660~~	~~2.8~~	~~3.8~~	~~1884.1~~	~~2.5~~
	R1G2[2]	~~14ap02e71~~	~~0.281501~~	~~0.000042~~	~~0.001256~~	~~0.000068~~	~~0.028598~~	~~0.001423~~	~~1.467234~~	~~0.000101~~	~~-45.4~~	~~1.5~~	~~0.281456~~	~~-4.5~~	~~1.5~~	~~1884.1~~	~~2.7~~
	R2G3[2]	~~14ap02e72~~	~~0.281452~~	~~0.000047~~	~~0.000728~~	~~0.000013~~	~~0.015180~~	~~0.000243~~	~~1.467260~~	~~0.000133~~	~~-47.1~~	~~1.7~~	~~0.281426~~	~~-5.5~~	~~1.7~~	~~1884.1~~	~~3.7~~
	R3G2R	14ap02c73	0.281420	0.000035	0.000631	0.000014	0.013404	0.000268	1.467193	0.000044	-48.3	1.2	0.281398	-6.5	1.3	1884.1	2.4
	R1G2	14au11c15	0.281539	0.000056	0.001304	0.000045	0.029385	0.000831	1.467155	0.000091	-44.1	2.0	0.281492	-3.2	2.0	1884.1	2.8
	R3G2C	14au11c16	0.281492	0.000026	0.001052	0.000028	0.024630	0.000609	1.467189	0.000045	-45.7	0.9	0.281454	-4.5	1.0	1884.1	2.2
	R4G1	14au11c17	0.281736	0.000042	0.001122	0.000163	0.024533	0.002869	1.467155	0.000074	-37.1	1.5	0.281696	4.1	1.5	1884.1	2.5
	Mean		**0.281547**						**1.467173**					**-2.6**			
	2SD		**0.000271**						**0.000041**					**9.2**			
KRN-11-05	**hanging wall**																
mount 4	R2G1	14ap02c74	0.281436	0.000041	0.001519	0.000056	0.037229	0.001257	1.467217	0.000062	-47.7	1.4	0.281382	-7.2	1.5	1880.5	1.7
	R3G2	14ap02c75	0.281413	0.000052	0.001071	0.000108	0.026422	0.002850	1.467214	0.000056	-48.5	1.8	0.281375	-7.4	1.9	1880.5	1.9
	R3G3R	14ap02c76	0.281451	0.000029	0.001035	0.000029	0.025593	0.000653	1.467206	0.000056	-47.2	1.0	0.281414	-6.1	1.1	1880.5	2.3
	R4G2	14ap02c77	0.281430	0.000048	0.001470	0.000291	0.032545	0.005547	1.467241	0.000061	-47.9	1.7	0.281377	-7.4	1.8	1880.5	2.2
mount 6	R1G3[2]	~~14ap02a36~~	~~0.281435~~	~~0.000116~~	~~0.001028~~	~~0.000032~~	~~0.024502~~	~~0.000845~~	~~1.467875~~	~~0.000030~~	~~-47.7~~	~~4.1~~	~~0.281398~~	~~-6.6~~	~~4.1~~	~~1880.5~~	~~2.0~~
	R2G4[2]	~~14ap02a37~~	~~0.281296~~	~~0.000022~~	~~0.000874~~	~~0.000063~~	~~0.021957~~	~~0.001713~~	~~1.467784~~	~~0.000109~~	~~-52.7~~	~~0.8~~	~~0.281264~~	~~-11.4~~	~~0.8~~	~~1880.5~~	~~2.6~~
	R2G4b[2]	~~14ap02a38~~	~~0.281380~~	~~0.000051~~	~~0.001351~~	~~0.000023~~	~~0.034887~~	~~0.000525~~	~~1.467913~~	~~0.000139~~	~~-49.7~~	~~1.8~~	~~0.281332~~	~~-9.0~~	~~1.9~~	~~1880.5~~	~~2.1~~
	R2G5[2]	~~14ap02a39~~	~~0.281368~~	~~0.000087~~	~~0.001175~~	~~0.000065~~	~~0.028889~~	~~0.001534~~	~~1.467903~~	~~0.000088~~	~~-50.1~~	~~3.1~~	~~0.281326~~	~~-9.2~~	~~3.1~~	~~1880.5~~	~~3.1~~

continued on next pages. C: analyses in core, R: analyses in rim; a, b two analyses in similar zone of the same grain; D: > 5% discordant at 2σ level. All data are corrected as described in text in appendix C. [1]Invariant ratio off, [2]not enough data points.

Table 8-7 – continued. LA-MC-ICPMS Lu-Hf isotopic analyses of zircon from Kiruna, Sweden. Strike-through data were not used due to analytical problems.

sample	grain	analyses	$^{176}Hf/^{177}Hf$	2SE	$^{176}Lu/^{177}Hf$	2SE	$^{176}Yb/^{177}Hf$	2SE	$^{178}Hf/^{177}Hf$	2SE	$\varepsilon_{Hf}(0)$	2SE	$^{176}Hf/^{177}Hf_i$	$\varepsilon_{Hf}(i)$	2SE	Assigned age (Ma)	Mean Hf (V)
KRN-11-05	**hanging wall - continued**																
mount 6	R3G1[1]	~~14ap02a40~~	~~0.281382~~	~~0.000040~~	~~0.001767~~	~~0.000028~~	~~0.045535~~	~~0.000755~~	~~1.467877~~	~~0.000082~~	~~-49.6~~	~~1.4~~	~~0.281319~~	~~-9.4~~	~~1.4~~	~~1880.5~~	~~2.2~~
	R3G1b[2]	~~14ap02a41~~	~~0.281368~~	~~0.000033~~	~~0.000793~~	~~0.000023~~	~~0.019888~~	~~0.000657~~	~~1.467538~~	~~0.000093~~	~~-50.1~~	~~1.2~~	~~0.281340~~	~~-8.7~~	~~1.2~~	~~1880.5~~	~~2.8~~
	R3G2a, D	14ap02a43	0.281436	0.000042	0.000808	0.000079	0.019782	0.002037	1.467403	0.000063	-47.7	1.5	0.281407	-6.3	1.5	1880.5	2.1
	R3G2b	14ap02a44	0.281441	0.000035	0.001363	0.000082	0.034848	0.002180	1.467334	0.000050	-47.5	1.3	0.281392	-6.8	1.3	1880.5	2.2
	R3G3[2]	~~14ap02a45~~	~~0.281509~~	~~0.000110~~	~~0.003450~~	~~0.000177~~	~~0.090653~~	~~0.004616~~	~~1.467334~~	~~0.000088~~	~~-45.1~~	~~3.9~~	~~0.281386~~	~~-7.0~~	~~3.9~~	~~1880.5~~	~~2.4~~
	R4G1[2]	~~14ap02a46~~	~~0.281474~~	~~0.000050~~	~~0.001333~~	~~0.000007~~	~~0.034725~~	~~0.000160~~	~~1.467338~~	~~0.000091~~	~~-46.4~~	~~1.8~~	~~0.281427~~	~~-5.6~~	~~1.8~~	~~1880.5~~	~~3.3~~
	R4G3	*14ap02a47*	*0.282141*	*0.000024*	*0.000413*	*0.000095*	*0.009971*	*0.002132*	*1.467266*	*0.000055*	*-22.8*	*0.8*	*0.282126*	*7.2*	*0.9*	*1349.0*	*3.7*
	R4G4	14ap02a48	0.281410	0.000046	0.001155	0.000060	0.029634	0.001616	1.467318	0.000052	-48.6	1.6	0.281368	-7.7	1.6	1880.5	2.7
	mean		**0.281431**						**1.467276**					**-7.0**			
	2SD		**0.000030**						**0.000152**					**1.2**			
KRN-11-06	**altered hanging wall**																
	R1G2[2]	~~14ap02a28~~	~~0.281367~~	~~0.000035~~	~~0.001118~~	~~0.000052~~	~~0.027630~~	~~0.001427~~	~~1.467502~~	~~0.000074~~	~~-50.2~~	~~1.2~~	~~0.281327~~	~~-9.2~~	~~1.3~~	~~1880.1~~	~~2.7~~
	R1G4[2]	~~14ap02a29~~	~~0.281559~~	~~0.000097~~	~~0.002816~~	~~0.000150~~	~~0.073717~~	~~0.004129~~	~~1.467478~~	~~0.000045~~	~~-43.3~~	~~3.4~~	~~0.281459~~	~~-4.5~~	~~3.5~~	~~1880.1~~	~~2.8~~
	R2G4[2]	~~14ap02a30~~	~~0.281432~~	~~0.000042~~	~~0.001123~~	~~0.000043~~	~~0.028141~~	~~0.001144~~	~~1.467466~~	~~0.000060~~	~~-47.9~~	~~1.5~~	~~0.281392~~	~~-6.9~~	~~1.5~~	~~1880.1~~	~~2.9~~
	R2G1	14ap02a31	0.281434	0.000048	0.000953	0.000073	0.023822	0.001910	1.467413	0.000051	-47.8	1.7	0.281400	-6.6	1.7	1880.1	2.2
	R3G5[2]	~~14ap02a34~~	~~0.281442~~	~~0.000044~~	~~0.000769~~	~~0.000012~~	~~0.018952~~	~~0.000343~~	~~1.467408~~	~~0.000090~~	~~-47.5~~	~~1.6~~	~~0.281415~~	~~-6.0~~	~~1.6~~	~~1880.1~~	~~2.9~~
	R4G2[1]	~~14ap02a35~~	~~0.281387~~	~~0.000031~~	~~0.000723~~	~~0.000027~~	~~0.017377~~	~~0.000651~~	~~1.467618~~	~~0.000068~~	~~-49.4~~	~~1.1~~	~~0.281362~~	~~-7.9~~	~~1.2~~	~~1880.1~~	~~2.5~~
	R2G4b[2]	~~14au11b16~~	~~0.281560~~	~~0.000061~~	~~0.001419~~	~~0.000127~~	~~0.036837~~	~~0.003490~~	~~1.467216~~	~~0.000117~~	~~-43.3~~	~~2.2~~	~~0.281510~~	~~-2.7~~	~~2.2~~	~~1880.1~~	~~2.3~~
	R2G5[2]	~~14au11b17~~	~~0.281563~~	~~0.000100~~	~~0.000913~~	~~0.000033~~	~~0.023044~~	~~0.000945~~	~~1.467306~~	~~0.000180~~	~~-43.2~~	~~3.6~~	~~0.281530~~	~~-1.9~~	~~3.6~~	~~1880.1~~	~~1.4~~
	R4G2b	14au11b18	0.281393	0.000050	0.001009	0.000041	0.024671	0.001197	1.467165	0.000079	-49.2	1.8	0.281357	-8.1	1.8	1880.1	1.7
	R2G1b[2]	~~14au11b19~~	~~0.281388~~	~~0.000062~~	~~0.001071~~	~~0.000087~~	~~0.027665~~	~~0.002362~~	~~1.467176~~	~~0.000120~~	~~-49.4~~	~~2.2~~	~~0.281350~~	~~-8.3~~	~~2.2~~	~~1880.1~~	~~2.0~~
	mean		**0.281413**						**1.467289**					**-7.3**			
	2SD		**0.000058**						**0.000350**					**2.2**			
KRN-12-02	**intrusion**																
	R1G1	14ap02a49	0.281442	0.000067	0.001391	0.000025	0.035829	0.000697	1.467356	0.000057	-47.5	2.4	0.281392	-6.8	2.4	1880.6	2.0
	R1G1b[2]	~~14ap02a50~~	~~0.281401~~	~~0.000058~~	~~0.001893~~	~~0.000041~~	~~0.049115~~	~~0.001160~~	~~1.467356~~	~~0.000111~~	~~-49.0~~	~~2.1~~	~~0.281333~~	~~-8.9~~	~~2.1~~	~~1880.6~~	~~2.7~~
	R1G3, D	14ap02a53	0.281520	0.000040	0.002878	0.000161	0.081595	0.005294	1.467254	0.000063	-44.7	1.4	0.281417	-5.9	1.4	1880.6	2.3
	R1G4	14ap02a54	0.281470	0.000043	0.001454	0.000036	0.037123	0.000935	1.467195	0.000060	-46.5	1.5	0.281419	-5.9	1.5	1880.6	2.0
	R2G1	14ap02a55	0.281470	0.000035	0.002036	0.000052	0.053801	0.001615	1.467215	0.000074	-46.5	1.2	0.281397	-6.6	1.2	1880.6	1.9
	R2G2	14ap02a56	0.281401	0.000041	0.001108	0.000016	0.028441	0.000404	1.467264	0.000057	-49.0	1.5	0.281361	-7.9	1.5	1880.6	2.2
	R3G5	14ap02a57	0.281418	0.000032	0.001207	0.000015	0.030919	0.000331	1.467259	0.000054	-48.3	1.1	0.281375	-7.4	1.1	1880.6	2.3
	R4G1a	14ap02a58	0.281399	0.000031	0.001546	0.000013	0.040923	0.000304	1.467204	0.000058	-49.0	1.1	0.281344	-8.5	1.1	1880.6	2.0
	R4G b	14ap02a59	0.281419	0.000036	0.001358	0.000039	0.034606	0.001049	1.467177	0.000055	-48.3	1.3	0.281370	-7.6	1.3	1880.6	1.7
	R4G4[2], D	~~14ap02a60~~	~~0.281669~~	~~0.000265~~	~~0.002167~~	~~0.000090~~	~~0.058502~~	~~0.002819~~	~~1.467071~~	~~0.000173~~	~~-39.5~~	~~9.4~~	~~0.281591~~	~~0.3~~	~~9.4~~	~~1880.6~~	~~4.1~~
	mean		**0.281443**						**1.467241**					**-7.1**			
	2SD		**0.000084**						**0.000135**					**2.1**			
KRN-12-03	**intrusion**																
	R4G2	14ap02a61	0.281442	0.000053	0.001137	0.000054	0.031664	0.001740	1.467159	0.000067	-47.5	1.9	0.281401	-6.5	1.9	1880.6	1.7
	R1G3, D	14au11b20	0.281479	0.000049	0.001726	0.000032	0.054684	0.001159	1.467180	0.000063	-46.2	1.7	0.281418	-5.9	1.8	1880.6	1.4
	R2G2, D	14au11b21	0.281520	0.000040	0.002674	0.000130	0.088806	0.004302	1.467160	0.000071	-44.7	1.4	0.281425	-5.7	1.5	1880.6	1.7
	R2G3, D	14au11b22	0.281628	0.000064	0.003676	0.000164	0.107500	0.008138	1.467125	0.000135	-40.9	2.3	0.281497	-3.1	2.3	1880.6	1.8
	R3G2, D	14au11b23	0.281469	0.000041	0.002608	0.000149	0.082511	0.005406	1.467219	0.000074	-46.5	1.5	0.281376	-7.4	1.5	1880.6	1.6
	mean		**0.281508**						**1.467169**					**-5.7**			
	2SD		**0.000146**						**0.000068**					**3.2**			

continued on next pages. C: analyses in core, R: analyses in rim; a, b two analyses in similar zone of the same grain; D: > 5% discordant at 2σ level. All data are corrected as described in text in appendix C. [1]Invariant ratio off, [2]not enough data points.

Table 8-7 – continued. LA-MC-ICPMS Lu-Hf isotopic analyses of zircon from Kiruna, Sweden. Strike-through data were not used due to analytical problems.

sample	grain	analyses	$^{176}Hf/^{177}Hf$	2SE	$^{176}Lu/^{177}Hf$	2SE	$^{176}Yb/^{177}Hf$	2SE	$^{178}Hf/^{177}Hf$	2SE	$\varepsilon_{Hf}(0)$	2SE	$^{176}Hf/^{177}Hf_i$	$\varepsilon_{Hf}(i)$	2SE	Assigned age (Ma)	Mean Hf (V)
KRN-12-05	**intrusion**																
mount 6	R1G1[2]	~~14ap02a05~~	~~0.281258~~	~~0.000022~~	~~0.001147~~	~~0.000044~~	~~0.028742~~	~~0.001087~~	~~1.467216~~	~~0.000077~~	~~-54.0~~	0.8	0.281218	~~-13.2~~	~~0.8~~	~~1874.2~~	~~3.7~~
	R1G1b[2]	~~14ap02a06~~	~~0.281229~~	~~0.000057~~	~~0.001187~~	~~0.000026~~	~~0.029562~~	~~0.000711~~	~~1.467216~~	~~0.000068~~	~~-55.0~~	2.0	0.281186	~~-14.3~~	~~2.0~~	~~1874.2~~	~~3.8~~
	R1G5	14ap02a07	0.281448	0.000041	0.001037	0.000067	0.026366	0.001758	1.467209	0.000056	-47.3	1.5	0.281412	-6.3	1.5	1874.2	2.5
	R2G1	14ap02a08	0.281423	0.000041	0.001452	0.000030	0.036464	0.000890	1.467166	0.000093	-48.2	1.4	0.281371	-7.7	1.5	1874.2	2.3
	R3G7	14ap02a09	0.281419	0.000048	0.002651	0.000043	0.068219	0.001062	1.467246	0.000071	-48.3	1.7	0.281324	-9.4	1.7	1874.2	1.7
	R4G5	14ap02a10	0.281216	0.000058	0.001447	0.000050	0.035168	0.001255	1.467857	0.000060	-55.5	2.1	0.281164	-9.5	1.3	1874.2	3.0
	R4G4, D	14ap02a11	0.281383	0.000042	0.001738	0.000166	0.044915	0.004516	1.467345	0.000062	-49.6	1.5	0.281321	-7.5	1.1	1874.2	2.7
	R4G1	14ap02a12	0.281371	0.000035	0.001372	0.000016	0.035381	0.000495	1.467343	0.000062	-50.0	1.2	0.281322	-9.5	1.5	1874.2	2.0
	R4G2	~~14ap02a15~~	~~0.281423~~	~~0.000031~~	~~0.001269~~	~~0.000064~~	~~0.032198~~	~~0.001763~~	~~1.467356~~	~~0.000039~~	~~-48.2~~	~~1.1~~	~~0.281378~~	~~-15.1~~	~~2.1~~	~~1874.2~~	~~2.0~~
	R5G2[2], D	~~14ap02a16~~	~~0.281410~~	~~0.000056~~	~~0.001406~~	~~0.000041~~	~~0.035008~~	~~0.000980~~	~~1.467775~~	~~0.000076~~	~~-48.6~~	~~2.0~~	~~0.281360~~	~~-8.1~~	~~2.0~~	~~1874.2~~	~~2.8~~
	R5G6[2]	~~14ap02a17~~	~~0.281403~~	~~0.000025~~	~~0.001047~~	~~0.000043~~	~~0.026762~~	~~0.001247~~	~~1.467690~~	~~0.000067~~	~~-48.9~~	~~0.9~~	~~0.281366~~	~~-7.9~~	~~0.9~~	~~1874.2~~	~~2.9~~
mount 4	R5G7	14ap02c78	0.281431	0.000044	0.001771	0.000038	0.045726	0.001170	1.467227	0.000058	-47.9	1.6	0.281368	-7.8	1.6	1874.2	1.5
	R4G7	14ap02c79	0.281310	0.000041	0.001494	0.000104	0.036782	0.002516	1.467237	0.000082	-52.1	1.5	0.281257	-11.8	1.5	1874.2	1.9
	mean		**0.281398**						**1.467253**					**-8.6**			
	2SD		**0.000094**						**0.000134**					**3.6**			
REK-12-01	**altered host rock**																
	R1G2	14ap02c14	0.281637	0.000032	0.000792	0.000031	0.019527	0.000799	1.467280	0.000049	-40.6	1.1	0.281609	0.8	1.2	1876.2	1.8
	R1G4C	14ap02c15	0.281635	0.000030	0.000702	0.000041	0.018700	0.001370	1.467245	0.000044	-40.7	1.1	0.281610	0.8	1.1	1876.2	1.9
	R2G2	14ap02c16	0.281678	0.000041	0.001303	0.000060	0.035004	0.001517	1.467223	0.000061	-39.1	1.5	0.281632	1.6	1.5	1876.2	1.6
	R2G3	14ap02c17	0.281635	0.000034	0.000890	0.000012	0.022096	0.000371	1.467192	0.000070	-40.7	1.2	0.281604	0.6	1.3	1876.2	2.4
	R2G4, D	14ap02c18	0.281647	0.000038	0.000744	0.000020	0.018511	0.000492	1.467292	0.000057	-40.2	1.3	0.281621	1.2	1.4	1876.2	2.6
	R2G5C	14ap02c19	0.281642	0.000043	0.001047	0.000056	0.026374	0.001631	1.467213	0.000061	-40.4	1.5	0.281605	0.6	1.6	1876.2	1.7
	R4G6[2]	~~14ap02e20~~	~~0.281668~~	~~0.000094~~	~~0.000994~~	~~0.000048~~	~~0.025007~~	~~0.001492~~	~~1.467191~~	~~0.000084~~	~~-39.5~~	~~3.4~~	~~0.281632~~	~~1.6~~	~~3.4~~	~~1876.2~~	~~3.7~~
	R4G4	14ap02c21	0.281579	0.000043	0.001012	0.000078	0.025609	0.002133	1.467247	0.000064	-42.6	1.5	0.281543	-1.6	1.6	1876.2	2.7
	R3G4	14ap02c23	0.281257	0.000033	0.000627	0.000103	0.011971	0.001837	1.467509	0.000068	-54.0	1.2	0.281235	-12.5	1.2	1876.2	2.1
	R3G1	14ap02c24	0.281389	0.000056	0.001670	0.000272	0.050002	0.009429	1.467913	0.000104	-49.4	2.0	0.281330	-9.2	2.0	1876.2	2.3
	R5G3[2]	~~14ap02e25~~	~~0.280703~~	~~0.000046~~	~~0.000903~~	~~0.000024~~	~~0.024051~~	~~0.000904~~	~~1.473333~~	~~0.000702~~	~~-73.6~~	~~1.6~~	~~0.280671~~	~~-32.6~~	~~1.7~~	~~1876.2~~	~~2.1~~
	R5G5	14ap02c26	0.281665	0.000026	0.000998	0.000006	0.026254	0.000230	1.467236	0.000062	-39.6	0.9	0.281630	1.5	1.0	1876.2	2.0
	mean		**0.281577**						**1.467335**					**-1.6**			
	2SD		**0.000279**						**0.000443**					**10.0**			
NUK-12-01	**footwall**																
	R1G1[2]	~~14ap02e27~~	~~0.281557~~	~~0.000097~~	~~0.001600~~	~~0.000098~~	~~**0.040891**~~	~~0.002410~~	~~1.467220~~	~~0.000155~~	~~-43.4~~	~~3.4~~	~~0.281500~~	~~-3.0~~	~~3.5~~	~~1881.7~~	~~2.1~~
	R1G3	14ap02c28	0.281428	0.000050	0.001177	0.000114	0.029567	0.002929	1.467219	0.000070	-48.0	1.8	0.281387	-7.0	1.8	1881.7	2.2
	R1G4[2]	~~14ap02e29~~	~~0.281457~~	~~0.000055~~	~~0.001036~~	~~0.000076~~	~~0.025283~~	~~0.001692~~	~~1.467249~~	~~0.000106~~	~~-47.0~~	~~1.9~~	~~0.281420~~	~~-5.8~~	~~2.0~~	~~1881.7~~	~~2.6~~
	R1G5	14ap02c30	0.281420	0.000039	0.001092	0.000064	0.024596	0.001409	1.467242	0.000049	-48.3	1.4	0.281381	-7.2	1.4	1881.7	2.4
	R2G1[2]	~~14ap02e33~~	~~0.281435~~	~~0.000068~~	~~0.001121~~	~~0.000123~~	~~0.028118~~	~~0.003309~~	~~1.467229~~	~~0.000181~~	~~-47.7~~	~~2.4~~	~~0.281395~~	~~-6.7~~	~~2.4~~	~~1881.7~~	~~2.7~~
	R3G2	14ap02c34	0.281385	0.000031	0.001146	0.000012	0.028488	0.000382	1.467187	0.000060	-49.5	1.1	0.281344	-8.5	1.1	1881.7	2.3
	R3G3[2]	~~14ap02e35~~	~~0.281436~~	~~0.000036~~	~~0.001395~~	~~0.000189~~	~~0.034431~~	~~0.005721~~	~~1.467162~~	~~0.000077~~	~~-47.7~~	~~1.3~~	~~0.281386~~	~~-7.0~~	~~1.4~~	~~1881.7~~	~~2.5~~
	R3G6	14ap02c36	0.281442	0.000046	0.001054	0.000053	0.026136	0.001374	1.467205	0.000078	-47.5	1.6	0.281404	-6.4	1.7	1881.7	1.8
	R2G4[2]	~~14ap02e37~~	~~0.281462~~	~~0.000099~~	~~0.001636~~	~~0.000151~~	~~0.041077~~	~~0.004196~~	~~1.467181~~	~~0.000104~~	~~-46.8~~	~~3.5~~	~~0.281404~~	~~-6.4~~	~~3.5~~	~~1881.7~~	~~2.7~~
	R3G8	14ap02c38	0.281422	0.000025	0.001238	0.000039	0.026178	0.000904	1.467224	0.000068	-48.2	0.9	0.281378	-7.3	0.9	1881.7	3.4
	R3G9	14ap02c39	0.281423	0.000045	0.001503	0.000157	0.039946	0.005488	1.467236	0.000056	-48.2	1.6	0.281369	-7.6	1.6	1881.7	1.8
	R4G8	14ap02c40	0.281456	0.000045	0.001305	0.000094	0.032688	0.002353	1.467259	0.000068	-47.0	1.6	0.281409	-6.2	1.6	1881.7	2.1
	R4G5[2]	~~14ap02e41~~	~~0.281377~~	~~0.000037~~	~~0.001166~~	~~0.000011~~	~~0.029433~~	~~0.000363~~	~~1.467158~~	~~0.000061~~	~~-49.8~~	~~1.3~~	~~0.281336~~	~~-8.8~~	~~1.4~~	~~1881.7~~	~~2.7~~
	mean		**0.281425**						**1.467225**					**-7.2**			
	2SD		**0.000044**						**0.000048**					**1.6**			

continued on next pages. C: analyses in core, R: analyses in rim; a, b two analyses in similar zone of the same grain; D: > 5% discordant at 2σ level. All data are corrected as described in text in appendix C. [1]Invariant ratio off, [2]not enough data points.

Table 8-7 – continued. LA-MC-ICPMS Lu-Hf isotopic analyses of zircon from Kiruna, Sweden. Strike-through data were not used due to analytical problems.

sample	grain	analyses	$^{176}Hf/^{177}Hf$	2SE	$^{176}Lu/^{177}Hf$	2SE	$^{176}Yb/^{177}Hf$	2SE	$^{178}Hf/^{177}Hf$	2SE	$\varepsilon_{Hf}(0)$	2SE	$^{176}Hf/^{177}Hf_i$	$\varepsilon_{Hf}(i)$	2SE	Assigned age (Ma)	Mean Hf (V)
NUK-12-02	**ore**																
	R1G3[1]	~~14ap02a18~~	~~0.281610~~	~~0.000025~~	~~0.000958~~	~~0.000128~~	~~0.024211~~	~~0.003351~~	~~1.467801~~	~~0.000048~~	~~-41.6~~	~~0.9~~	~~0.281575~~	~~-0.4~~	~~0.9~~	~~1877.1~~	~~2.6~~
	R1G5	14ap02a19	0.281604	0.000023	0.000593	0.000083	0.015572	0.002526	1.467560	0.000041	-41.8	0.8	0.281582	-0.2	0.8	1877.1	2.5
	R2G2	14ap02a20	0.281651	0.000037	0.001085	0.000114	0.030696	0.003495	1.467401	0.000047	-40.1	1.3	0.281613	0.9	1.3	1877.1	2.0
	R3G1	14ap02a21	0.281697	0.000030	0.001274	0.000089	0.032684	0.002392	1.467333	0.000049	-38.5	1.1	0.281651	2.3	1.1	1877.1	2.0
	R3G3	14ap02a22	0.281636	0.000036	0.000757	0.000011	0.019535	0.000276	1.467333	0.000054	-40.6	1.3	0.281609	0.8	1.3	1877.1	2.2
	R3G6[1]	~~14ap02a24~~	~~0.281505~~	~~0.000030~~	~~0.000566~~	~~0.000038~~	~~0.014280~~	~~0.001047~~	~~1.468535~~	~~0.000126~~	~~-45.3~~	~~1.1~~	~~0.281484~~	~~-3.6~~	~~1.1~~	~~1877.1~~	~~2.5~~
	R4G5[1]	~~14ap02a25~~	~~0.281477~~	~~0.000034~~	~~0.000569~~	~~0.000050~~	~~0.014658~~	~~0.001409~~	~~1.468710~~	~~0.000082~~	~~-46.2~~	~~1.2~~	~~0.281457~~	~~-4.6~~	~~1.2~~	~~1877.1~~	~~2.2~~
	R4G2a[1]	~~14ap02a26~~	~~0.281576~~	~~0.000029~~	~~0.000475~~	~~0.000034~~	~~0.011545~~	~~0.000858~~	~~1.467801~~	~~0.000056~~	~~-42.8~~	~~1.0~~	~~0.281559~~	~~-1.0~~	~~1.1~~	~~1877.1~~	~~2.8~~
	R4G1[1]	~~14ap02a27~~	~~0.281559~~	~~0.000031~~	~~0.000582~~	~~0.000051~~	~~0.015017~~	~~0.001621~~	~~1.467922~~	~~0.000049~~	~~-43.4~~	~~1.1~~	~~0.281538~~	~~-1.7~~	~~1.1~~	~~1877.1~~	~~2.3~~
	R1G1, D	14au11b06	0.281648	0.000028	0.001130	0.000033	0.030685	0.001138	1.467115	0.000053	-40.2	1.0	0.281608	0.7	1.0	1877.1	2.4
	R1G4, D	14au11b07	0.281673	0.000051	0.001749	0.000223	0.044623	0.005774	1.467137	0.000054	-39.3	1.8	0.281611	0.9	1.9	1877.1	2.1
	R2G6, D	14au11b08	0.281589	0.000033	0.000347	0.000015	0.008410	0.000448	1.467216	0.000071	-42.3	1.2	0.281576	-0.4	1.2	1877.1	1.8
	R2G2R	14au11b09	0.281651	0.000029	0.000528	0.000030	0.013397	0.000807	1.467196	0.000064	-40.1	1.0	0.281632	1.6	1.1	1877.1	2.4
	R3G1b	14au11b10	0.281707	0.000042	0.001790	0.000228	0.045977	0.006221	1.467181	0.000062	-38.1	1.5	0.281644	2.0	1.5	1877.1	2.0
	R4G1b	14au11b11	0.281684	0.000027	0.000446	0.000006	0.011132	0.000162	1.467198	0.000072	-38.9	0.9	0.281668	2.9	1.0	1877.1	2.5
	R4G3	14au11b12	0.281673	0.000032	0.000794	0.000100	0.020716	0.002806	1.467166	0.000048	-39.3	1.1	0.281645	2.1	1.2	1877.1	2.0
	R4G4	14au11b13	0.281595	0.000042	0.001034	0.000108	0.030007	0.004795	1.467216	0.000056	-42.1	1.5	0.281558	-1.0	1.5	1877.1	2.0
	mean		**0.281651**						**1.467254**					**1.1**			
	2SD		**0.000078**						**0.000258**					**2.3**			

C: analyses in core, R: analyses in rim; a, b two analyses in similar zone of the same grain; D: > 5% discordant at 2σ level. All data are corrected as described in appendix C. [1]Invariant ratio off, [2]not enough data points.

Table 8-8. Summary SIMS U-Pb dates, oxygen analyses and LA-MC-ICPMS Lu-Hf ratios of zircon from Kiruna for individual grains.

sample	grain	Age zrc (Ma)	± 1σ	Disc. % 2σ limit	ox analyses #	$\delta^{18}O$ zrc	±‰	Hf analyses #	$^{176}Hf/^{177}Hf$	2SE	$^{176}Lu/^{177}Hf$	2SE	$\varepsilon_{Hf}(0)$	2SE	$^{176}Hf/^{177}Hf$ (i)	ε_{Hf} (i)	2 SE
K-1 ore		1874.1	7.1														
mount 4	R1G2 C	1852.3	3.1	-8.0	n4721ox_K1_@4	6.23	0.14	14ap02c61	0.281700	0.000043	0.002255	0.001104	-38.4	1.5	0.2816193	1.1	2.1
	R1G4 C	1863.4	4.0	-5.5	n4721ox_K1_@6	6.04	0.18	~~14ap02c62~~	~~0.281689~~	~~0.000050~~	~~0.001133~~	~~0.000243~~	~~-38.8~~	~~1.8~~	~~0.2816484~~	~~2.1~~	~~1.8~~
	R1G7	1877.0	3.1	-0.7	n4721ox_K1_@10	5.79	0.14	14ap02c63	0.281574	0.000047	0.000889	0.000019	-42.8	1.7	0.2815425	-1.6	1.7
	R2G3	1860.9	4.4	-7.4	n4721ox_K1_@13	8.66	0.18	~~14ap02c68~~	~~0.281535~~	~~0.000076~~	~~0.002610~~	~~0.001605~~	~~-44.2~~	~~2.7~~	~~0.2814421~~	~~-5.2~~	~~3.4~~
	R2G6	1876.5	3.2	-1.8	n4721ox_K1_@16	6.26	0.14	14au11c09	0.281740	0.000066	0.002436	0.000911	-37.0	2.3	0.2816533	2.3	2.6
	R2G7	1869.2	7.1	-0.3	n4721ox_K1_@17	5.87	0.18	~~14ap02c65~~	~~0.281525~~	~~0.000072~~	~~0.001922~~	~~0.000433~~	~~-44.6~~	~~2.6~~	~~0.2814564~~	~~-4.7~~	~~2.6~~
	R2G8	1850.9	3.4	-10.0	n4721ox_K1_@18	7.54	0.13	~~14ap02c64~~	~~0.281423~~	~~0.000215~~	~~0.002368~~	~~0.000972~~	~~-48.2~~	~~7.6~~	~~0.2813389~~	~~-8.9~~	~~7.7~~
	R3G3	1871.7	4.0	-2.0	n4721ox_K1_@21	8.88	0.37	~~14ap02c67~~	~~0.281662~~	~~0.000049~~	~~0.003577~~	~~0.000373~~	~~-39.7~~	~~1.7~~	~~0.2815351~~	~~-1.9~~	~~1.8~~
	R3G5 C	1883.5	2.7	-2.2	n4721ox_K1_@22	6.01	0.13	~~14ap02c66~~	~~0.281709~~	~~0.000040~~	~~0.000688~~	~~0.000047~~	~~-38.1~~	~~1.4~~	~~0.2816842~~	~~3.4~~	~~1.5~~
KRN-11-03 footwall		1884.1	3.7														
mount 4	R2G1	1885.7	4.2	-0.1	n4722ox_KRN11-03_@3	5.88	0.11	~~14ap02c70~~	~~0.281705~~	~~0.000106~~	~~0.001262~~	~~0.000036~~	~~-38.2~~	~~3.7~~	~~0.2816600~~	~~2.8~~	~~3.8~~
	R2G3	1881.5	3.2	-0.4	n4722ox_KRN11-03_@5	5.86	0.23	~~14ap02c72~~	~~0.281452~~	~~0.000047~~	~~0.000728~~	~~0.000013~~	~~-47.1~~	~~1.7~~	~~0.2814261~~	~~-5.5~~	~~1.7~~
	R3G2 C	1889.3	4.7	-0.2	n4722ox_KRN11-03_@6	7.06	0.24	14au11c16	0.281492	0.000026	0.001052	0.000028	-45.7	0.9	0.2814543	-4.5	1.0
	R3G2 R	1883.3	3.4	0.0	n4722ox_KRN11-03_@7	5.14	0.15	14ap02c73	0.281420	0.000035	0.000631	0.000014	-48.3	1.2	0.2813978	-6.5	1.3
KRN-11-05 hanging wall		1880.5	4.5														
mount 4	R2G1	1889.5	5.7	-0.5	n4723ox_KRN11-05_@7	3.17	0.11	14ap02c74	0.281436	0.000041	0.001519	0.000056	-47.7	1.4	0.2813818	-7.2	1.5
	R3G2	1891.4	7.7	-0.1	n4723ox_KRN11-05_@14	3.89	0.16	14ap02c75	0.281413	0.000052	0.001071	0.000108	-48.5	1.8	0.2813749	-7.4	1.9
	R3G3 R	1875.6	4.2	0.0	n4723ox_KRN11-05_@16	3.41	0.15	14ap02c76	0.281451	0.000029	0.001035	0.000029	-47.2	1.0	0.2814138	-6.1	1.1
	R4G2	1877.1	3.9	0.0	n4723ox_KRN11-05_@21	3.30	0.20	14ap02c77	0.281430	0.000048	0.001470	0.000291	-47.9	1.7	0.2813770	-7.4	1.8
mount 6	R1G3	1878.9	7.3	-0.7	n4900ox-R1-G3	4.66	0.18	~~14ap02a36~~	~~0.281435~~	~~0.000116~~	~~0.001028~~	~~0.000032~~	~~-47.7~~	~~4.1~~	~~0.2813982~~	~~-6.6~~	~~4.1~~
	R2G4	1883.3	7.3	0.0	n4900ox-R2-G4	2.47	0.21	~~14ap02a37~~	~~0.281296~~	~~0.000022~~	~~0.000874~~	~~0.000063~~	~~-52.7~~	~~0.8~~	~~0.2812644~~	~~-11.4~~	~~0.8~~
	R2G5	1871.0	8.4	0.0	n4900ox-R2-G5	3.29	0.17	~~14ap02a39~~	~~0.281368~~	~~0.000087~~	~~0.001175~~	~~0.000065~~	~~-50.1~~	~~3.1~~	~~0.2813259~~	~~-9.2~~	~~3.1~~
	R3G1	1871.7	6.4	0.0	n4900ox-R3-G1	2.67	0.19	~~14ap02a40~~	~~0.281382~~	~~0.000040~~	~~0.001767~~	~~0.000028~~	~~-49.6~~	~~1.4~~	~~0.2813193~~	~~-9.4~~	~~1.4~~
	R3G2 a	1840.6	9.5	-47.0	n4900ox-R3-G2a	3.32	0.20	14ap02a43	0.281436	0.000042	0.000808	0.000079	-47.7	1.5	0.2814070	-6.3	1.5
	R3G2 b	1885.8	8.5	0.0	n4900ox-R3-G2b	2.54	0.19	14ap02a44	0.281441	0.000035	0.001363	0.000082	-47.5	1.3	0.2813919	-6.8	1.3
	R3G3	1884.6	4.3	0.0	n4900ox-R3-G3	3.33	0.20	~~14ap02a45~~	~~0.281509~~	~~0.000110~~	~~0.003450~~	~~0.000177~~	~~-45.1~~	~~3.9~~	~~0.2813860~~	~~-7.0~~	~~3.9~~
	R4G3	1349.0	13.1	0.0	n4900ox-R4-G3	6.32	0.23	14ap02a47	0.282141	0.000024	0.000413	0.000095	-22.8	0.8	0.2821258	7.2	0.9
	R4G4	1880.1	5.4	0.0	n4900ox-R4-G4	3.53	0.18	14ap02a48	0.281410	0.000046	0.001155	0.000060	-48.6	1.6	0.2813684	-7.7	1.6
KRN-11-06 altered hanging wall		1880.1	2.7														
mount 6	R1G2	1885.4	6.3	0.0	n4901ox-R1-G2	2.77	0.19	~~14ap02a28~~	~~0.281367~~	~~0.000035~~	~~0.001118~~	~~0.000052~~	~~-50.2~~	~~1.2~~	~~0.2813269~~	~~-9.2~~	~~1.3~~
	R1G4	1888.0	5.3	-0.8	n4901ox-R1-G4	2.92	0.20	~~14ap02a29~~	~~0.281559~~	~~0.000097~~	~~0.002816~~	~~0.000150~~	~~-43.3~~	~~3.4~~	~~0.2814590~~	~~-4.5~~	~~3.5~~
	R2G1	1871.0	9.8	-1.3	n4901ox-R2-G1	3.27	0.20	14ap02a31	0.281434	0.000048	0.000953	0.000073	-47.8	1.7	0.2813997	-6.6	1.7
	R2G4	1890.9	7.1	0.0	n4901ox-R2-G4	3.31	0.21	~~14ap02a30~~	~~0.281432~~	~~0.000042~~	~~0.001123~~	~~0.000043~~	~~-47.9~~	~~1.5~~	~~0.2813916~~	~~-6.9~~	~~1.5~~
	R2G5	1880.4	9.6	0.0	n4901ox-R2-G5	2.51	0.20	~~14au11b17~~	~~0.281563~~	~~0.000100~~	~~0.000913~~	~~0.000033~~	~~-43.2~~	~~3.6~~	~~0.2815301~~	~~-1.9~~	~~3.6~~
	R3G5	1956.7	15.2	0.0	n4901ox-R3-G5	2.46	0.19	~~14ap02a34~~	~~0.281442~~	~~0.000044~~	~~0.000769~~	~~0.000012~~	~~-47.5~~	~~1.6~~	~~0.2814150~~	~~-6.0~~	~~1.6~~
	R4G2	1884.0	9.5	0.0	n4901ox-R4-G2	2.74	0.22	~~14ap02a35~~	~~0.281387~~	~~0.000031~~	~~0.000723~~	~~0.000027~~	~~-49.4~~	~~1.1~~	~~0.2813617~~	~~-7.9~~	~~1.2~~

continued on next pages. C: analyses in core, R: analyses in rim; a, b two analyses in similar zone of the same grain. All data are corrected as described in appendix C.

Table 8-8 - continued**.** SIMS U-Pb dates, oxygen analyses and LA-MC-ICPMS Lu-Hf ratios of zircon from Kiruna for individual grains.

sample	grain	Age zrc (Ma)	± 1σ	Disc. % 2σ limit	ox analyses #	$\delta^{18}O$ zrc	± ‰	Hf analyses #	$^{176}Hf/^{177}Hf$	2SE	$^{176}Lu/^{177}Hf$	2SE	$\varepsilon_{Hf}(0)$	2SE	$^{176}Hf/^{177}Hf$ (i)	ε_{Hf} (i)	2 SE
KRN-12-02 intrusion		1880.6	3.7														
mount 6	R1G1	1878.3	7.0	0.0	n4899ox-R1-G1	2.84	0.22	14ap02a49	0.281442	0.000067	0.001391	0.000025	-47.5	2.4	0.2813924	-6.8	2.4
	R1G4	1877.4	6.2	0.0	n4899ox-R1-G4	3.20	0.21	14ap02a54	0.281470	0.000043	0.001454	0.000036	-46.5	1.5	0.2814185	-5.9	1.5
	R2G1	1854.9	7.0	-1.0	n4899ox-R2-G1	2.72	0.22	14ap02a55	0.281470	0.000035	0.002036	0.000052	-46.5	1.2	0.2813974	-6.6	1.2
	R2G2	1880.9	7.1	0.0	n4899ox-R2-G2	3.00	0.20	14ap02a56	0.281401	0.000041	0.001108	0.000016	-49.0	1.5	0.2813610	-7.9	1.5
	R3G5	1876.4	6.7	0.0	n4899ox-R3-G5	2.93	0.21	14ap02a57	0.281418	0.000032	0.001207	0.000015	-48.3	1.1	0.2813751	-7.4	1.1
	R4G1 a	1878.7	5.6	0.0	n4899ox-R4-G1a	2.87	0.21	14ap02a58	0.281399	0.000031	0.001546	0.000013	-49.0	1.1	0.2813442	-8.5	1.1
	R4G1 b	1886.4	8.6	0.0	n4899ox-R4-G1b	3.01	0.19	14ap02a59	0.281419	0.000036	0.001358	0.000039	-48.3	1.3	0.2813705	-7.6	1.3
KRN-12-03 intrusion		1880.6	3.7														
mount 6	R4G2	1883.6	5.5	-0.4	n4898ox-R4-G2	3.82	0.28	14ap02a61	0.281442	0.000053	0.001137	0.000054	-47.5	1.9	0.2814015	-6.5	1.9
KRN-12-05 intrusion		1874.2	3.8														
mount 6	R1G1	1888.1	8.8	0.0	n4897ox-R1-G1	3.03	0.22	~~14ap02a05~~	~~0.281258~~	~~0.000022~~	~~0.001147~~	~~0.000044~~	~~-54.0~~	~~0.8~~	~~0.2812175~~	~~-13.2~~	~~0.8~~
	R1G5	1870.3	6.9	0.0	n4897ox-R1-G5	3.04	0.21	14ap02a07	0.281448	0.000041	0.001037	0.000067	-47.3	1.5	0.2814115	-6.3	1.5
	R2G1	1870.8	10.5	0.0	n4897ox-R2-G1	2.77	0.26	14ap02a08	0.281423	0.000041	0.001452	0.000030	-48.2	1.4	0.2813709	-7.7	1.5
	R3G7	1879.7	6.0	0.0	n4897ox-R3-G7	3.63	0.21	14ap02a09	0.281419	0.000048	0.002651	0.000043	-48.3	1.7	0.2813241	-9.4	1.7
	R4G1	1872.9	7.7	0.0	n4897ox-R4-G1	3.47	0.22	14ap02a12	0.281371	0.000035	0.001372	0.000016	-50.0	1.2	0.2813225	-9.5	1.5
	R4G2	1873.1	13.3	0.0	n4897ox-R4-G2	4.20	0.21	~~14ap02a15~~	~~0.281423~~	~~0.000031~~	~~0.001269~~	~~0.000064~~	~~-48.2~~	1.1	0.2813778	~~-15.1~~	~~2.1~~
	R4G5	1885.2	6.9	0.0	n4897ox-R4-G5	3.60	0.24	14ap02a10	~~0.281216~~	~~0.000058~~	~~0.001447~~	~~0.000050~~	~~-55.5~~	2.1	0.2811641	-9.5	1.3
REK-12-01 Rektorn porphyry		1876.2	6.8														
mount 4	R1G2	1885.5	4.9	0.0	n4732ox_REK12-1_@15	4.47	0.10	14ap02c14	0.281637	0.000032	0.000792	0.000031	-40.6	1.1	0.2816089	0.8	1.2
	R1G4 C	1883.6	3.1	0.0	n4732ox_REK12-1_@18	6.24	0.12	14ap02c15	0.281635	0.000030	0.000702	0.000041	-40.7	1.1	0.2816101	0.8	1.1
	R2G3	1890.9	3.0	0.0	n4732ox_REK12-1_@22	5.63	0.13	14ap02c17	0.281635	0.000034	0.000890	0.000012	-40.7	1.2	0.2816036	0.6	1.3
	R2G5 C	1883.7	3.6	0.0	n4732ox_REK12-1_@24	6.01	0.14	14ap02c19	0.281642	0.000043	0.001047	0.000056	-40.4	1.5	0.2816051	0.6	1.6
	R3G1	1884.4	5.3	0.0	n4732ox_REK12-1_@27	3.02	0.12	14ap02c24	0.281389	0.000056	0.001670	0.000272	-49.4	2.0	0.2813296	-9.2	2.0
	R3G4	1896.4	5.6	0.0	n4732ox_REK12-1_@28	6.10	0.14	14ap02c23	0.281257	0.000033	0.000627	0.000103	-54.0	1.2	0.2812347	-12.5	1.2
	R4G4	1886.2	3.9	0.0	n4732ox_REK12-1_@29	4.94	0.15	14ap02c21	0.281579	0.000043	0.001012	0.000078	-42.6	1.5	0.2815429	-1.6	1.6
	R4G6	1878.5	2.8	0.0	n4732ox_REK12-1_@30	6.14	0.13	~~14ap02c20~~	~~0.281668~~	~~0.000094~~	~~0.000994~~	~~0.000048~~	~~-39.5~~	~~3.4~~	~~0.2816321~~	~~1.6~~	~~3.4~~
	R5G3	1878.7	2.3	0.0	n4732ox_REK12-1_@33	5.73	0.13	~~14ap02c25~~	~~0.280703~~	~~0.000046~~	~~0.000903~~	~~0.000024~~	~~-73.6~~	~~1.6~~	~~0.2806707~~	~~-32.6~~	~~1.7~~
	R5G5	1874.6	3.6	0.0	n4732ox_REK12-1_@35	7.05	0.13	14ap02c26	0.281665	0.000026	0.000998	0.000006	-39.6	0.9	0.2816295	1.5	1.0
NUK-12-01 footwall		1881.7	2.3														
mount 4	R1G1	1885.0	4.4	0.0	n4719ox_NUK12-1_@39	2.87	0.14	~~14ap02c27~~	~~0.281557~~	~~0.000097~~	~~0.001600~~	~~0.000098~~	~~-43.4~~	~~3.4~~	~~0.2814997~~	~~-3.0~~	~~3.5~~
	R1G3	1874.6	5.4	0.0	n4719ox_NUK12-1_@41	3.49	0.17	14ap02c28	0.281428	0.000050	0.001177	0.000114	-48.0	1.8	0.2813866	-7.0	1.8
	R1G4	1878.2	4.7	0.0	n4719ox_NUK12-1_@42	3.49	0.12	~~14ap02c29~~	~~0.281457~~	~~0.000055~~	~~0.001036~~	~~0.000076~~	~~-47.0~~	~~1.9~~	~~0.2814197~~	~~-5.8~~	~~2.0~~
	R1G5	1875.8	4.7	-0.9	n4719ox_NUK12-1_@43	3.42	0.13	14ap02c30	0.281420	0.000039	0.001092	0.000064	-48.3	1.4	0.2813813	-7.2	1.4
	R2G1	1883.9	7.0	0.0	n4719ox_NUK12-1_@8	3.71	0.18	~~14ap02c33~~	~~0.281435~~	~~0.000068~~	~~0.001121~~	~~0.000123~~	~~-47.7~~	~~2.4~~	~~0.2813949~~	~~-6.7~~	~~2.4~~
	R2G4	1886.4	6.5	-0.1	n4719ox_NUK12-1_@11	3.23	0.13	~~14ap02c37~~	~~0.281462~~	~~0.000099~~	~~0.001636~~	~~0.000151~~	~~-46.8~~	~~3.5~~	~~0.2814041~~	~~-6.4~~	~~3.5~~
	R3G2	1881.3	4.9	-0.2	n4719ox_NUK12-1_@16	3.21	0.20	14ap02c34	0.281385	0.000031	0.001146	0.000012	-49.5	1.1	0.2813442	-8.5	1.1
	R3G3	1876.0	4.9	0.0	n4719ox_NUK12-1_@17	3.97	0.13	~~14ap02c35~~	~~0.281436~~	~~0.000036~~	~~0.001395~~	~~0.000189~~	~~-47.7~~	~~1.3~~	~~0.2813862~~	~~-7.0~~	~~1.4~~
	R3G6	1883.9	6.6	0.0	n4719ox_NUK12-1_@19	3.55	0.15	14ap02c36	0.281442	0.000046	0.001054	0.000053	-47.5	1.6	0.2814041	-6.4	1.7
	R3G8	1888.0	3.6	-0.3	n4719ox_NUK12-1_@21	5.21	0.16	14ap02c38	0.281422	0.000025	0.001238	0.000039	-48.2	0.9	0.2813778	-7.3	0.9

continued on next page. C: analyses in core, R: analyses in rim; a, b two analyses in similar zone of the same grain. All data are corrected as described in appendix C.

Table 8-8 - continued**.** SIMS U-Pb dates, oxygen analyses and LA-MC-ICPMS Lu-Hf ratios of zircon from Kiruna for individual grains.

sample	grain	Age zrc (Ma)	±	Disc. % 2σ limit	ox analyses #	$\delta^{18}O$ zrc	± ‰	Hf analyses #	$^{176}Hf/^{177}Hf$	2SE	$^{176}Lu/^{177}Hf$	2SE	$\varepsilon_{Hf}(0)$	2SE	$^{176}Hf/^{177}Hf$ (i)	ε_{Hf} (i)	2 SE
NUK-12-01 continued																	
	R3G9	1887.3	5.5	0.0	n4719ox_NUK12-1_@22	3.57	0.12	14ap02c39	0.281423	0.000045	0.001503	0.000157	-48.2	1.6	0.2813693	-7.6	1.6
	R4G5	1877.1	5.4	0.0	n4719ox_NUK12-1_@27	3.97	0.21	~~14ap02c41~~	~~0.281377~~	~~0.000037~~	~~0.001166~~	~~0.000011~~	~~-49.8~~	~~1.3~~	~~0.2813355~~	~~-8.8~~	~~1.4~~
	R4G8	1881.9	6.0	-3.3	n4719ox_NUK12-1_@29	3.03	0.14	14ap02c40	0.281456	0.000045	0.001305	0.000094	-47.0	1.6	0.2814093	-6.2	1.6
NUK-12-02 ore		1877.1	3.5														
mount 6	R1G3	1887.3	3.5	-0.7	n4896ox-R1-G3	6.80	0.20	~~14ap02a18~~	~~0.281610~~	~~0.000025~~	~~0.000958~~	~~0.000128~~	~~-41.6~~	~~0.9~~	~~0.2815753~~	~~-0.4~~	~~0.9~~
	R1G5	1890.3	4.8	-0.3	n4896ox-R1-G5	7.13	0.19	14ap02a19	0.281604	0.000023	0.000593	0.000083	-41.8	0.8	0.2815824	-0.2	0.8
	R2G2	1881.6	6.1	0.0	n4896ox-R2-G2a	6.97	0.20	14ap02a20	0.281651	0.000037	0.001085	0.000114	-40.1	1.3	0.2816125	0.9	1.3
	R2G2 R	1870.6	6.2	-1.3	n4896ox-R2-G2b	6.64	0.20	14au11b09	0.281651	0.000029	0.000528	0.000030	-40.1	1.0	0.2816321	1.6	1.1
	R3G1	1880.1	5.1	0.0	n4896ox-R3-G1	7.02	0.19	14ap02a21	0.281697	0.000030	0.001274	0.000089	-38.5	1.1	0.2816513	2.3	1.1
	R3G3	1881.2	5.4	0.0	n4896ox-R3-G3	6.94	0.18	14ap02a22	0.281636	0.000036	0.000757	0.000011	-40.6	1.3	0.2816089	0.8	1.3
	R3G6	1884.8	6.5	0.0	n4896ox-R3-G6	5.47	0.20	~~14ap02a24~~	~~0.281505~~	~~0.000030~~	~~0.000566~~	~~0.000038~~	~~-45.3~~	~~1.1~~	~~0.2814845~~	~~-3.6~~	~~1.1~~
	R4G1	1888.3	5.5	0.0	n4896ox-R4-G1	6.98	0.18	~~14ap02a27~~	~~0.281559~~	~~0.000031~~	~~0.000582~~	~~0.000051~~	~~-43.4~~	~~1.1~~	~~0.2815378~~	~~-1.7~~	~~1.1~~
	R4G5	1890.9	8.4	0.0	n4896ox-R4-G5	7.37	0.19	~~14ap02a25~~	~~0.281477~~	~~0.000034~~	~~0.000569~~	~~0.000050~~	~~-46.2~~	~~1.2~~	~~0.2814569~~	~~-4.6~~	~~1.2~~

C: analyses in core, R: analyses in rim; a, b two analyses in similar zone of the same grain. All data are corrected as described in appendix C.

Table 8-9. Calculation of theoretical oxygen isotopic compositions for rhyolite and dacite magmas in equilibrium with magnetite from Kiruna (values from Nyström et al., 2008). 1000lnα (magnetite-andesite) = -4.7 ‰, 1000lnα (mag-dacite) = -4.3 ‰ from Zhao and Zheng (2003), and values for 1000lnα (mag-water 800 ºC) = - 5.3 ‰ and 1000 ln a (mag-water 400 ºC) = - 7.9 ‰ from Zheng (1991).

sample	$\delta^{18}O$ (‰) measured	Sample type	Rhyolite $\delta^{18}O$	Dacite $\delta^{18}O$	Fluid at 800 ºC, $\delta^{18}O$	Fluid at 400 ºC, $\delta^{18}O$
PG-531	2.2	apatite bearing ore with apparent crossbedding	6.9	6.5	7.5	10.1
PG-235	1.7	Stratified ore rich in apatite	6.4	6	7.0	9.6
KIR-51	1.1	vesicular ore	5.8	5.4	6.4	9.0
PG-K9	1.8	ore with dendritic actinolite after pyroxene	6.5	6.1	7.1	9.7
PG-K14	0.9	ore with dendritic actinolite after pyroxene	5.6	5.2	6.2	8.8
PG-K8	2.1	skeleton ore	6.8	6.4	7.4	10.0
PG-37:6	0.7	skeleton ore	5.4	5	6.0	8.6
HjL-1	1.3	columnar magnetite	6.0	5.6	6.6	9.2
KUJ-3	1.1	columnar magnetite	5.8	5.4	6.4	9.0
PG-530	-0.2	columnar magnetite	4.5	4.1	5.1	7.7
PG-618	-0.7	magnetite-banded apatite rock	4.0	3.6	4.6	7.2
KIR-86	1	ore amgydule from footwall	5.7	5.3	6.3	8.9
4564:240	0.3	ore amgydule from footwall	5.3	4.6	5.6	8.2
4564:297	1.2	ore amgydule from footwall	5.9	5.5	6.5	9.1

Table 8-10. Calculation of theoretical oxygen isotopic compositions of fluids in equilibrium with metavolcanic and intrusive rocks from Kiruna (whole rock data from Blake, 1992) at different temperatures, 1000lnα (water-rock) from Zhao and Zheng (2003).

sample	$\delta^{18}O$ (‰) measured	Sample type	200 ºC	400 ºC	600 ºC	800 ºC
	1000lnα (andesite-water)		6.71	1.36	-0.11	-0.52
K90/26	6	footwall	-0.7	4.6	6.1	6.5
K89/23	6.4	footwall	-0.3	5.0	6.5	6.9
K89/17	6.7	footwall	0.0	5.3	6.8	7.2
K90/24	6.6	footwall	-0.1	5.2	6.7	7.1
K90/27	6	footwall	-0.7	4.6	6.1	6.5
K90/25	7.3	footwall	0.6	5.9	7.4	7.8
K89/21	7.2	footwall	0.5	5.8	7.3	7.7
K89/19	7.7	footwall	1.0	6.3	7.8	8.2
K89/24R	7.3	footwall	0.6	5.9	7.4	7.8
	1000lnα (syenite-water)		7.54	1.89	0.26	-0.24
K89/10	6.9	syenite	-0.6	5.0	6.6	7.1
K89/13	6.2	syenite	-1.3	4.3	5.9	6.4
K89/11	6.1	syenite	-1.4	4.2	5.8	6.3
K89/8	6.5	syenite	-1.0	4.6	6.2	6.7
K89/12	6.2	syenite	-1.3	4.3	5.9	6.4
	1000lnα (rhyolite-water)		8.80	2.69	0.84	0.19
K89/36	7.5	hanging wall	-1.3	4.8	6.7	7.3
K89/37	8	hanging wall	-0.8	5.3	7.2	7.8
K89/39	7.8	hanging wall	-1.0	5.1	7.0	7.6
	1000lnα (granite-water)		9.1	2.7	0.84	0.19
K90/CA1	6.8	granite	-2.0	4.1	6.0	6.6
K89/GP9	7.7	granophyre dike	-1.1	5.0	6.9	7.5